

Aug., 2008

JEM-EUSO Mission Phase-A Research 2007 Report



JEM – EUSO Collaboration



JEM-EUSO Mission Collaborators List

Participating countries and participants in JEM-EUSO (as of Apr., 2008)

156 members from 10 countries and 57 institutes are participating.

Japan: Toshikazu Ebisuzaki, Hitoshi Omori, Kouki Maekawa, Yosuke Hachisu, Kazuhiko Katahira, Masayoshi Mizutani, Yoshiya Kawasaki, Yoshiyuki Takizawa, Satoshi Wada, Kazuhiko Kawai, Hiroshi Mase, Kenji Shinozaki, Takayo Ogawa(RIKEN),

Fumiyoshi Kajino, Michinori Sakata, Yoshiaki Yamamoto, Fumitaka Sato, Noboru Ebizuka, Tokonatsu Yamamoto (Konan Univ.), Motohiko Nagano, Yoshiro Miyazaki (Fukui Univ. of Technology), Toru Shibata, Naoto Sakaki (Aoyamagakuin Univ.), Naoya Inoue (Saitama Univ.), Yukio Uchibori (National Institute of Radiological Sciences), Kenichi Nomoto (Tokyo Univ.), Yukihiko Takahashi (Tohoku Univ.), Masahiro Takeda (ICRR), Hirohiko Shimizu, Yasuo Arai, Yoshimasa Kurihara, Junpei Fujimoto (KEK), Shigeru Yoshida, Keiichi Mase (Chiba Univ.) , Yoshihiko Mizumoto, Jun-ichi Watanabe, Susumu Inoue, Katsuaki Asano, Toshiki Kajino (NAOJ), Hirokazu Ikeda, Mutsumi Suzuki, Hajime Yano (ISAS/JAXA), Toshio Murakami, Daisuke Yonetoku (Kanazawa Univ.), Naoshi Sugiyama (Nagoya Univ.), Yoshitaka Itow (STE, Nagoya Univ.), Shigehiro Nagataki (Yukawa Institute for Theoretical Physics, Kyoto Univ.), Akinori Saito (Graduate School of Science, Faculty of Science, Kyoto Univ.), Shinsuke Abe, Makoto Nagata (Kobe Univ.), Toshiki Tajima (Japan Atomic Energy Agency), Michuyuki Chikawa(Kinki Univ.), Fumiko Tajima (Hiroshima Univ.), Mitsuteru Sato (Hokkaido Univ.)

USA: J. H. Adams, S. Mitchell, M.J. Christl, J. Watts Jr., A.English, Roy Young (NASA/MSFC) , Y. Takahashi, D. Gregory, M. Bonamente, V. Connaughton, K. Pitalo, J.Hadaway, J. Geary, R.Lundquist, P. Reardon, T. Blackwell (Univ. Alabama), H. Crawford, E. Judd, C. Pennypacker (LBL, Univ. California ,Berkeley), V. Andreev, K. Arisaka, D. Cline (UCLA), A. Berlind ,T. Weiler, S. Czorna (Vanderbilt Univ.) , R. Chipman, S. McClain (Univ. Arizona).

France: D. Allard, J-N. Capdevielle, J.Dolbeau, P. Gorodetzky, J-J.Jaeger, E. Parizot, T. Patzak, D. Semikoz, J. Weisbard (APC Paris)

Germany: M. Teshima, H. Miyamoto, T.Schweizer (Max Planck Munich), A. Santangelo, E.Kendziorra, F.Fenu (Univ. Tübingen), P. Biermann (MPI Bonn), K. Mannheim (Wuerzburg), J.Wilms (Univ. Erlangen)

Italy: E. Pace, M. Focardi, P. Spillantini (Univ. Firenze) V.Bratina, A. Zuccaro, L.Gambicorti (CNR-INOA Firenze), A. Anzalone, O. Catalano, M.C. Maccarone, P. Scarsi, B. Sacco, G. La Rosa (IASF-PA/INAF), G. D'Ali Staiti, D. Tegolo (Univ. Palermo), M. Casolino, M.P. De Pascale, A. Morselli, P. Picozza, R. Sparvoli (INFN and Univ. Rome "Tor Vergata"), P. Vallania (IFSI-INAF Torino), P. Galeotti, C. Vigorito, M. Bertaina (Univ. Torino), F. Isgro, F.Guario, D. D'Urso, S. Russo (Univ. "Federico II" di Napoli), G. Osteria, D. Campana, M. Ambrosio, C. Aramo, G. De Rosa (INFN-Nappli)

Mexico: G. Medina-Tanco, J.C.D'Olivo, J.F.Valdés (Mexico UNAM), H.Salazar, O.Martines (BUAP), L.Villaseñor (UMSNH)

Republic of Korea: S. Nam, I. H. Park, J. Yang, J.H. Park, T. Chung (Ehwa W. Univ.), T.W. Kim (Ajou Univ.), S.W. Kim (Yonsei Univ.), K.K. Joo(Chonnam National Univ.)

Russia: Garipov G.K., Khrenov B.A., Klimov P.A. Panasyuk M.I., Yashin I.V. (SINP MSU), Naumov, D., Tkachev. L (Dubna JINR)

Switzerland: A. Maurissen, V. Mitev (Neuchatel, Switzerland)

Spain: D.Rodriguez-Frias, L.Peral, J.Gutierrez, R.Gomez-Herrero (Univ. Alcala)

Science Objectives

- Main Objectives : Astronomy and astrophysics through particle channel with extreme energies above 10^{20} eV
 - Identification of sources by the high-statistics arrival direction analysis
 - Measurement of the energy spectra from individual sources to constrain acceleration or emission mechanisms
 - ✧ Verification of GZK process by the detailed study of GZK features of individual sources
 - ✧ Confirmation of GZK recovery
 - ✧ Search for top-down components from cosmological origins
- Exploratory Objectives
 - Detection of extreme energy gamma-rays
 - ✧ Detection of primary gamma-rays from nearby sources
 - ✧ Detection of secondary gamma-rays from propagation process
 - ✧ Constraints on superheavy particles decay model and z-burst model
 - Detection of extreme energy neutrinos
 - ✧ Search for sources in the deep universe
 - ✧ Measurement of neutrino cross section in extreme energy
 - ✧ Constraints on the physics beyond the standard theory: superheavy particles, extra dimensions, and mirror symmetry
 - Study of the Galactic magnetic field
 - Verification of the relativity and the quantum gravity effect in extreme energy
 - Global observations of nightglows, plasma discharges and lightning

JEM-EUSO Executive Summary

Scientific Objectives

- Main Objectives : Astronomy and astrophysics through particle channel with extreme energies above 10^{20} eV
 - Identification of sources by the high-statistics arrival direction analysis
 - Measurement of the energy spectra from individual sources to constrain acceleration or emission mechanisms

- Exploratory Objectives
 - Detection of extreme energy gamma-rays
 - Detection of extreme energy neutrinos
 - Study of the Galactic magnetic field
 - Verification of the relativity and the quantum gravity effect in extreme energy
 - Global observations of nightglows, plasma discharges and lightning

Parameters of Instruments

- Field of View: $\pm 30^\circ$
- Aperture Area: 4.5m^2
- Optical bandwidth: 330—400nm
- Angular Resolution: 0.1°
- Pixel Size: 4.5mm
- Number of Pixels: $\sim 2.0 \times 10^5$
- Pixel Size at ground: 750m
- Duty Cycle: $\sim 20\%$
- Observational Area: $1.9 \times 10^5 \text{ km}^2$

Parameters of Mission

- Time of launch: year 2013
- Operation Period: 3 years (+ 2 years)
- Launching Rocket : H2B
- Transportation to ISS: non pressurized Carrier of H2 Transfer vehicle
- Site to Attach: Japanese Experiment Module/ Exposure Facility #2
- Mass: 1880 kg
- Power: 998 (operative), 424 W (non-operative)
- Data Transfer Rate: 297 kpbs
- Height of the Orbit: $\sim 430\text{km}$
- Inclination of the Orbit: 51.6°

Table of Contents

1. Mission Overview	4
2. Science objectives	7
2.1 Main Objective: Astronomy and Astrophysics through particle channel with extreme energy above 10^{20} eV	7
2.1.1 Identification of sources by the high-statistics arrival direction analysis	9
2.1.2 Measurement of the energy spectra from individual sources to constrain acceleration or emission mechanisms	12
2.2 Exploratory Objectives	16
2.2.1 Detection of extreme energy gamma rays	16
2.2.2. Detection of extreme energy neutrinos	20
2.2.3. Study of Galactic magnetic field.....	23
2.2.4. Verification of the relativity and the quantum gravity effect in extreme energies	24
2.2.5. Global observation of nightglows, plasma discharges, and lightning	25
3. Observation principle and instrumental and subsystem requirements	30
3.1. Observation principle.....	30
3.2. Accuracies of observables.....	31
3.2.1. Effective area	31
3.2.2. Accuracies on EAS observables	31
3.2.3. Dark current	33
3.3. Requirements against telescope performance.....	34
3.3.1. Scientific requirements	34
3.3.2. Success criteria.....	34
3.3.3. Observation capability	34
3.3.4. Instruments.....	34
3.3.5. Optics	34
3.3.6. Focal surface detector	35
3.3.7. Calibration system	35
3.3.8. Atmospheric monitor	35
3.3.9. Miscellaneous	35
4. Instrument	37
4.1. Overview	37
4.2. Optics Module.....	41
4.2.1. Overview	41
4.2.2. Lens materials	43
4.2.3. Optics module design.....	45
4.2.4. Performance	49
4.2.5. Tolerance analysis.....	53
4.2.6. Lens support structure.....	55
4.2.7. Filter.....	55
4.2.8. Lens manufacturing	56
4.2.9. Operation.....	61
4.2.10. Summary	61
4.3. Focal Surface Instrument	67
4.3.1. General.....	67
4.3.2. FS Detector	69
4.3.3 Focal Surface Electronics	85

4.3.4.	Operation.....	118
4.3.5.	Summary	119
4.4.	Atmospheric Monitor.....	123
4.4.1.	Outline.....	123
4.4.2.	Infrared Camera	124
4.4.3.	Light detection and ranging (Lidar)	130
4.4.4.	Slow data.....	136
4.4.5.	Operation.....	137
4.4.6.	Summary	137
4.5.	Calibration subsystem.....	141
4.5.1.	Definition	141
4.5.2.	Outline of the calibration system	141
4.5.3.	Pre-flight calibration	143
4.5.4.	Calibration in flight.....	146
4.5.5.	Operation.....	155
4.5.6.	Summary	155
4.6.	Support Sensor	158
4.7.	Bus System	158
4.7.1.	Structure part.....	158
4.7.2.	Structure Control (Mechanism) system	162
4.7.3.	Data Processing Unit / Power Distribution Unit.....	164
4.7.4.	Thermal Control and Thermal Analysis	166
4.7.5.	Interface	167
4.7.6.	Summary	169
5.	Expected Performance	175
5.1.	General Outline of END-to-END Simulation.....	175
5.2.	Baseline Estimation	176
5.2.1	JEM-EUSO Effective Acceptance.....	176
5.2.2	Triggering Efficiency	177
5.2.3	Expected Number of Triggered Events.....	178
5.2.4	Angular Resolution	179
5.2.5	X_{\max} Resolution	179
5.2.6	Energy Resolution.....	180
5.2.7	Detection Sensitivity for UHE Neutrinos	181
5.2.8	Comparison with Other Instruments.....	182
5.3.	Advanced Estimation.....	183
5.3.1.	Reconstruction of Observed Events in Cloudy Sky.....	183
5.3.2.	Performance with Advanced Optics and Photosensitive Device	183
5.4.	Summary	184
6.	Operation	186
6.1.	Launch and attachment to JEM-EUSO Port.	186
6.2.	Commissioning	186
6.3.	Regular observation	187
6.3.1.	Observation	187
6.3.2.	Trouble shooting	188
6.3.3.	JEM-EUSO telescope pointing.....	189
6.4.	Ground segment	189

6.4.1.	Mission activity planning and telecommand unit	189
6.4.2.	Data process and system monitor unit	189
6.4.3.	Data management and archiving unit	189
6.4.4.	SODC staff on duty	190
7.	Development Plan	191
7.1.	Feasibility study phase	191
7.1.1.	Plan	191
7.1.2.	Implementation structure	191
7.2.	Development phase	192
7.3.	Cost Budget	192
8.	Preparations status	195
8.1.	JEM-EUSO working group	195
8.2.	Activity of Planning Committee at RIKEN Discovery Research Institute	195
8.2.1.	Selection as the mission candidates of 2nd phase utilization of JEM-EF	195
8.2.2.	International Collaboration Meeting and International symposium	195
8.2.3.	Preparation of budget and improvement of organization at RIKEN	196
8.3.	Preparation status in each country	196
8.3.1.	U.S.A.	196
8.3.2.	Europe	196
8.3.3.	Korea	197
8.3.4.	Mexico	197
8.3.5.	Russia	197
8.4.	Development Schedule	198
Annex 1	: Dictionary of abbreviations	199
Annex 2	: Temperature analysis	201
Annex 3	: Recommendation by International Advisory Board	204
Annex 4	: Research Advancement Group of Extreme Space	208

1. Mission Overview

JEM-EUSO (Extreme Universe Space Observatory on Japanese Experiment Module) is a new type of observatory that uses the whole earth as a detector including the International Space Station (ISS) where a remote sensor is located. It observes transient luminous phenomena taking place in the earth's atmosphere caused by particles and waves coming from space. The sensor is a super wide-field telescope that detects extreme energy particles with energy above 10^{20} eV. This remote-sensing instrument orbits around the earth every ~ 90 minutes on board of the International Space Station (ISS) at the altitude of ~ 430km (Figure 1-1). An extreme energy particle collides with a nucleus in the earth's atmosphere and produces an Extensive Air Shower (EAS) that consists of numerous electrons, positrons, and photons. JEM-EUSO captures the moving track of the fluorescent UV photons and reproduces the calorimetric development of EAS.

The JEM-EUSO telescope has a super-wide Field-of-View ($\pm 30^\circ$) with two double sided curved Fresnel lenses and records the track of an EAS with a time resolution of $2.5 \mu\text{s}$ and a spatial resolution of about 0.75 km (corresponding to 0.1 degrees). These time-segmented images allow determining the energies and directions of the primary particles. The focal surface of the JEM-EUSO telescope is formed by about 6,000 multi-anode photomultipliers. The number of pixels is about two hundred thousands.

JEM-EUSO instrument can reconstruct the incoming direction of the extreme energy particles with accuracy better than several degrees. Its observational aperture of the ground area is a circle with 250 km radius and its atmospheric volume above it with a 60-degree field-of-view is about 1 tera-ton or more. The target volume for upward neutrino events exceeds 10 tera-tons. The instantaneous aperture of JEM-EUSO is larger than the Pierre Auger Observatory by a factor of 56 - 280 (Figures 1.1 and 1.2) when attached to ISS (Figure 1.3).

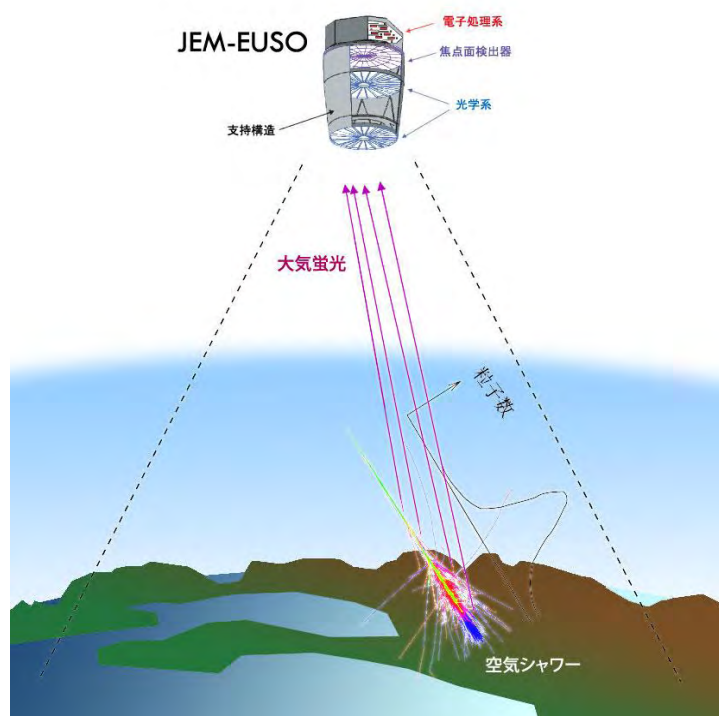


Figure 1-1 Principle of the JEM-EUSO telescope to detect extremely energy particles

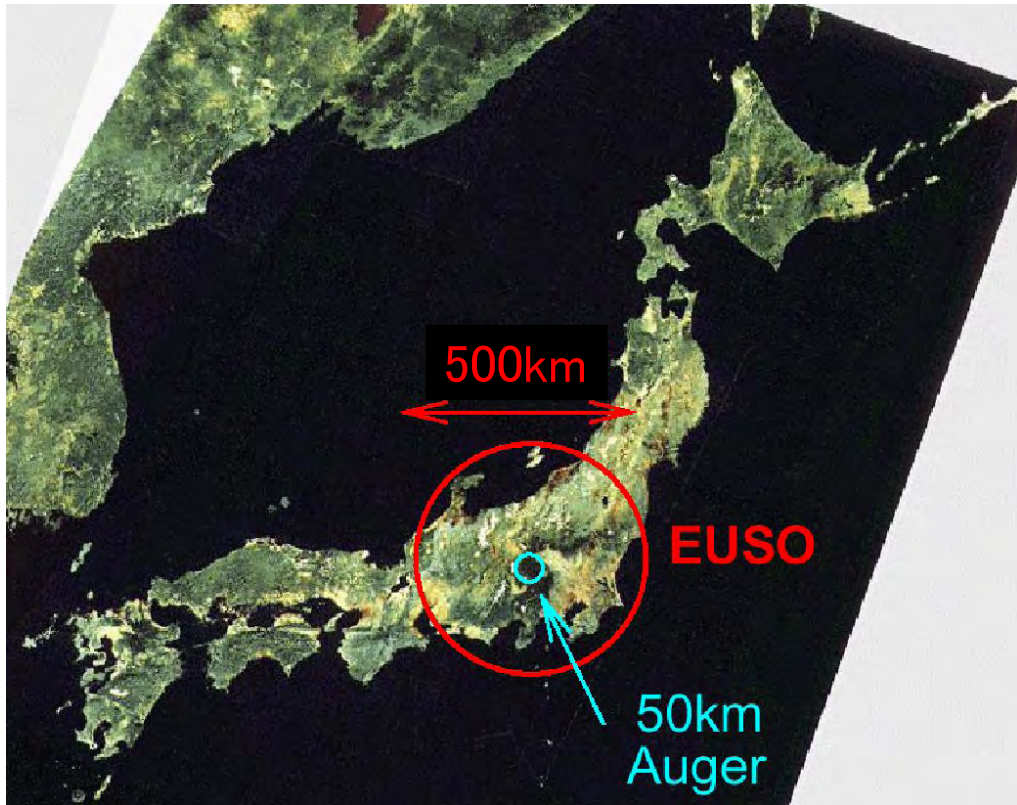


Figure 1-2 Area observed by the JEM-EUSO telescope in one shot

EUSO was originally selected by the European Space Agency (ESA) as a mission attached to the European Columbus module of the ISS. The phase-A study has been successfully completed in June 2004 under ESA. However, because of financial problems in ESA and European countries, the start of phase-B has been postponed for a long time. Japanese and U.S. teams re-defined EUSO as a mission attached to the Japanese Experiment Module/ Exposure Facility (JEM/EF) of ISS. They renamed it as JEM-EUSO and started the preparation targeting the launch of 2013 in the framework of the second phase utilization of JEM/EF utilization.



Nadir mode

Tilted mode

Figure 1-3 Artistic illustration of the JEM-EUSO telescope attached to the Japanese

Experiment Module of the International Space Station

JEM-EUSO reduces the threshold energy down to around 10^{19} eV and increases the effective area by means of advances in technology and to superior features of JEM/EF. The reduction in the threshold energy is realized by 1) new lens material and improved optical design, 2) detectors with higher quantum efficiency, 3) improved algorithm for event trigger. The increase in effective area is realized by inclining the telescope from nadir which is named as tilted mode (figure1-3). In this tilted mode, the threshold energy gets higher since the mean distance to EAS and atmospheric absorption both increase. First half of the mission lifetime is devoted to observe lower energy region in nadir mode and second half of the mission to observe high energy region by tilted mode. JEM-EUSO is planned to be attached to JEM/EF of ISS, which will be launched in 2013 by H2B rocket and conveyed by HTV (H-II transfer Vehicle) to ISS.

2. Science objectives

Science objectives of JEM-EUSO consist of two main objectives and five exploratory objectives.

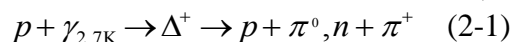
2.1 Main Objective: Astronomy and Astrophysics through particle channel with extreme energy above 10^{20} eV

Main objective of the JEM-EUSO is to start the new field of astronomy that uses particle channel with extreme energies (10^{19} eV $<$ E $<$ 10^{21} eV). JEM-EUSO is planned to detect more than one thousand events in the atmosphere above 7×10^{19} eV in its five years operation. The number of events first exceeds the critical quantity that observe the events from all the objects inside several hundreds Mpc and make possible the followings:

- Identification of sources by the high-statistics arrival direction analysis
- Measurement of the energy spectra from individual sources to constrain acceleration or emission mechanisms

The energy spectrum of charged particles from space (cosmic-ray) on the earth is beautifully expressed by a power law function of $\sim E^{-3}$ over eleven orders of magnitude (from 10^9 eV to 10^{20} eV; (Figure 2-1). The highest energy particles that we are concerned here correspond to the highest end of the spectrum with energies around 10^{20} eV. Gigantic accelerators must exist somewhere in the universe: Their acceleration energy is eight orders of magnitudes higher than those of most advanced accelerators ever made on earth.

The discussion on where the break of this power law spectrum is, can be traced back to 40 years ago, which is just after the discovery of the microwave cosmic background. Penzias and Wilson [21] reported the discovery of the cosmic 2.7 K thermal black body radiation which was produced very early in the history of the Universe and which led to the undisputed acceptance of the “Big Bang” theory of the origin of the Universe. The perfect thermal character and smoothness of the CMB (cosmic microwave background) proved conclusively that this radiation is indeed cosmological and that, at the present time, it fills the entire Universe with a 2.7 K spectrum of radio to far-infrared photons with a density of ~ 400 cm $^{-3}$. Shortly after the discovery of the CMB, Greisen [1] and Zatsepin & Kuz'min [2] independently predicted that pion-producing interactions of extreme energy protons with CMB photons should produce a cutoff at $\sim 5 \times 10^{19}$ eV. Since then, this predicted effect is known as the GZK (Greisen-Zatsepin-Kuz'min) effect. For protons, this occurs when the pion production threshold is reached. The reaction,



slows down the proton and leads to an effective attenuation length of 50 Mpc for a proton of 10^{20} eV. The length of 50 Mpc is about the size of the Virgo Cluster to which Our Galaxy belongs, and is just a small fraction of the total size of the Universe.

On the other hand, a spectral steeping can be also explained by the acceleration limit in the case of bottom-up scenario. The highest energy of the particles is determined by the product of the size and the strength of the magnetic field (Figure 2-2). The celestial objects that satisfy the condition for acceleration up to 10^{20} eV are neutron stars with a super strong magnetic field ($> 10^{12}$ – 10^{13} G), jets of the active galactic nuclei (AGNs), gamma-ray bursts (GRB), radio galaxies, and clusters of galaxies. Since these sources are all lined up along the theoretical upper-limit to the energy of 10^{20} eV (see Figure 2-2), it is likely that the spectrum of extreme energy particles shows an acceleration limit in its spectrum around 10^{20} eV in addition to the trans-GZK complex. If an acceleration limit is not seen in the spectrum, it is strongly suggested that new unknown astronomical objects located in the blank region (upper-right corner) of the Hillas diagram should exist. There is no theoretical

reason of the absence of such objects.

In the case of top-down scenario, EECRs are produced by a decay or annihilation of a super-heavy particle (SHP: $m \sim 10^{22} - 10^{25} \text{ eV}/c^2$). The end products of this process are well studied: the neutrinos and gamma rays are abundant compared with nucleons. By a factor or two of three [4, 5]. The energy spectrum is as hard as $E^{-1.9}$ [6, 7, 8, 9].

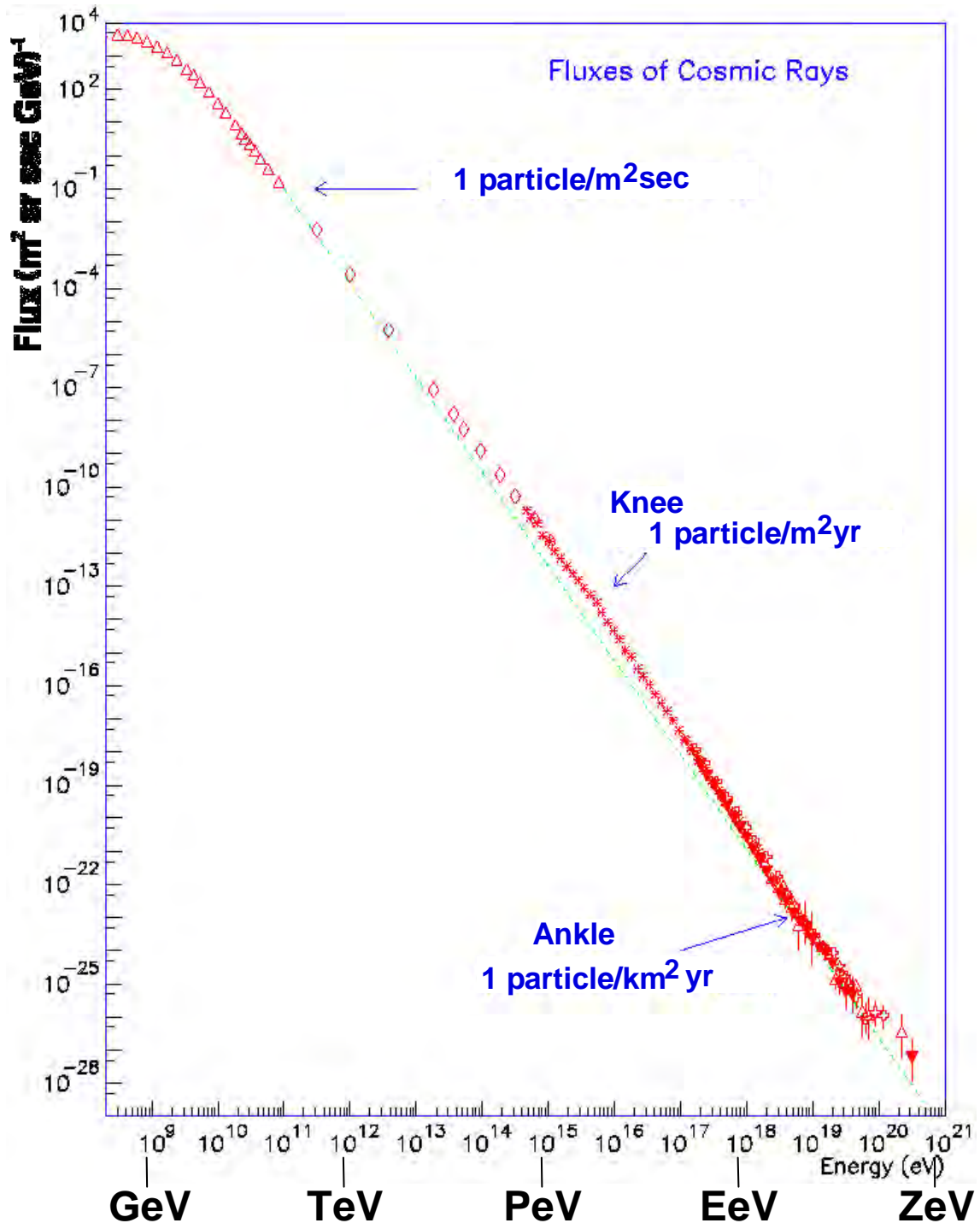


Figure 2-1 Energy spectrum of cosmic rays. The flux is well expressed by a power-law function proportional to E^{-3} over eleven orders of magnitude from 10^9 eV up to 10^{20} eV.

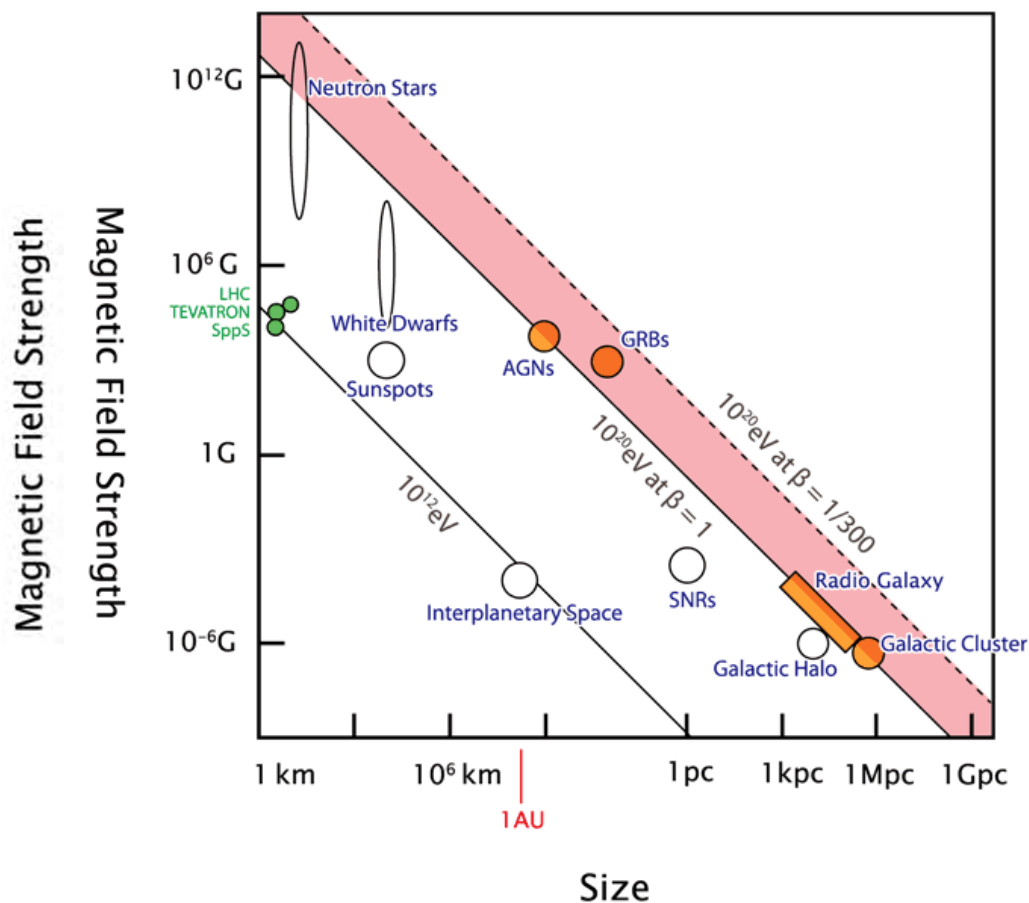


Figure 2-2 Hillas diagram showing theoretical upper limits on the energy of the particle determined by the size and strength of magnetic field on the celestial objects.

2.1.1 Identification of sources by the high-statistics arrival direction analysis

JEM-EUSO is designed to identify the origins of EECRs by the high-statistics arrival direction analysis. The extreme energy particles are not deflected by the magnetic field more than one degree (in the case of proton) and one can be traced back to their origin in the measured arrival directions with accuracies better than a few degrees. The arrival direction analysis is divided into point source analysis and global anisotropy analysis.

First, the point source analysis seeks small-scale clusters about the accuracy of the instrument. In fact, AGASA experiment [14] reported small-scale anisotropy (cluster; Figure 2-3) and some correlation in the arrival direction of EECRs with AGNs (blazars). HiRes experiment [15] also indicated such a cross-correlation with AGNs. Furthermore, the Auger experiment reported a correlation between the arrival direction of the EECR events above 6×10^{19} eV and the distribution of nearby AGNs[16; Figure2-4], though it does not reject the possibility of GRBs as the sources of

EECRs: the distribution of AGN is known to have a similar to that of the material distribution in general. If this report of the Auger experiments is in the case, JEM-EUSO with much higher statistics will identify several dozen sources which several dozen events belong to and will allow us to identify them to known astronomical objects (Figure2-5). In other words, we will know the distances to the individual sources. This makes spectral analysis much clearer than the current situation, as discussed in the next sections.

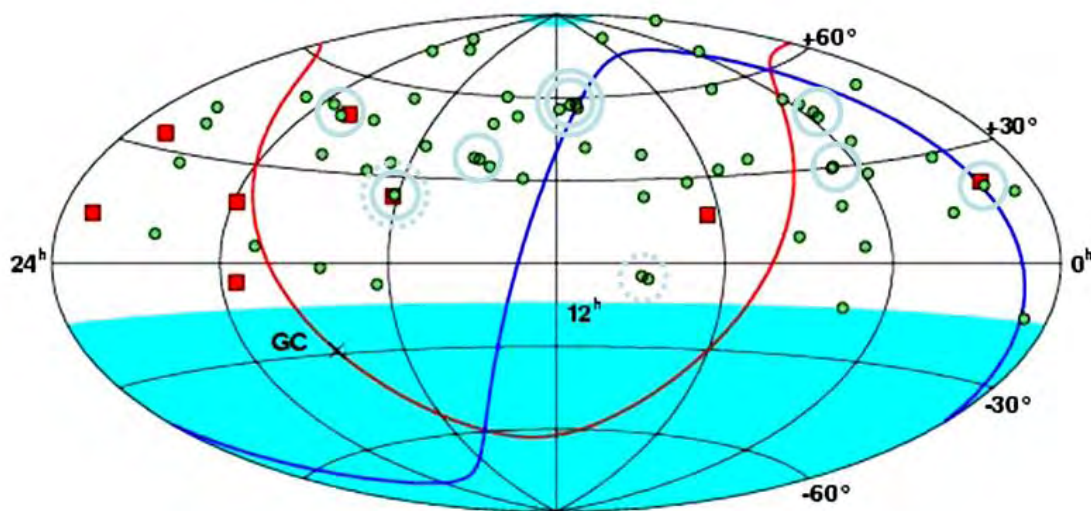


Figure 2-3 Distribution of arrival direction of extreme energy particles by AGASA experiment [14]. Red squares and green circles denote the events above $E > 10^{20}$ eV and the event of $E = (4-10) \times 10^{19}$ eV, respectively.

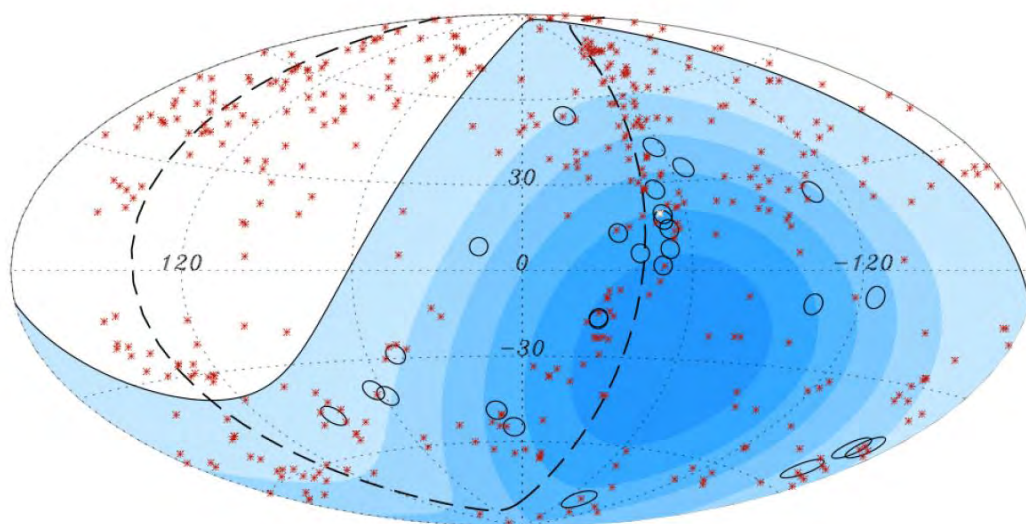


Figure 2-4 Distribution of the arrival directions of the events above 5.7×10^{19} eV (open circle) by Auger experiment. The directions of nearby AGN within 71 Mpc distance are shown by crosses (Galactic coordinates and the center is the galactic center) [16].

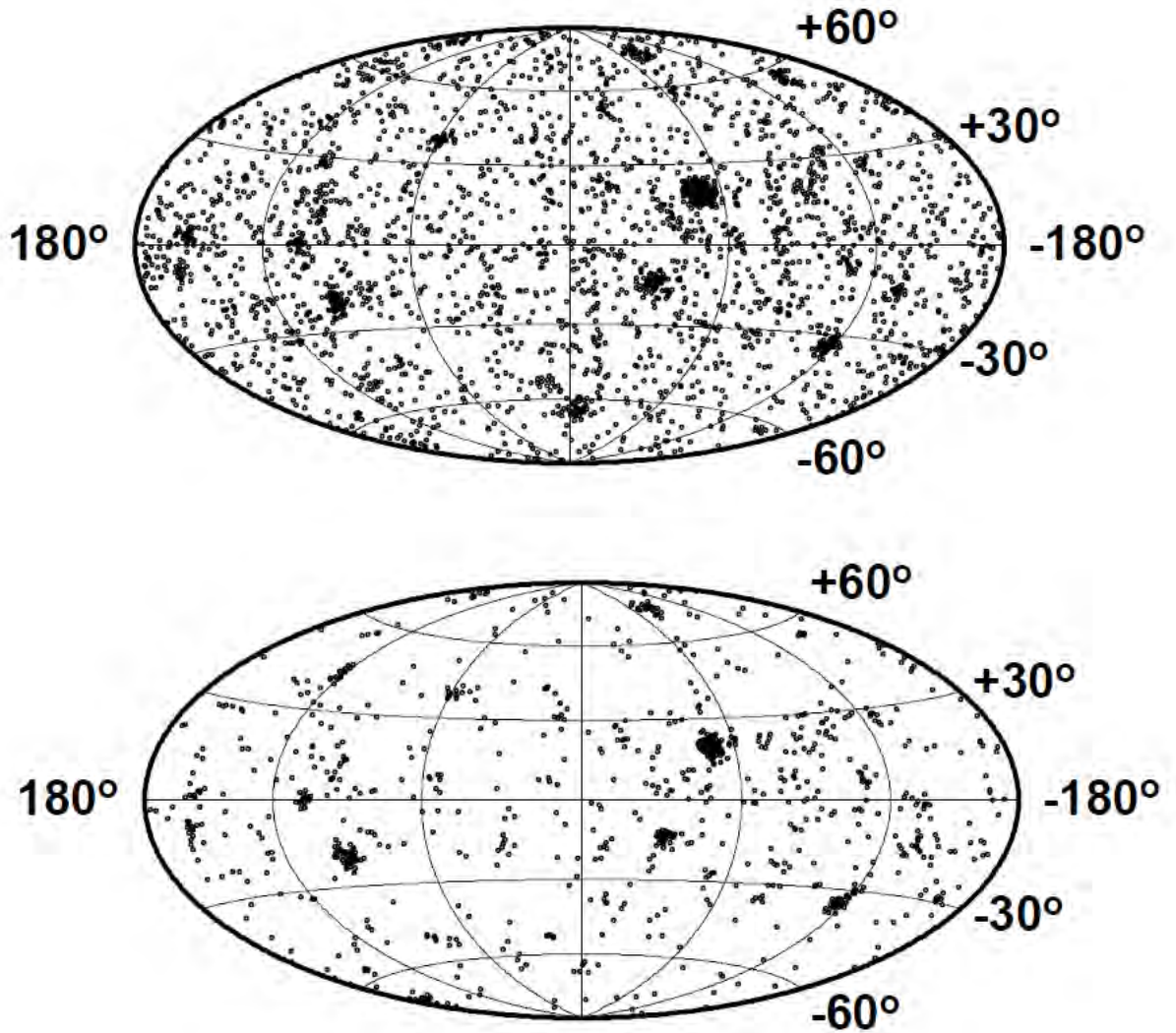


Figure 2-5 Numerically simulated arrival direction distribution of EECRs if AGNs are the sources of EECRs[17]. Here, we assume that 42 AGNs are sources of EECRs and their particle luminosity is proportional to X-ray luminosity observed by INTEGRAL. Upper and lower diagrams correspond to the sky maps observed by JEM-EUSO for $>5 \times 10^{19}$ eV (3000 events) and for $>7 \times 10^{19}$ eV (1000 events) .

In a global anisotropy analysis, arrival directions are integrated for spherical harmonics. Such an analysis should reveal the source distributions of extreme energy particles. For the best analysis, the exposure must be uniform over the whole sky. ISS has an inclination of 51.6 degrees, and onboard JEM-EUSO can observe both north and south skies equally and would offer a nearly uniform exposure for all over the entire celestial sphere.

If the extreme energy particles come from cosmological distances as those of GRBs and AGNs, several dozen sources uniformly distributed in the sky will be discovered. If the source belongs to the Milky Way Galaxy, the distributions would show an enhancement in the direction of Sagittarius. If they belong to clusters of galaxies, they show an enhancement in the directions of Virgo, Pisces,

Perseus, and Hercules [19].

On the other hand, in the top-down scenario, SHPs are certainly CDM (cold dark matter) that are supposed to broadly distribute with an enhancement toward the galactic center can also produce extreme energy particles. If the source of extreme energy particles is such a SHP dark matter, it could be concentrated in our Milky Way Galaxy and might show an enhancement in the direction of Sagittarius [20,21,22], and small clumps can be seen in the outer region [10,11,12,13].

In the Z-burst model [23, 24], which follows the standard model of the particle physics, a high energy neutrino/anti-neutrino annihilates with a relic anti-neutrino /neutrino in the galactic halo to produce charged extreme-energy particles. The annihilation of a neutrino pair produces about 20 gamma rays and about two nucleons on average. If the annihilation takes place in nearby clusters of galaxies, daughter nucleons may arrive to the earth without GZK loss. On the other hand, gamma rays are hardly observed, since their mean-free paths are much shorter (100 kpc – 1 Mpc) than the distances to the nearby clusters. If the sources of extreme energy neutrino/anti-neutrinos come from point sources, resultant charged particles show small-angle anisotropy. If the neutrino mass is heavy enough, the arrival direction of the resultant charged particles shows an enhancement towards the center of the galaxy or nearby clusters of galaxies [25]. This is recognized as the unique method to detect cosmic neutrino background (CNB), which is originated from the very early Universe just one second after the Big Bang. With Information carried by CNB, one can trace back 400 thousands years before the cosmic microwave background (CMB) epoch in hydrogen atoms were formed from plasma. CNB is the last undetected important component of the relic of the Big Bang. In such a way, JEM-EUSO explores the Z-burst model and aim at the detection of CNB. If the detection of neutrinos is achieved, then the key discriminator of models is if such neutrinos are abundant form, the direction of super-cluster. This kind of neutrino anisotropy measurement will give a constraint on Z-burst model and give us a chance to estimate the absolute mass of neutrinos.

Such a complete arrival direction analysis can be done only with JEM-EUSO. For, example, Auger experiment has some difficulties to make a comprehensive analysis of the arrival direction due to relatively low statistics. Since the aperture of Auger experiment is 20 times smaller than that of JEM-EUSO, the statistics of EECR events is also significantly limited and is less than 100 events above 10^{20} eV even after 10 years operation. In addition, the Auger experiment operated in the Southern hemisphere suffers from the very strong galactic magnetic fields in the southern sky dominated by the galactic center and galactic plane. If one uses lower energy events, for example, at 4×10^{19} eV, the deflection by the galactic magnetic field (~5 times stronger) is as large as 10 degrees. That is enough to erase possible signatures of any small angle anisotropy.

Furthermore, most of the southern sky is covered by zone of avoidance for which optical observations are difficult in optical wavelength. It makes very difficult to perform correlation analysis to AGNs.

2.1.2 Measurement of the energy spectra from individual sources to constrain acceleration or emission mechanisms

Many experiments, such as AGASA, HiRes, and Auger are planned and materialized to confirm the theoretical prediction of spectral steeping by GZK process. Figure 2-6 summarizes their results [26]. HiRes experiment[27]、Auger experiment [28] released the report arguing that there are a spectral steeping around 6×10^{19} eV. However, this spectral steeping can be caused by the acceleration limit as well as GZK process.

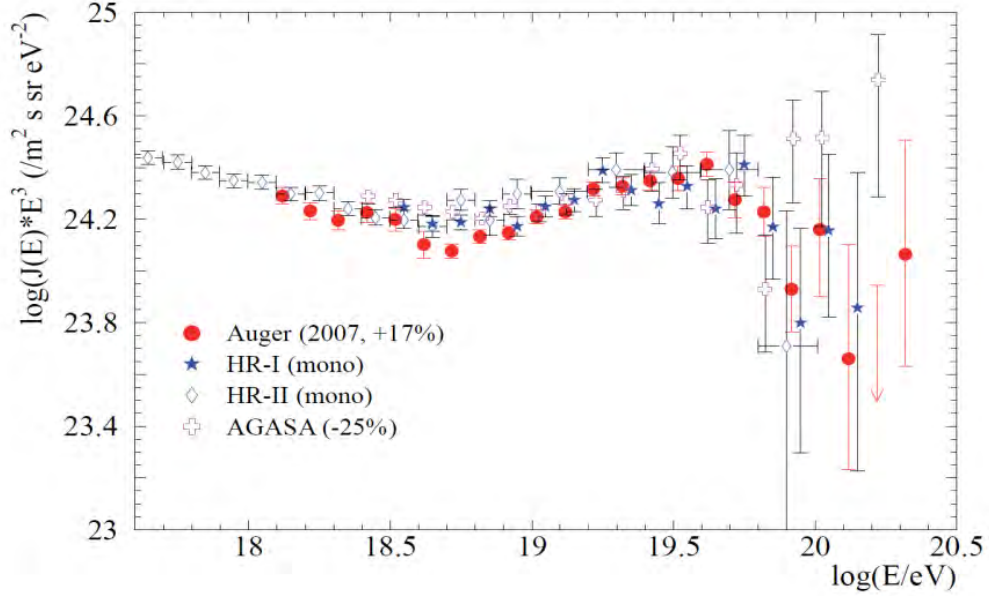


Figure 2-6 Energy spectra of EECRs observed by Auger, HiRes, and AGASA [26]. Here, the energy scale is shifted by +17% for Auger and by -25% for AGASA by -25%. The vertical axis is multiplied by E^3 .

However, two effects can be separated by comparison with the energy spectra of spatially separated sources identified to the known astronomical objects. Figure 2-7 shows the energy spectrum expected from the sources at different distances from the Earth. The GZK features are not prominent in the sources within 10Mpc. In other words, We can get direct clue to understand acceleration mechanisms by the comparison with the spectral properties of these nearby sources and the other observational facts of the identified sources in different energy bands.

On the other hand, GZK features are dominantly prominent in the energy spectra from the sources distant than 50 Mpc if GZK process is in the case [29]. When we see the spectrum breaks correlated with distance of identified objects as expected by the GZK mechanism from these relatively distant sources, we can firmly conclude the break is due to the GZK mechanism and Lorentz invariance is verified in the very high Lorenz factor of $>10^{11}$.

In addition to that, if a strong source lies around or outside of the GZK horizon, all of the GZK features, including GZK recovery, would be observed. It allows us to construct the firm theory of the trans-GZK complex and the acceleration limit. The comparison between theoretical and observed spectra gives us the absolute energy calibration in this energy region. This is a real breakthrough to understand the origins of high energy cosmic rays with $E > 10^{15}$ eV and to explore the extreme universe and fundamental physics.

Furthermore, the acceleration limit is much higher than 10^{20} eV: It suggests some unknown objects (ones not in Hillas diagram) accelerating particles or new acceleration mechanisms in bottom-up scenario, or top down scenario.

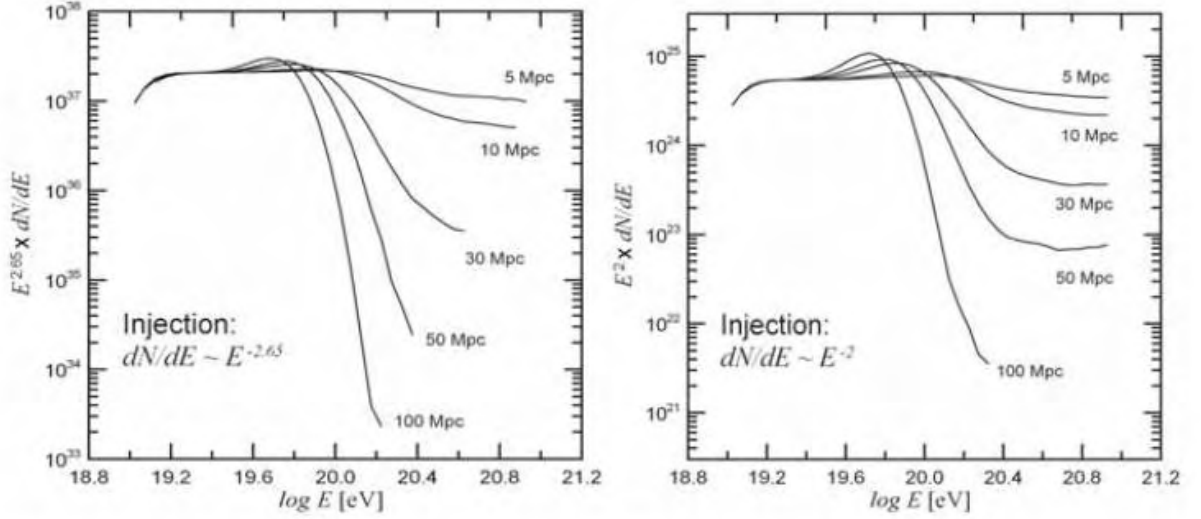


Figure 2-7 GZK features strongly depend on the distances to the sources. Left: in the case the intrinsic spectral index is $E^{-2.65}$. Right: in the case the intrinsic spectral index is E^{-2}

Concerning the GZK energy spectrum, Stecker [31] and Berezhinsky [30] independently calculated the mean energy loss time for protons propagating through the CMB in intergalactic space as a function of energy. According to them, GZK process is responsible for the trans-GZK complex in the energy spectrum, which consists of:

- (1) Steepening spectral slope at $(5-10) \times 10^{19}$ eV, the so-called GZK cutoff
- (2) GZK bump at $(4-8) \times 10^{19}$ eV. It is formed by particles arriving from distances of several or several dozen D_{GZK} , which lose energy on their path. The observed spectrum of such particles results from accumulation around GZK cut off energy.
- (3) Ankle region feature around $(0.3-3) \times 10^{19}$ eV. Highly red-shifted GZK bump made by particles coming from cosmological distances.
- (4) GZK recovery, that arises above 3×10^{20} eV. It consists of particles produced at distances smaller than D_{GZK} .

The trans-GZK complex, as a whole, reflects the history of the Universe. JEM-EUSO will figure out this complex by determining (1), (2), and (4) of the trans-GZK complex with much more statistics than any other ground-based experiment. These three features give us the absolute energy calibration for the fluorescence method. So far, the reported energy spectra are significantly different in energy scale. The detailed comparison with the results of the ground-based experiments allows us to unite the energy spectra above the ankle region.

Here we have considered just the GZK effect and spectral modification from steady EECR sources, however, it shall be also discussed the case of transient EECR sources. If the major sources of EECRs are transient and the time scale of the emission of EECRs is shorter than the energy dependent time lag due to the propagation in the magnetized universe, the drastic change of the spectrum can be expected like a discussion by E. Waxman, i.e., the energy spectrum becomes mono energy (peak energy simply depends on the distance and the age of the explosion). With GZK effect, the resultant spectra and time evolution from the single source may become very complicated. So far there are no such dynamic calculations including the GZK effect on EECRs from transient sources. Of course, the secondary neutrino may show very an interesting energy-time development.

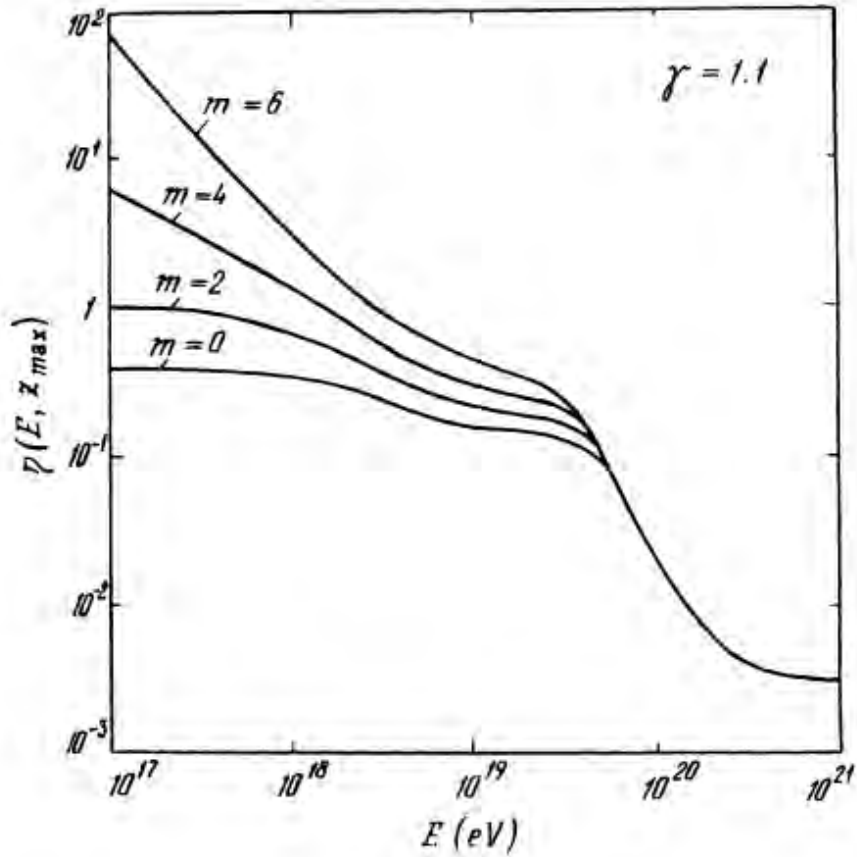


Figure 2-8 Theoretically predicted modification function, η , of the spectrum of extreme energy particles due to the effect of propagation through the space. Here, m is a parameter that represents the degree of evolution effect of the origin objects of them. Energy spectrum is obtained multiplication of η and intrinsic spectrum before propagation [30].

Ground-based experiments, such as Auger and Telescope Array experiments, have major problems to perform the analysis described above. Besides the limited statistics, the Auger experiment, which uses water tanks with a stronger sensitivity to muons than electromagnetic components as ground particle detectors, suffer from a systematic error of several tens percent. This is caused by model dependence on muon production in the first collision between the extreme energy particle and the nucleus in the atmosphere, and statistical fluctuations. The shape of the energy spectrum easily changes depending on the treatment of the muon production models.

In case of the Telescope Array experiment, the feasible exposure by ten years operation is as small as about 10 times of that of AGASA. Only several dozen extreme energy events above 10^{20} eV are expected, which limits the detailed the discussions on their origin. The Telescope Array experiment, using scintillation detector as its surface array detector, is relatively free from the problems of the interaction model dependence. This may provide the firm result of the energy spectrum. Against the Auger experiment, it locates in Northern Hemisphere and hence the effect of the Galactic magnetic field is moderate. This is a merit and in particular, existence of the small angle clusters, transferring the heritages of AGASA and plays a role of a guidepost for JEM-EUSO.

The observation from the ground still suffers from another problem. EAS in the energy region above 3×10^{20} eV develops in a quite different way in the dense atmosphere near ground due to the Landau-Pomeranchuk-Migdal (LPM) effect [32,33]. Conventional energy determination method cannot be applied to EAS affected by such LPM showers. Even with fluorescence telescopes on the ground, it is also difficult to determine energy with a high accuracy. For extreme energy events in most cases, they detect far distant and low elevation showers with relatively poor qualities.

Apart from the large aperture, the merit of JEM-EUSO is relatively free from the problems which ground-based experiments have. Fluorescence telescopes including JEM-EUSO telescope measure the electromagnetic component that carries 90% of the energy of EAS. Observing from the space, JEM-EUSO telescope may observe EASs that develop at high altitudes (above 20 km) where the LPM effect does not work due to low atmospheric density. With high accuracy in energy determination and high statistics allow us to reveal the mystery of origin and propagation of the extreme energy particles. These achievements will imitate the new astronomy through particle channel, which only JEM-EUSO is able to.

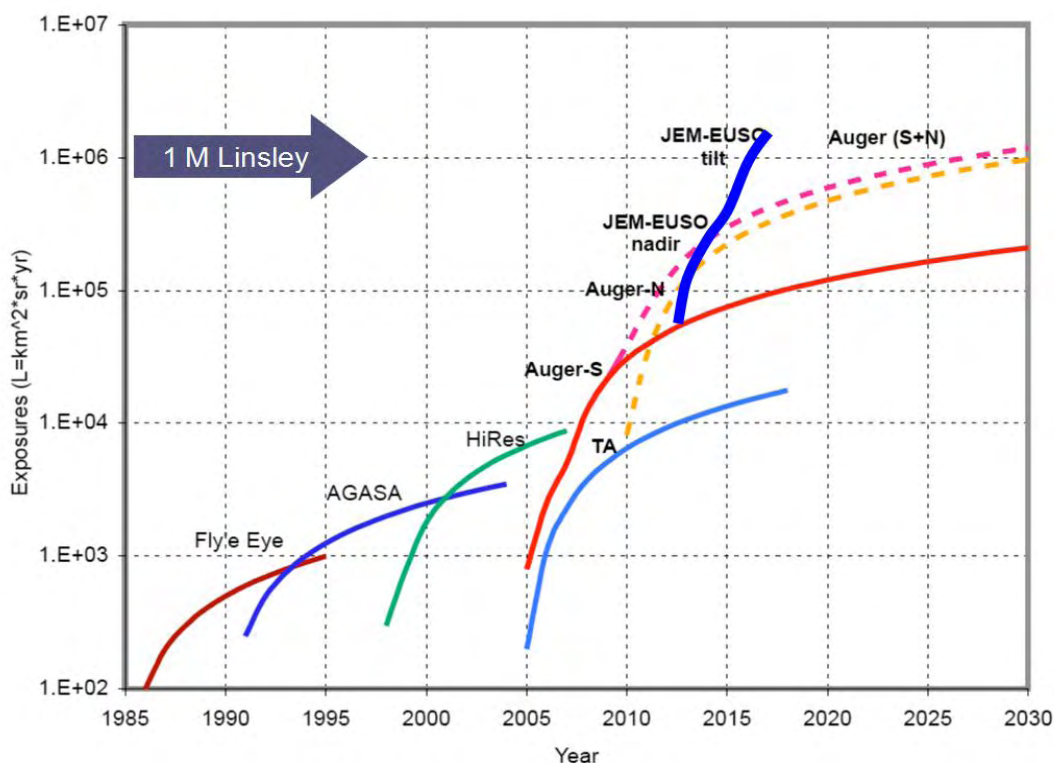


Figure 2-9 Expected cumulative exposure of JEM-EUSO (Thick blue curve). For comparison, the evolution of exposure by other retired and running EECR observatories is shown.

2.2 Exploratory Objectives

2.2.1 Detection of extreme energy gamma rays

The air showers produced by gamma rays can be distinguished by X_{\max} (the slant depth of shower maximum) from those by nucleons and nuclei. Gamma rays above 5×10^{19} eV collide in the deeper atmosphere since their collision cross section significantly shrinks due to the LPM effect. In other words, X_{\max} of the gamma rays significantly increases with energy. On the other hand, gamma rays

above 5×10^{19} eV interact with the geomagnetic field at the altitude of $\sim 1,000$ km from the ground and produce positron-electron pairs. The electromagnetic shower including several hundred synchrotron photons has been already developed before it reaches the upper atmosphere. This process makes X_{\max} smaller. Since the threshold energy of such interaction is determined by the strength of the geomagnetic field perpendicular to the direction of the particle, strong north-south effect appears in X_{\max} distribution at certain energy. In other words, the gamma rays from the direction of the poles have a smaller probability for pair-creation and show larger X_{\max} [34]. Figure 2-10 shows the probability of gamma rays to interact with geomagnetic field in various point of the earth [35].

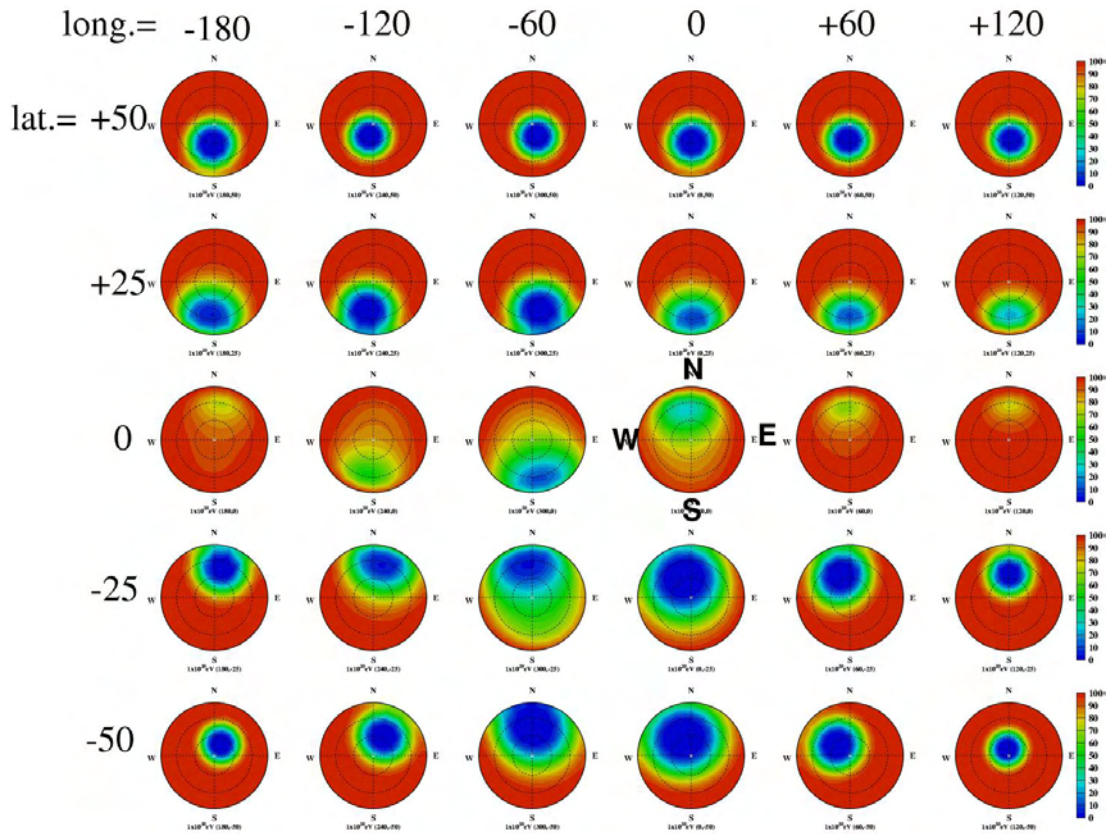


Figure 2-10 Angular dependence of the probability of the extreme energy gamma rays interacting with the geomagnetic field [35]. Each panel shows horizontal coordinates at the different longitude and latitude on the Earth. From the bluer patches of the sky, extreme energy gamma rays more likely to initiate an EAS with large X_{\max} due to the LPM effect.

Extreme energy gamma rays tend to produce an EAS that develop significantly slowly compared with the case of proton primaries. JEM-EUSO Mission is capable of detecting more than 3000 (1000) events above 5×10^{19} eV (7×10^{19} eV), which enable to determine the flux of gamma ray primaries at high accuracy.

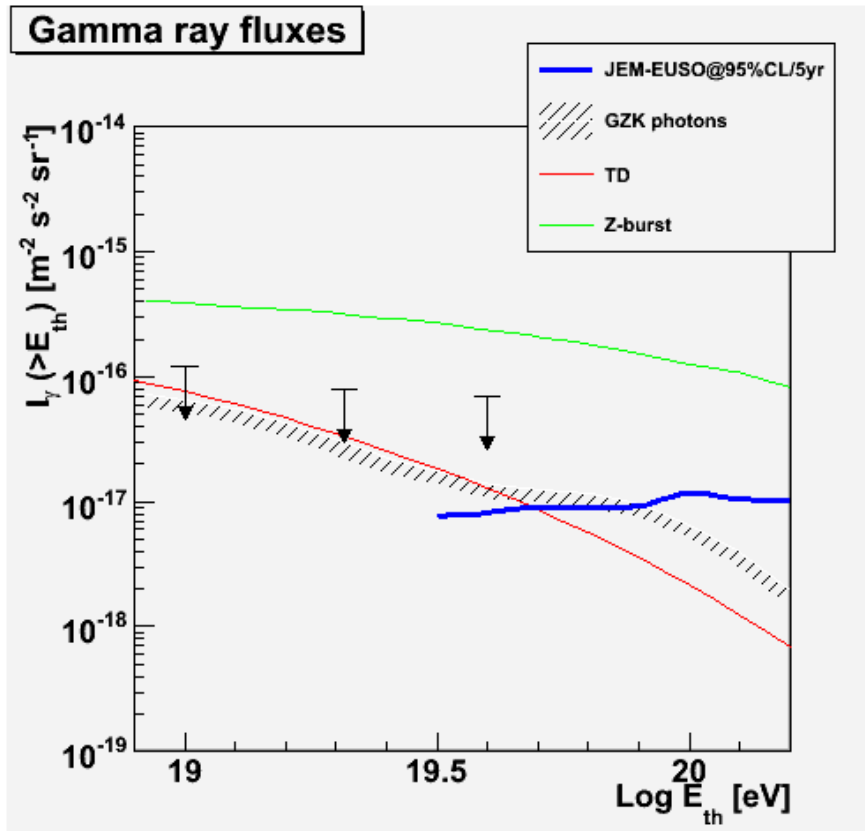


Figure 2-11 Sensitivity of gamma rays by five years operation of JEM-EUSO Mission. The blue curve indicates the expected upper limit of gamma ray flux at 95% confidence level (CL) under a null gamma ray assumption. The arrows are the upper limits at the same CL given by Pierre Auger Observatory [36]. Green, red and shaded curves show the theoretical prediction by Z-burst [37], TD [38] and GZK photon [38] models, respectively.

The flux of gamma rays in extreme energy is a key parameter to discriminate origin models. Figure 2-11 shows the sensitivity of gamma rays by five years operation of JEM-EUSO Mission. The Auger experiment recently reported the upper limit on gamma ray flux that a few percent of EECR flux above 10^{19} eV. Under null gamma ray assumption, JEM-EUSO is capable of putting more stringent upper limit by an order of magnitude at overlapping energies. To give the constraint on origin models or their parameters, the gamma ray flux above 10^{20} eV is essential and is extracted by the five years operation of JEM-EUSO.

Extreme energy gamma rays create electron-positron pair due to the CMB photons or infrared background photons and therefore they are restricted to propagate large distances. As energy increases, the off-shell component overwhelms this restriction and the Universe gets more transparent against electromagnetic component.

Figure 2-12 shows such effect. Above 10^{20} eV, gamma ray detection is expected and therefore large-scale experiment is desired.

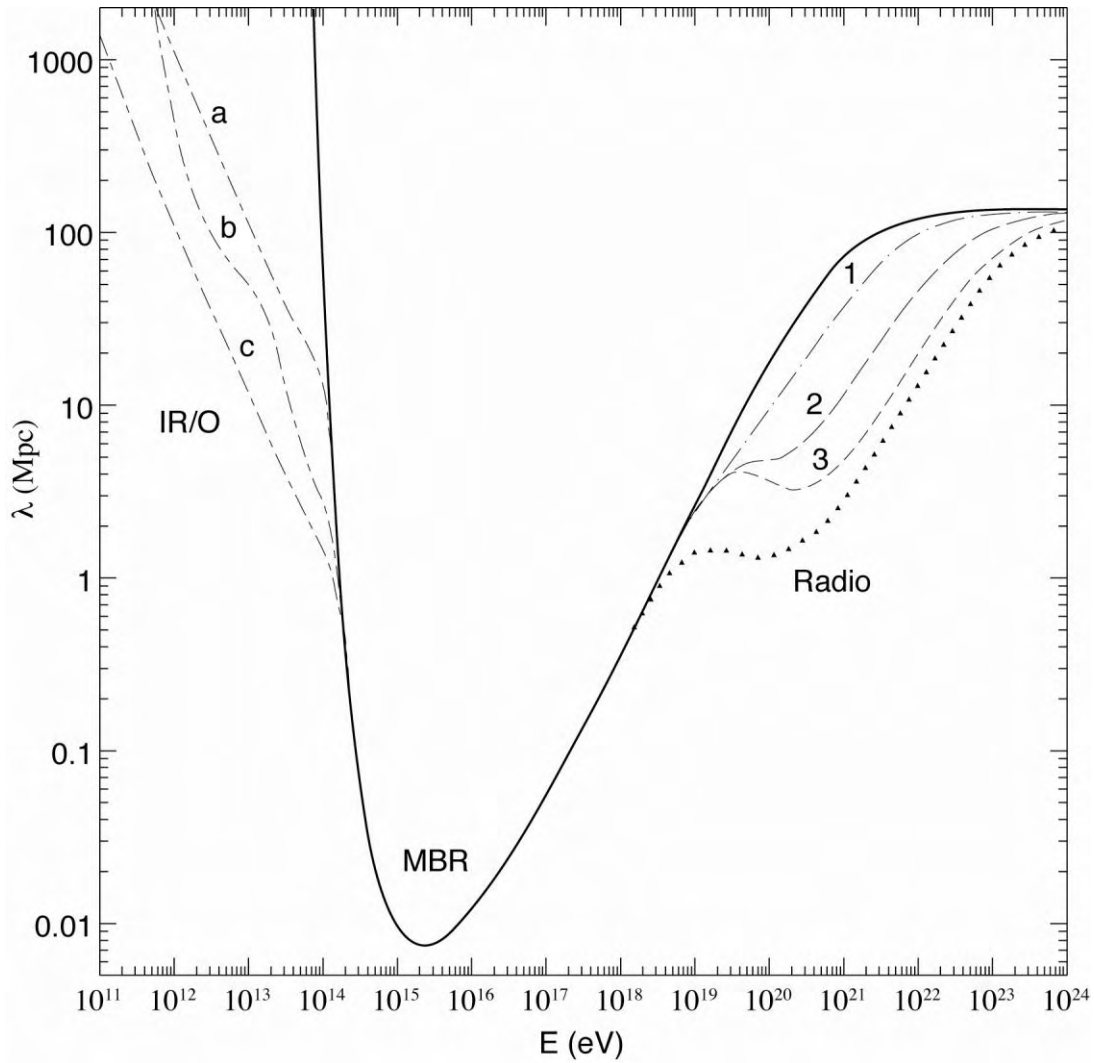


Figure. 2-12 Mean free path of gamma rays through propagation in CMB photons as a function of energy [39]. Around 10^{13} eV, the mean free path is sharply shortened as energy increase. Below 10^{14} eV, the gamma rays interact with radio background and CMB photons. Curves a, b and c demonstrates the effect by different assumed infrared background flux. Curves 1,2 and 3 show the case of cutoff frequency of extragalactic radio backgrounds of 5, 2 and 1 MHz, respectively. The triangle indicates the case of lower limit of radio background flux.

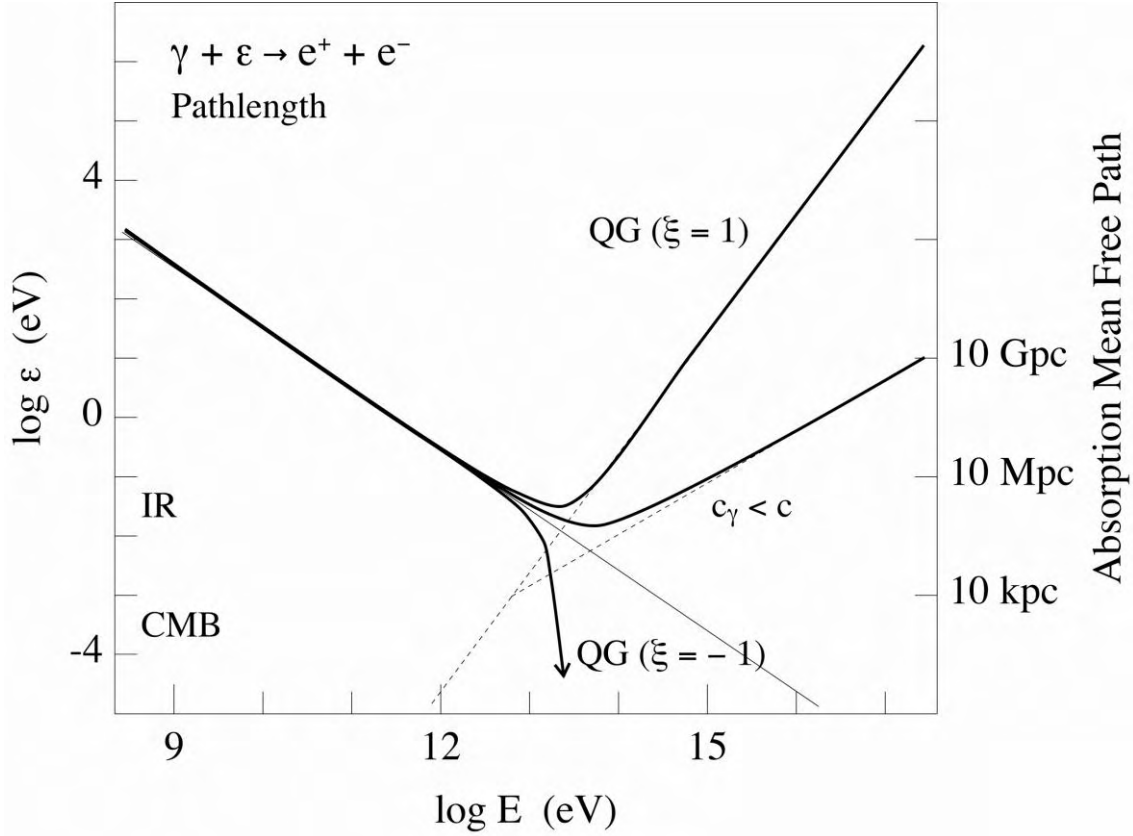


Figure. 2-13 Propagation distance of electromagnetic component in the Universe [40,41]. At higher energies, the pair creation process is suppressed by quantum gravity effect and the propagation distance sharply increases. This enables to observe the deep universe by electromagnetic component

2.2.2. Detection of extreme energy neutrinos

Cosmogenic neutrinos may steadily be produced in universe in the GZK process in which an extreme energy proton loses its energy through the collisions with CMB photons (Figure 2-14). Many authors have already pointed out the possibility that neutrinos are also produced during acceleration in high-energy objects such as AGNs or GRBs. Neutrinos have so small an interaction cross-section with matter that they can directly convey the information of the acceleration site. They escape the source region without being blocked by the matter. They do not suffer from deflections by magnetic fields and propagate far longer than the distance to the cosmological horizon. This characteristic makes neutrinos be the best probe to understand EECR accelerators at cosmological distance. In Z-burst mode [23,24], neutrinos themselves are considered to be the origin of EECRs. The observation of neutrinos enables to identify the EECR sources at cosmological distances. The determination of neutrino flux is a probe for the evolution parameter of EECR production (m in Figure. 2-8) at $z=1-2$ since they are highly dependent each other.

The neutrino-nucleus cross-section at extreme energies is the key parameter to discuss feasibility of the neutrino detection. It is only little known and is extrapolated from the lower energy manmade accelerator experiment. The electron-proton collision accelerator HERA experiment reported the neutrino-nucleus cross-section to be $\sigma_{\nu N}^{CC} \sim 2 \times 10^{-34}$ [cm²] at $\sqrt{s} = 314$ [GeV]. This

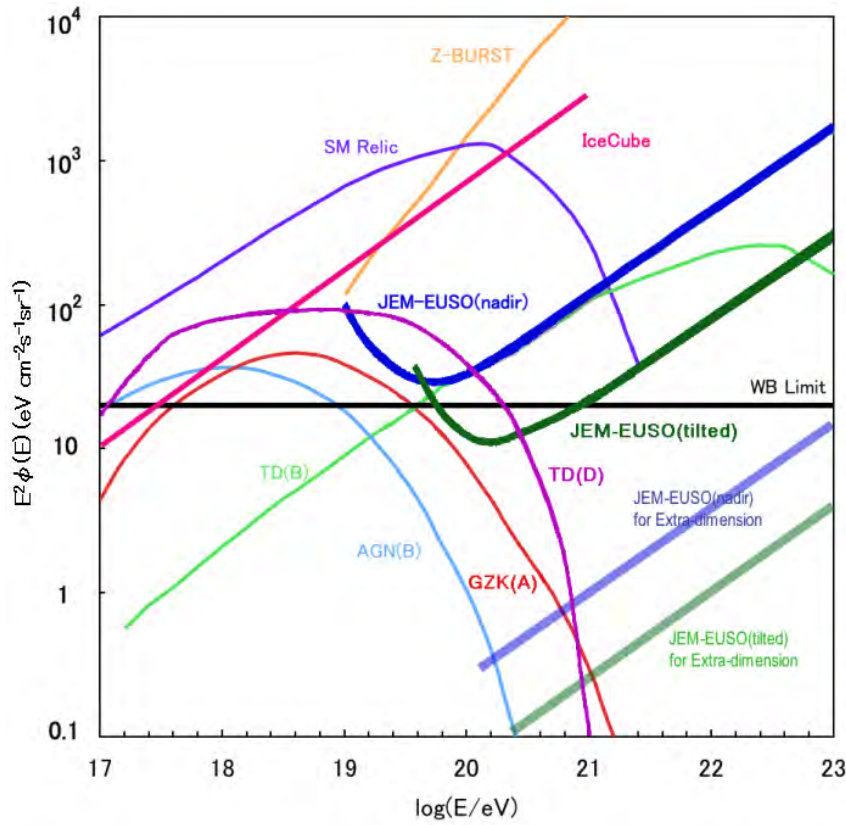


Figure 2-16 The flux sensitivity of JEM-EUSO detecting 1 event /energy-decade per year. An observational efficiency of 25% is assumed. Blue and green dark curve shows the case of nadir and tilt modes, respectively. Straight lines at high energies indicate the case of extra-dimension model. As of IceCube (red line), 2.3 events/energy-decade per 10 years is assumed. Black line denotes the Waxman-Bahcall limit.

By its three-years of operation in tiled mode, JEM-EUSO can set a more stringent upper-limit on neutrino flux than the Waxman-Bahcall limit [31] around 10^{20} eV (Figure 2-16). It is expected that the JEM-EUSO detects at least a few cosmogenic neutrino events (GZK(A) in Figure. 2-14). If top-down scenario for super-GZK particles (blue and green curves) is the valid case, at least several events are expected in a year. On the other hand, if JEM-EUSO does not observe a significant number of neutrino events exceeding a few events, it would exclude most of the top-down models, as well as the extra-dimensional models.

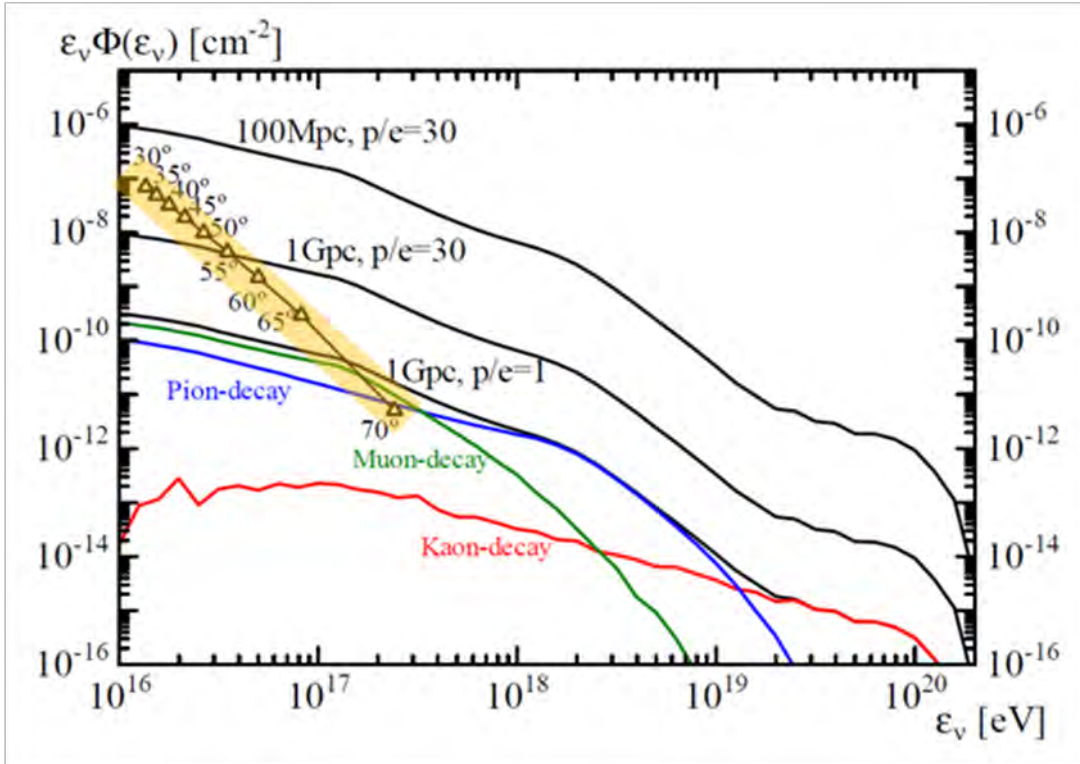


Figure. 2-17 Expected flux of tau neutrino from GRB as a function of energy [45]. The sensitivity of JEM-EUSO at tilt-mode for the different titling angles.

Neutrinos, for example ones from GRBs, interact in the Earth crust around a few hundred m or a few km and initiate UAS. The Čerenkov beam from UAS originated by the tau-neutrino directly impinges onto the JEM-EUSO telescope and brightens only one pixel in one GTU (2.5 μ s in baseline design). The observable threshold energy depends upon neutrino cross-section, the distance to EAS, angle to EAS etc. Such direct Čerenkov events in general are so strong that EAS event above 10^{16} eV are detectable (Figure 2-17). In case of the nearby (~ 1 Gpc) GRB event occurring in the field of view of JEM-EUSO, a bunch of upward direct Čerenkov events are expected. Such GRB events are estimated to occur ~ 1.2 time per year. In order to confirm such events real UAS events, some sophisticated selection criteria have to be added to distinguish from detector noise or from the reflected Čerenkov mark of standard downward lower energy EAS.

The neutrino cross-section is uncertain and highly model-dependent. The extra-dimension models [46] in which the Universe is supposed to consist of ten or eleven dimensions are among the favored models to unify the quantum mechanics and gravitation theory. In these models, the neutrino cross-section is predicted to enhance more than 100 times of one predicted in the Standard model. As a result, hundreds of neutrino events are expected to be observed by JEM-EUSO and therefore the number of neutrino events may be a first experimental probe of the extra-dimension models. In addition, the ratio of events between HAS and UAS gives an quantitative estimation of neutrino cross-section around 10^{14} eV at center of mass system [43].

2.2.3. Study of Galactic magnetic field

Once the point sources are seen for events above 10^{20} eV, other member events of these sources at different energies can be also identified. Changes in apparent point-spread-function depend on energy, magnitude and direction helps determine the Galactic magnetic field (GMF) [47]. Since

Larmor radius is much larger than the galactic planes that dominantly contributes to GMF, particles are deflected adiabatically: GMF do not spread away the cluster of EECR events around the sources but only deform the shapes to several degrees depending on the energy the strength of GMF along the line of sight.

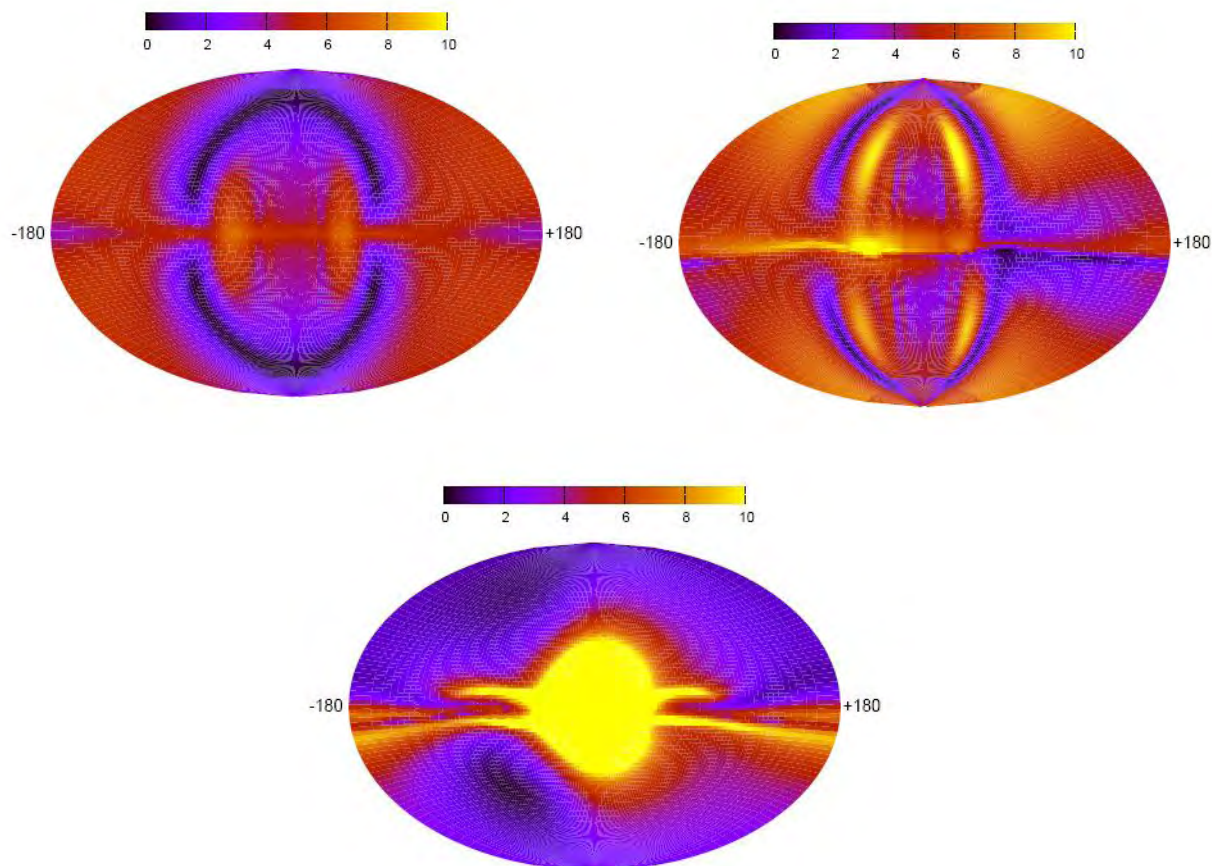


Figure 2-18 Deflection angle by the model of different magnetic field for the EECR with a rigidity of 4×10^{19} eV [47]. Top: Tinyakov and Tkachev (BBS-A)[48]; Middle: Harari, Mollerach and Roulet (BBS-S) [49]; Bottom: Prouza and Smida (BBS-S)[50]

GMF is poorly known so far due to the limited data only from Faraday rotation of polarized radio sources. Independent direct measurement of GMF will provide new information, which is performable by extreme energy particle deflections. When JEM-EUSO finds several bright sources less than 10 Mpc, GMF structure will be directly determined by charged particles since the deflection by extragalactic magnetic field is negligibly small.

2.2.4. Verification of the relativity and the quantum gravity effect in extreme energies

The energy in the center of mass system in the interaction between an extreme energy particle and a target nucleus in atmosphere exceeds the energy reachable by the Large Hadron Collider (LHC) by more than three orders of magnitude. In the extreme energy frontier, many new physics that may change the spectral shape in the trans-GZK energies have been proposed and seriously discussed.

JEM-EUSO can examine the Lorentz invariance at very high Lorentz factors of $\gamma \sim 10^{11}$. Special relativity is undoubtedly confirmed at lower energies so that the GZK cutoff is expected to be imminent. Gamma ray mean free path in vacuum is shorter than 100 kpc by interactions with CMB unless strong quantum gravity effect prohibits $\gamma\gamma \rightarrow e^+e^-$ process. Hence, no gamma ray events are expected as extreme energy particles in the standard physics. However, if GZK-process itself would not appear as expected [32, 33, 34, 35, 36], it could imply some local limitations of Lorentz invariance in the presence of external fields. In such ways, extreme energy particles offer a unique way to experimentally test the relativity and quantum gravity theories. The standard quantum physics also predicts that EAS suffers from large fluctuations of cascading due to the LPM effect [19, 20]. It becomes considerable from 5×10^{20} eV (5×10^{21} eV) for proton (iron nucleus). JEM-EUSO can observe such fluctuations in EAS developments with high statistics. Furthermore, the existence of SHP can be tested if they decay or annihilate into extreme energy particles delivering photons and neutrinos as well as nucleons.

2.2.5. Global observation of nightglows, plasma discharges, and lightning

JEM-EUSO will also observe atmospheric luminous phenomena such as lightning, nightglow, and meteors. The nightglow in the wavelength between 330 nm - 400 nm is dominated by the emission from oxygen molecules in Herzberg I band around the boundary region at an altitude of 95 km between mesosphere and thermosphere. This emission is reported to have a strong correlation with the green line (557.7nm) of oxygen atom [57]. The stripes (width of 40km) of the emission of this green line are observed to move in the observation from the ground [58]. These stripes are believed to be produced by the gravity wave formed in troposphere and propagated to the upper atmosphere (Figure 2-19) [58]. This propagation of gravity wave may affect the energy and angular momentum transfer to the mesosphere and thermosphere. In order to study these phenomena, rockets and satellite observations are actively planned [59].

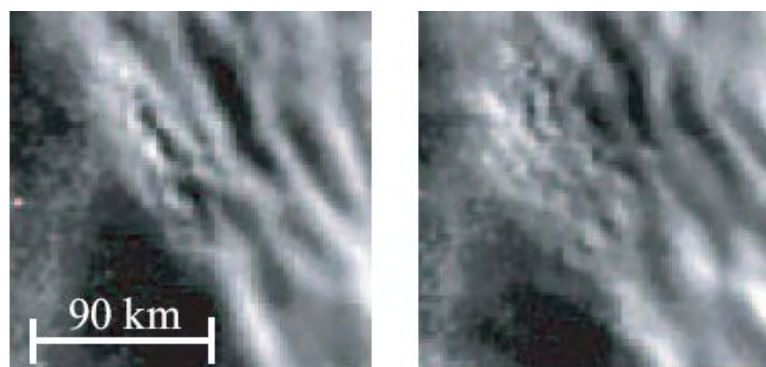


Figure 2-19 The stripes observed in the night glow by OH molecules. Similar stripes are expected to be observed in near UV band.

When the heating of the ground surface has set up the severe updraft and resulting instable stratification in the troposphere, a cumulonimbus or thundercloud will develop to dissolve the instability. Generally, a thundercloud is an aggregate of convective cells that accompany severe updrafts or downdrafts whose wind speed reaches several 10 m/s. Each convective cell has its own unique life cycle, which consists of developing phase, mature phase and decaying phase. During the developing phase in this lift cycle, collisions between ice crystals, graupels, and droplets

will accelerate the electrification in the thundercloud. When the electric field between the charging layers inside a thundercloud and between the thundercloud and the ground exceeds the threshold of the breakdown electric field, a discharge will occur between them to neutralize the charges. These discharge phenomena are called as lightning discharges.

Recently, lightning-emitted optical flashes and electromagnetic waves are successfully measured by satellites. These results are essentially useful for climatology, disaster prevention science, water cycle science, and other research fields. One of these results is derived from the FORTE satellite. FORTE satellite first succeeds in detecting electromagnetic waves emitted by lightning discharges in the VHF band. Using FORTE data, results showing the discharge morphology of Narrow Bipolar Events (NBEs) and Cloud-to-Ground events (CG) are reported. NBE is a discharge event that has a time constant of $<1 \mu\text{s}$, 100m-order discharge path length, and radiation energy of $>100 \text{ kW}$. It is suggested that NBE detected at the satellite altitude is the most powerful VHF emission radiated by lightning discharges and that the optical emission related to NBE would be very weak though it has not been observed simultaneously at the satellite yet. In contrast, CG event is the electromagnetic emission radiated from the negative leader or return stroke, which has current amplitude of several 10 kA. It is reported that NBE is only observed at the initiation phase of the negative cloud-to-ground discharges. From the intensive satellite and ground-based observations it is also reported that the NBE is strongly related with the cloud-to-cloud discharges occurring at the 10-20 km altitude. Gurevich and Zybin 2004 [62] suggested that NBE would reasonably explained by the runaway breakdown triggered by EAS that consists of mainly 3 MeV relativistic electrons. Thus, the wavelength of the optical emission related to NBE is not in the visible range but in the near UV range (330-400 nm) same as EAS. This scenario is consistent with the observational result showing that the visible optical emission of NBE is very weak. Optical energy of NBE is estimated to be 10-100 J, which can be detected by JEM-EUSO (16 J corresponds to 10^{20} eV). If the simultaneous observation of NBE using optical and electromagnetic instruments of JEM-EUSO and JEM-GLISM mission which will be installed at JEM EF in 2011 is realized, it may be possible to obtain direct observational evidence showing that NBE is generated by cosmic rays and that lightning discharges are triggered by cosmic rays. Research groups of the JEM-EUSO mission initiated the establishment of the agreement of the future collaborative observations with the JEM-GLISM and ASIM mission (lightning and TLE observation mission led by ESA).

New type of lightning-associated discharge phenomena above thunderclouds has been identified in 1990s, called as sprites, elves, and blue jets (Fig 2-20). It is suggested that sprites are discharge phenomena related to cloud-to-ground discharges, which generate quasi-electrostatic field above the thundercloud and accelerate ambient electrons. Recently it is implied that the electromagnetic pulse from the horizontal lightning current may play an important role to determine the occurrence condition of TLEs. In order to clarify them, it is essential to carry out nadir observation of sprites and to identify horizontal distribution of sprites. However, it is difficult to carry out nadir observation of TLEs since the optical instruments naturally watch both lightning emission and TLE emission almost simultaneously. It is known that the lightning discharges generating TLEs has a time constant of $\sim 1 \text{ ms}$ and that the delay time of sprites from the parent lightning discharges is $>1 \text{ ms}$. Thus, one solution to distinguish both emissions is to employ high-speed imaging technique with the time resolution of 1 ms at least. Since the time resolution of JEM-EUSO imaging observation is $2.5 \mu\text{s}$, it is possible to identify the spatial distributions of sprites and clarify the generation mechanism of sprites. Moreover, JEM-EUSO has an enough potential to detect weak optical emission originated from the streamers, which may precede the main discharges of TLEs.

Furthermore, satellites detect several GRBs probably associated with lightning from the earth

[64] . Such runaway electrons produced by cosmic-rays might be accelerated by the quasi-static electric field of the discharge associated with lightning. JEM-EUSO would keep monitoring both EECR tracks and runaway phenomena to see whether there is any recognizable relationship. Other atmospheric phenomena that would be observable by JEM-EUSO have been included in the mission studies.

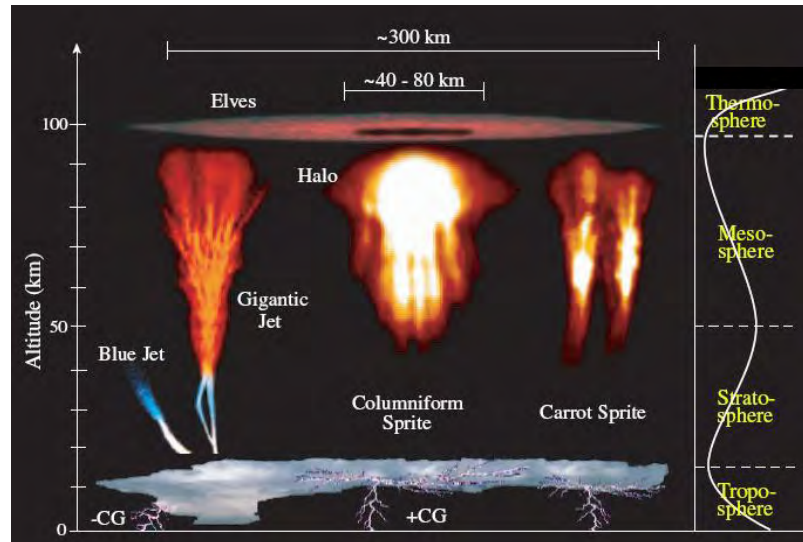


Figure 2-20 Various transient luminous events associated with lightning

References

- 1) Penzias, A.A. and Wilson, R.W. 1965, *Astrophys. J.* 141, 419.
- 2) Greisen, K., 1966, *Phys. Lett.* 16, 148.
- 3) Zatsepin, G. T. and Kuz'min, V. A. 1966, *JETP Phys. Lett.* 4, 78.
- 4) Berezhinsky, V. Kachelriess, M. and Vilenkin, A., *Phys.Rev. Lett.* 79, 4302, 1997.
- 5) Aloisio, R. Berezhinsky, V., and Kachelrieb, M., *Physical Review, D.* 69, 094023, 2004.
- 6) Sakar, S. and Toldra, R. *Nucl. Phys..* B621, 495, 2002
- 7) Berezhinsky, V. and Kachelrieb, M., *Physical Review, D.* 63, 034007, 2001.
- 8) Birkel, M. and Sarkar, S., *Astropart. Phys.* 9, 297 1998.
- 9) Barbot, C. and M. Drees, M., *Phys. Lett. B* 533, 107 2002; *Astropart. Phys.* 20, 5 2003.
- 10) Navarro, J. F., Frenk, C. S., and White, S.D.M, *Astrophys. J.* 462, 563, 1996
- 11) Moore, B. *et al. Adtrophys. J. Lett.* 524, L19, 1999
- 12) Fukushige, T. Kawai, A. and Makino, J., *Astrophys. J.*, 606, 625-634, 2004.
- 13) Diemand, J., Kuhlen, M., Madau, P. *astro-ph/0611370*, 2006.
- 14) Takeda, M. *et al.* 1999, *Astrophys. J.*, 522, 255.
- 15) Gorbunov, D.S. and Troitsky, S.V. *Astroprt. Phys.* 23, 175; Abbasi, R. U.et.al, 2006, *Astrophys. J.*, 636, 680.
- 16) Auger Collaboration, *Science* 318, 896, 2007.
- 17) Ghisellini, G. *et al.*, arXiv:0806.2393.
- 18) Takami, H., private communication / Takami, H., and Sato, K., arXiv:0710.0767
- 19) Takami, H., Yoshiguchi, H. and Sato, K. *Astrophys. J.*, 639, 803-815, 2004.
- 20) Berezhinsky, V., Blasi, P. and Vilenkin, A., *Phys.Rev.D*, 58:103515,1998
- 21) Berezhinsky, V. Mikhailov, A.A. *Phys. Rev. D.*, 58, 10315, 1998.
- 22) Medina-Tanco, G. and Watson, A., *Astropart. Phys.* ,12, 25, 1999.
- 23) Weiler, T. J. *Phys. Rev. Lett.*, 49, 234, 1982.
- 24) Weiler, T. J. *Astrophys. J.*, 285, 495, 1984.
- 25) Ringwald. A. and Wong, Y.Y.Y., *J. Cosmol. Astropart. Phys.* 12, 005, 2004.
- 26) Medina-Tanco, G., Teshima, M. and Takeda, M. *Proc. 29th ICRC Tsukuba*, 747.
- 27) Abbasi, R.U. *et al.*, *Phys. Rev. Lett.* 100, 101101, 2008.
- 28) Pierre Auger Collaboration, *Phys. Rev. Lett.* 101, 061101, 2008.
- 29) Medina-Tanco 2008, private communication.
- 30) Berezhinsky, V.S. and Grigorieva, S.I, 1988, *Astron.Astrophys.* 199, 1.
- 31) Stecker, F.W. *Nature*, 1989, 342, 401.
- 32) Landau, L.D. and Pomeranchuk, I.J., *Dokl.Akad.Nauk SSSR*, 92,535, 1953.
- 33) Migdal, A.B., *Phys. Rev.* ,103,1811, 1956.
- 34) Vankov, H. P., Inoue, N., and Shinozaki, K., *Physical Rev. D*, 67, 043002 , 2003.
- 35) Sakaki, N. *International Journal of Modern Physics*, 20, 7020-7022, 2005.
- 36) Aglietta, M. et al. (the Pierre Auger Collaboration), 2008, *Astropart. Phys.*, 29, 243-256.
- 37) Semikov, DV. for the Pierre Auger Collaboration, *Proc. of Int. Cosmic Ray Conf.*
- 38) Gelmini, GB; Kalashev, OE and Semikoz, DV., 2005, arXiv:astro-ph/0506128.
- 39) Coppi, P.S., and Aharonian, F.A. 1997, *Astrophys. J. Letters*, 487, L9-L12.
- 40) Kifune, T. 1999, *Astrophysical Journal*, 518, L21-24.
- 41) Coleman, S. and Glashow, S.L., 1999, *Phys. Rev. D*, 59, 116008.
- 42) Lieu, R. and Hillman, L.W. 2003, *Astrophys. J.*, 585, L77-L80.
- 43) Palimares-Ruiz, S.,Irimia,A.,and Weiler, T.J, *Physical Rev. D*, 73, 083003, 2006.
- 44) Waxman, E and Bahcall, J., *Phys.. Rev.. D*, 59, 23002, 1999.
- 45) Asano, K. private communication / Asano, K., and Nagataki S., *Astrophys. J.* 640 L9-L12,

2006.

- 46) Anchordoqui, L.A., Feng, J.L. and Goldberg, H., *Physics Letters B*, 535, 1-4, 302-308, 2002.
- 47) Kacheliess, M., Serpico, P. and Teshima, M., *Astropart. Physics*, 26 378, 2006.
- 48) Tinyakov, P. G. and Tkachev, I. I., *Astropart. Phys.* 18, 165, 2002.
- 49) Harari, D., Mollerach, S. and Roulet, E. , *JHEP* 9908, 022, 1999.
- 50) Prouza, M. and Smida, R., *Astron. Astrophys.* 410, 1 (2003)
- 51) Jain, A., Jain, P. Mackay, D.W., and Palston, J., *International Journal of Modern Physics A*, 17, 533-554, 2002.
- 52) Sato, H. and Tati, T., *Prog. Theor. Phys.* 47, 1788, 1972.
- 53) Yamaguchi, Y., *Prog. Theor. Phys.*, 2003, 110, 611., Y. Yamaguchi, *Prog. Theor. Phys.*, 111, 545, 2004.
- 54) Amelio-Camelia, G. *et al.*, *Nature*, 393, 763, 1998.
- 55) Ellis, J., Mavromatos, N.E., and Nanopoulos, D.V., *Phys. Rev. D*, 63, 124025, 2001.
- 56) Thomas, R. J. *Journal of Geophysical Research*, 86, 206, 1981.
- 57) Onoma, F. *et al. Annales Geophysicae*, 23, 2385, 2005.
- 58) Horinouchi, T. Nakamura, T., and Kosaka, J. *Geophysical research Letters*, 29, 2007.
- 59) Iwagami, N. *et al. Advance in Space Research*, 2005, 35, 1964.
- 60) Jacobson, A.R. and Shao, X., *Journal of Geophysical Research*, 107, D22, 4661, 2002.
- 61) Jacobson, A.R., *Journal of Geophysical Research*, 108, D24, 4778, 2003.
- 62) Gurevich, A.V. and Zybin, K.P., *Physics, Letters*, A329, 341-347, 2004.
- 63) Pasko, V.P. and George, J.J. *Journal of Geophysical Research*, 107, A12, 1458, 2002.
- 64) Fishman, G.J. *et al.*, *Science*, 264, 131, 1994.

3. Observation principle and instrumental and subsystem requirements

3.1. Observation principle

In the JEM-EUSO Mission, EECR observation is based upon the measurements of the extensive air shower (EAS) phenomenon induced by the primary EECR particle incident to the atmosphere. In a 10^{20} eV EECR, for example, as many as an order of 10^{11} particles are produced as a result of series of subsequent interactions in EAS. Among them, secondary particles in general are relativistic and the charged ones excite the nitrogen molecule to emit ultraviolet fluorescence light. These particles are so super-luminal that they emit Cherenkov light beaming within 1.3 degrees along their trajectories.

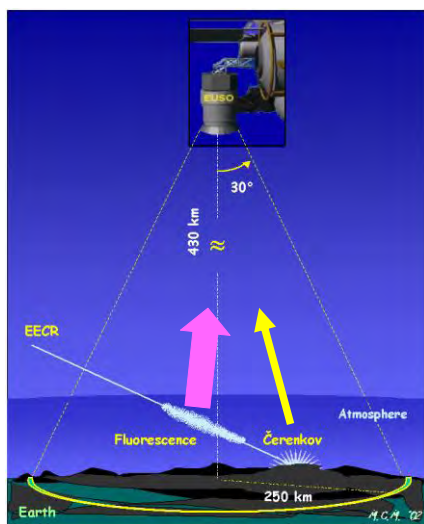


Fig. 3.1 JEM-EUSO principle of EECR Observation

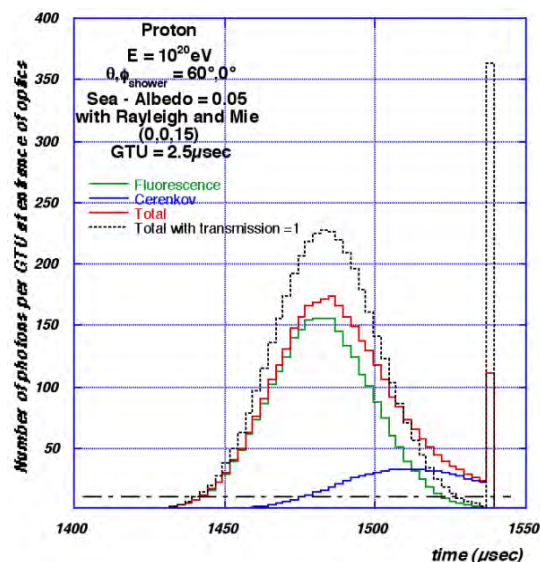


Fig. 3.2 Observed time profile of photon from typical EAS. The green and blue histograms represent the fluorescence and Cherenkov components. The red one is the sum of both components. The case of full atmospheric transmittance is shown by the black one.

With the JEM-EUSO on the orbit, EAS is observed as a luminous dot moving at speed of light (Fig 3.1).

Fig. 3.2 shows the time profile of the typical EAS (10^{20} eV, 60 degree zenith angle) observed by the JEM-EUSO. The vertical axis denotes the number of the arrival photons from the EAS. The green and blue histograms represent the fluorescence and Cherenkov components, respectively and the red one is the sum of both components. For comparison, the case of full atmospheric transmittance is shown by the black histogram. The sharp peak, the so-called Cherenkov mark, at the end of the shower profile is of Cherenkov light scattered on ground or the top of the cloud that help locate where EAS lands.

The International Space Station (ISS) orbits at ~ 8 km per second around 400 km above the surface of the Earth with an inclination of 51.6 degrees. The JEM-EUSO monitors $200,000 \text{ km}^2$ area on the surface of the Earth that yields the fiducial volume of 10^{12} tons atmosphere. The merits of JEM-EUSO are listed as follows:

- More than an order of magnitude larger aperture providing with 1000 EECRs all over the entire celestial sphere. This is also important for detecting rare neutrino interacting events.
- Limited uncertainty in distance to EAS. EAS only develops below ~ 20 km from the surface of Earth. This ensures that one can determine luminous fluorescence events being EECR events.
- Limited uncertainty in atmospheric absorption of photons from EAS. Different from ground-based experiments,

3.2. Accuracies of observables

In the present section, we discuss fundamental requirements against detector segments with capability of observing a 10^{20} eV EAS with 60° zenith angle.

3.2.1. Effective area

The saturated effective area is determined by the following equation:

$$A_{eff} = \eta_C \eta_O (1 - \tau_{dead}) \pi h^2 \tan^2 \gamma_M \quad (3-1)$$

where ~ 400 [km] is the orbital altitude of JEM-EUSO detector, $\gamma_M \sim 30^\circ$ is half of field of view, $\eta_O \sim 0.20$ — 0.25 is duty cycle and η_C is efficiency due to cloud presence and is estimated to ~ 0.7 by TOVS database of ICCPD.

Compared with the effective area of the Pierre Auger Observatory, JEM-EUSO observatory must satisfy the following relationship:

$$\eta_O (1 - \tau_{dead}) \tan^2 \gamma_M \geq 0.066 \quad (3-2)$$

to exceed by an order of the effective area

3.2.2. Accuracies on EAS observables

The key parameters that define the fundamental telescope performance are effective aperture of photon collection (including focusing power, filter transmittance and response of photo detector), pixel size and time resolution.

The optimal time resolution δ_T is required to be short enough to dissolve the time profile of the EAS development. In case of typical EAS event, the duration of EAS development is ~ 60 μ s and therefore δ_T with $\sim \mu$ s order is desired. The optimal δ_T is chosen to be comparable to the time scale of light crossing a distance corresponding to pixel size as follows:

$$\delta_T = \left(\frac{\delta h_0}{c} \right) = 2.3 [\mu\text{s}] \left(\frac{\delta}{0.1^\circ} \right) \left(\frac{h}{400[\text{km}]} \right) \quad (3-3)$$

where δ is the angle corresponding to the pixel dimension.

In order to avoid pile-up of the signal from the Cherenkov mark, the effective time resolution is required to be as short as 10 ns to assure the wide enough dynamic range.

We discuss the requirements upon the effective optical aperture S_{eff} and pixel size δ . In case of the typical EAS of interest, ~ 550 photons per square meter arrive to JEM-EUSO telescope. The length of EAS track L_{EAS} is $\sim 1.5^\circ$ and duration T_{EAS} is ~ 60 [μ s]. The total number of photons

from EAS N_{EAS} is expressed as follows:

$$N_{EAS} = n_{EAS} S_{eff} \quad (3-4)$$

where $n_{EAS} \sim 550$ is the density of photons reaching the JEM-EUSO.

If the focal spot size is comparable to the pixel size, the contaminating night sky background within the pixels within EAS, N_B , track is expressed as follows:

$$N_B = n_B \delta L_{EAS} S_{eff} \quad (3-5)$$

where $n_B = 500$ [photons / m² ns sr] is the typical night sky background flux in ultraviolet band.

The scientific requirements of energy and angular resolutions are 30% and 2.5°, respectively. To assure the margin to the reconstruction procedure, we herein require the half of these resolutions as the following relationships:

$$\frac{\sqrt{N_{EAS} + N_B}}{N_{EAS}} \leq 0.15 \quad (3-6)$$

$$\Delta\beta = \left(\frac{\delta_g}{L_{EAS}} + \frac{\delta_T}{T_{EAS}} \right) \sqrt{\frac{N_{EAS} + N_B}{N_{EAS}}} \leq 1.25^\circ \quad (3-7)$$

Figure 3.3 shows the permissible parameter region for S_{eff} and δ for a constant $\delta_T = 2.5$ [μ s]. The red and blue curves draw the lower limits of S_{eff} as a function of δ that are defined by Eqs. (3-6) and (3-7). To trigger the DAQ by an EAS event, at least 5 photoelectrons per pixel is needed around the maximum of the EAS development. This limit is shown by green line in the figure. The star represents the S_{eff} and δ parameter for the baseline design detector and satisfy the above three conditions.

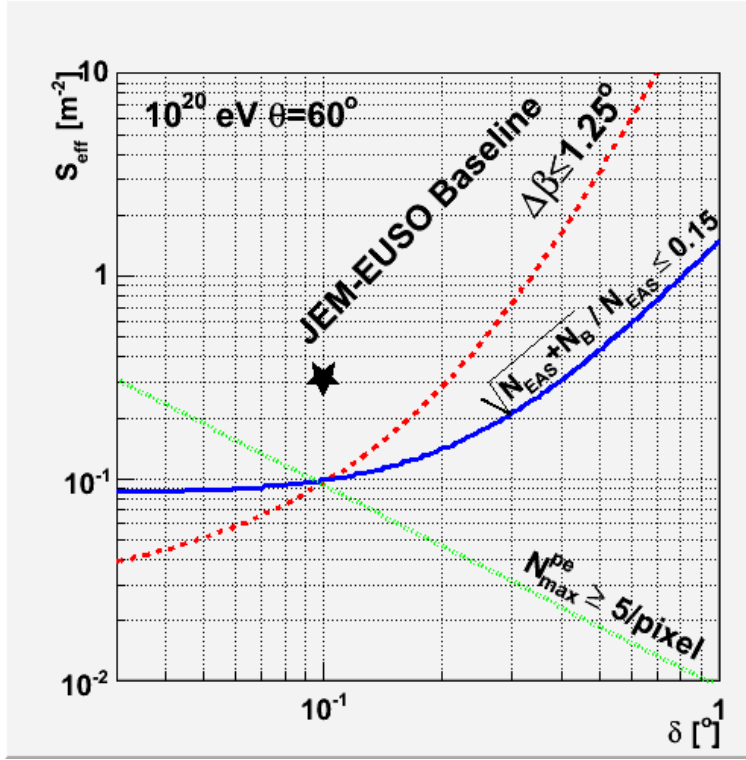


Figure 3.3 Permissible lower limit of S_{eff} as a function δ . $\delta_T = 2.5$ [μ s] is assumed herein. The red and blue curves draw the lower limits from Eqs. (3-6) and (3-7). The green line draws the lower limit for at least 5 photoelectrons per at the maximum of the EAS development. The star represents the baseline design detector.

The determination error of X_{max} which is the key EAS parameter to discriminate primary particles is required to be less 120 g/cm^2 from the scientific objects. Assuming EAS development profile by a Gaussian function, its root mean square L_{RMS} is 0.4° . An ad hoc estimate of angular position of the EAS development maximum is determined with an accuracy of $\sim L_{EAS} \sqrt{\frac{N_{EAS} + N_B}{N_{EAS}}}$ if only statistical is taken into account. The corresponding error in X_{max} is evaluated by the following equation:

$$\sim \left(\frac{L_{RMS}}{[\text{rad}]} \right) \sqrt{\frac{N_{EAS} + N_B}{N_{EAS}}} \left(\frac{h}{1[\text{cm}]} \right) \left(\frac{\rho_{air}}{1[\text{g/cm}^3]} \right) / \sin \theta \quad (3-8)$$

where ρ_{air} is the density of air at the maximum of EAS development. In case of a typical EAS event (note that the zenith angle of arrival is 60°), it reaches the maximum around 7 km above sea level and $\rho_{air} \sim 0.6 \times 10^{-3} [\text{g/cm}^3]$. If the number of photons from EAS exceeds the limit of Eq. (3-6), then error of X_{max} is smaller than 30 g/cm^2 and therefore the requirement for X_{max} is satisfied.

3.2.3. Dark current

The dark current level is required to be less than ~ 50 GHz. This limit is far smaller than the level of

night sky background which is $(3—10) \times 10^{11}$ Hz over the entire focal surface detector.

3.3. Requirements against telescope performance

3.3.1. Scientific requirements

[SR1] Statistics: ≥ 1000 events detection above 7×10^{19} eV

[SR2] Angular resolution: Better than a few degrees to investigate EECR origin

[SR3] Energy resolution: Trans-GZK structure in cosmic ray energy spectrum

[SR4] EECR primary identification capability: discriminating among nucleus, gamma ray and neutrino

3.3.2. Success criteria

3.3.2.1. Minimum success

The criterion of minimum success of JEM-EUSO Mission is acquisition of more than half of the statistical requirement of EECR events [SR1], namely ≥ 500 events above 7×10^{19} eV.

3.3.2.2. Full success

Advent of new generation astronomy via EECR particles [SR1,SR2,SR3,SR4].

3.3.2.3. Extra success

Achieving one or all subjects described in scientific objects.

3.3.3. Observation capability

[OR1] Acceptance: $\geq 7 \times 10^5 (h[\text{km}]/400)^2 [\text{km}^2 \text{ sr}]$ ($E=10^{20}$ [eV] and 60° zenith angle) [SR1]

[OR2] Angular resolution: $\leq 2.5^\circ$ ($E=10^{20}$ [eV] and 60° zenith angle) [SR2]

[OR3] Energy resolution: $\leq 30\%$ ($E=10^{20}$ [eV] and 60° zenith angle) [SR3]

[OR4] X_{max} determination error: $\leq 120 [\text{g}/\text{cm}^2]$ ($E=10^{20}$ [eV] and 60° zenith angle) [SR4]

[OR5] Energy threshold: $\leq 7 \times 10^{19}$ [eV] [SR1]

3.3.4. Instruments

[IR1] Observation duty cycle: $\geq 10\%$ [SR1]

[IR2] Instrumental duty cycle: $\geq 30\%$ [SR1]

[IR3] Lifetime: Longer than two years. Two years storage is also required before the launch [SR1]

[IR4] Attitude determination accuracy: $\leq 0.05^\circ$ (This may be achieved by offline analysis) [OR2,OR3,OR4]

[IR5] Precision of Absolute time: $\leq 1 \mu\text{s}$ [OR2]

[IR6] Wavelength band: Containing EAS fluorescence lines in 330—400 nm [OR1,OR2,OR3,OR5]

[IR7] Synchronization precision among subsystems: ≤ 200 [ns] [ASR1]

[IR8] Protection against stray light: Less than GHz level [OR5,OR2]

3.3.5. Optics

[OPR1] Effective aperture: $\geq 1.5 [\text{m}^2]$ (taking into account photon collection efficiency) [OR3,OR5,OR2]

[OPR2] Field of view: $\geq 60^\circ$ [OR1]

[OPR3] Spot size: ≤ 5 [mm] (root mean square) [OR2,OR3,OR5]

[OPR4] Focusing power: $\geq 50\%$ (along optical axis) [OR3,OR5,OR2]
 $\geq 30\%$ (30° off optical axis)

[OPR5] Transmittance of filter: $\geq 90\%$ (degrading during operation period should be less than 10% level) [OR3,OR5,OR2]

3.3.6. Focal surface detector

[FSR1] Shape of focal surface: spherical

[FSR2] Photon detection efficiency: ≥ 0.12 [OR3,OR5,OR2]

[FSR3] Average pixel size: ≤ 4.5 mm [OPR3]

[FSR4] Focal surface area: ≥ 3.6 m² [OPR2]

[FSR5] Trigger efficiency: ≥ 0.95 ($E_0=10^{20}$ eV, zenith angle 60°) [OR5]

[FSR6] Gate time: ≤ 2.5 μ s [OR2,OR3,OR4]

[FSR7] Dynamic range: 200 photons within gate time (TBC) [SR2]

[FSR8] Dead time: $\leq 3\%$ [OR1]

[FSR9] Dark current noise: ≤ 50 GHz [OR5]

3.3.7. Calibration system

[CSR1] Wavelength: 330—400nm [IR6]

[CSR2] Accuracy: $\leq 18\%$ (TBC) [OR2,OR3,OR4]

3.3.8. Atmospheric monitor

[ASR1] Accuracy of cloud top altitude: ≤ 500 m over field of view [OR3,OR4]

3.3.9. Miscellaneous

- Robustness, compactness, low mass, small volume, low power consumption, structure, radiation tolerance, magnetic field tolerance (against \sim gauss level) and stability in 2—5-year operation
- Mountable on International Space Station
- Telescope protected against potential hazards
- Instrumental success criterion: More than 80% instruments work in good order after five years operation. The Mission success probability should be more than 95% that fulfill the above instrumental success criterion.
- Detectors and their circuits are modularized and are capable of self-operation.

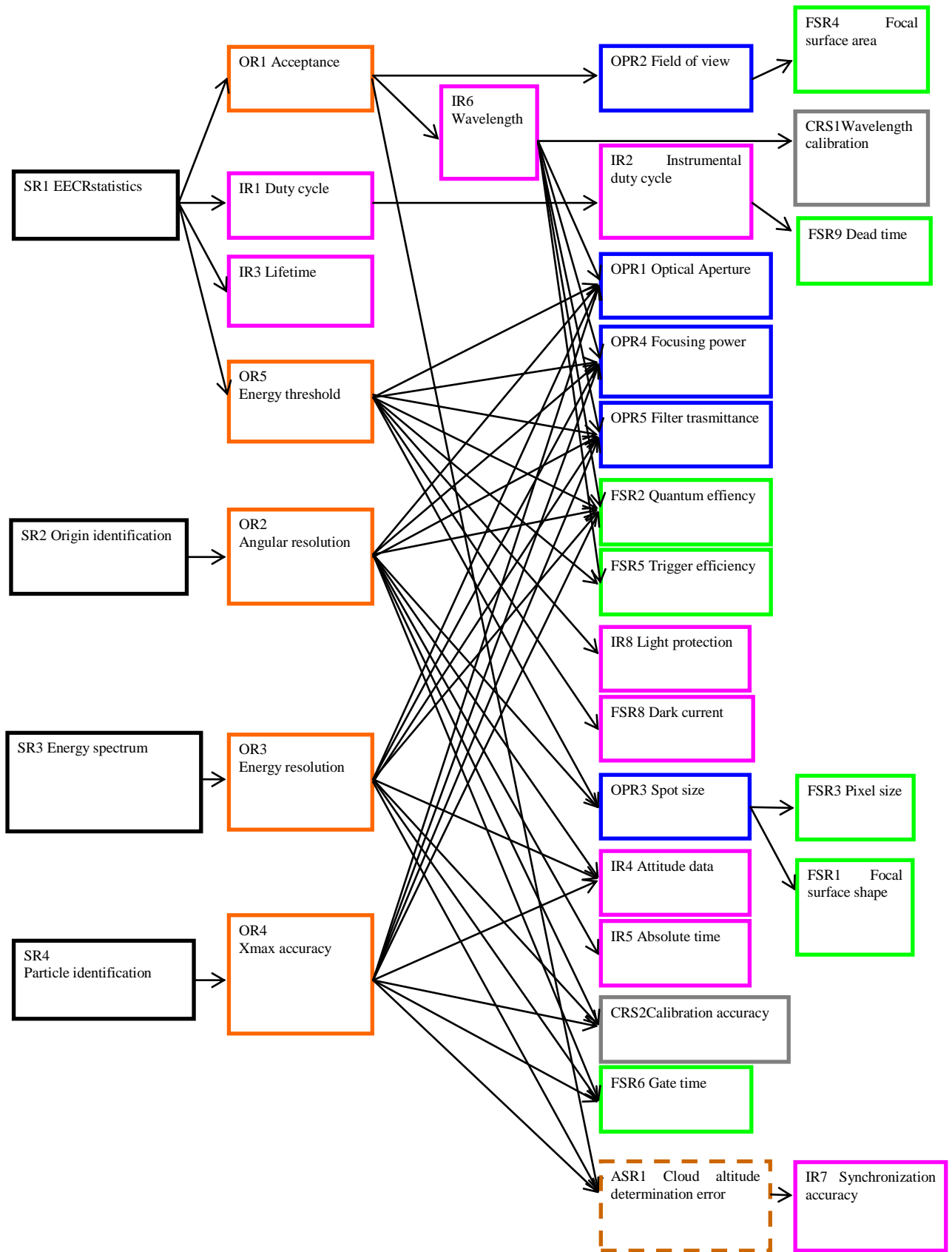


Fig 3.4 Trees of scientific and instrumental requirements in JEM-EUSO

4. Instrument

4.1. Overview

Phase-A study of EUSO mission has been done from Mar. 2003 through Jun. 2004 under the supervision of ESA and the detailed report is written and accepted. Thereafter, Japan has been promoted the concept design as supervisor of the mission.

The instrument of JEM-EUSO's mission consists of 4 parts: optics, focal surface detector, atmospheric monitoring camera and calibration system (Figure 4.1.1, Figure 4.1.2). Figure 4.1.3 shows the deploying state of JEM-EUSO telescope in JEM-EF, figure 4.1.4 shows the block diagram of JEM-EUSO telescope system, and figure 4.1.5 shows the orthographic views of JEM-EUSO telescope.

Optics is composed of two Fresnel lenses of 2.65 m in diameter, of which the lateral part is cut to 1.9 m in length (Figure 4.1.5), and one diffractive lens. It collects near ultraviolet photons (330 nm - 400 nm) from $\pm 30^\circ$ field of view with an angular resolution of 0.1° on the focal surface.

The focal surface detector converts an incoming photon into an electric pulse with duration of 10ns by means of multianode photomultiplier (MAPMT). The electronics counts-up the number of the electric pulses in the period of $2.5\mu\text{s}$ and records them to the memory. When it finds a signal pattern coming from extreme energy particle events, it issues a trigger signal and transmits it to the ground, tracking back image information in the memory.

As for the atmospheric monitoring, we will use an infrared camera and a Lidar (Light Detection and Ranging) with ultraviolet laser, with the objective of determining effective observation time of the telescope, and of increasing the reliability of the events around the energy threshold.

JEM-EUSO reduces the roles of Lidar to the following: to observe the condition of clouds in several points and to calibrate the table of transformation between the altitude of cloud tops and their temperature. Then, it sends the obtained data by means of near ultraviolet radiation to the whole telescope of JEM-EUSO.

As for the onboard calibration system, a set of three LEDs (TBC) with different wavelengths (from 300 to 500nm) will be installed in the telescope cylinder as diffusive light sources. By measuring with the focal surface detector the light from these light sources passing through the optics and reflected at reflecting surface of the interior side of the lid, we will calibrate gain and detection efficiency of the detector. Xe-flasher lamps will be installed in about 10 to 20 places on the ground and when JEM-EUSO passes over them once a day or so, it will detect such lights and measure the total atmospheric ultraviolet absorption by the atmosphere and, therefore, calibrate the device. In order to estimate the systematic error in the energies and arrival directions of the primary cosmic rays, JEM-EUSO telescope observes the ultraviolet laser from the ground as the simulated EAS. This observation also allows us to estimate the transmittance of the atmosphere as a function of the altitude. In addition to the calibration of the devices before the launch, all the above calibrations will be used complementarily to obtain the possible influences caused by the long-term variation in the sensitivity of the device and by the variable atmospheric environment.

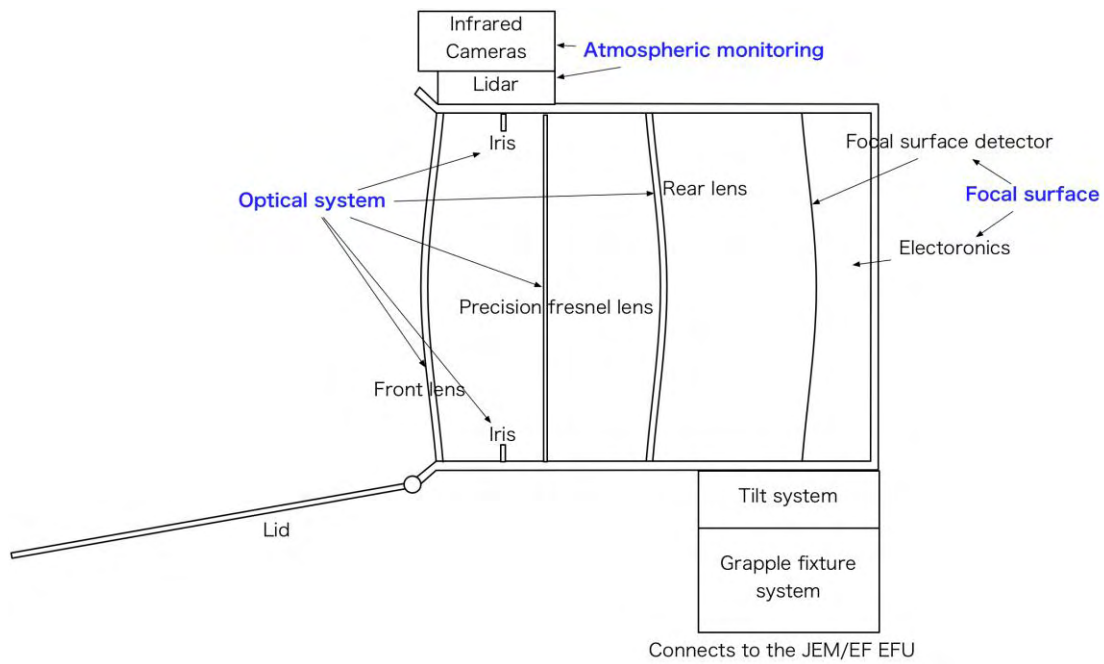


Figure 4.1.1 Conceptual diagram of JEM-EUSO Telescope

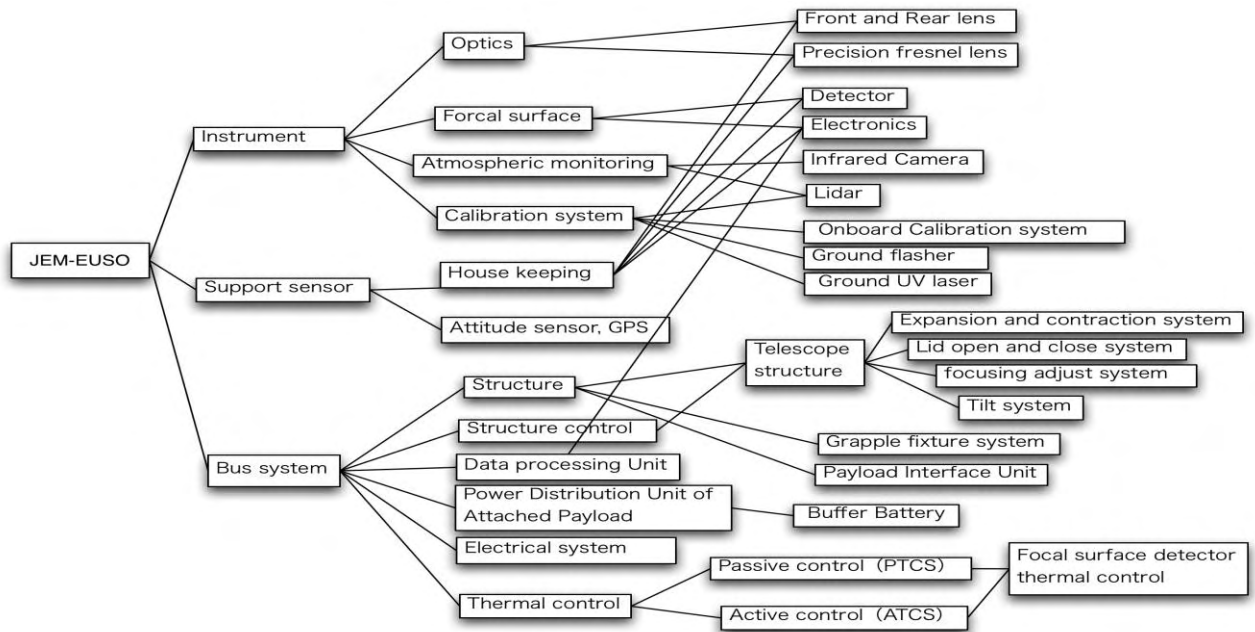


Figure 4.1.2 Breakdown of JEM-EUSO Telescope

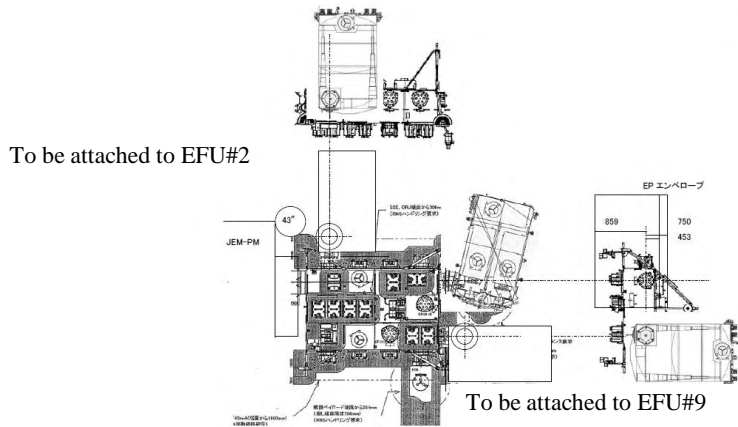


Figure 4.1.3 Attached state of JEM-EUSO to JEM/EF

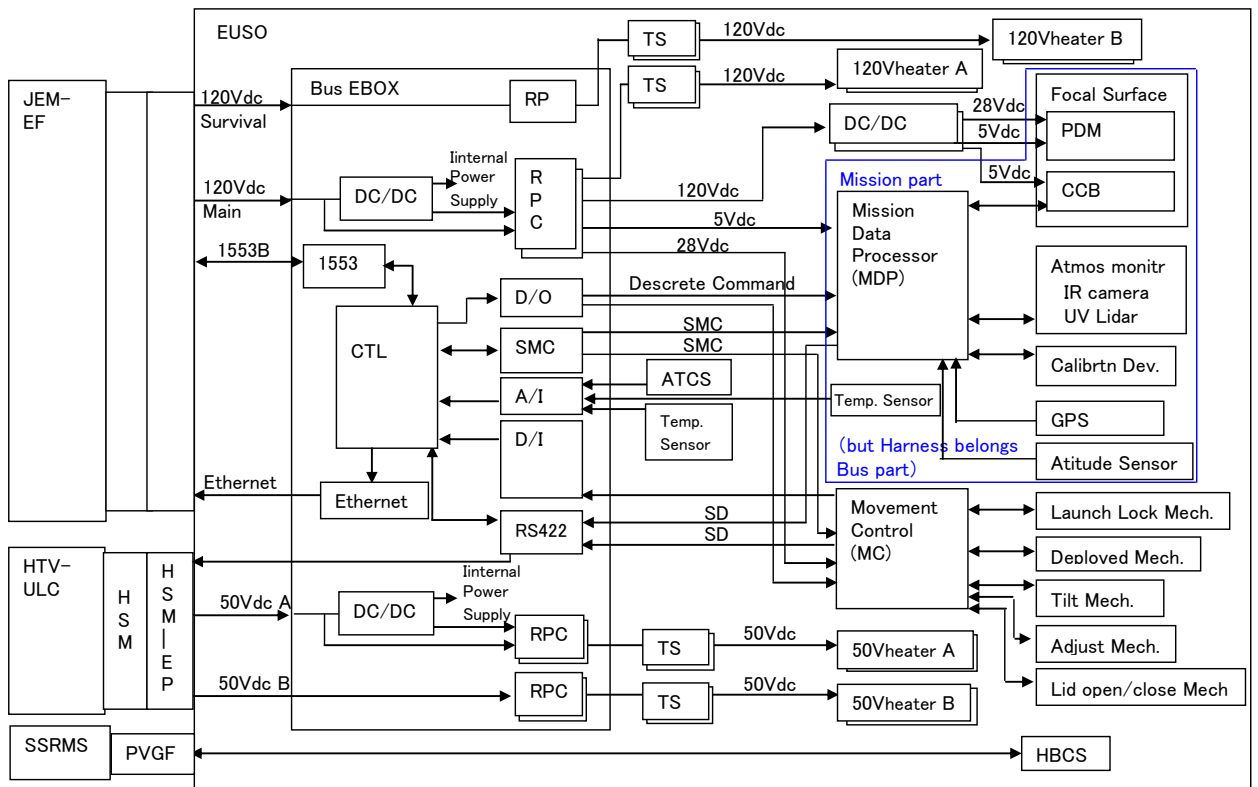


Figure 4.1.4 System block diagram

SD: Serial Digital Telemetry
 SMC: Serial Magnitude Command
 TS: Thermostat

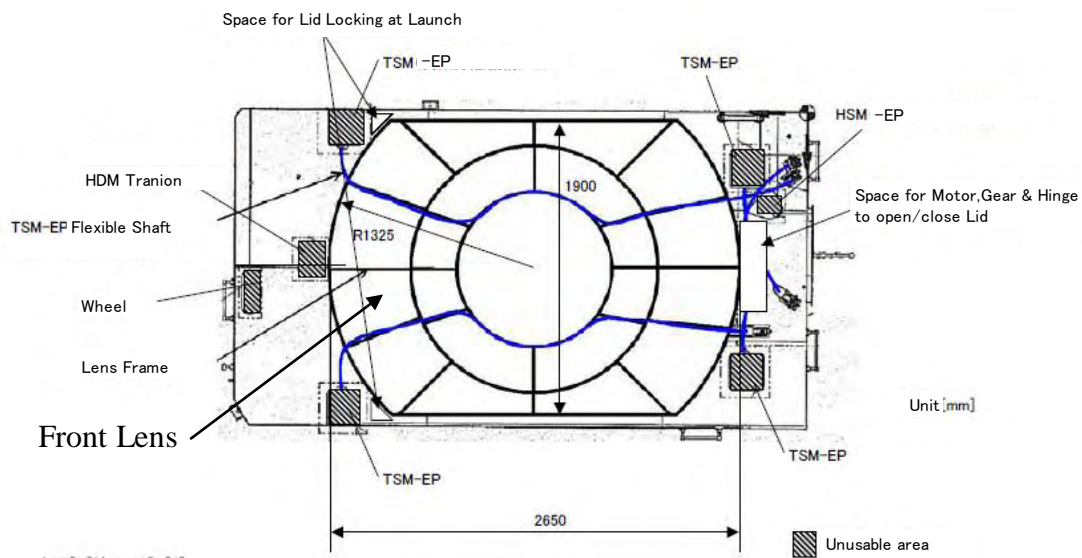
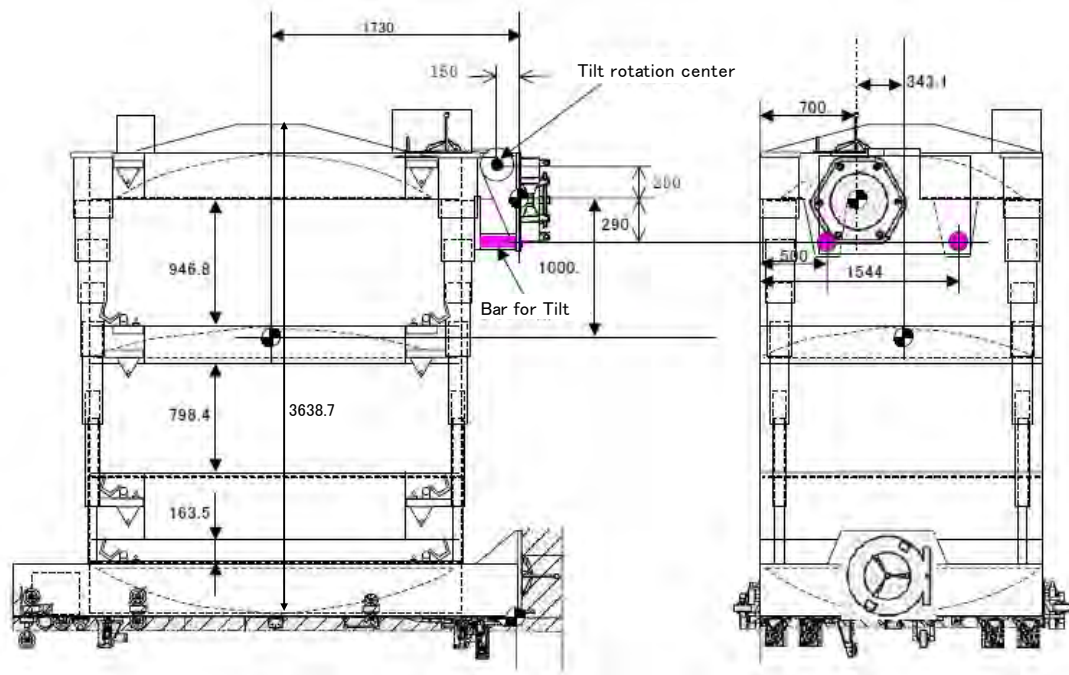


Figure 4.1.5 Orthographic views of JEM-EUSO

4.2. Optics Module

4.2.1. Overview

Optics Module (OM) has 2 curved doublet Fresnel lenses, a flat precision Fresnel lens for chromatic aberration correction, and a curved focal surface. The basic study of OM had been done in the ESA-EUSO Phase-A study [1].

Baseline optics has 2 curved doublet Fresnel lenses and one curved precision lens, which materials are PMMA 000 (Mitsubishi rayon co. product). Verification of PMMA 000 had been done in the ESA-Phase-A study [1].

In the JEM-EUSO Phase-A study, we have verified Advanced optics design, which has much higher performance than Baseline optics. Advanced optics has 2 curved doublet Fresnel lenses, which material is CYTOP (AGC co. product), and one flat precision lens, which material is PMMA 000. This material of precision Fresnel lens is defined from the point of view of manufacturing a fine grating structure.

Fig 4.2.1 shows a schematic view of the optics module. The details of lens materials are described in the section 4.2.2. The OM design is described in the section 4.2.3. Optics performance is described in the section 4.2.4. Tolerance is described in the section 4.2.5. Lens frame is described in the section 4.2.6. Filter design is described in the section 4.2.7. Lens manufacturing is described in the section 4.2.8. Operation is described in the section 4.2.9. Optics summary is described in the section 4.2.10.

These sections describe 2.5 m diameter telescope. For the installation to HTV, we are designing side cut type telescope, which extends from 2.5m diameter to 2.65m diameter and cuts 2 sides of the lens edge. Its lens width across side cuts is 1.9m. In the section 4.2.4.4, the performance of HTV install model is discussed. In the section 5, we describe about observation performance of the HTV install model by using End to End simulation.

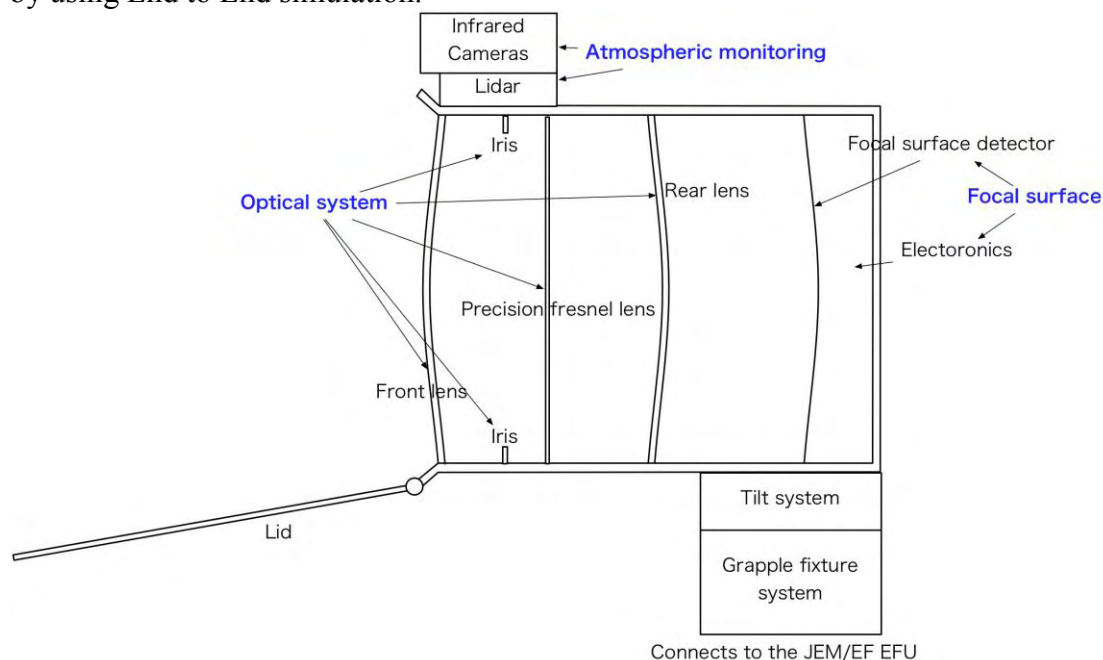


Fig. 4.2.1 Schematic view of the JEM-EUSO telescope

4.2.1.1. Definition of Optics system

JEM-EUSO optics collects photons to a pixel of focal surface detector, which is set on optical focal surface. Optics collects photons with following requirements.

- 1) Field of view of optics is larger than ± 30 degree.
- 2) Spot size is smaller than pixel size of focal surface detector.

4.2.1.2. Coordinate of optics system

Optics uses following a coordinate system.

- 1) The origin of the coordinate axes is a cross point of 1st lens surface and optical axis.
- 2) Z-axis accords with optical axis. Its plus direction is from the 1st lens to focal surface.
- 3) X-axis is parallel with the direction of ISS movement, when observation mode is nadir mode. Its plus direction is anti-direction of ISS.
- 4) Y-axis is defined by the Cartesian coordinates of the above-mentioned X and Z-axis.

4.2.1.3. The set place of optics

Optics is set to focus on the focal surface detector.

4.2.1.4. Main parts of optics

Optics consists of following parts.

- 1) 1st lens (Curved doublet Fresnel lens)
- 2) Stop
- 3) 2nd lens (Precision Fresnel lens)
- 4) 3rd lens (Curved doublet Fresnel lens)
- 5) Filter
- 6) Lens frame
- 7) Focusing adjust system
- 8) House keeping sensor

4.2.1.5. Life span of optics

Optics has life span that is defined by JEM-EUSO system design.

4.2.1.6. Requirements optics

4.2.1.6.1. Performance requirements

Optics is required as following.

- 1) Optics is able to detect atmospheric fluoresces light and Cherenkov light from cosmic ray air shower.
- 2) Optics is able to determine the emission point with spatial resolution.
- 3) Optics is able to collect photons, between 330nm and 400nm, to a pixel of detector as higher efficiency as possible.
- 4) Spot size satisfies that spatial resolution is 0.1 degree or less.
- 5) Life span of optics is 5 years or more.
- 6) Optics has to satisfy space qualifications.

4.2.1.6.2. Physical requirements

Optics is required as following.

- 1) Mass of optics is defined by JEM-EUSO system design.
- 2) Center of gravity of optics is on the Z-axis with TBD mm or less.
- 3) Optics has to fall into the JEM-EUSO telescope envelope.

4.2.1.6.3. Temperature requirements

Optics basically depends on the surrounding environment. Fluctuations of each lens have to 10 degree C or less.

4.2.2. Lens materials

CYTOP is amorphous, soluble perfluoropolymer (Asahigarasu Corp. product). CYTOP combines the excellent properties of highly fluorinated polymers with solubility in selected perfluorinated solvents to provide outstanding coatings for optical, electronic and other applications. CYTOP has a 95 % high transmittance between UV and near-IR. Table 4.2.1 shows the characteristics of CYTOP.

PMMA000 is special Grade UV transmittance polymethyl metacrylate (Mitsubishi rayon corp. product). PMMA000 was selected the ESA-EUSO lens material in the ESA-Phase-A study. Table 4.2.2 shows the characteristics of PMMA000[1].

Table 4.2.1 Characteristics of CYTOP and PMMA000

	CYTOP	PMMA000
Product Company	AGC (Asahi Glass co.)	Mitsubishi Rayon co.
density (25°C)	2.03 g/cm ³	1.19~1.20 g/cm ³
Glass transition temp.	108°C	105~120°C
Water absorption	<0.01	0.3
Coefficient of Linear Expansion	7.4×10^{-5} cm/cm/degree C	8.0×10^{-5} cm/cm/ degree C
Mechanical properties		
Rupture Strength	40MPa	65~73 MPa
Break Elongation	150%	3~5%
Yield Strength	40MPa	(65) MPa
Tensile Strength	1200MPa	3000 MPa

4.2.2.1. Refractive index

4.2.2.1.1. Refractive indexes of CYTOP and PMMA000 in the near UV region

Refractive indexes of CYTOP and PMMA000 in the near UV region are shown in Fig. 4.2.2. Refractive index dispersion of CYTOP is smaller than PMMA000. Therefore, CYTOP reduces color aberration effect as compared with PMMA000.

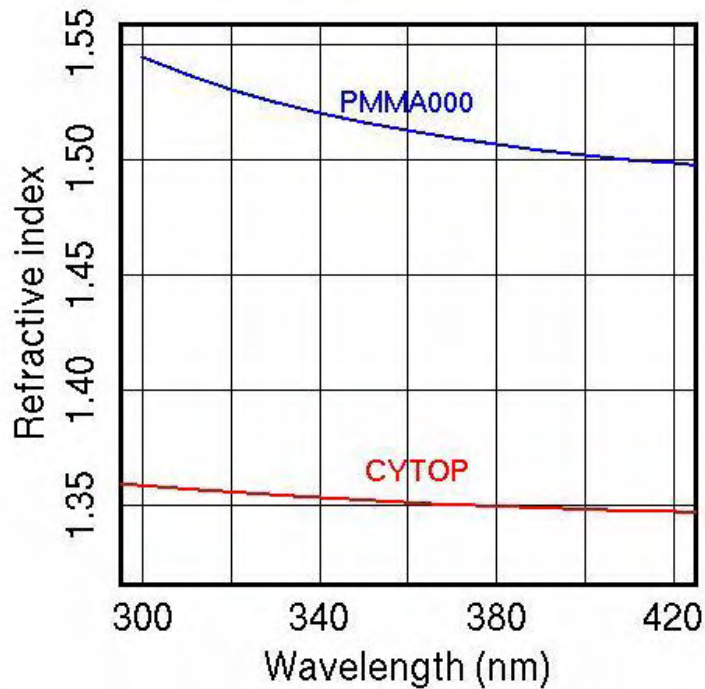


Fig. 4.2.2 Refractive indexes of CYTOP and PMMA000 in the near UV region.

4.2.2.1.2. Temperature dependence of refractive index

JEM-EUSO orbits around the earth in 90 minutes. Therefore, each lens has a thermal cycle synchronizing orbit. Refractive index is shifted by temperature change. This refractive index change causes de-focus effect. Thermal analyses predicted that each lens shift $\pm 10^{\circ}\text{C}$ from the each equilibrium temperature (see table 4.2.2 and 4.2.3). On the other hand, optics analysis by using numerical raytrace method requires that temperature shift amount is below $0.0013/10^{\circ}\text{C}$. The measurement results of temperature dependence of refractive index are shown in Table 4.2.2 (CYTOP) and Table 4.2.4 (PMMA). The temperature shift amount per 10°C is CYTOP : $0.0007/10^{\circ}\text{C}$ and PMMA000: $0.0009/10^{\circ}\text{C}$. We confirmed each value is below the requirement value of $0.0013/10^{\circ}\text{C}$.

Table 4.2.2 Thermal analyses of Baseline optics design

	Max temperature	Min temperature	Differential Value
1 st lens front side	-15.65	-19.00	3.35
1 st lens back side	-14.73	-16.46	1.73
2 nd lens front side	-6.51	-6.70	0.19
2 nd lens back side	-4.70	-4.86	0.16
3 rd lens front side	6.90	6.88	0.02
3 rd lens back side	10.86	10.82	0.04

Table 4.2.3 Thermal analyses of Advanced optics design

	Max temperature	Min temperature	Differential Value
1 st lens front side	-15.77	-19.63	3.36
1 st lens back side	-14.41	-15.92	1.51

2 nd lens front side	-6.47	-6.65	0.18
2 nd lens back side	-4.73	-4.87	0.14
3 rd lens front side	6.54	6.51	0.03
3 rd lens back side	12.47	12.42	0.05

Table 4.2.4 Temperature dependence measurement of refractive index (CYTOP)(404.656nm h line)

Temperature	Refractive index	Differential refractive index value from 0°C
25°C	1.3481	-0.0018
0°C	1.3499	0.0
-18°C	1.3511	0.0012

Table 4.2.5 Temperature dependence measurement of refractive index (PMMA 000)(404.656nm h line)

Temperature	Refractive index	Differential refractive index value from 0°C
25°C	1.5060	-0.0024
0°C	1.5084	0.0
-18°C	1.5100	0.0016

4.2.2.2. Transmittance

Transmittance (15mm thickness) of CYTOP and PMMA 000 are shown in the Fig. 4.2.3.

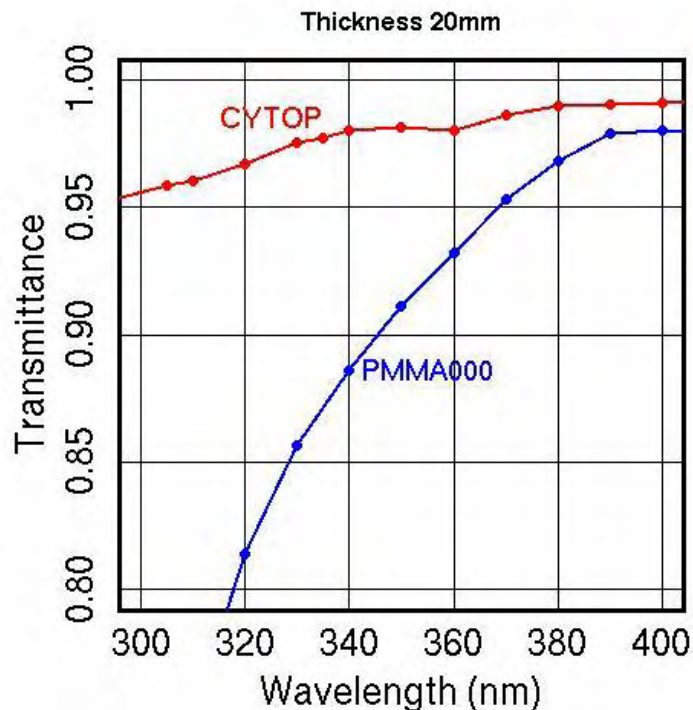


Fig. 4.2.3 Transmittance (15mm thickness) of CYTOP and PMMA 000

4.2.3. Optics module design

Cross-section view of Baseline and Advanced optics design are shown in Fig.4.2.4. Each optics design parameters are shown in table 4.2.6, 4.2.7 and 4.2.8. This document reports about advanced

optics design, because base line optics (PMMA 000 lens optics) had been studied in the ESA-Phase-A study.

Throughput performance of each optics is shown in fig 4.2.5. Advanced optics is higher performance than the base line optics has similar. These performances are considered surface roughness, surface reflection and scatter loss, material absorbance, etc. Advanced optics has better performance than baseline, because CYTOP has better transmittance than PMMA 000. Furthermore, Advanced Optics can select smaller spot size (2.5mm spot size) than base line optics, because CYTOP is smaller dispersion of refractive index than PMMA,

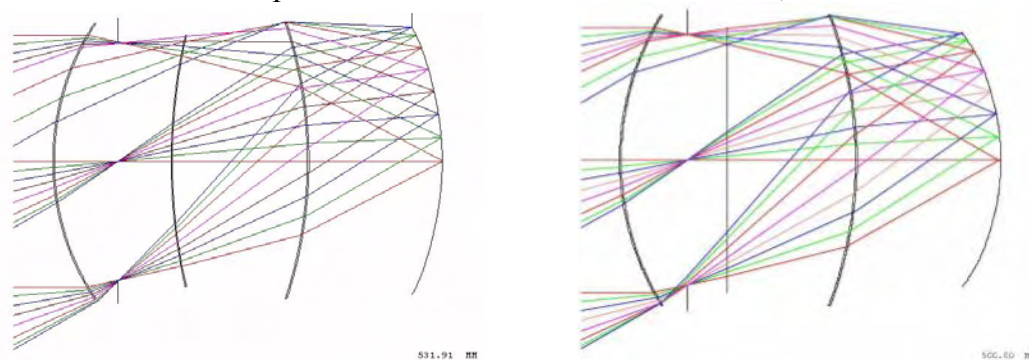


Fig 4.2.4 Cross section view of Baseline (left) and Advanced optics design (right)

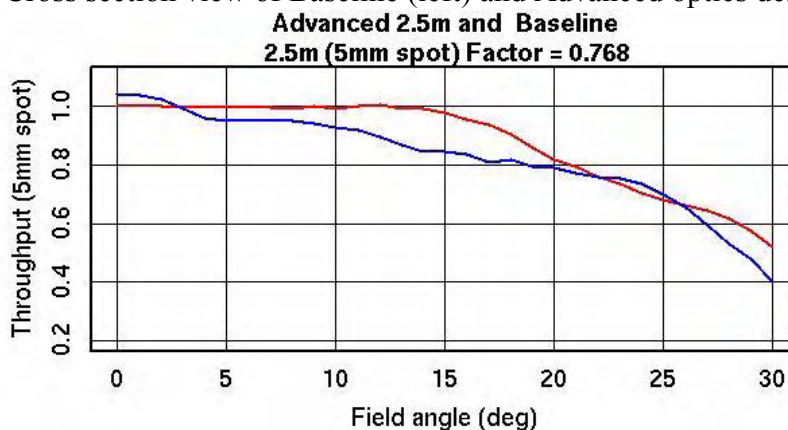


Fig 4.2.5 Comparison of throughput performances between baseline and advanced optics

Green line: Baseline optics, Blue line : Advanced optics

Each line is normalized by the throughput value of the advanced optics with incident angle 0 degree.

Table 4.2.6 Requirements of Optics and design parameters of Baseline and Advance optics

	Requirements	Baseline optics	Advanced optics
F number	< 1.25	1.0	1.0
Diameter of lens	2.5m <	2.5m	2.5m
Spot size (RMS)	5mm <	5.0mm	5.0mm (2.5mm)
Throughput	50% @ 0-10° 40% @ 10-20° 30% @ 20-30°	59% @ 0-10° 52% @ 10-20° 39% @ 20-30°	62% @ 0-10° 58% @ 10-20° 42% @ 20-30°
Filter transmittance	90% <	90% <	90% <

Table 4.2.7 Parameters of Baseline optics [2]

	1 st lens	2 nd lens	3 rd lens	Focal surface
Material	PMMA000	PMMA000	PMMA000	See 4.3
Lens type	Curved doublet Fresnel lens	Curved Fresnel lens + precision Fresnel lens	Curved doublet Fresnel lens	N/A
Diameter (mm)	2500	2366.895	2500	2289.268
Radius of curvature (mm)	2278.382	5175.611	4052.703	
Thickness (mm)	15	10	15	N/A
Weight (BEE) (kg)	95.4	59.3	89.8	See 4.3

Table 4.2.8 Parameters of Advanced optics [3]

	1 st lens	2 nd lens	3 rd lens	Focal surface
Material	CYTOP	PMMA000	CYTOP	See 4.3
Lens type	Curved doublet Fresnel lens	Flat Fresnel lens + precision Fresnel lens	Curved doublet Fresnel lens	N/A
Diameter (mm)	2500	2241.433	2500	2212
Radius of curvature (mm)	2432.7	N/A	3632.1	
Thickness (mm)	15	10	15	N/A
Weight (BEE) (kg)	163	51	157	See 4.3

Design file : zuccaro_0824_fl_2300_cy_pm_1d_1

4.2.3.1. Detail of lenses

This document reports about Advanced optics design, because base line optics (PMMA 000 lens optics) had been studied in the ESA-Phase-A study. 1st lens and 3rd lens is curved doublet Fresnel lens. Curved doublet Fresnel lens had been studied and confirmed basic performance during ESA-Phase-A study. Therefore, this section describes 2nd lens. The 2nd lens has 2 surface, Flat Fresnel lens and precision Fresnel lens. This lens is newly added lens to improve optics performance.

(1) Flat Fresnel surface of 2nd lens

Role of This surface is field lens. This surface is able to make the spot size to be sharper. RMS spot size is improved from 5 mm to 2.5 mm, when this surface is added. Surface structure is shown in the Fig. 4.2.6. The Fresnel structure' facets are only 26. Therefore, scatter loss of facet backcuts is negligible.

(2) Precision Fresnel surface of 2nd lens

Refractive index dispersion of CYTOP is lower than PMMA000, therefore, color aberration effect is reduced by using CYTOP as 1st lens and 3rd lens's material. Role of this surface is to reduce still remained color aberrations by using diffractive effect. Concept of diffractive effect is shown in the Fig 4.2.7. Diffractive lens has opposite dispersion of refract lens, therefore, diffractive lens can cancel color aberration of refract lens.

Precision Fresnel surface of 2nd lens has grooves of height 0.694 um and width from 6um to 100um on the PMMA surface. Manufacturing accuracy of groove height requirement is $\pm 10\%$ of 2λ , $\lambda = 357\text{nm}$, that is below $\pm 0.072\text{um}$. A diameter 10 cm manufacturing result was $\pm 0.036\text{um}$. This value was satisfied requirements of accuracy of groove height , and, its surface roughness was below 16 nm (RMS), which value was satisfied requirements of below 20 nm (RMS) (see4.2.8.1.2).

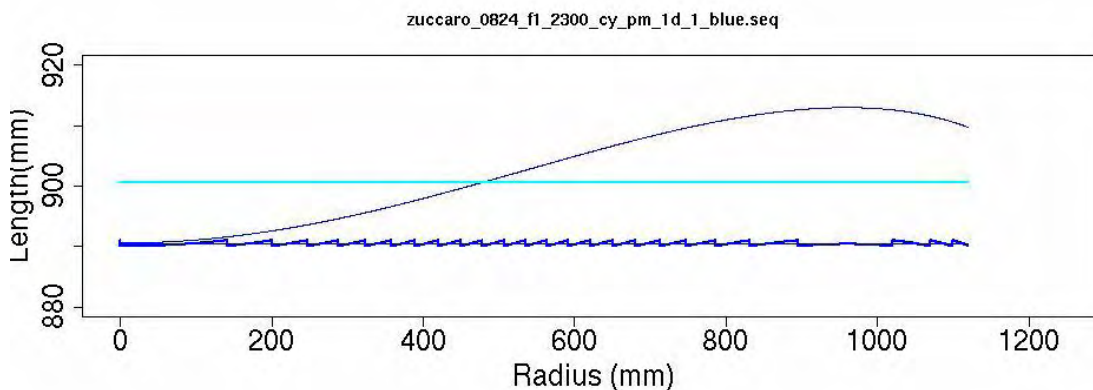


Fig4.2.6 Flat Fresnel surface of 2nd lens

Light blue line: precision Fresnel surface、 Blue line: Fresnel surface (Blue curve line is superimposed on Fresnel surface)

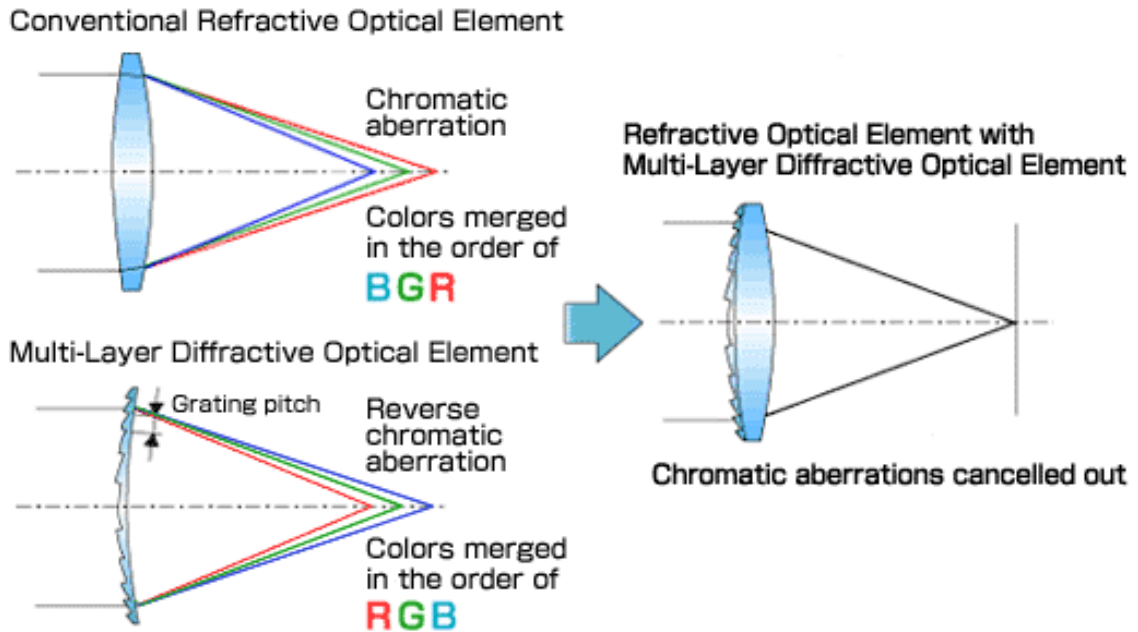


Fig 4.2.7 Concept of color aberration cancels by using diffractive element.

4.2.4. Performance

In this section, 2.5m in diameter optical system is described. HTV install type side cut optics is described in the section 4.2.4.4.

Encircled Energy (EE) and throughput are defined as following.

- Encircled Energy (EE) is ratio of photons in spot area divided by photons which reached on the focal surface.
- Throughput is ratio of photons in spot area divided by photons which passed through the iris.

EE and throughput were estimated by using a raytrace code. This raytrace is included a) material absorption, b) Fresnel structure, c) surface reflection. Surface roughness LOSS and precision Fresnel structure depth error LOSS are estimated by formulas. These formulas were verified in the ESA-Phase-A study. Surface roughness LOSS is shown in fig 4.2.8, 4.2.9. Transmittance with surface roughness LOSS is estimated by a formula 4.2.1.

$$T = \exp\left[-\left(\frac{2\pi}{\lambda} \cdot RMS \cdot \Delta n\right)^2\right] \quad (4.2.1)$$

λ : Wavelength (nm), Δn : Difference optical index between vacuum and material, RMS: surface roughness (nm RMS).

Precision Fresnel structure depth error LOSS is shown in fig 4.2.10. Transmittance with depth error LOSS is estimated by formula 4.2.2 and 4.2.3.

$$\eta(\Delta z, \lambda) = \text{sinc}^2\left[\left(\frac{\lambda_0 - \Delta z}{\lambda} - 1\right) \cdot \Delta n\right] \quad \text{here, } \text{sinc}(x) = \frac{\sin(\pi x)}{\pi x} \quad (4.2.2)$$

Δz : depth error (nm), λ_0 : Optimized wavelength (nm), λ : Wavelength (nm), Δn : Difference optical index between vacuum and material.

Assuming that a distribution of Δz is Gaussian (σ nm RMS), average of 1st order diffraction efficiency is,

$$T(\lambda, \sigma) = \frac{1}{\sigma\sqrt{\pi}} \int \eta(z, \lambda) \cdot e^{-\left(\frac{z}{\sigma}\right)^2} dz \quad (4.2.3)$$

We are, also, using 12% loss as support structure obscuration, and 10% loss as Fresnel facet backcuts Root & Peak tool error. These losses are summarized in table 4.2.9.

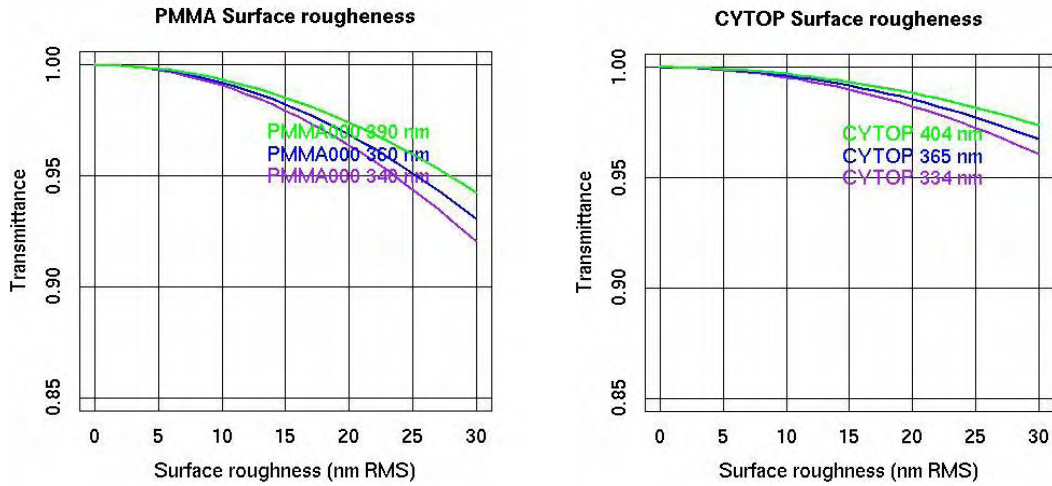


Fig 4.2.8 Transmittance depend on surface roughness on a surface
 Left: PMMA 000, Right: CYTOP
 Left : Purple line: 337nm, Blue line: 357nm, Green line: 391nm
 Right : Purple line: 337nm, Blue line: 357nm, Green line: 391nm

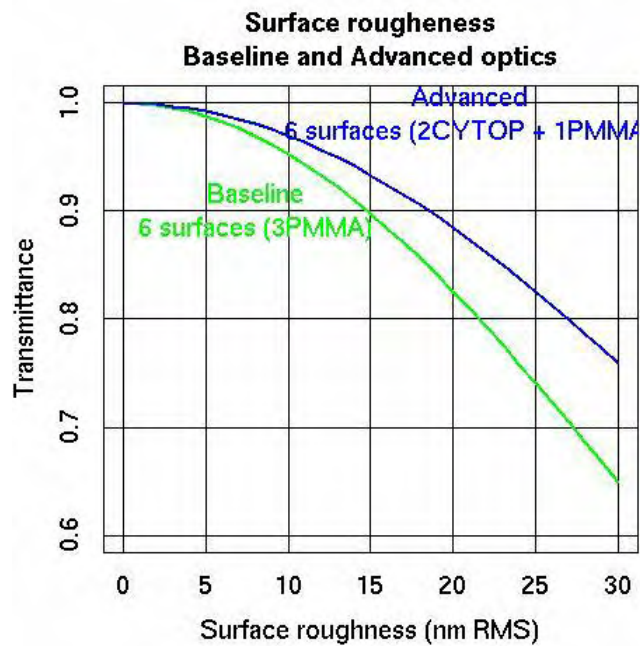


Fig 4.2.9 Transmittance depend on surface roughness on a surface
 Green line: Baseline optics, Blue line: Advanced optics

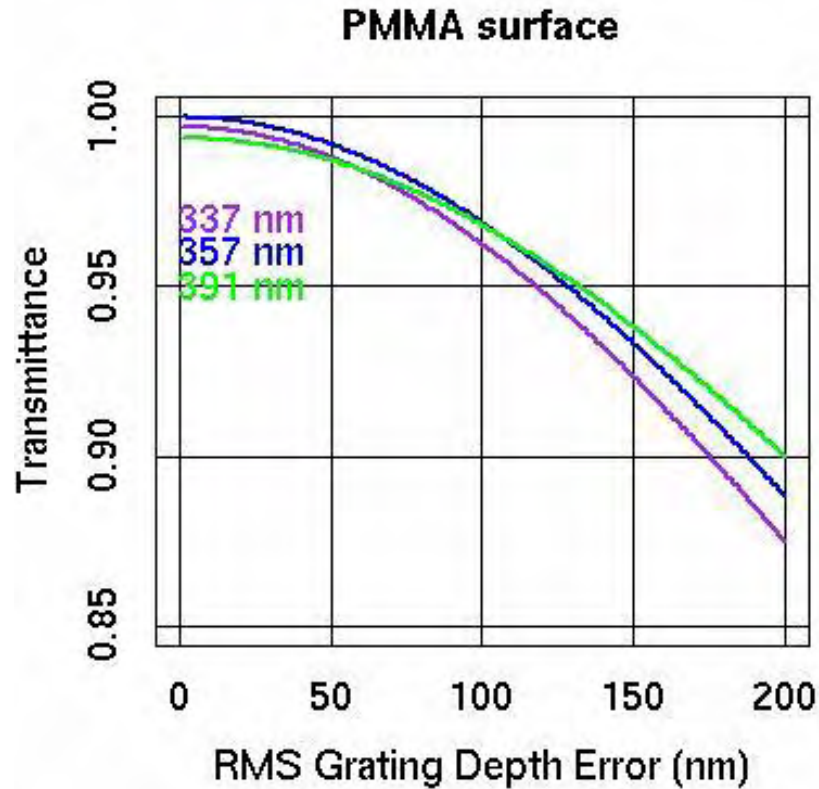


Fig 4.2.10 Transmittance depend on precision Fresnel structure depth error LOSS
 Blue line: 337nm、Green line: 357nm、Red dash line: 391nm

Table 4.2.9 Summary of LOSS items

Items	Loss factor
Surface roughness	3% (15nm RMS)
Precision Fresnel structure depth error	1%
Fresnel facet backcuts Root & Peak tool error	10%
Support structure obscuration	12%

4.2.4.1. Spot size

In the 2007 study, RMS spot size is improved from 5 mm to 2.5 mm by adding Fresnel surface on the 2nd lens. Spot diagrams are shown in fig. 4.2.11.

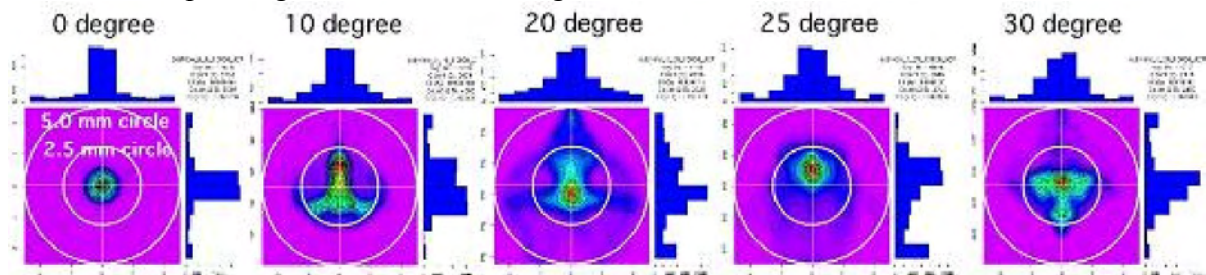


Fig 4.2.11 Spot diagrams of Advanced optics (outer circle : 5mm ϕ 、inter circle : 2.5mm ϕ)

4.2.4.2. Encircled Energy (EE) of advanced optics

Two kinds of EE (advanced optics) are shown in the Fig. 4.2.12. One is 5mm spot size, another is 2.5mm spot size.

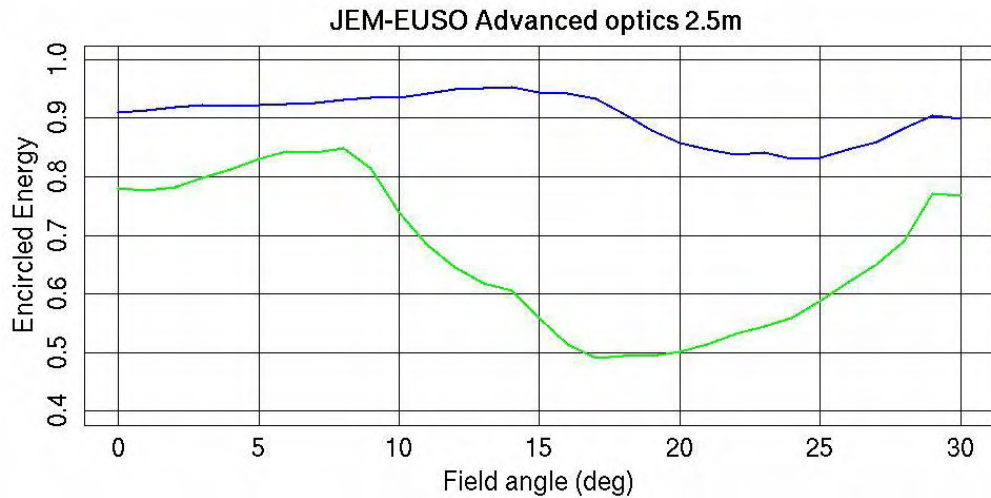


Fig 4.2.12 Encircled energy of Advanced optics.
Blue line: 5mm spot size、 Green line: 2.5mm spot size.

4.2.4.3. Throughput of advanced optics

Two kinds of Throughput (advanced optics) are shown in the Fig. 4.2.13. One is 5mm spot size, another is 2.5mm spot size.

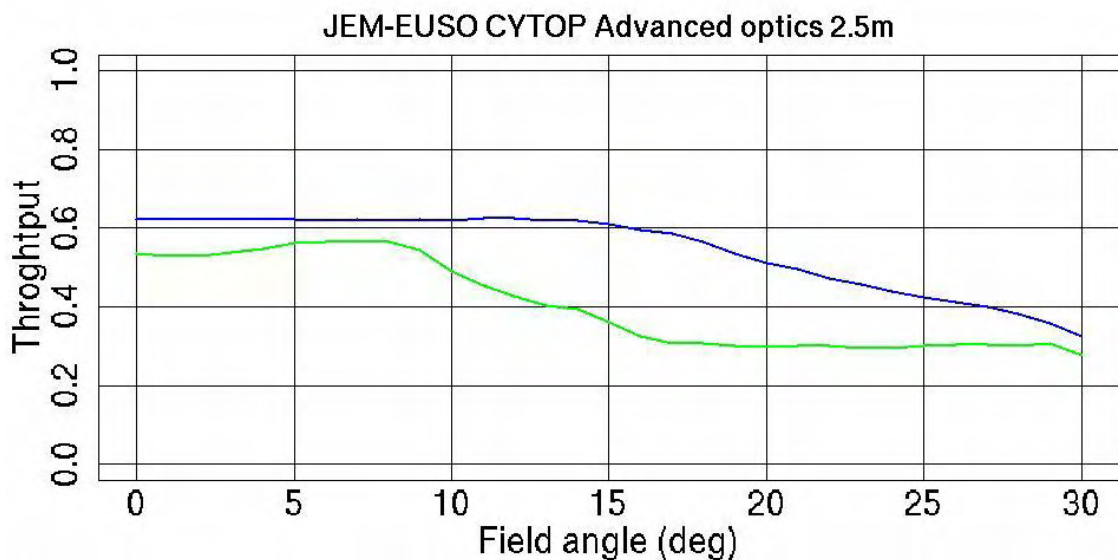


Fig 4.2.13 Throughput of advanced optics
Blue line : 5mm spot size、 green line : 2.5mm spot size.

4.2.4.4. The performance of HTV stowing type optics

We have a telescope design to fit configuration of HTV stowing. Detail of the design is described in section 4.7.1.2. Optics is enlarged from 2.5m to 2.65m in diameter and cut side. The lens shape is 2.65m in diameter \times 1.9m width. The side cut optics has about 90% aperture of 2.5m in diameter

lens (original design). Performance of the side cut optics is shown in Fig 4.2.14. HTV stowing optics keeps performance of 2.5m optics till 15-degree field angle. Field of view of side cut direction is limited about 24 degree.

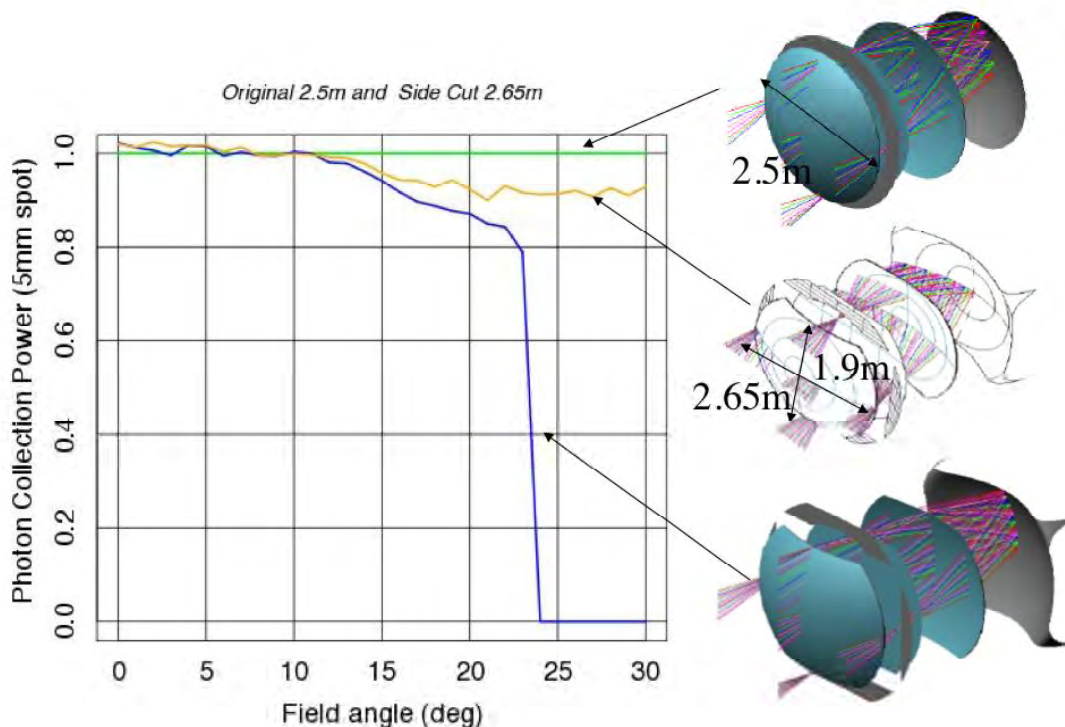


Fig 4.2.14 the performance of HTV stowing type optics

The performance of HTV stowing type optics is normalized by original 2.5m optics performances.

Green line: Performance of the original 2.5m optic, Blue line: Performance of HTV stowing type (vertical direction from side cut), Yellow line: Performance of HTV stowing type (parallel direction from side cut)

4.2.5. Tolerance analysis

JEM-EUSO optics does not need diffraction limit resolution like astronomical telescope. JEM-EUSO angular resolution tolerance is roughly 300 thousands times larger than the diffraction limit. Tolerance of the optics is much lower than astronomical telescope. JEM-EUSO optics tolerances an error of less than spot size, because F number is 1 and incident angle of rays to the focal surface are less than 30 degree.

We verified tolerance of 2 types spot size, 5mm and 2.5mm, by using the raytrace code. The result of spot size 5mm is similar to ESA-Phase-A result [1]. We define tight tolerances based on spot size 2.5mm for securing possibility of using small pixel size detector.

Each component of optics has 3 degree of freedoms, axial displacement, Lateral displacement and Tilt (see Fig 4.2.15). The tolerances are shown in Table 4.2.10.

Table 4.2.10 Tolerance requirements

Degree of freedom	Requirement
Lateral displacement	Less than $\pm 2.5\text{mm}$

Tilt	Less than $\pm 2.5\text{mrad}$
Axial displacement	Less than $\pm 2.5\text{mm}$

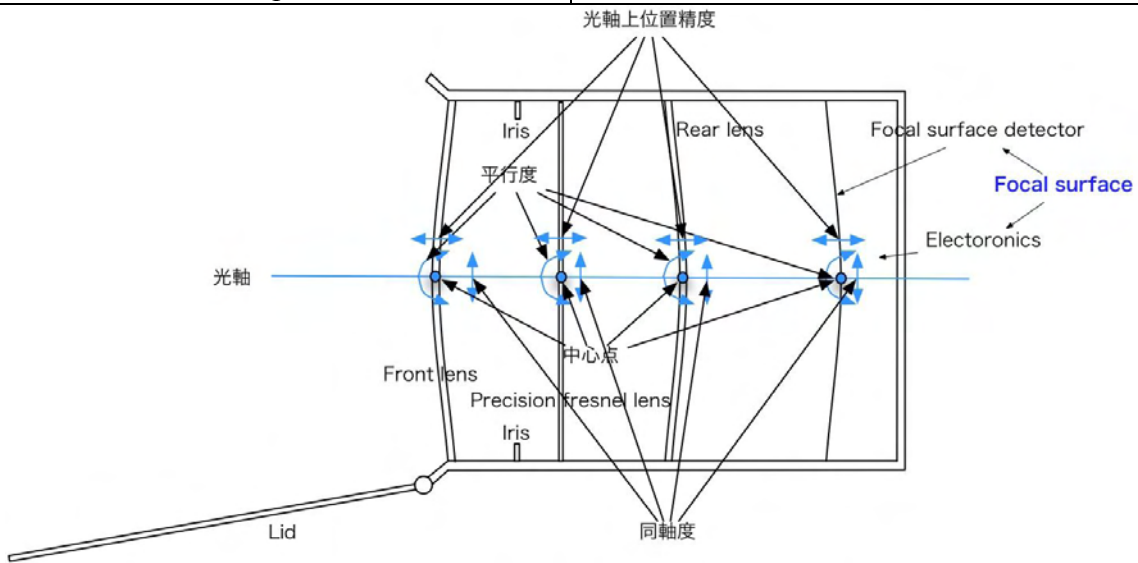


Fig 4.2.15 Definition of degree of freedom

4.2.5.1. Requirement for focusing adjust mechanism

JEM-EUSO optics has a focusing adjust mechanism at the focal surface or 3rd lens to cancel thermal expansion of telescope structure, etc.

We define adjust stroke and adjust step in table 4.2.11. These values will be redefined, when details of telescope structure will be defined. A conceptual design (provided by IHA aerospace) of a focusing adjust mechanism is shown in fig. 4.2.16.

Table 4.2.11 Requirement for focusing adjust mechanism

Item	Requirement
Adjust stroke	Longer than $\pm 12.5\text{mm}$
Adjust step	Less than 1.25mm

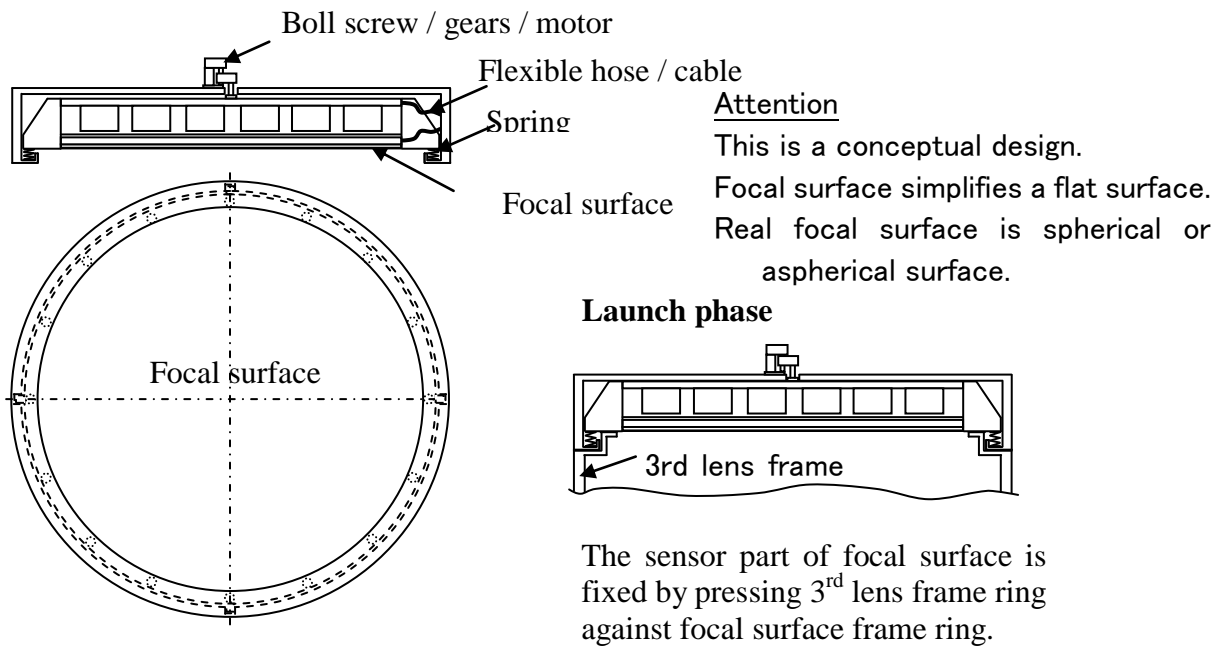


Fig 4.2.16 Conceptual design of a focusing adjust mechanism, was provided by IHA aerospace co.

4.2.6. Lens support structure

Basic design had been done in the ESA-Phase-A study. We will define lens support structure design to consider HTV stowing telescope design in FY 2008.

4.2.7. Filter

4.2.7.1. BG3 baseline filter

Optics uses band pass filter (330nm - 400nm) to cut photon above 400nm wavelength. The filters are set on each window of multi anode photo multiplier. We selected BG3 filter as baseline filter. BG3 filter transmittance is shown in Fig 4.2.17.



Fig 4.2.17 Transmittance of BG3 baseline filter
Green line: BG3 filter

4.2.7.2. Advanced filter

JEM-EUSO observes 3 Nitrogen lines (337nm, 357nm, 391nm). BG3 baseline filter, however, transmits photons between 250 nm and 500 nm. JEM-EUSO observes Nitrogen lines and background photons. Therefore, S/N ratio of detector is not best under the influence of background photons.

Advanced filter is able to pass through only around 3 Nitrogen lines. Advanced filter is a multilayer filter, which has 25 pair layers of Ta₂O₅/SiO₂.

We coated the multilayer and tested its transmittance performance. If Advanced filter is used, S/N ratio is improved 1.4 times high. Advanced filter performances are shown in fig 4.2.18.

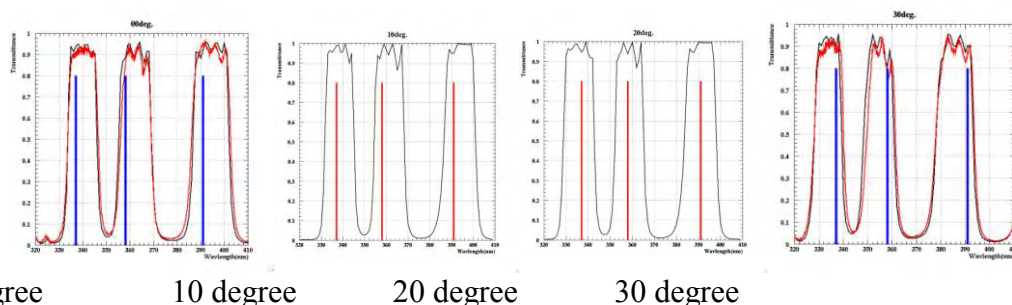


Fig 4.2.18 Transmittance performance of Advanced filter.

4.2.8. Lens manufacturing

4.2.8.1. 10 cm in diameter test piece manufacturing

4.2.8.1.1. CYTOP Fresnel structure manufacturing

Fresnel structure was manufactured by the Materials Fabrication Laboratory of RIKEN. We confirmed surface roughness is less than 15 nm (RMS), which satisfied the requirements value 20nm (RMS).



Fig 4.2.19 Pictures of manufacturing and test piece.

4.2.8.1.2. PMMA 000 precision Fresnel structure manufacturing

Precision Fresnel structure is manufacturing on PMMA 000 by Materials Fabrication Laboratory of RIKEN. Grating depth of precision Fresnel structure is 0.694μm. Grating pitch has various values between 6μm and 100μm. Grating depth requirement is smaller than $\pm 0.072\mu\text{m}$, which is 2λ of $\pm 10\%$, to concentrate diffraction efficiency on the first order. Here, wavelength λ is 357nm. Manufacturing result was $\pm 0.036\mu\text{m}$. This value is half of grating depth requirement. Surface roughness is less than 15 nm (RMS), which satisfied the requirements value 20nm (RMS).

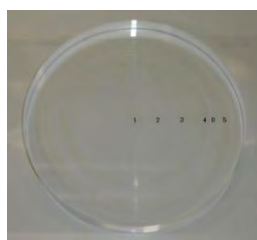


Fig 4.2.20 PMMA 000 precision Fresnel structure manufacturing

4.2.8.2. Large lens manufacturing and test

4.2.8.2.1. Large lens manufacturing

We are shifting to large lens manufacturing. June 2008, manufacturing machine was installed at IKEGAMI mold corp. The machine is UTD-3400 (Toshiba machine corp. product) is able to manufacture 3.4m in diameter lens (see Fig 4.2.21). UTD-3400 is tuning up phase during from June to August 2008. UTD-3400 will start to manufacture 3 subscale PMMA 000 lenses ($>1.5\text{m}$ in diameter) from September 2008. A reason for why we will manufacture PMMA 000 lenses is we had confirmed that the machine which has capability to manufacture PMMA 000 has capability to manufacture CYTOP by the 10 cm in diameter test piece manufacturing. These lenses will be transported to NASA and done optical test by using NASA's facility. (see section 4.2.8.2.2).



Fig 4.2.21 Large lens manufacturing machine UTD-3400 (Toshiba machine corp.)

4.2.8.2.2. Test and Verification for the Phase B demonstration systems

To assist in raising the Technology Readiness Level (TRL) of the JEM-EUSO optics our US partners at NASA MSFC will propose to MSFC management the use of Technology Investment Program (TIP) funds for testing two demonstration systems that will be manufactured in Japan. The first system will be a subscale prototype and is made up of the central 1.5 meters of all three optical elements, assembled in a non-flight structure and used for optical testing. The second system will be a single flat PMMA disk of 2.6 meters diameter that has a series of cuts between .75 and 1.3 meters radius. The cuts should demonstrate manufacturing the most difficult parts of the JEM-EUSO optical prescription, the Fresnel pattern and the blazed grating on the diffractive surface at the edge of the lenses.

Current industry standard Fresnel lens characterization typically includes a visual inspection of groove geometry using a high-powered microscope followed by an optical performance test. Techniques for evaluating the unique performance of the multiple element JEM-EUSO optical system have not been addressed in industry but were developed by the U.S. EUSO team during their MIDEX Phase A, and reported in the Concept Study Report.

If the TIP proposal is accepted, in the U.S. we will measure the surface roughness and the local profiles of the Fresnel and diffractive surfaces of both demonstration systems in the radial and tangential directions at the center of the lenses and the edges using a special optical instrument developed for measuring the Chandra x-ray telescope mirrors and a contact profilometer. The results of these measurements will be compared to manufacturing errors (tolerances) required for the optics to meet JEM-EUSO requirements as determined by optical simulations. These

simulations should establish limits on surface roughness (or errors at high spatial frequency); radial and tangential slope errors (at lower spatial frequencies) and plunge cut depth errors in the blazed grating. The comparison will allow the verification of the manufacturing processes and machines that will be used to make the 2.6m flight optics.

In addition, if the TIP proposal is accepted, using a 2 meter collimator located at a facility at the U.S. Army in Huntsville, Alabama we will perform a full aperture optical test of 1.5m prototype at 300-400 nm at incident angles from 0 to 30 degrees. Planned measurements of the optical properties include: imaging accuracy and resolution, photometric influence distribution, and veiling glare and stray-light measurements.

All these measurements and test results will be used to validate our models for the JEM-EUSO optics so that we can predict the true performance of the 2.6 meter diameter flight optics system.

4.2.8.2.3. Test and Verification for the 2.6m flight system

If the U.S. EUSO proposal to NASA is accepted, the U.S. EUSO project will conduct extensive verification on the Optical System (OS) to ensure that it meets all requirements. Our verification approach will rely heavily on the testing of the flight hardware as shown on Figure 4.2.22 and discussed below. Other verification methods will include analysis, and inspections.

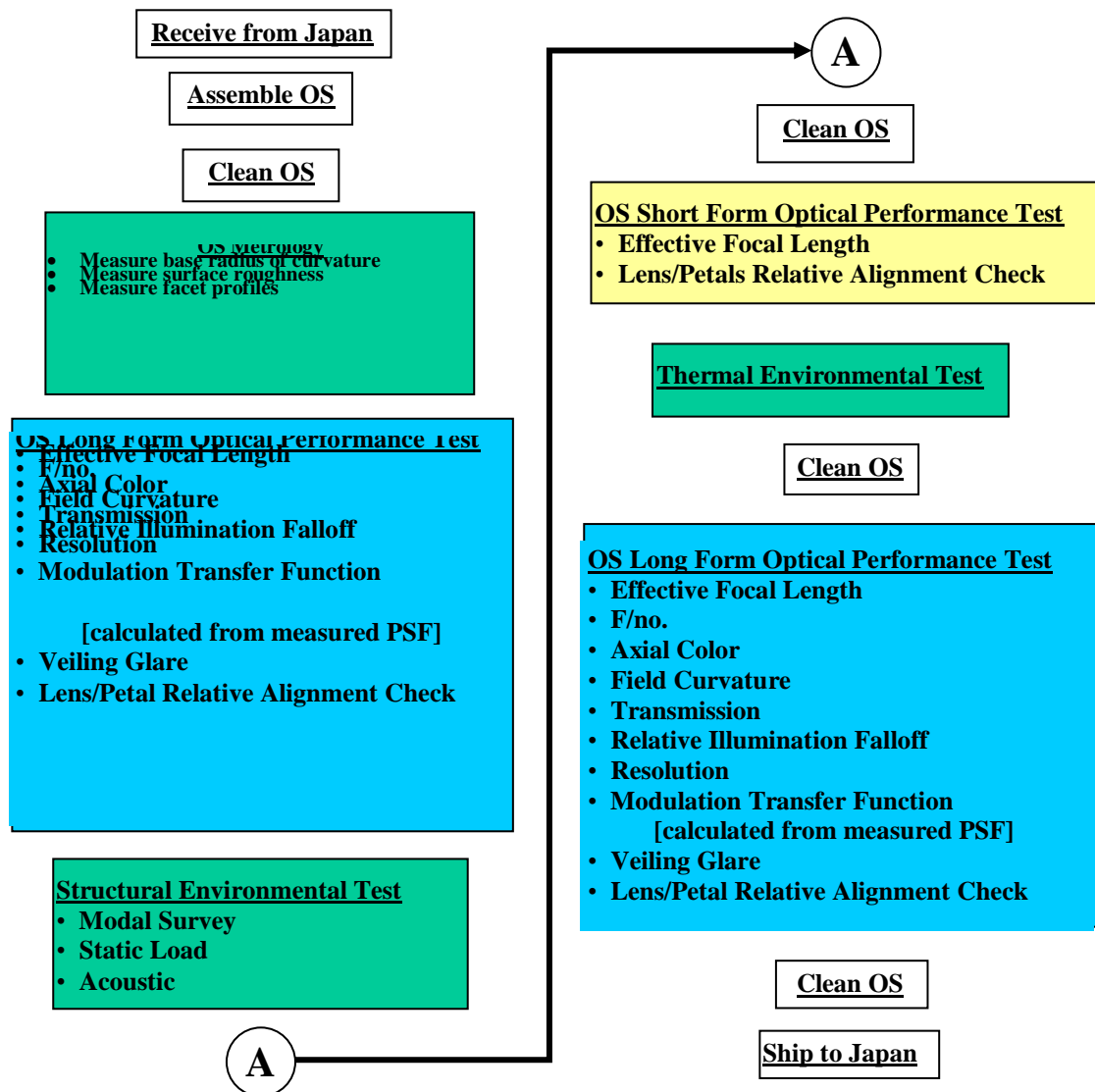


Fig 4.2.22 – OS Test Flow

The U.S. EUSO team will follow a protoflight test program. Protoflight is a term used to indicate the type of testing program that will occur at the subsystem level and means that the deliverable end item used for flight will also be used to qualify the design for the expected environments and to provide acceptance for design and performance requirements. Two complete OS units will be built. One set will be the flight unit, and the other will be used as a spare.

After the optical element frames, the focusing mechanisms, the GSE metering structure and the shipping container have been completed, they will be assembled. After the optical elements have been manufactured and inspected, they will be mounted in the frames and aligned using laser retro-reflectors to establish reference points (see 4.2.23). These retro-reflectors will be utilized during all phases of the optics testing to ensure the alignment of the lens segments and the lenses relative to each other. The frames will then be installed in the GSE metering structure whose

purpose is to hold the lenses in the same relative positions as they will be on orbit, so that their optical performance may be measured and baselined prior to delivery. The GSE metering structure containing the lenses in their frames will be shipped to MSFC.

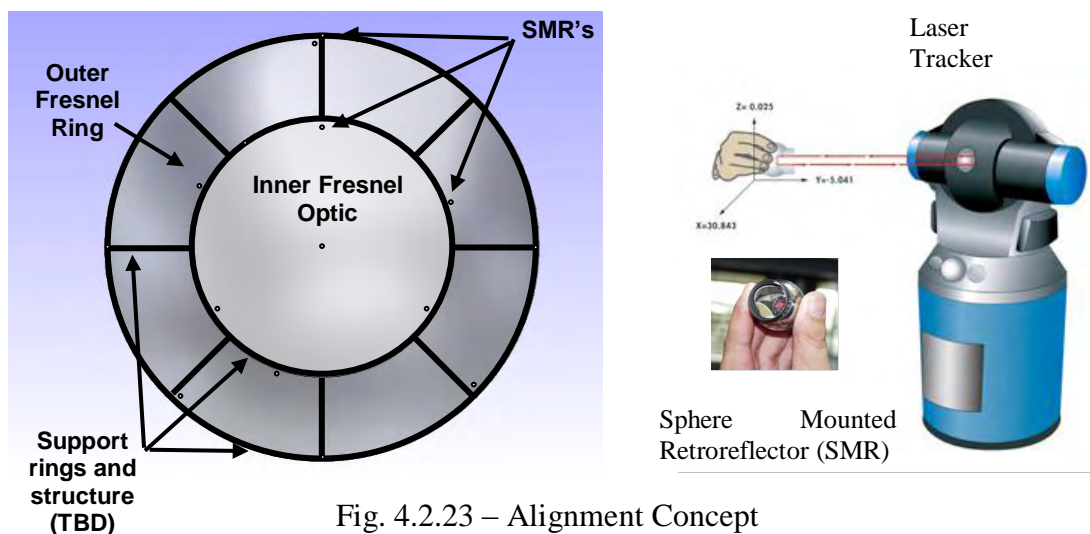


Fig. 4.2.23 – Alignment Concept

At MSFC, a modal survey will be made of the lens/frame assemblies. The lens/frames assemblies will then be cleaned and placed in a thermal vacuum chamber to measure thermal conductance across attach points. These data are necessary for system thermal analysis by JAXA.

Following testing at MSFC, the lens/frame/metering structure assembly, along with a GSE focal surface attachment for mounting light detectors, will be placed in its shipping container and taken to Wright-Patterson AFB for optical performance testing. After attachment of the focal surface and detectors, the assembly will be placed in a chamber with a large-diameter collimated light source to measure and baseline the system's ability at full aperture to concentrate and focus light across the full field of view. These tests will be conducted in vacuum and at temperatures over the range expected in flight. They will include tests of the focusing mechanism.

Following the Optical Performance Test, the assembly will be brought back to MSFC for cleaning and inspection and then returned to its shipping container and transported to Japan. JAXA will complete the integration and system testing there, including thermal vacuum bake-out.

Environmental Test Philosophy

For the JEM-EUSO Instrument, the environmental testing philosophy is to develop and test a proto-flight unit, verifying design via the subscale prototype and incorporating knowledge from its testing into the proto-flight unit. Testing will provide confidence that the designs will perform as expected in the prescribed environments, which will be defined by JAXA in ICD's to be provided at the beginning of Phase B. Sufficient margin will be included in the designs to satisfy both NASA and JAXA requirements applicable to HTV transport and ISS installation. The testing of U.S. provided hardware is necessarily limited to the component and subassembly levels of integration.

These tests will cover mechanical structure, thermal and material properties, and space

environmental effects. Specifically, the tests will include acoustic-vibration environments relevant to ground and HTV transportation, and ensure thermal-vacuum compatibility and compliance with both HTV and ISS environments.

4.2.9. Operation

Table 4.2.12 Operation of optics

Operation phase	Operation mode
Before launch	Keeps constant temperature and keeps out of shock. Covers on lens surfaces to protect from falling objects
Transportation to ISS	
Launch	Follows environment of HTV un-pressurized module. Protects from falling objects by using lid.
Standing by phase to attach the ISS and Attaching Phase	Follows environment of ISS. Protects from debris and sunlight by closing lid.
Observation phase	
Normal operation	Follows environment of ISS. Opens/Closes the lid synchronizing with orbit to protect form debris and sunlight.
Approaching Transportation Vehicle Phase and ISS attitude controlled phase	Close the lid. If needs, transforms to HTV stowing mode.
Onboard calibration mode	Adjusts focal position by using focal adjust system
End of mission	Transforms to HTV stowing mode.

4.2.10. Summary

4.2.10.1. Optics summary table

1) Requirements

Table 4.2.13 Requirements

	Item	Required value	Note
IR1	Wavelength	330-400 nm	Including 337,359,391nm lines of nitrogen
OPR1	Aperture diameter	$\geq 2.5m$	
OPR2	Field of view	$\geq \pm 30^\circ$	
	F number	≤ 1.25	OPR1/OPR2
OPR3	Angular resolution	$\leq 0.1^\circ$	For determining the arrival direction of the primary particles of the air shower within few degrees
OPR3	Spot size	$\leq 5mm$ in diameter	Corresponding to the pixel size less than 4.5mm of the light detector. Corresponding to less than 0.1° in angular resolution.
OPR4	Photon collecting efficiency (Throughput)	50% @ 0-10° 40% @ 10-20° 30% @ 20-30°	Indicating the focus efficiency on a spot size 5mm in diameter on the focal surface. Upon consideration of: Structure of Fresnel lens (back cuts, etc.), transmittance of materials,

			reflection on lens surface, error in diffractive optics manufacturing, error in Fresnel lens manufacturing, and loss in lens support structure.
OPR5	Transmittance of filter	$\geq 90\%$	Should avoid a degradation of the performance by more than 10% during the mission

2) Technical Readiness Level

Table 4.2.14 Technical Readiness Level

	Item	Technical Readiness Level and its reason when selected in Feb./'07	Verification status of technical readiness level and reason (as of Apr./'08)	Expected technical readiness level and activities at SDR time (Mar./'09)
IR1	Observational wavelength	<p>TRL4</p> <p>Verified by observed spot size with test lens of 20cm, 40cm and 1m diameter, lens in ESA-Phase-A study[1]</p> <p>Wavelength dependence of CYTOP material on refraction and transmittance was verified.</p>	<p>TRL4</p> <p>In addition to the left column, the following 4 verifications were accomplished:</p> <ul style="list-style-type: none"> • Verification of the optical performance in case of the usage of CYTOP by using optics design software CodeV • Optimization of designing to reduce the spot size to 1/2 by using CodeV. • Measurement of refractive index and its temperature dependence and transmittance in case of the usage of CYTOP. • Verification of the manufacturing CYTOP lens using a small piece of 10cm\varnothing. 	<p>TRL5</p> <p>Fabricate 2.5m lens dividing it into 2 parts: a central part of 1.5 m and the circular ring part.</p> <p>Optical performance of the central part to be verified (before Mar./'09).</p>
OPR1	Entrance diameter	<p>TRL3</p> <p>Verified by using CodeV. Further enlargement of the diameter and stowing capability</p>	<p>TRL4</p> <p>Stowing capability in HTV was verified by enlarging the diameter to 2.65m\varnothing (cutting lateral parts).</p>	<p>TRL5</p> <p>The same as above</p>

		in HTV to be verified.		
OPR 2	Field of view	TRL4 Verified by means of optics design software CodeV.	TRL4 Refer to IR1.	TRL5 The same as above
OPR 3	Angular resolution	TRL4 Verified by using CodeV.	TRL4 Refer to IR1.	TRL5 The same as above
OPR 3	Spot size	TRL3 Verified by using CodeV. There is some room to optimize the design for a further improvement of the performance by reducing the spot size.	TRL4 Refer to IR1.	TRL5 The same as above
OPR 4	Photon collecting power (Throughput)	TRL3 Verified by using CodeV. It is necessary to verify the possibility of processing CYTOP material.	TRL4 Refer to IR1.	TRL5 The same as above

3) Main parts

Table 4.2.15 Main parts of optics

Item	Number	Supplier	Result of test	Comments
1 st lens Baseline optics : PMMA000 Advanced optics : CYTOP	2(PFM, FM)	Manufacturing: RIKEN Material: Mitsubishi rayon Material: AGC	Space qualifications : see[1] Manufacturing : Verified by test piece manufacturing	
2 nd lens Baseline optics : PMMA000 Advanced optics : PMMA000	2(PFM, FM)	Manufacturing: RIKEN Material: Mitsubishi rayon	Space qualifications : see[1] Manufacturing : Verified by test piece manufacturing	
3 rd lens Baseline optics : PMMA000 Advanced optics : PMMA000	2(PFM, FM)	Manufacturing: RIKEN Material: Mitsubishi rayon Material: AGC	Space qualifications : see[1] Manufacturing : Verified by test piece manufacturing	
Lens frame	1 (Share with PFM and FM)	IHI aerospace co. Nippi co.	Under designing	

Focusing adjust system	1 (Share with PFM and FM)	IHI aerospace co. Nippi co.	Under designing	
------------------------	---------------------------	--------------------------------	-----------------	--

4) Temperature requirement

Table 4.2.16 Temperature requirement of optics

Item	Operation temperature	Non-operation temperature	Comments
3 lenses + frame	$T_0 \pm 10^\circ\text{C}$ ($-30 < T_0 < 30^\circ\text{C}$)	$-45 \sim +55^\circ\text{C}$	Each lens has a independent equilibrium temperature T_0 .

5) House keeping requirement

Temperature monitor 15 points 5 points/lens (Center 1 point + circular parts 4 points)

Sampling 10-12 samplings/orbit

Focusing adjust system position monitor 1 sampling/orbit

6) Mass, Power and Telemetry

Table 4.2.17 Mass budget (Baseline optics)

Parts	BEE (kg)	Margin (%)	Total (kg)	Comments
1 st lens	89	15	103	PMMA000 15mm thickness
Frame of the 1 st lens	-	-	-	Included in Pallet frame
Stop	-	-	-	Included in 2 nd lens frame
2 nd lens	55	15	64	PMMA 10mm thickness
Frame of the 2nd lens	55	15	64	
3rd lens	84	15	97	PMMA000 15mm thickness
Frame of the 3rd lens	55	15	64	
Focusing adjust system	20	15	23	
Total	358		415	

Table 4.2.18 Mass budget (Advanced optics)

Parts	BEE (kg)	Margin (%)	Total (kg)	Comments
1 st lens	150	15	173	CYTOP 15mm thickness
Frame of the 1 st lens	-	-	-	Included in Pallet frame
Stop	-	-	-	Included in 2 nd lens frame
2 nd lens	47	15	55	PMMA 10mm thickness
Frame of the 2nd lens	55	15	64	
3rd lens	144	15	166	CYTOP 15mm thickness
Frame of the 3rd lens	55	15	64	

Focusing adjust system	20	15	23	
Total	471		545	

Table 4.2.19 Power budget

Parts	BEE (Watt)	Margin (%)	Total (Watt)	Comments
Focusing adjust system	10	15	12	

Table 4.2.20 Telemetry budget

Parts	BEE (kbps)	Margin (%)	Total (kbps)	Comments
Focusing adjust system	TBD	15	-	
HK	TBD	15	-	

4.2.10.2. Cost

The cost table between FY08 and FY13 is shown in table 4.2.20.

	FY08	FY09	FY10	FY11	FY12	FY13
PHASE A/B	\$183,124	\$4,049,433	\$1,199,981			
PHASE C/D			\$9,093,931	\$7,136,476	\$6,490,009	\$4,044,885
PHASE E						\$247,639
PHASE F						
PI Mission Cost	\$183,124	\$4,049,433	\$10,293,912	\$7,136,476	\$6,490,009	\$4,292,523
Contributions	\$461	\$3,786	\$5,833	\$5,999	\$6,176	\$134,716
SEO Activities	\$0	\$0	\$0	\$0	\$0	\$0
Total Enhanced Mission Cost	\$183,585	\$4,053,218	\$10,299,745	\$7,142,475	\$6,496,185	\$4,427,239

Total : 32.6M\$ ≅ 3.3B¥

4.2.10.3. Schedule

Schedules of FY 2008 and after FY 2008 are shown in table 4.2.21 and 4.2.22. We will manufacture 3 subscale lenses of baseline optics by using the UTD-3400 machine by the end of November 2008. Seizes of these lenses are larger than 1.5m in diameters. These lenses will be sent to NASA after the end of November 2008. US team will do optical test of the 3 subscale lenses of baseline optics and report by April 2009.

Table 4.2.21 Schedules of FY 2008

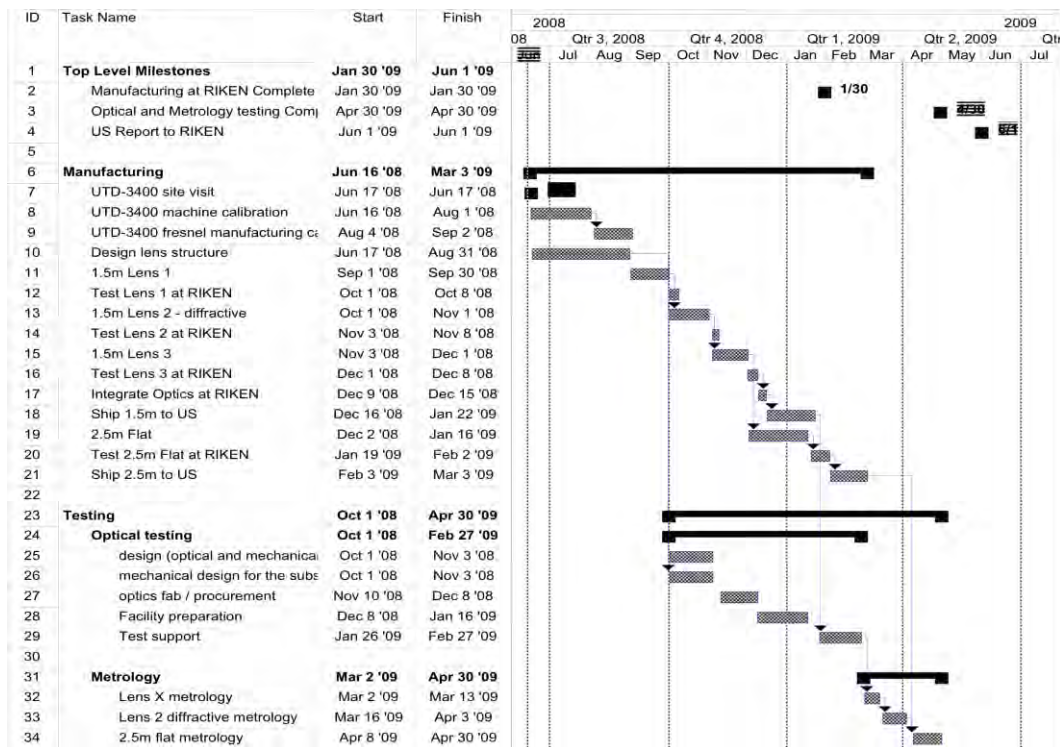


Table 4.2.22 Schedules after FY 2008

	FY2008	FY2009	FY2010	FY2011	FY2012	FY2013
Proto type model lens.		Manufacturing				
Preflight model		Manufacturing	Testing			
Fright model			Manufacturing, Testing	Deployment		

4.2.10.4. Organization

Subsystem leader : Roy Young (NASA/MSFC), Yoshiyuki TAKIZAWA (RIKEN)

Members:

Japan: Hitoshi Omori, Kouki Maekawa, Yousuke Hachisu, Toshikazu Katahir, Masayoshi Mizutani.

US: J. H. Adams, S. Mitchell, M.J. Christl, J. Watts Jr., A.English, Roy Young (NASA/MSFC) , Y. Takahashi, D. Gregory, M. Bonamente, V. Connaughton, K. Pitalo, J.Hadaway, J. Geary, R.Lindquist, P. Reardon, T. Blackwell (Univ. Alabama), H. Crawford, E. Judd, C. Pennypacker (LBL, Univ. California ,Berkeley), V. Andreev, K. Arisaka, D. Cline (UCLA), A. Berlind ,T. Weiler, S. Czorna (Vanderbilt Univ.) , R. Chipman, S. McClain (Univ Arizona)

Reference

- [1]: EUSO-OM-DESIGN-001-2
- [2]: Optics design file, 1114_f1_2300_pm_1d_3
- [3]: Optics design file, 0824_f1_2300_cy_pm_1d_1

4.3. Focal Surface Instrument

4.3.1. General

The Focal Surface(FS) of JEM-EUSO has a curved surface of about 2.3m in diameter, and it is covered with about 5,000 multi-anode photomultiplier tubes (Hamamatsu R8900-M36: MAPMT). The FS detector consists of Photo-Detector Modules (PDMs), each of which consists of 9 Elementary Cells (ECs) arranged in an array of 3×3 . About 1,233 ECs or about 137 PDMs are arranged on the whole FS (Figure 4.3.1.1).

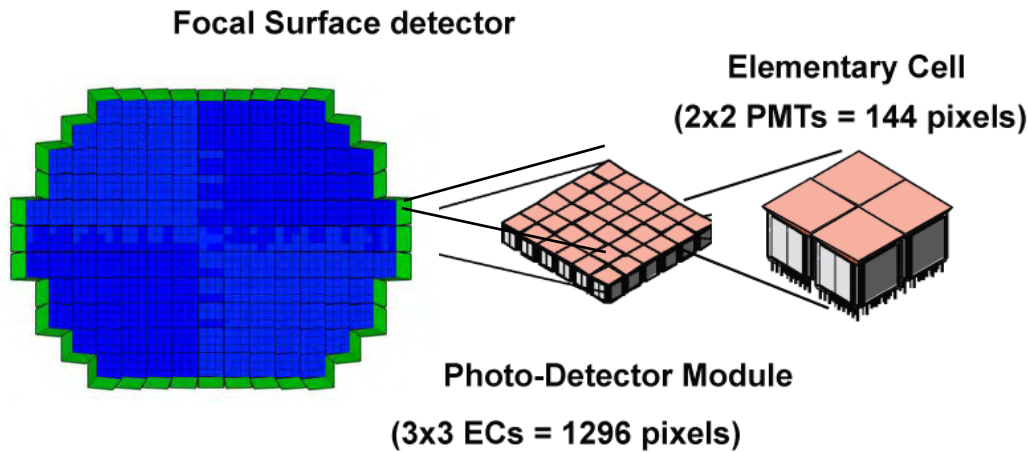


Fig. 4.3.1.1 Focal surface detector and its structure

4.3.1.1. FS Definition

The FS of the JEM-EUSO instrument is the Photo-Detector and the Read-Out electronics of the JEM-EUSO experiment, located onto the focal surface of the optics.

4.3.1.2. FS Coordinate

The coordinates within the FS are defined as follow;

- 1) Origin of the Cartesian axes: at the center (vertex) of the FS.
- 2) The z-axis passes by the center of the optics, in the direction from the FS to the optics, i.e., towards earth.
- 3) The x-axis is parallel to the moving direction of the ISS, in the same direction as the ISS.
- 4) The y-axis together with the above x- and z-axis is defined by the right-handedness of the coordinate system.

4.3.1.3. FS Location

The surface of the Photo-Detector of the FS is accommodated on the focal surface of the optics.

4.3.1.4. FS Components

The main components are:

- a) FS Detector
- b) FS Electronics

4.3.1.5. Lifetime

The Lifetime of the FS is defined in the JEM-EUSO System Specification.

4.3.1.6. REQUIREMENTS

4.3.1.6.1. Functional Requirements

The main functional requirements for FS are as follows:

- 1) The FS shall be capable to detect the EAS by observing the fluorescence light produced during the EAS development and the Cherenkov light.
- 2) The FS shall be capable to determine the position of the arriving photons as a function of time and to follow the space-time development of the EAS.
- 3) The FS shall have single-photon sensitivity in the 330 nm ÷ 400 nm wavelength range to detect EAS as faint as possible.
- 4) The FS shall have fast response (well below 0.1 μ s) to follow the space-time development of the EAS.
- 5) The FS pixel size shall correspond to an earth pixel size no greater than $\Delta\alpha=0.1^\circ$.
- 6) Cross talk between neighboring pixels shall be less than 10 % (TBC).
- 7) The noise rate shall be two orders smaller than the rate of the night airglow background.
- 8) Overall detection efficiency shall be good and uniform. The overall detection efficiency, averaged over all the FS, shall be: $\varepsilon_{PD} \geq 0.12$
- 9) The FS shall cover the optical focal surface with a sensitive area as large as possible by reducing dead or inefficient areas.
- 10) The FS shall have low sensitivity to magnetic fields of the order of magnitude of around one gauss.
- 11) The FS shall be highly reliable and stable over at least a 5 years' time.
- 12) The FS shall be compatible with the requirements imposed by a space mission.

4.3.1.6.2. Physical Requirements

The main physical requirements for FS are as follows:

- 1) The mass is required by the JEM-EUSO Instrument System.
- 2) The center of gravity shall be on the z-axis with a tolerance of less than TBD mm.
- 3) The FS structure shall be able to be installed within the JEM-EUSO telescope structure.

4.3.1.6.3. Shape of the FS

The FS generated by the optical system has an aspheric shape given by the following equation (in cylindrical coordinates).

$$z[r] = \frac{r^2}{\left(1 + \sqrt{1 - \frac{(1+k)r^2}{\rho^2}}\right)\rho} + ar^4 + br^6 + cr^8 + dr^{10} + z_0 \quad r \equiv \sqrt{x^2 + y^2}$$

where:

$$\begin{aligned} \rho &= -2551.41 \text{ mm} \\ k &= +0.480130 \\ a &= -0.430458 \times 10^{-10} \text{ mm}^{-3} \\ b &= +0.138070 \times 10^{-15} \text{ mm}^{-5} \\ c &= -0.126951 \times 10^{-21} \text{ mm}^{-7} \\ d &= +0.353757 \times 10^{-28} \text{ mm}^{-9} \end{aligned}$$

and z_0 is the quota of the vertex of the FS.

On the other hand, on the focal surface detector, modules of identical shape are arranged on an approximate spherical shape.

The shape of the FS shall be assumed to be a spherical surface:

$$z_s[r] = \sqrt{\beta^2 - r^2} - \beta \quad r \equiv \sqrt{x^2 + y^2}$$

where $\beta = 2114.15\text{mm}$.

4.3.1.6.4. Thermal Requirements

The FS shall be designed so that the temperature does not exceed 50°C at any time to protect the bi-alkali photocathode.

In addition, to figure out the property of the device, we measure the temperature with the accuracy within $\Delta T = \pm 5^\circ\text{C}$ on the whole region of the focal surface.

The FS shall be also designed so that the temperature must not fall below -30°C for the operation of the electronics.

4.3.2. FS Detector

4.3.2.1. Components of the FS

The FS is composed of the following devices:

- 1) Photo-detector (multi-anode photomultiplier)
- 2) MAPMT suspension structure
- 3) PDM components
- 4) High Voltage divider
- 5) High Voltage Power Supply
- 6) FS structure

4.3.2.2. Photo Detector

JEM-EUSO is a photon-hungry experiment and its FS should have large detection efficiency. The FS should have the single photon counting capability in near-ultraviolet wavelength region to avoid the systematic errors, which may be introduced through the gain drift. It should be reliably and stably operational in the space environment for at least 3 or 5 years mission period. For the above reason, Multi-anode photomultipliers (MAPMT) with UV-glass entrance window are employed on the FS.

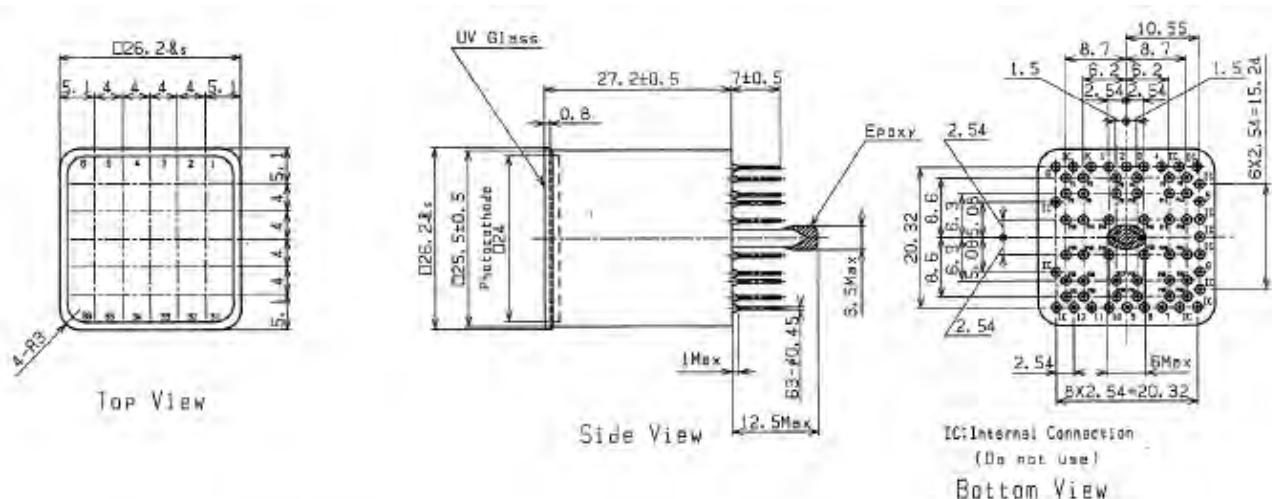




Figure 4.3.2.1: MAPMT for JEM-EUSO (R8900-03-M36)

4.3.2.2.1. MAPMT Specification

Present baseline choice is the Hamamatsu R8900-03-M36 (see fig. 4.3.2.1), which has been developed by RIKEN in collaboration with Hamamatsu Photonics K.K. It has an ultra-bialkali photo-cathode and transforms photons into electrons then focuses them by means of a weak focusing electric field, and amplifies photo-electrons by means of a stack of metal channel dynodes. The signals are taken from the anode, formatted as an array of 6×6 squares. Compared with the former R7600 series, the R8900 MAPMT has 1.75 times higher quantum efficiency and 1.9 times larger sensitive area. The total detection efficiency of R8900 is over 3 times higher than that of R7600 (see fig. 4.3.2.2).

The main specifications of R8900-03-M36 are as follows:

- 1) The 6×6 square pixels have a side of 4.3 mm and a pitch of 4.3 mm, giving a maximum sensitive area of 24 mm \times 24 mm.
- 2) The physical dimension of the MAPMT section is 25.7 mm \times 25.7 mm (26.2 mm maximum) and the length is 27.2 mm. The mass is 27.3 g.
- 3) The tube is equipped with an ultra-bialkali photo-cathode and a 0.8 mm thick UV-transmitting window. This ensures quantum efficiency higher than 35% (maximum 40%) for wavelengths from 330 nm to 400 nm.
- 4) Detection efficiency (ε_3) of photons has the following temperature dependence:

$$d\varepsilon_3/dT = a\varepsilon_3, \quad a = -0.37\%/^{\circ}\text{C}$$

- 5) The device has a metal channel dynode structure with 12 stages, providing a gain of the order of 10^6 at 0.9 kV with a tapered voltage divider.
- 6) The anode pulse rise-time is about 1.5 ns.
- 7) The transit time spread is about 0.3 ns.
- 8) Cross talk is about 7%.
- 9) Gain non-uniformity between different anodes on the same MAPMT is 1:3.
- 10) Average gain non-uniformity between different MAPMT is within 1:2.
- 11) The anode MAPMT capacitance is about 2.8 pF.
- 12) The overall anode dark current after 30 minutes storage in darkness is of the order of 1 nA.
- 13) The voltage divider ratio: PK (0.6,1.8,2.4,1,1,1,1,1,1,1,1,1,1,1,1,1) A.

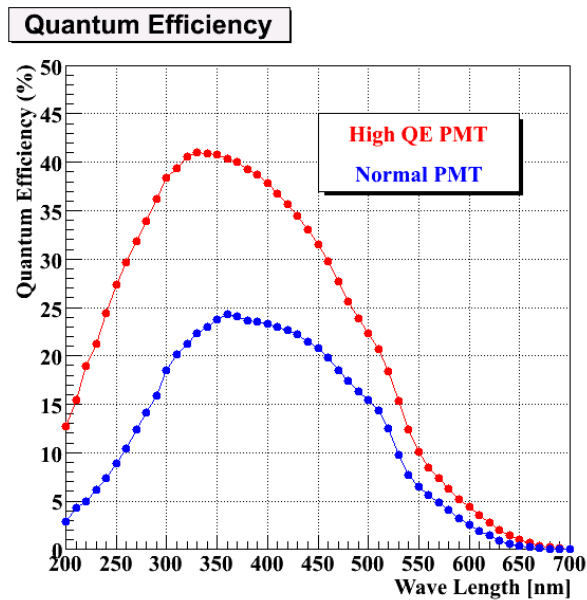


Figure 4.3.2.2: Quantum Efficiencies of the Ultra-bialkali photocathode (High QE PMT) and the normal-bialkali photocathode

The environmental specification for R8900-03-M36 is:

- 1) Optimal operating temperature: $-10^{\circ}\text{C} < T < +30^{\circ}\text{C}$.
- 2) Non operating temperature: $-30^{\circ}\text{C} < T < +50^{\circ}\text{C}$.
- 3) Temperature of each MAPMT should be monitored with the accuracy of $\pm 4.5^{\circ}\text{C}$ or better.
- 4) Max acceleration: 18 Grms [break-point is beyond 20 Grms by test].
- 5) Magnetic field effects: 0.1 relative gain variation at 2 gauss.
- 6) Gain goes down after 3(+2) years operation: 81%(78%).
- 7) Reliability for 3(+2) years operation: 99.1%(98.5%).

4.3.2.2.2. Requirements of Systematic errors

The following requirements have the objective of minimizing systematic errors within $\pm 5\%$ (TBC).

- 1) The uncertainty on the sensor efficiency ($\Delta\varepsilon_{\text{PMT}}/\varepsilon_{\text{PMT}}$): $\pm 5\%$ or smaller
- 2) The uncertainty on threshold value of Front-end-comparator ($\Delta x/x$): $\pm 25\%$ or smaller
- 3) The accuracy of the High Voltage supply (ΔHV): $\pm 24\text{V}$ or smaller
- 4) Temperature uncertainty (ΔT): $\pm 13.5^{\circ}\text{C}$ or smaller
- 5) Anode cross talk uncertainty: $\pm 5\%$ or smaller
- 6) Dynode and pre-amplifier gain uncertainty: $\pm 5\%$ or smaller

4.3.2.2.3. Radiation Environment

The radiation influences the transparency of the entrance window. The influence on the cathode sensitivity and electron amplification is negligibly small compared with the transparency degradation. The transparency is degraded to 90% beyond 1.4×10^5 R for gamma-rays in the MeV energy region, or is degraded to 95% beyond 100 krad for 70 MeV protons. The estimated radiation dose in 5 years mission period is around 10 krad.

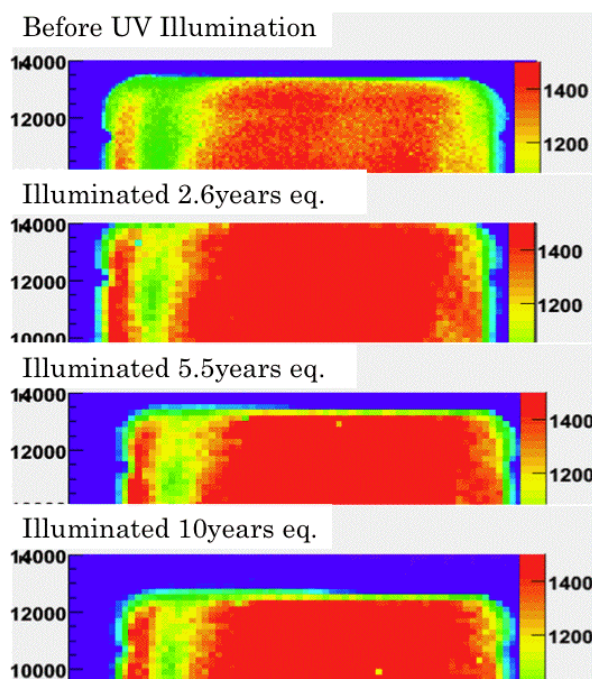
4.3.2.2.4. Vacuum Monitoring

The voltage applied to the MAPMT is around -1 kV. Accidental increase of local pressure in the range of 100-1000 Pa may cause a fatal damage due to the discharge, therefore a pressure monitor

will turn off the high voltage power supply. In addition for security reason, all the HV lines are supposed to be potted with a suitable resin (Dow Corning DC-93500 etc.).

4.3.2.2.5. UV Environment

When the lid of the JEM-EUSO telescope does not close by some failure, the daylight of the earth illuminates the FS. In such a case, the HV Power Supply of the photomultipliers is turned off, and the dynodes are not damaged. However, the photocathode itself may be damaged. Therefore, we have measured the damage of the photocathode by means of a strong UV light illumination with the power supply switched off. We did not recognize any damage for the UV light illumination which is equivalent to 10 years daylight from the earth (see fig. 4.3.2.3).



Sensitivity & Uniformity

	Sensitivity	Uniformity
Before	1.00	1.4
2.6years	1.11	1.4
5.5years	1.11	1.4
10years	1.10	1.4

D.E. Map vs. Illuminated time

Figure 4.3.2.3: Sensitivity variation for UV light illumination

4.3.2.3. MAPMT Support Structure

The main functions of the MAPMT Support Structure are as follows:

- 1) To allow packing of the MAPMT as close as possible with precise relative positioning.
- 2) To have common high voltage inputs and every anode signal outputs.
- 3) To be able to support MAPMTs safely against the vibration at the launch.
- 4) To minimize outgas.

The figures and the main specifications of the prototype model of the MAPMT Support Structure are as follows:

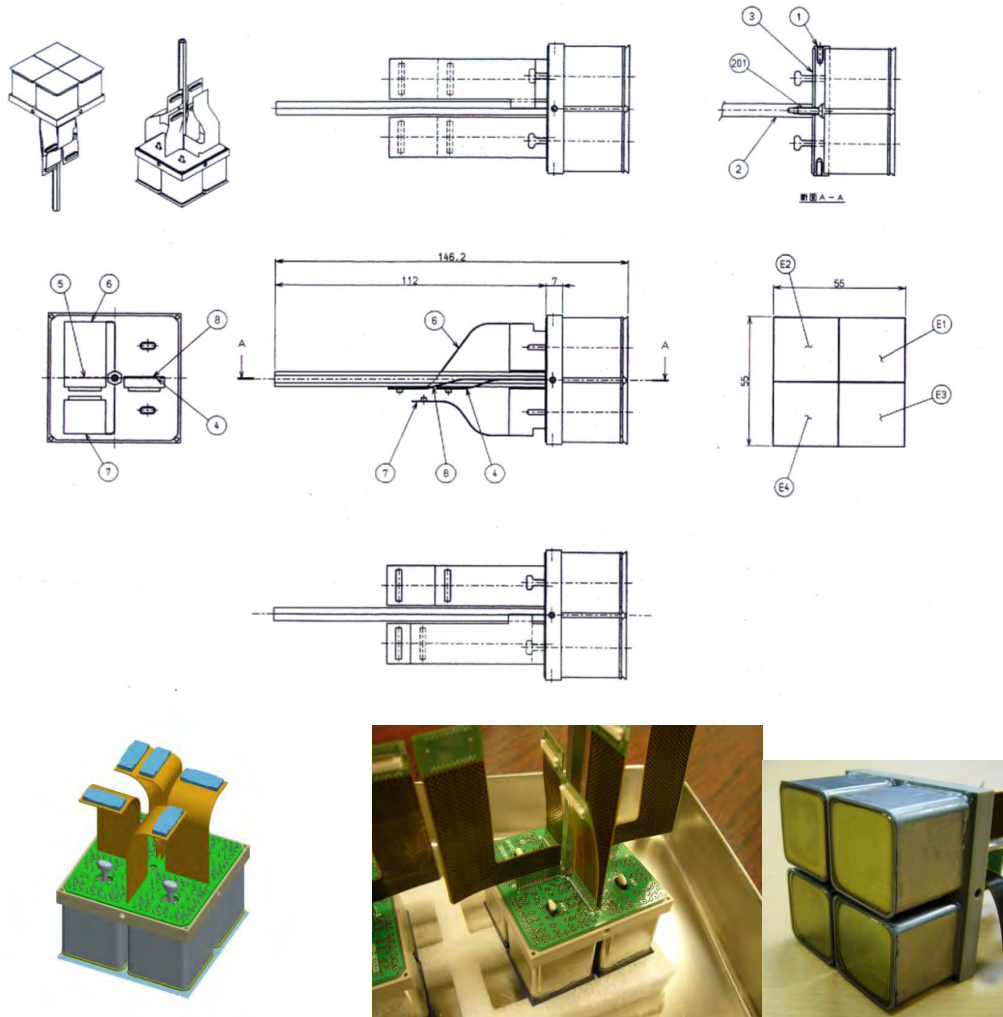


Figure 4.3.2.4: Drawings of MAPMT Support Structure & its prototype

- 1) It supports 4 MAPMTs.
- 2) It has a pair of high voltages input and provide them to 4 MAPMTs.
- 3) It has every anode signal output.
- 4) It doesn't destroy the MAPMT when the PDM is vibrated with 20Grms.
- 5) Physical dimension: 56mm×56mm×7mm.

4.3.2.4. PDM Structure

The main functions of the PDM Structure are as follows:

- 1) To allow packing of the MAPMT Support Structure as close as possible.
- 2) To have the EC electronics boards and the PDM electronics board inside.
- 3) To have a High-Voltage Power Supply inside.
- 4) To be able to endure vibrations at the launch.
- 5) To minimize outgas.
- 6) To evacuate efficiently the heat from internal circuits.

The figures and the main specifications of the PDM Structure are as follows:

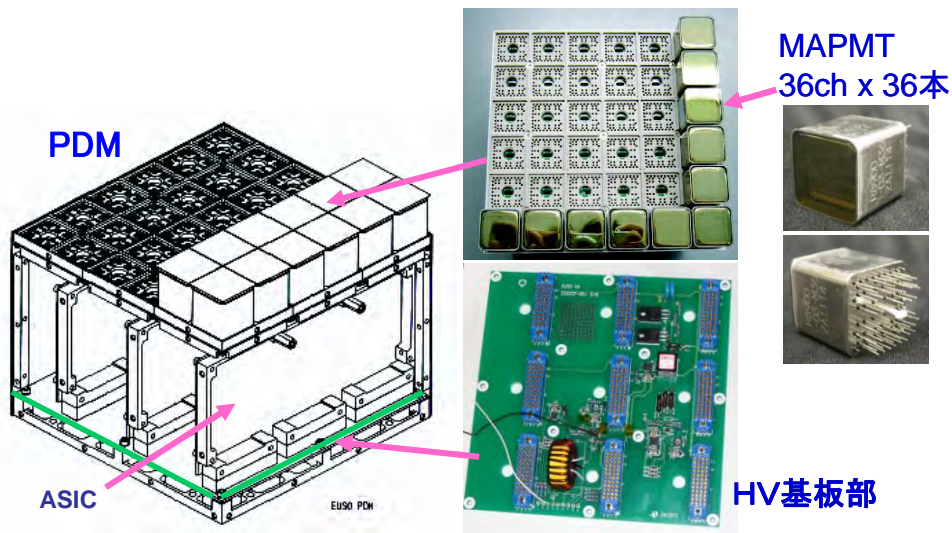


Figure 4.3.2.5 Drawings of PDM Structure & its prototype

- 1) It supports 9 MAPMT Support Structures.
- 2) It has 3 EC electronics boards and the HV Power Supply system.
- 3) It endures vibrations of the PDM with 20Grms.

4.3.2.5. High-Voltage Divider

Active high-voltage dividers of power saving type are used to supply high voltage to the MAPMT dynodes. In addition, the divider current is defined as 10 times larger than the anode current for the standard nightglow background. The High-Voltage Power Supply is designed to supply arbitrary voltage in the range between 0V and 1,000V. The above characteristics have been verified through the designing, production, electrical tests, radiation tests and a balloon flight, etc.

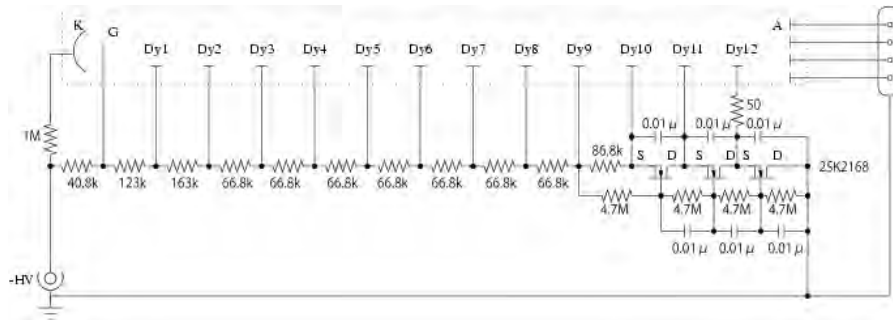


Figure 4.3.2.6 Active High Voltage Divider

In addition, we have developed the high-voltage divider including a protection circuit. It protects the MAPMT from an instantaneous large amount of light such as the lightning. We can operate it more safely by quickly interrupting the photoelectron multiplication using a Photo-MOS relay.

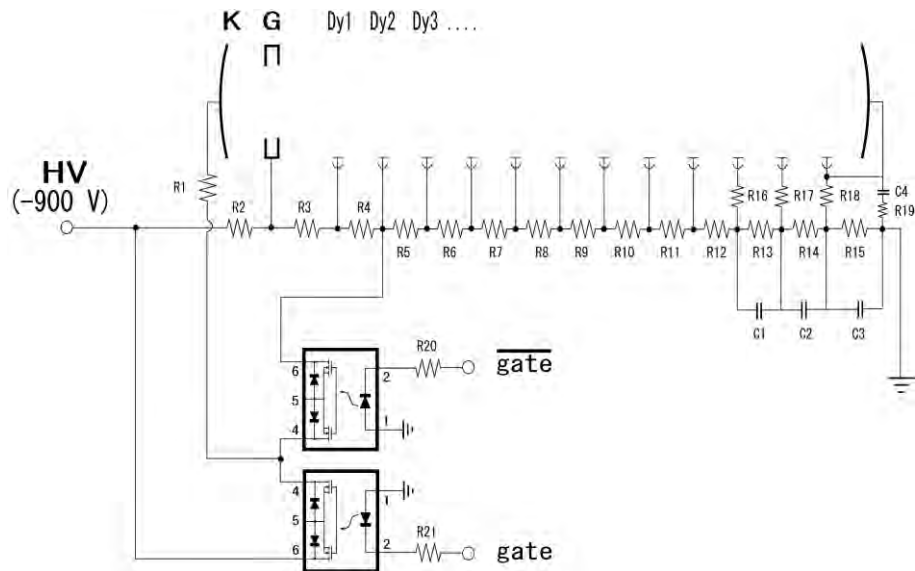


Figure 4.3.2.7 Test circuit of the HV divider with protection from large amount of light

4.3.2.6. High-Voltage Power Supply

The High-Voltage Power Supply system is designed to decrease the failure rate, the complexity of wiring and the danger associated with it, by means of the distributed control method shown in Figure 4.2.3.8.

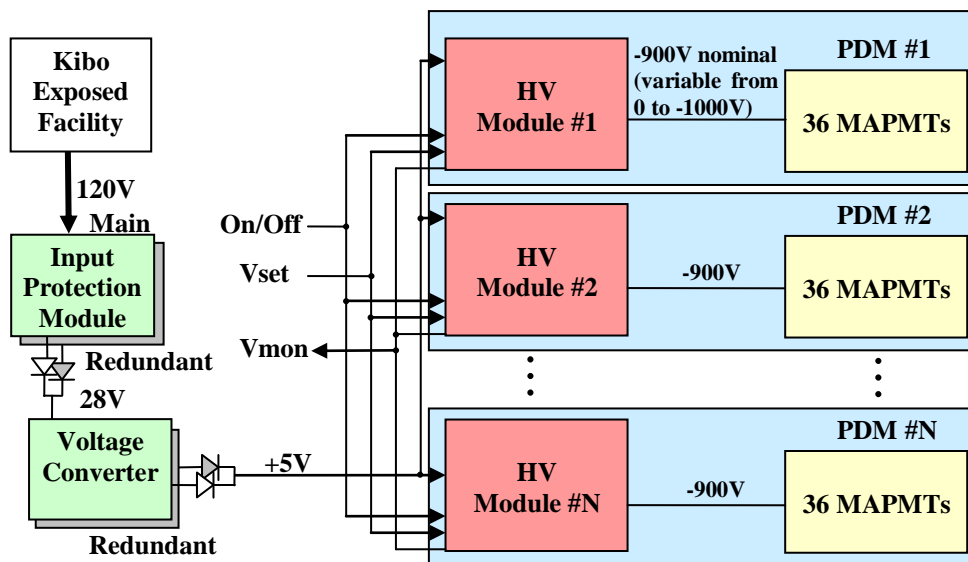


Fig.4.3.2.8 Basic diagram of the HV PS system for the JEM-EUSO focal surface. Each HV PS module is mounted on the PDM. The module drives 36 MAPMTs of each PDM.

The structure of each high voltage power supply is shown in Figure 4.3.2.9. Trigger Control Unit (TCU) gives instructions of high voltage value, and then it is converted to an analog value from 0V to +5V, by the DA converter. When the DC-HV converter receives this voltage, it generates a high voltage from 0V to 1000V. This voltage is transferred to the Bleeder resistance of the MAPMT, and it starts its operation. This voltage is supposed to be monitored through the AD converter after reducing its value.

This high voltage device was stowed on a balloon flight and its operation has already been

verified. In addition, its radiation tolerance has also been tested at the National Institute of Radiological Sciences, by doing tests using proton beams.

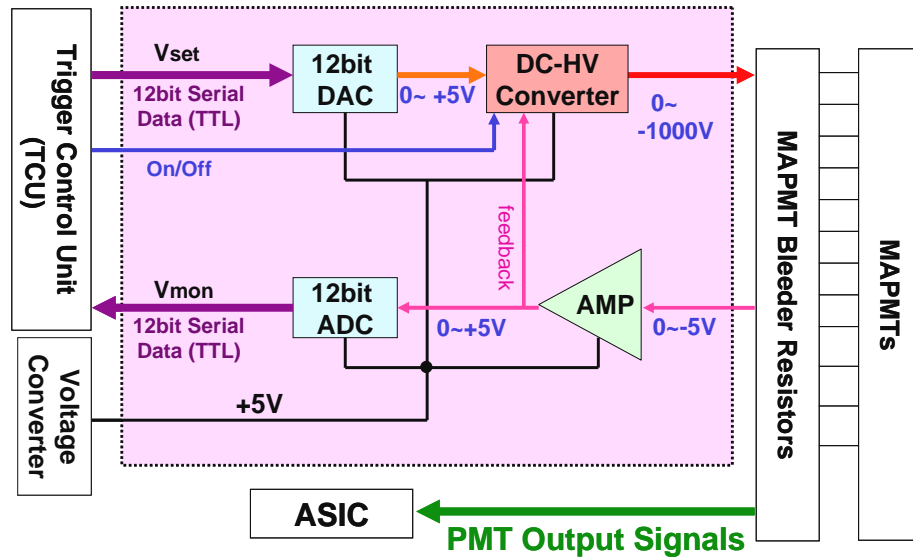


Fig.4.3.2.9 Basic block diagram of the HV PS module.

4.3.2.7. FS Structure

The shape of the focal surface is a spherical surface with about 2114mm radius. The PDMs should have a layout which minimizes the gaps on that surface. Figure 4.3.2.10 shows the PDM layout in case of 137 PDMs.

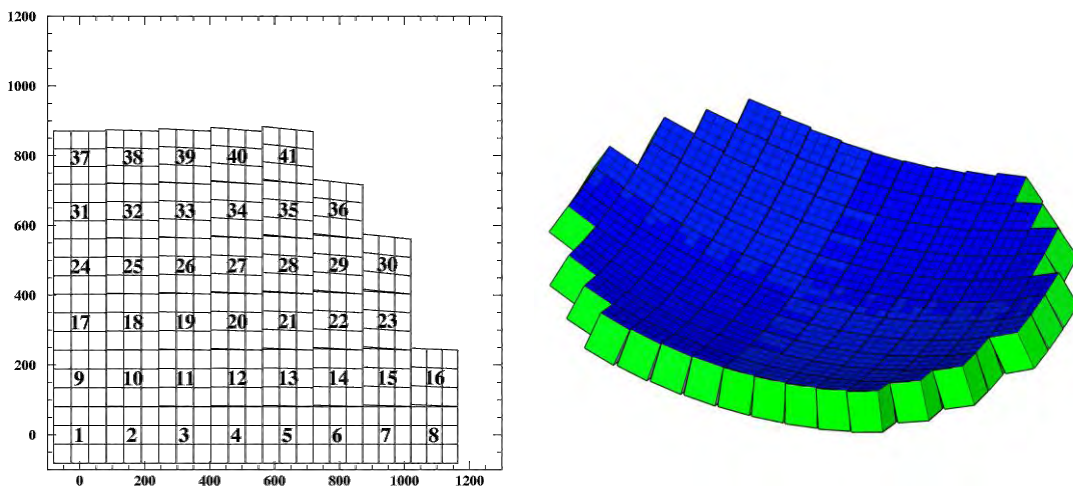


Figure 4.3.2.10: PDM Layout. The figure on the left shows the layout of the PDMs covering 1/4 of the whole FS.

4.3.2.8. Advanced Option

If we can make the spot size of optics smaller, in parallel the S/N ratio will improve. This will make possible to reduce the pixel size of the focal surface. Therefore, we can expect an improvement in the detection efficiency of cosmic rays.

In the baseline design, to match the spot size of 5mm, we use the M36 type MAPMTs, which are 1"×1" and 6×6 channels. If the spot size becomes half, 2.5mm in diameter, the corresponding pixel size of M144 is the most appropriate. In this case, the pixel size becomes 2.2mm, which is difficult

to realize with the currently existing MAPMTs, so it becomes necessary to adopt the SiPM. In addition, we studied both MAPMT and SiPM cases for M64, which is in between M36 and M144. If we reduce the pixel size as a consequence of the fact that the spot size becomes smaller, the size of the air shower signal, which is the point light source, remains unchanged, while the intensity of the background light, becomes smaller in proportion to the dimension of the pixel. Therefore, S/N ratio will improve. As we know from the analysis that the energy threshold to trigger cosmic ray air shower roughly varies inversely with S/\sqrt{N} , if the pixel size is reduced, the energy threshold becomes lower.

In addition, we esteem that by using the SiPM, the photon detection efficiency improves by 1.5 times or higher. This fact also contributes to a further improvement of the S/N ratio. On the other hand, if the pixel size is reduced, the total pixel number on the focal surface becomes larger. This fact may cause some demerits such as the increase of package density of the readout electronics and the increase of electric power consumption for readout, etc. The following table shows the summary of the above effects.

Table 4.3.2.1. Effects of the different number of pixels and type of device

Pixel number and type	MAPMT		SiPM	
	M36 (Baseline)	M64	M64 equivalent	M144 equivalent
S/ \sqrt{N}	1.00	1.33	2.00	3.00
Power	1.00	1.33	1.02	1.75

4.3.2.8.1. MAPMT with reduced pixel size

Although the pixel size of current MAPMT is reduced, the expected effect is not completely achieved due to the signal cross talk. Therefore, we modified a dynode structure design with M64 and M100 MAPMT, which have 8×8 and 10×10 channels in 1" square, respectively. The following figure is a preliminary design drawing of M100 MAPMT. The sensitive area is slightly smaller.

外形寸法図

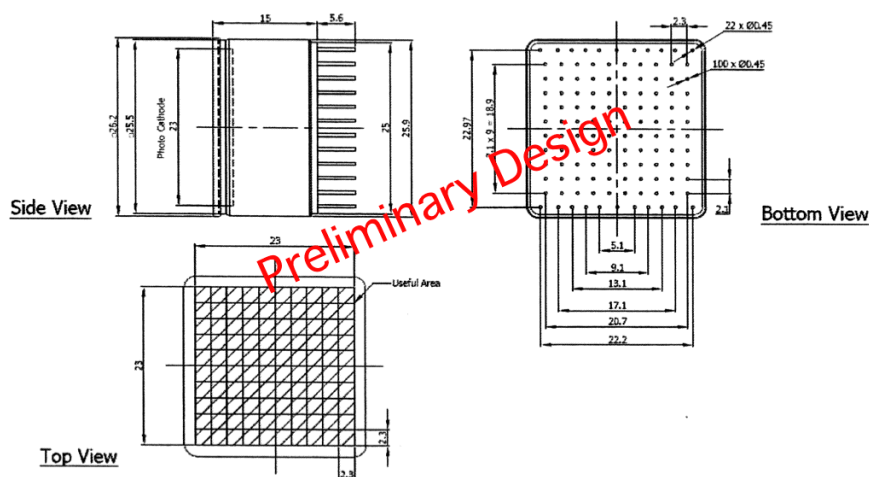


Fig.4.3.2.11 preliminary design drawing of M100 MAPMT

4.3.2.8.2. SiPM

4.3.2.8.2.1.Introduction

A Silicon Photomultiplier (SiPM) is a novel type of optical semiconductor elemental device which has the photon counting ability. It is compact, low cost, it has a high quantum efficiency, high multiplication factor, and fast response (<100ps). It also has the big advantage, compared to Photomultiplier Tubes (PMT), of being able to operate at low voltages (<100V), without being affected by magnetic fields.

A SiPM consists of multiple, from several hundreds to around ten thousands, of avalanche Photodiodes (APDs), which are operated in Geiger mode. APD is a high-speed and high-sensitivity photo-diode, whose photo-electric current is multiplied by applying a reverse bias voltage. If the reverse bias is set above its breakdown voltage the inner electric field becomes higher and the multiplication factor suddenly rises up ($10^5 \sim 10^6$). This phenomenon is called Geiger mode. In this case, each APD pixel is operated in binary mode, which outputs a fixed signal current, regardless of the detected number of photons. Eventually, the output signal from a SiPM is the total charge of all the APD signals, which is proportional to the number of the detected incident photons.

The PDE (Photon Detection Efficiency) of a SiPM depends on the transmittance of the surface, fill factor of the sensitive area, quantum efficiency (QE), and Geiger efficiency of the device.

$$\text{PDE} = \text{Transmittance} \times \text{Fill factor} \times \text{QE} \times \text{Geiger Efficiency}$$

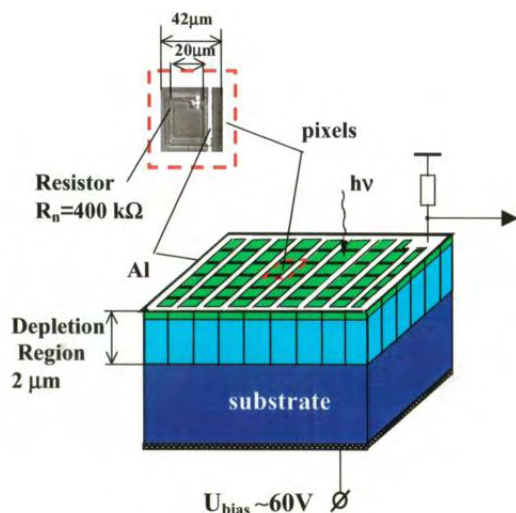


Fig. 4.3.2.12 A schematic view of a SiPM

A SiPM consists of a multiple array of APDs operated in Geiger (binary) mode. The output of a SiPM is an analogue signal, which is the sum of all APD signals and proportional to the number of incident photons.

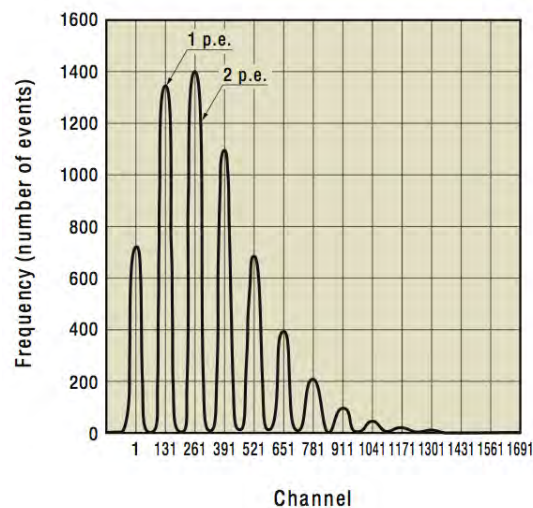


Fig 4.3.2.13 An example of charge histogram of the output pulse. Light intensity can be measured by single photon counting.

4.3.2.8.2.2.Status of SiPM Development

Several kinds of SiPMs, as candidates for JEM-EUSO focal surface plane, are being developed by Hamamatsu, MPI-HLL (Max-Planck Institute for Physics – Halbreiter Semiconductor Laboratory), and MPI-MEPHI (Max-Planck Institute for Physics –

Moscow Engineering Physical Institute).

• Hamamatsu : MPPC

Multi-Pixel Photon Counter (MPPC) was developed and released by Hamamatsu. They have a high sensitivity in the short-wavelength region. Compared to many other SiPMs, they have less thermal noise.

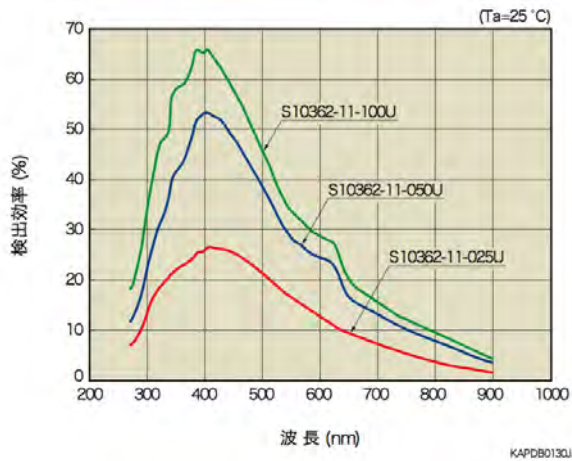


Fig. 4.3.2.14 Wavelength dependence of PDE. The green, blue and red lines represent the PDE for 100, 50 and 25 micron pitch MPPC, respectively.

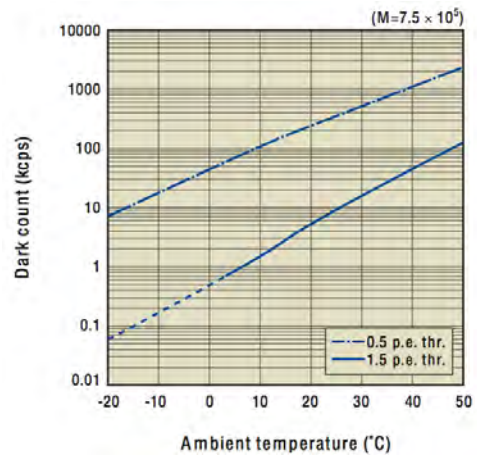
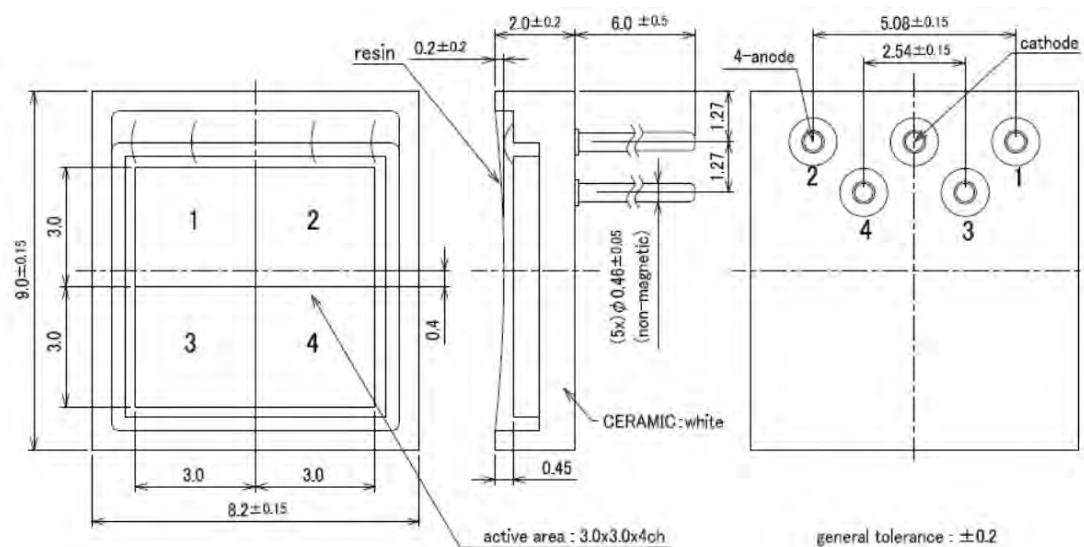


Fig. 4.3.2.15 Temperature dependence of dark current. The rate is $\sim 10\text{kHz}/\text{mm}^2$ at -15°C at single photoelectron level. A $3\times 3\text{mm}^2$ device would have a rate of $\sim 100\text{kHz}$ at that temperature.

Hamamatsu has already developed and released several types of MPPC. In addition, arrays of 2×2 or 4×4 of $3\text{mm}\times 3\text{mm}$ size are being developed. The test of the 2×2 array is already going on at MPI.



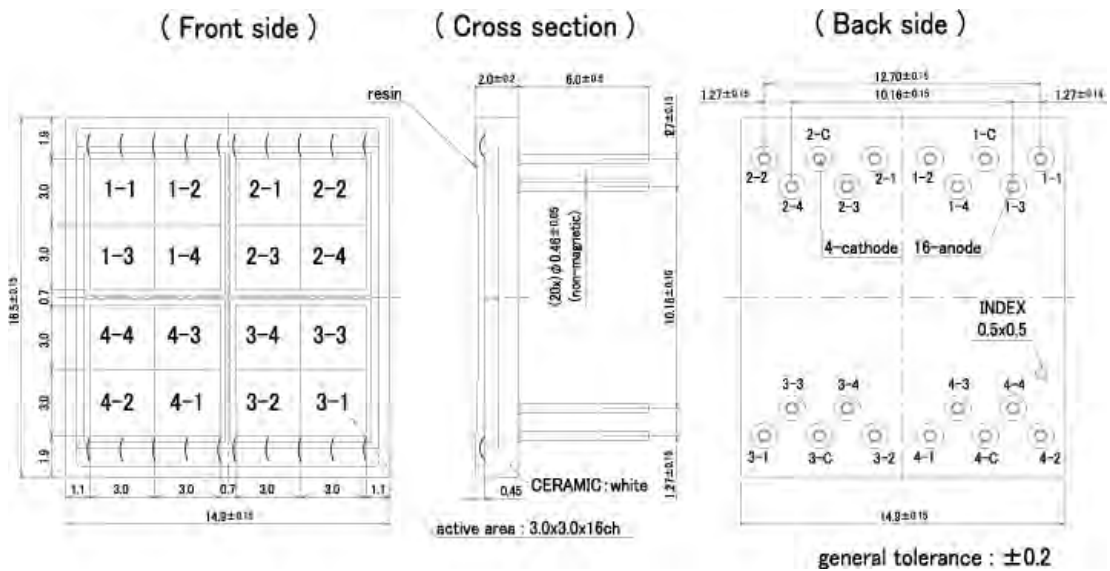


Fig. 4.3.2.16 Design drawing of 2×2(Upper) and 4×4(Lower) array of 3×3 mm² sized MPPCs

• MPI-HLL : SiMPL

MPI for Physics and MPI Semiconductor Laboratory are developing a bulk resistor type of SiPM named SiMPL. In the normal SiPM, the quench resistors and signal lines are placed on the surface, where the incoming radiation hits the detector, while SiMPL doesn't have this structure on the surface, therefore we can improve the filling factor dramatically. In addition, by effectuating anti-reflection coating, we can improve the photon detection efficiency. In this way, we expect to achieve 60% or higher PDE.

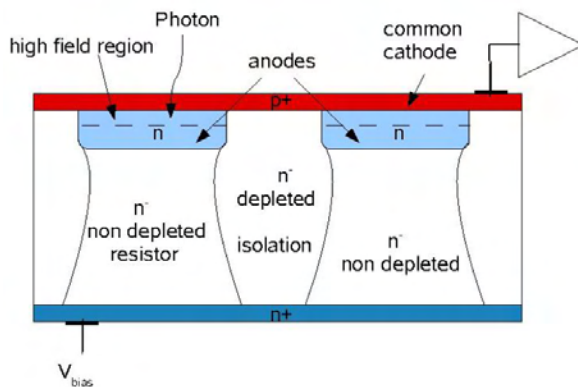


Fig. 4.3.2.17 Schematic view of SiMPL (bulk resistor type) with P-on-N structure, which makes it sensitive to UV. By removing a complicated structure on the surface of the incoming radiation, we can increase the filling factor. As the structure, is simple, it can be produced at low cost.

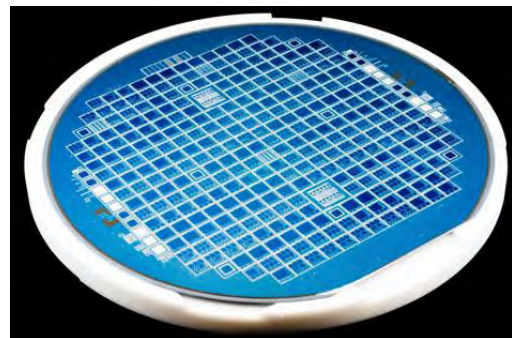


Fig. 4.3.2.18 First silicon wafer of the prototype of SiMPL. As of June 2008, it is already tested at wafer level and device tests are ongoing.

• MPI-MEPHI : SiPM

SiPMs have been developed by MPI for Physics and MEPHI for more than 6 years.

The former n-on-p structure was not UV sensitive (<400nm), while the new structure, p-on-n type, is UV sensitive. The dark noise rate at the room temperature is relatively high but low enough around the JEM-EUSO operation temperature ($-10\pm 5^{\circ}\text{C}$) ($\sim 500\text{ kHz}/3\text{x}3\text{mm}^2$).

4.3.2.8.2.3. Application of SiPMs

The temperature dependence of SiPM gain is one of the most important things to consider in the case of SiPM application to JEM-EUSO. The temperature dependence of gain is around $-3\%/^{\circ}\text{C}$ at a certain bias voltage. We developed a bias voltage compensation circuit using a thermistor as shown in fig. 4.3.2.19 which enables us to reduce the temperature coefficient down to around $0.3\%/^{\circ}\text{C}$, equivalent to a PMT. The circuit, whose bias voltage is regulated following the temperature, works as shown in fig. 4.3.2.19. By using this circuit, we obtained a static gain fluctuation stabilized within $0.1\%/^{\circ}\text{C}$, and $\sim 0.5\%/^{\circ}\text{C}$ in the case of rapidly changing ambient temperature as shown in fig. 4.3.2.20.

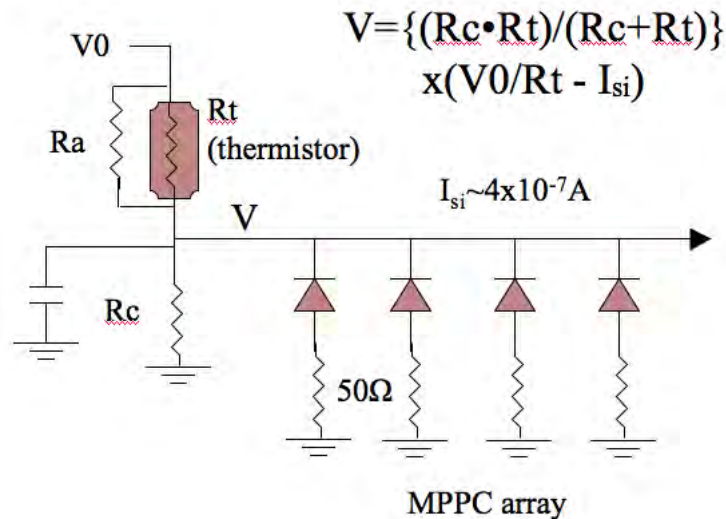


Fig. 4.3.2.19 A circuit diagram for temperature compensation of SiPM bias voltage. We verified that the fluctuations of the static gain (measured at different temperatures) were stabilized within $0.1\%/^{\circ}\text{C}$ by operating Hamamatsu MPPC by means of this bias voltage.

The fig. 4.3.2.20 shows plots of the device temperature and the gain fluctuation of a Hamamatsu MPPC as a function of time while the device temperature was changed periodically from -8°C to -18°C in a sudden way. The vertical axis of the upper plot is the MPPC gain and bottom one is the device temperature, and the horizontal axes of both top and bottom plots indicate time. We found that in case of a wider temperature range, the gain fluctuations are stabilized within $0.5\%/^{\circ}\text{C}$ using this circuit. By decreasing thermal resistance between the thermistor and the MPPC device, even less gain fluctuation is expected.

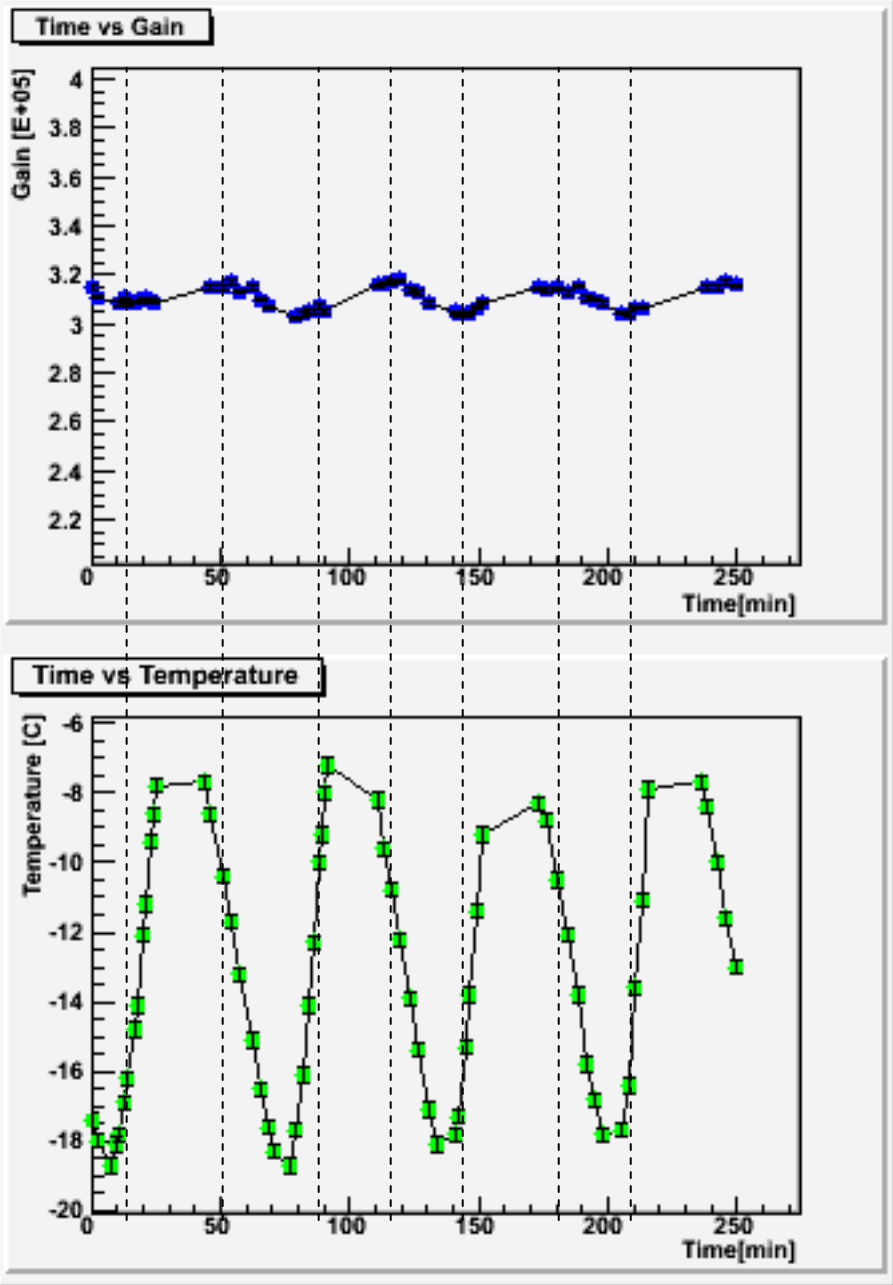


Fig. 4.3.2.20 We operated a MPPC with a temperature compensation circuit to control the bias voltage. The gain fluctuation is within 0.5%/°C. We consider the gain fluctuation at this level is acceptable with a careful online calibration.

4.3.2.8.2.4.SiPM vs PMT

Table 4.3.2.2 SiPM vs PMT

Parameter	MAPMT(UBA)	MPPC	SiMPL	SiPM
PDE (400nm)	0.7 x 40%	50%	61%	40%
Operation voltage	900V	70V	40V	40V
Effect of Magnetic Field	Yes	No	No	No
Charge Resolution (ability of counting the number of photons)	Good	very good	very good	very good
price/pixel	¥4,200	¥4,300	~¥5,000	~¥5,000
Sensitive area/pixel	4×4 mm ²	3×3 mm ²	3×3 mm ²	3×3 mm ²
Weight/pixel	1.4g	0.11g	--	--
Dark Count (-15°C)	~kHz	~100kHz	--	~500kHz
Matrix Type	6×6	2×2, 4×4	1	1
Status	on sale	on sale	prototype	prototype

4.3.2.8.2.5.Outlook for the SiPM application to JEM-EUSO

With the objective of applying SiPM/MPPC to JEM-EUSO, we aim to further improve their photo-detection efficiency at device level, and quickly design the module and the prototype which have a more stable and safe operation in space. We construct an optimized front-end electric circuit considering gain, impedance, floating capacitance associated to its implementation, which matches with the read-out circuit.

Then, as the last evaluation of their performance, we will observe Cherenkov light by implementing in parallel a camera composed of SiPM/MPPC with another one composed of MAPMT to a ground based telescope.

We should consider in concrete the following points:

- Stability of gain (<~0.3%/°C)

As mentioned before SiPM/MPPC normally have around 3%/°C of temperature dependence of gain, however, we can limit it till around ~-0.1%/°C by using an adequate thermistor as temperature compensation circuit. We should design the detection module so that the temperature of SiPM/MPPC inside it is uniform and stable.

- Dark current (<~100kHz)

In the advanced design of JEM-EUSO, the environmental temperature of JEM-EUSO can be decreased till $-15^{\circ}\text{C} \pm 2\sim 3^{\circ}\text{C}$, therefore, the noise rate caused by the dark current by SiPM/MPPC becomes low enough. However, in the design, we should place SiPM/MPPC as much as possible far away from the heat of the front-end electric circuit.

- Radiation Tolerance

Radiation might cause the increase of the dark current of SiPM/MPPC, and a degradation of the resolution, because the collision of protons or neutrons produces defects in the lattice structure of the silicon crystals. There is small influence of electrons and γ rays. Radiation tolerance tests have already been done inside and outside Japan and we concluded that there was no problem in their use in JEM-EUSO for more than 5 years at the altitude of the international space station. However, we should design protections from unexpected huge flares from the sun. In addition, we should

also study in advance the influences on trigger and recorded data in case of degradation.

- **Stability of photon detection efficiency**

Photon detection efficiency may vary due to the damage of the entrance window. Therefore, we should do a measurement of radiation tolerance and stability of photon detection efficiency at the same time.

- **Designing focal surface and focal surface modules**

We assume to use Hamamatsu $3 \times 3 \text{ mm}^2$ MPPC in a 4×4 matrix (Fig. 4.3.2.16). As in figure 4.3.2.21, we fix the basic module using a 4×4 matrix placed on a grid of 8×8 , and provide a common bias voltage adjusting the temperature by means of thermistor-based temperature compensating circuit. We will keep the temperature of the whole module uniform by supporting it with copper plate. We estimate that the temperature of the focal surface will be low enough to keep the optimal gain and the dark noise rate. However, to realize more stable operation, we will uniform the temperature inside the module with the abovementioned copper plates. In addition, we will minimize the dead space by installing Winston Cones in each MPPC array. Furthermore, we will uniform the temperature by adhering and fixing the MPPC array, copper plates and the PCB for bias voltage supply and pulse readout by means of thermal conductive adhesive.

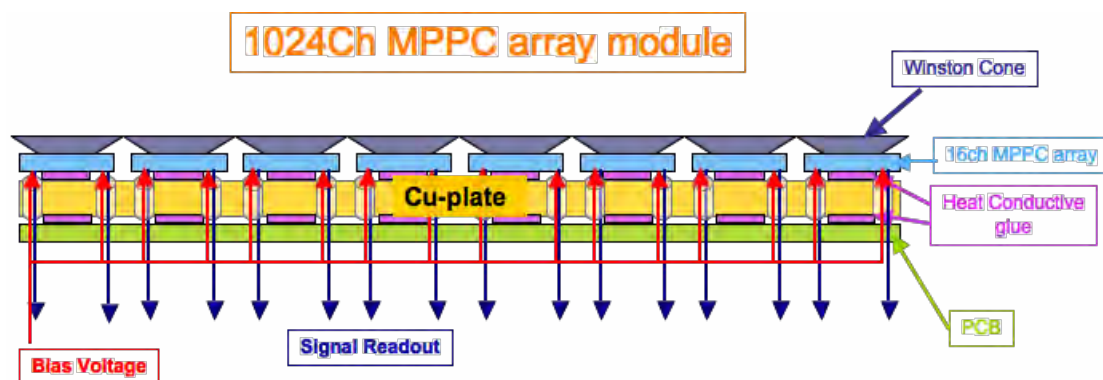


Fig. 4.3.2.21 Conceptual design of the FS basic module with 16ch MPPC. First, make the heat of the whole module uniform by attaching Winston Cones to each MPPC placed in an 8×8 array form by means of optical adhesive. Then, attach and fix it again to the PCB and aluminum panel by means of thermal conductive adhesive. The gain of MPPC will be kept stable by means of thermistor-based temperature compensation circuit.

- **Readout circuit**

We should design carefully the part which transmits the pulse to the readout circuit considering sufficiently the following points: impedance matching between SiPM/ MPPC, degradation of time character of pulse due to floating capacitance, increase of electric noise accompanied with the implementation, electric interference among channels.

4.3.3 Focal Surface Electronics

The Focal Surface Assembly (FSA) position-sensitive layer consists of a large array of Multi Anode PhotoMultiplier Tubes (MAPMTs). The Focal Surface Assembly includes proximity electronics for MAPMT data collection, MAPMT driving circuit. A LIDAR and an IR camera assembly will also be provided for atmosphere sounding, which is an important complement for the main data analysis. A Control Electronics will manage all those subsystems and will provide the electrical interface between JEM-EUSO and the ISS via the JEM (Japanese External Module) platform. Other ancillary subsystems, such as Thermal Control and Calibration, Alignment and Monitoring will also be managed by the Control Electronics.

The principal electronics of JEM-EUSO are Focal Surface Electronics and Control Electronics. Focal Surface Electronics is located inside the FS structure, and Control Electronics (CPU etc.) is located both in normal and redundant electronic boxes. The places of the following electronics have to be decided.

- 1) Atmospheric sounding subsystem (LIDAR and IR camera)
- 2) Lid mechanism (end-switch, sensors)
- 3) Calibration, Alignment and Monitoring devices
- 4) Thermal control (sensors, heaters)

The FS Electronics include:

- 1) front end electronics (ASIC)
- 2) PDM electronics
- 3) Cluster control electronics
- 4) FSA power supply system (DC/DC converters to generate LV and HV)

The Control Electronics include:

- 1) ISS (JEM) communication interface (I/F)
- 2) ISS (JEM) power I/F
- 3) FSA communication I/F
- 4) Scientific Functions management system
- 5) HK collection management system
- 6) LIDAR management system
- 7) IR camera management system
- 8) Thermal Control management system
- 9) Calibration, Monitoring and Alignment devices management system (TBD)
- 10) Lid mechanism management system
- 11) Management of the system to determine the instantaneous absolute orientation of the JEM-EUSO Instrument (TBC)

4.3.3.1. Functions

The main functions of the Focal Surface Electronics are as follows:

- The front end electronics directly interfaces the MAPMTs and provides the first main level of trigger (analogue and digital).
- The PDM circuit provides the second and third Main level of trigger and provides the ring memory buffers and the communication I/F between the FSA and the control electronics.
- The FSA power supply system provides the power to the MAPMT (HV) and to the first and

second front end electronics (LV).

- The ISS (JEM) communication I/F provide the JEM-EUSO communication capability with the external world for commands and data collection.
- The ISS (JEM) power I/F provides the JEM-EUSO powering capability from the JEM provided power busses.
- The FSA communication I/F provide the link between the FSA and the Control Electronics for command and data.
- The Scientific Functions management system includes all the science relevant HW and SW such as the trigger system, the data acquisition system and the temporary onboard storage capability.
- The HK collection management system provides the regular collection of engineering HK data from various locations within the instrument.
- The LIDAR and IR Camera management system provide all what is needed for the proper operation of the atmospheric sounding system, including power supply, configuration commands issuing, data retrieval and storage.
- The Thermal Control management system provides the instrument thermal control by means of proper temperature sensor readout and heaters activation.
- The Calibration, Monitoring and Alignment devices management system drives the devices used for calibration of the different instrument parts (TBD), those used to monitor the relative alignment of different Instrument parts (TBD) and those used to monitor important parameters.
- The Lid mechanism management system provides the proper motors drive capability and position sensors conditioning to operate the instrument lid.
- The system to determine the instantaneous absolute orientation of the JEM-EUSO Instrument will monitor the absolute orientation of the JEM-EUSO Instrument in case the available standard resources (normally from ISS, etc) are not able to provide this information with sufficient precision (TBC).

4.3.3.2. Trigger and read-out: concept design and definitions

4.3.3.2.1. Trigger Philosophy Specifications

The overall JEM-EUSO trigger philosophy is at the core of the concept of the instrument. Therefore, it has to be clearly described in this chapter. The goal of the trigger system is to detect the occurrence of a scientifically valuable signal among the background noise detected by the JEM-EUSO detector.

Since the total number of pixels in the array is very large (~ 200 K), a multi-level trigger scheme was developed. This trigger scheme rely on the partitioning of the Focal Surface in subsections, named PDM (Photo Detector Module), which are large enough to contain a substantial part of the imaged track under investigation (this depends on the energy of air shower and the zenith angle). PDMs will have a suitable shape and will be identified by a pair of coordinates XPDM, YPDM as well as the pixels inside the PDMs, generally named (X,Y).

The general JEM-EUSO trigger philosophy asks for a System Trigger organized into three Trigger-levels (TBC). The three Levels Trigger works on the statistical properties of the incoming photon flux in order to detect the physical events hindered in the background, basing on their position and time correlation.

The trigger is issued in accordance with the 3 stages (EC, PDM, PDM cluster).The table 4.3.3.1

gives a synthetic idea of the expected rate of signals at each stage, and the expected rejection power. The numbers here reported give a first rough estimation of the requirements. The exact power rejection of each trigger level will be optimized in future. The last row gives also a reference number on the expected rate of cosmic ray events, which could fluctuate by around one order of magnitude depending on the effective threshold of the detector.

Table 4.3.3.1 Outline of noise reduction capability.

Level		Rate of signals/triggers at PDM level	Rate of signals/triggers at FS level
1 st level trigger (EC)	photon trigger	$\sim 5.2 \cdot 10^8$ Hz	$\sim 7.8 \cdot 10^{10}$ Hz
	Counting trigger	$\sim 4 \cdot 10^5$ Hz	$\sim 6 \cdot 10^7$ Hz
2 nd level trigger (PDM)		~ 7 Hz	$\sim 10^3$ Hz
3 rd level trigger (PDM Cluster)		$\sim 6.7 \cdot 10^{-4}$ Hz	~ 0.1 Hz
Expected rate of cosmic ray events		$\sim 6.7 \cdot 10^{-6}$ Hz	$\sim 10^{-3}$ Hz

The First level Trigger has the two following types of triggers:

a) photon trigger

Anode-level trigger, basically edge and width counters coupled with a Q-t (electric charge-time) conversion, which act as a single photon counting method, in order to recognize the arrival of a signal over threshold, which will be identified as a single photoelectron. At this trigger-level, the electronic noise effect is greatly reduced due to the fact that the “strong” anodic pulses are easily discriminated above the preamplifier electronic noise.

b) Counting trigger (Red pixel trigger and Yellow pixel trigger)

Counting trigger consists of a gated counter and two digital comparators (*high* and *moderate levels*). The gate time is named GTU (from Gate Time Unit), and its duration is about 2.5 μ s (TBC). The counting trigger is issued whenever the number of single-photoelectrons exceeds a pre-set digital threshold value.

In every GTU, all the pixels in a PDM will be tagged depending on the number of single photo-electrons detected by each of them. Pixels that passed the *high level* threshold will be tagged as *Red pixels*, while those passing only the moderate level threshold will be tagged as *Yellow pixels*. All the other pixels will be discarded for the rest of the trigger stages.

At the first trigger-level, the random background (randomly arriving photons) can be greatly reduced by setting the digital threshold value above the observed background fluctuations. The threshold on Red pixels will be set in order to have ~ 1 pixel over threshold per PDM every few GTU (1-10). The threshold on Yellow pixels will be set in order to have < 100 pixels/GTU on a PDM.

The Second level Trigger is issued at PDM level and it is devoted to a further reduction of the background, by operating a ‘space proximity test’ of ‘hits’ in consecutive GTUs. The algorithm working as a 2nd level trigger, presently proposed for JEM-EUSO, is called ‘Linear Track Trigger’ method (LTT), which searches for light points moving with the light speed at 400 km ahead. The main aim of this trigger level is to further decrease background events, bringing the rate of triggered events at the level of ~ 1 Hz/PDM or below.

The Third level Trigger is issued at the cluster level and according to this trigger we make the final decision to start the readout procedure. The Third level Trigger logic must collect data coming from the whole Focal Surface divided in 18 subsections consisting of 8 PDMs. The Third level Trigger logic will provide a decision about the presence of any interesting feature, by collecting the Second level trigger coming from each PDM. The decision will be made in accordance with the optimized “trigger modes” for the different phenomena to be observed. At this level, the remaining statistical noise will be reduced to the point that only the “event-like” patterns will initiate the readout sequence.

The system-level trigger will be fully in-flight programmable in order to allow for any adjustment in the trigger modes.

4.3.3.2.2. Trigger Modes Specifications

The System Trigger shall be fully in-flight programmable in order to set it for all triggers modes.

The following trigger modes have been identified:

- 1) Standard EECR (Extreme Energy Cosmic Rays) mode
- 2) Slow mode
- 3) Fast mode
- 4) Analog Trigger (sub-mode)

The EECR mode shall be the standard one where the trigger looks for signals which rise above the Third level trigger for a duration between about 30 μ S and about 300 μ S (the exact value shall be in-flight programmable). The Extreme Energy Cosmic Rays (EECRs) are observed by means of this mode. Event which does not match the above duration window will be ignored.

The Slow mode shall be normally not active; it will be activated by tele-command when required by the observers or as a programmed feature in the System Trigger. When the Slow mode is activated, the signals with Third level trigger activity lasting more than a pre-set time (e.g. 300 μ S) will be anyway recorded, however, with a slower sampling frequency (GTU). Most atmospheric phenomena (e.g. meteoroids) are observed with this mode.

The Fast mode shall be normally not active; it will be activated by tele-command when required by the observers. When the Fast mode is activated, the sampling frequency is increased by a factor 8 with respect to the EECR mode, and signals with 3rd level trigger activity lasting less than a pre-set time (e.g. 30 μ S) will be anyway acquired. This feature will be used during on board calibration.

4.3.3.2.3. Read-out specifications

For every detected event within the foreseen classes, the JEM-EUSO electronics shall be able to record a set of raw data on a pixel-by-pixel base. By making use of the “free running” techniques, data are continuously sampled with fine time resolution (GTU) and sequentially stored into cyclic buffer memories. The buffer memories are designed to be properly deep in order to keep the maximum expected time-length for a track. Unless a read-out is started by the System-Trigger, the older data are dropped from the memory buffer in order to make room for the new ones. When a read-out is started by the System Trigger, the track data stored into the memory buffer is simply read out. As a baseline, the sampling period shall be related to trigger mode following table below:

Table 4.3.3.2 Trigger modes and sampling periods

Trigger Mode	Position Sampling Period	Remarks
--------------	--------------------------	---------

Standard (EECR)	2.5 μ s (TBD)	Gate Time Unit: GTU
Slow	40 μ s (TBD)	16 x GTUs
Fast	0.156 μ s (TBD)	1/8 of GTU
Auxiliary (sub-mode)	According to selected mode	

The general readout scheme is based on the PDM areas, used independently for the Second level trigger.

As a baseline, the data readout shall take place from the PDM that originated the trigger and from its “first neighbors”.

4.3.3.3. System Trigger & Read-out Hardware

The purpose of the System trigger is to discriminate, at detector level, the “event-like” signatures against the natural diffuse background noise. The requirements for the abovementioned overall JEM-EUSO trigger philosophy are as follows.

There are three Trigger levels within the detector as follows:

- First Level (EC);
- Second Level (PDM);
- Third level (PDM cluster);

The location of these trigger levels within the instrument is shown in Fig. 4.3.3.1 together with the basic associated HW function. A detailed description for each level of trigger is given in the next sections.

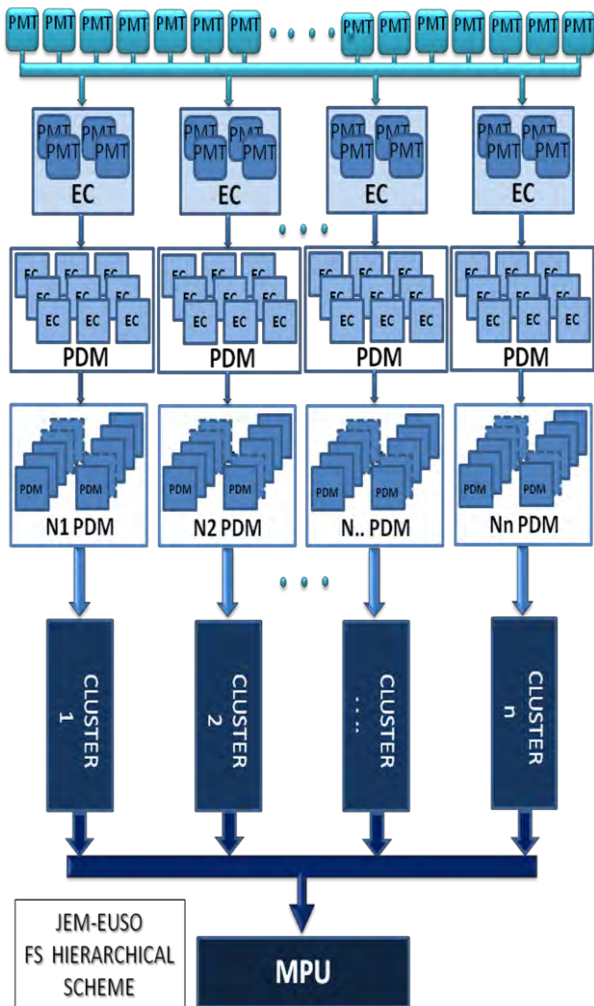


Figure 4.3.3.1 Different level structure of FS.

4.3.3.3.1. First level trigger (EC)

The trigger at MAPMT level is caused by an UV photon that impinges on the photocathode causing an avalanche multiplication of photoelectrons emitted by the photocathode and the dynodes. The produced photoelectrons will be amplified to $3-5 \times 10^5$ electrons, and reach the opposite laying anode. The anodic pulse described above is then delivered to the proper anodic input of the front-end ASIC. At front-end ASIC level, two trigger functions are performed:

- a) Analog threshold on the pulse amplitude: photon trigger
- b) Digital threshold on the pulse counts (see next paragraph): counting trigger

The First level trigger function is related to the discrimination of the anode signals coming from the MAPMT. This is the only analog section of the trigger.

The front-end ASIC for JEM-EUSO includes an impedance matching circuit, integrator circuit and comparator circuit as well as current-source and current-sink circuits which feed currents at the input node of the integrator (Fig.4.3.3.2). The impedance matching circuit acquires a pulse from a multi-anode PMT with low-impedance, and reduces cross talk between channels. Furthermore, the impedance matching circuit protects the entire circuit from a possible electro-static discharge. The output of the impedance matching circuit is sent to a comparator circuit via the integrator circuit. The comparator circuit delivers a logic H when the integrator's output exceeds a pre-determined

level. Once the comparator circuit delivers H, the current-source circuit is activated to linearly damp the integrator output voltage until the integrator output goes below the comparator threshold.

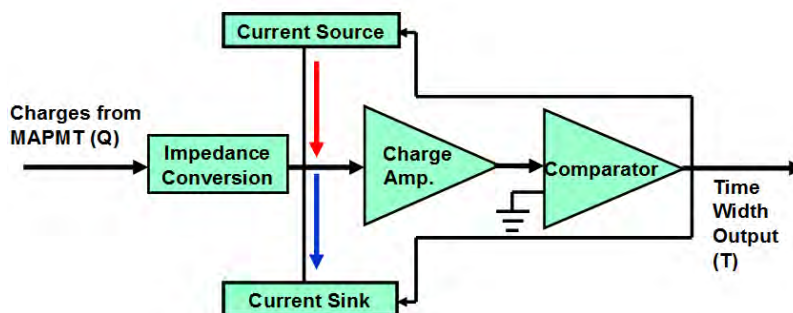


Fig.4.3.3.2 Block diagram of the front-end ASIC

When the pulse from the integrator circuit falls below the comparator threshold, the current-sink circuit is activated to very slowly raise the integrator output voltage (more slowly than that of the electric source circuit), and then, the comparator delivers a short pulse under a low period. However, its level remains enough lower than the effect of a background light. If the effective electric charge is injected from MAPMT, the input charge amount is converted to the output pulse duration.

The front-end ASIC has been designed and simulated using T-SPICE of Tanner Research Inc. The first version of the ASIC named “KI01” has been made by MOSIS Integrated Circuit Fabrication Service in 2006 (Fig. 4.3.3.3). There are 16 channels for the Q-T conversion circuit and various control circuits in a chip. The second version of the ASIC named “KI02” was made in 2007.

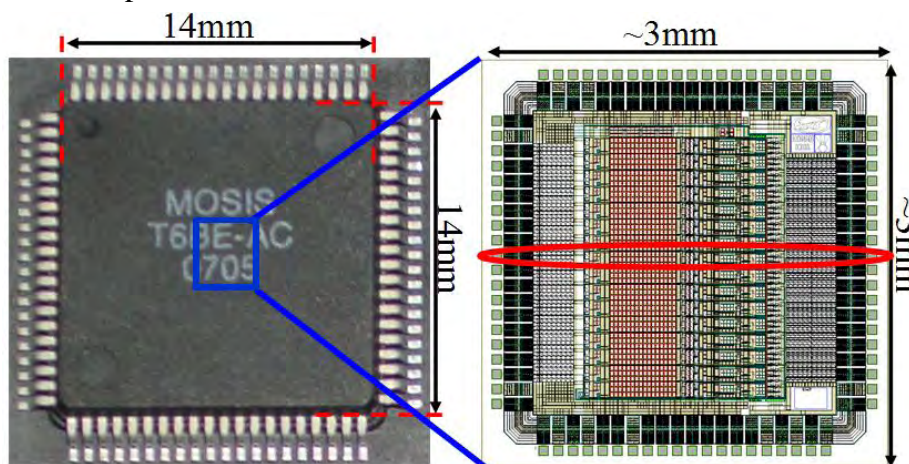


Fig.4.3.3.3 80pin QFP package (Left) and the ASIC layout of a bare chip (Right)

Regarding the above ASIC, we have tested and confirmed the followings:

- 1) Measured power consumption is 1.8 mW/ch, which is conform to the designed value.
- 2) Measured dynamic range of the Q-T conversion is at least 1-300 photoelectrons/2.5 μ s, which satisfies the designed value (Fig. 4.3.3.4).
- 3) Various adjust mechanisms work as designed.

This ASIC has been connected to the MAPMT and the output charges from the MAPMT were fed into the ASIC. It has been verified that the charges (Q) are converted to time width (T). Fundamental designed functioning of the ASIC was proved to work.

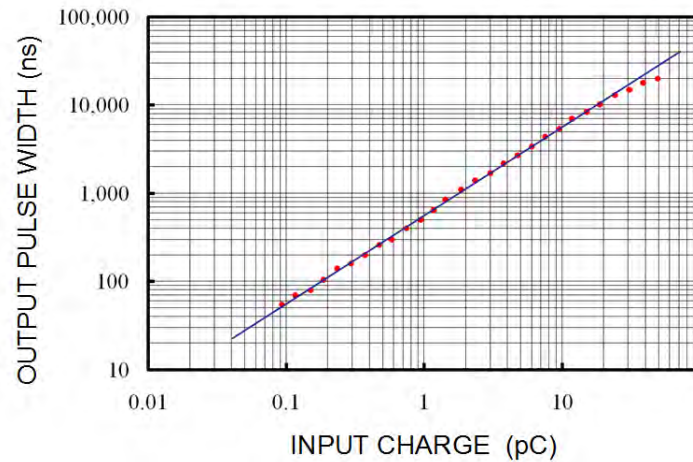


Fig. 4.3.3.4: Measured output pulse width as a function of input charge for the Q-T conversion ASIC.

The circuit design of the next version with the following improvements has almost been finished.

- 1) Power consumption will be decreased to 0.7 mW/ch, which may be decreased till around 0.4 mW/ch by the optimization.
- 2) Further noise reduction of the electric circuits.
- 3) Detection circuits of the single event upsets (SEU) caused by the radiation will newly be added.
- 4) The value of the Supply voltages will be changed for easy handling.

High-density bare chip mounting board will be adopted to be able to pack the required number of channels in the limited space.

4.3.3.3.2. Second Level Trigger (PDM)

The Second Level Trigger is implemented in a dedicated FPGA chip of the PDM module. Each PDM module is connected to 9 pieces of ECs (36 MAPMTs), handling 1,296 channels in total.

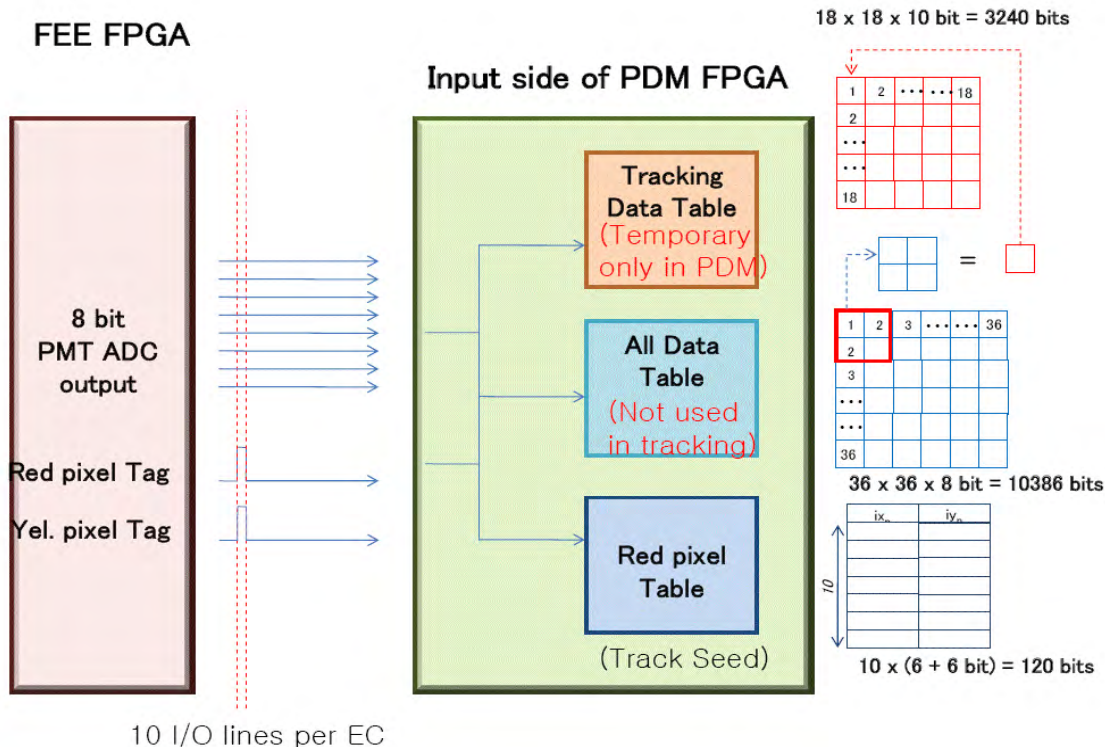


Figure 4.3.3.5: Data Flow from the First Level Trigger. Total 22 lines are needed to receive the all data from 36×36 pixels (two 8 bits lines), information of trigger type (two of 1 bit lines), a Clock line of 100MHz, and a Token line.

Together with “segment_counters” (PH_CNT) of each pixel and tag data from red and yellow pixels, issued by the First Level Trigger for every GTU, the Second Level Trigger performs the “Linear Track Trigger”, which aims to search for correlated hits during the track trigger time period ($dt = 11$ GTU) along the predefined track angles. The trigger issue is done in each GTU based on the saved data in ring buffer of the FPGA. If the trigger is issued, it will be sent to the Third Level Trigger.

The trigger algorithm is explained in detail in the section 4.3.3.4.2. However, it requires computing the sum of all pixel hit counts. Total of 16 predefined track directions are tested with trigger track time. The positive trigger decision is made when the hit sum is bigger than the Second Level Trigger Threshold for at least one of the 16 trigger track angles.

The key idea to perform the trigger logic computation, which has to be completed in the period of a GTU ($2.5 \mu s$), is to pick up simultaneously all relevant pixels data of track trigger time along a track direction under test, and to sum them up at a time.

In order to carry out this trigger logic, three types of data tables are prepared (Fig 4.3.3.5.): All Data Table (ADT), Tracking Data Table (TDT), and Red Pixel Table (RPT).

- ADT: a table containing *PH_CNT* data of all channels in an array of 18×18 pixels. Each pixel size is 8 bits. This table is not used in the trigger logic, but is stored in the ring buffer until the trigger decision is made.
- TDT: a summary table of *PH_CNT* in an array of 18×18 elements. Each element of the table is the sum in 10 bits of *PH_CNT* data of corresponding 2×2 channels.
- RPT: a list of pixel tagged as “RED”. This table has two columns for the pixel coordinates in x and y direction (each 6 bits).

The above three tables are filled with multiplexed data coming from the First Level Trigger. Considering the number of channels, GTU width, number of FPGA I/Os, and FPGA logic clock speed, total 22 input data lines are assigned between the First and the Second Level Trigger FPGAs: all 36×36 pixel data (two 8 bits lines), color definition information (two 1 bit lines), a Clock line, and a Token line. The FPGA is set to run in the clock speed of 100 MHz.

Parallel Processes: Loop over all Red pixels and all angles
 Receiving data, = 10 *16 trackings in a consequent clock series in a GTU
 Computing Tracks

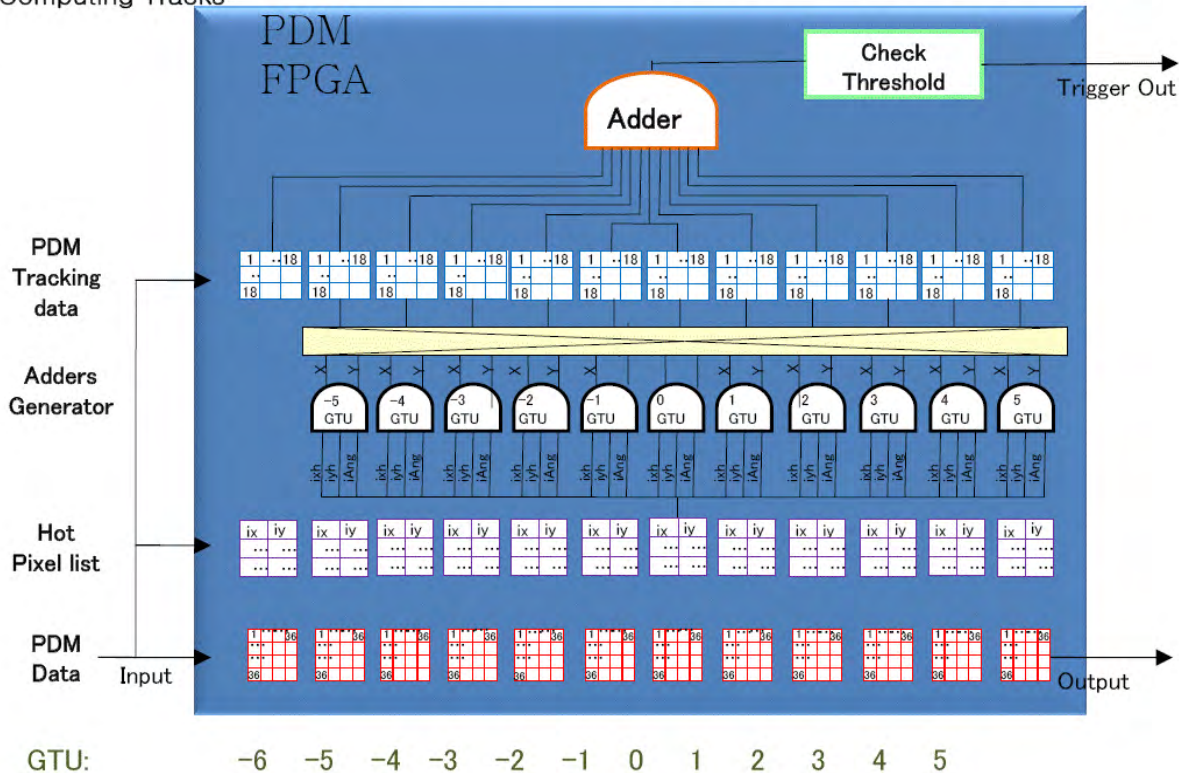


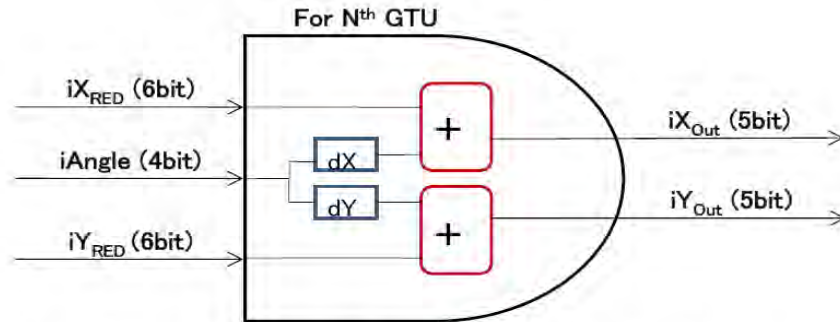
Figure 4.3.3.6: The structure of FPGA logic in Second Level Trigger. Starting from a red (=hot) pixel in a GTU, it checks the sum of charge amount of Yellow pixels in 11 GTUs along one of 16 predefined track angles and judge if the value surpasses the threshold.

Fig. 4.3.3.6 shows overall structure of FGPA logic in the Second Level Trigger. The three data tables filled with new data, every GTU are saved in the ring buffers. The depth of ring buffer should be at least over track trigger time (11 GTU). However, the depth for ADT should be more than 100 GTUs to store initial part of shower data in case that the trigger is issued at the maximum of the shower.

The trigger determination starts with reading out the Red Pixel Table (RPT) of each GTU. The position information (ix, iy) of a red pixel is sent to 9-11 pieces of Address Generators (AG) together with the angle number for the test. This AG is the key mechanism in Second Level Trigger. The position of Red pixel in the RPT (iXred=ix, iYred=iy) will be mentioned in the memory address (iXout, iYout) in TDT (Tracking Data Table) of the pixel along a test track. The AD does not need more than a couple of logic clocks because it refers to the look-up table stored inside.

Address Generator

Input: iX_{RED} (x coordinate of a RED pixel in the trigger starting GTU)
 iY_{RED} (y coordinate of a RED pixel in the trigger starting GTU)
 $iAngle$ (angle number (1-16) to search for a track)



Output: iX_{Out} (x coordinate of pixel in Track data table for N^{th} GTU)
 iY_{Out} (y coordinate of pixel in Track data table for N^{th} GTU)

Figure 4.3.3.7: Address Generator in Second Level Trigger Logic. Direction of pursuit ($iAngle$) is given to an address line of memory, and then the increased amount of the address of pixel, which corresponds to the direction of corresponding memory cells, will be added to the address of Red pixel, and then outputted.

Once the AG outputs become available, elements from 9-11 pieces of Tracking Data Table will be compared with the Second Level Trigger Threshold. And this logic will be repeated for all the 16 predefined track angles as well as for all the elements in Red Pixel Table for a GTU.

4.3.3.3.3. Third Level Trigger (PDM cluster)

The output from each 8 PDM boards is transmitted via dedicated LVDS protocol to one of 21 Cluster Control Boards (CCB), then CCBs in turn transmit pixel information which passed the fine trigger conditions via SpaceWire interfaces to the Mission Data Processor (MDP).

The heart of the CCB is a Digital Signal Processor (DSP). Currently we foresee to use the Texas Instruments TMS320C6713B chip, which is available in two speed grades for the extended temperature range from - 40 to 105°C, either as 167 MHz or 200 MHz version. Even at a clock frequency of 167 MHz, the TMS320C6713B delivers up to 1000 million floating-point operations per second (MFLOPS) and 1240 million instructions per second (MIPS). In addition, the chip needs two supply voltages, 1.2 V for the core of the processor, and 3.3 V for the I/O ports.

The group at IAAT (Institut für Astronomie und Astrophysik Tübingen) has some experiences with Texas Instruments DSPs for the German eROSITA project. In eROSITA project, a similar DSP was used to process the pixel data from a 384 x 384 pixel frame store CCD. The prototyping board for this processor was developed at IAAT. During Phase-B, we will use a hard and software development kit of Texas Instruments to investigate the performance of the DSP for application for the project.

4.3.3.3.4. Advanced option

In addition to the system trigger of the baseline, we are improving the function of FPGA of the 1st level trigger to do the filtering of events more efficiently. If it works as expected, we can reduce the number of events for the 2nd level trigger, and then we can reduce the energy consumption of

the whole system trigger.

The first level trigger in the advanced option is a three sub-levels trigger detailed here below:

- a) 1st level Anode-level trigger, basically an analog discriminator to recognize the arrival of a single photoelectron event at each anode.
At this trigger-level the electronic noise effect is greatly reduced due to the fact that the “strong” anodic pulses are easily discriminated above the preamplifier electronic noise.
- b) 2nd level Pixel-level digital trigger, basically a gated counter and a digital comparator. The gate time is named GTU (from Gate Time Unit), its duration is about 2.5 μ s (TBC). The 2nd level trigger is issued whenever the number of single-photoelectrons recorded by an anodic chain within a GTU exceeds a pre-set digital threshold value. At this trigger-level the random background (randomly arriving photons) is greatly reduced by setting the digital threshold value above the observed background fluctuation.
- c) 3rd level PDM digital trigger, basically a gated counter and a digital comparator.
The 3rd level trigger is issued whenever the activity above the 2nd level persists (persistency trigger) in consecutive GTUs, in a PDM or subset of it, up to a pre-set value. Whenever the activity above the 2nd level persists, dedicated pixel-counters are increased and the sum of the grouped pixels (2x2 or 3x3 pixels) is compared with a pre-set value when the persistency is met, otherwise the pixel counters are reset.

In the advanced option the 1st level trigger is implemented using a fast discriminator designed within each channel of the front-end ASIC coupling the discriminator directly to the MAPMT anode and it is located inside the Charge to Time ASIC device.

The sensitivity of the discriminator is such that it allows the discrimination of a single photoelectron pulse. The discriminator threshold can be set in between the electronic noise level and the single photoelectron average pulse amplitude.

The speed of the discriminator is such that it allows the discrimination of pulses within a time separation as low as 10 ns. If the discriminator analog threshold is exceeded, a fast pulse is generated. The output signal (DISCR_OUT) is a short pulse (less than 10 ns duration) with standard shape and amplitude.

The DISCR_OUT signal is used to increment a dedicated pixel-counter (note: one counter for each pixel) which is periodically re-set by an external signal (GTU_CLOCK).

The period of the GTU_CLOCK is named “GTU” (from Gate Time Unit). The counter value is continuously compared with a previously set Digital Threshold value: a Pixel_Trigger signal is issued whenever the counter reaches the Digital Threshold value (2nd level trigger).

The Pixel_Trigger level stays active for all the remaining part of the GTU.

Moreover, when the pixel trigger is active, a gate is enabled to let the single photon pulses go through for the remaining part of the GTU. In other words, the Photon Count fast output pulse (N1) is issued each time the comparator is fired while the pixel trigger is active.

The Gate Time Unit (GTU) is a parameter that can be set from ground and that can be changed autonomously on board. The value of this parameter is related to the speed of propagation of a particle shower. A reference value for GTU is 2.5 μ s when running in the normal (EECR) mode.

The 2nd level trigger is implemented in digital way as follows:

The signals (DISCR_OUT) coming from the 36 ASIC's hosted in 9 Elementary cells (i.e. one "standard" PDM) are collected and managed by the FPGA in the Read-Out & Control Board of the PDM.

The pixel-counter is periodically reset every GTU. A sufficient size for the counter is 8 bits. The counter value is continuously compared with a previously set Digital Threshold value (**N**) and a trigger signal (**N1**) is issued to the 3rd trigger level whenever the counter reaches the threshold value. The **N1** stay active for all the remaining part of the GTU and, at the beginning of the next GTU, it is reset. In addition, the counter value is stored in a dedicated ring memory at the end of each GTU.

With reference to a "standard" PDM, pixel-counters belong each Elementary Cell are grouped (2x2 or 3x3) and the sum (**S**) is compared with a pre-set value. The **OUT_EN** signal will be activated only if the 3rd level trigger met the persistency condition **P**.

The 3rd level trigger is implemented in digital way as follows:

Each time a PMT_TRIG signal is issued by one PDM, that PDM is marked as active for the current GTU.

The logic implemented in the FPGA looks for an activity continued for several contiguous GTU's. If any pre-set criteria for a valuable pattern are met, the system trigger wait for the pre-set (mode-dependent) exposure time and then issues a **ALERT_TRIGGER** signal to the Second Main Trigger level.

An auto-level-trigger function will be implemented within the First level Trigger: this will use the persistence rate measurements (number of consecutive active PDM_trigger) as the input of a SW algorithm that calculate the proper setting for the two digital trigger levels (level 2 and level 3).

This would allow for the instrument to set the optimum trigger levels in case of varying background conditions due to slowly transient phenomena (moon phase, clouds coverage, large urbanized area and so on). This special auto-trigger mode will be switchable ON/OFF and be fully re-programmable in flight.

4.3.3.3.5. Failure tolerance and Reliability Specifications

Any Single Point Failure shall not cause a loss of more than TBD % in the total number of pixel readout capability of JEM-EUSO. This requirement asks for the subdivision of the JEM-EUSO electronics into a suitable number of independent blocks so that the loss of each of them does not affect the whole functionality by more than the specified percentage. Any single point failure in any JEM-EUSO functional subdivision will not propagate to any of the others. All integrated circuits parts shall be mil 883/B level as minimum. (TBC)

4.3.3.4. Trigger & Readout Software

The basic Trigger & Readout algorithm shall be as follows:

- 1) The instrument normally stays in a "waiting" status or "free running mode", in which background noise is continuously written into the PDM ring memories. The written data are the PDM pixels array.
- 2) At the occurrence of an event (i.e. when 3rd level trigger fires), a dedicated signal runs the instrument for data acquisition.
- 3) The instrument continues to write data into the memories for a pre-set amount of time (exposure time).

- 4) At the end of the exposure time, the instrument goes in a “hold” status and the read-out phase starts.
- 5) During the read-out and write-out phase, the content of the memories of the “hit” PDMs is downloaded into the CPU data buffer.
- 6) At the end of the data download, the instrument re-starts from the “waiting” status.

4.3.3.4.1. First Level Trigger (EC)

The following Fig. 2.3.4.1.1 summarizes the System Trigger logic flow in case the instrument is set for standard EECR observation with automatic slow-mode enabled.

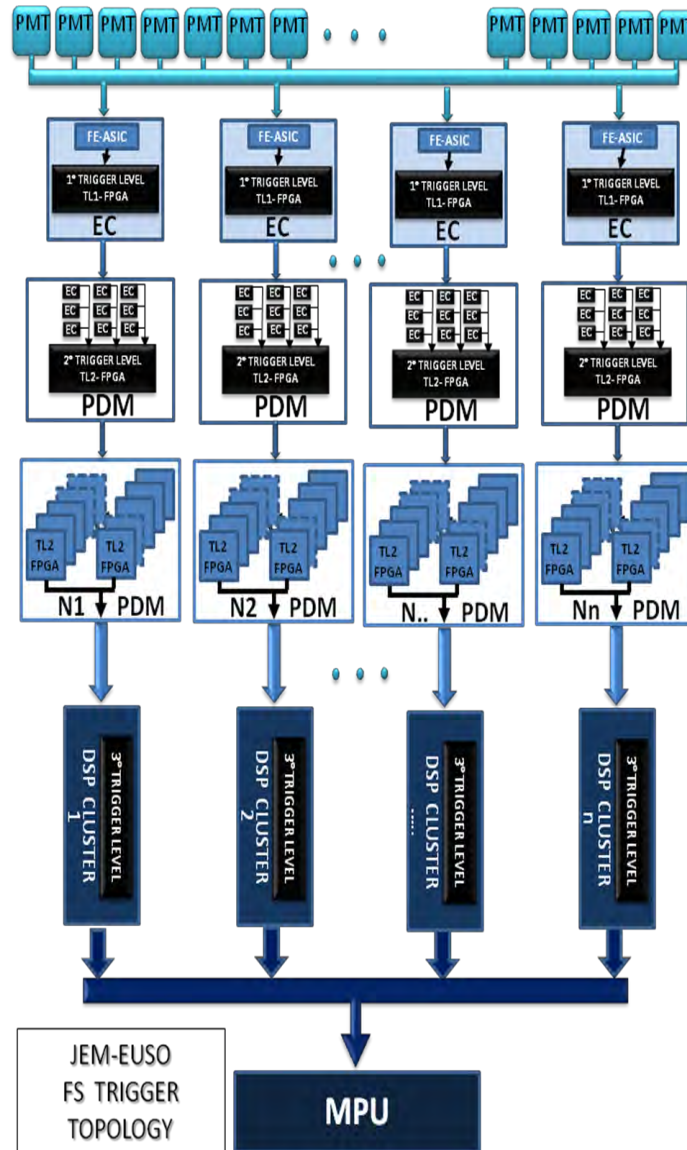


Fig. 4.2.1.2.1.1 Trigger flow diagram.

With reference to Fig. 4.2.1.2.1.1, the instrument is normally waiting for trigger. If a MC_TRIG persistency is detected, i.e. a given MC_TRIG stays active for a selected number of GTUs then the System Trigger is run. The System Trigger then checks the duration of the detected permanence until one of those cases happens:

- a) the persistency disappears
- b) the persistency duration exceeds a given duration of N2 (e.g. N2=300) GTUs and continues

In case b), the System Trigger autonomously switches the instrument in “slow mode” and continue to monitor the event evolution until case a) happens.

A “stuck check” routine is also executed in order to restart the System Trigger in case it is “stuck”. Basically, this routine should work as a sort of watchdog. In the “slow mode”, a *SLOW_DOWN* signal is sent in order to slow down the X and Y ring memories updating rate in order to keep trace of what is likely to be a long lasting event like e.g. a meteoroid. The *PH_CNT* ring memory continues to be updated at the standard speed.

In case a), the System Trigger checks if the event duration exceeds a given duration of N1 (e.g. N1=30) GTUs, then:

if the answer is **no** (a-a), the System Trigger checks if the Fast Mode is enabled.

if the fast mode is not enabled (a-a-b), then the trigger is restarted and the instrument restarts waiting for a next event (that means the event is considered as a spurious transient).

If the fast mode is enabled (a-a-b), then it is activated so to acquire possible interesting non-EECR phenomena and collect the data. if the answer is **yes** (a-b), then after a pre-set “exposure time” (e.g. 300 GTUs), the System Trigger issues the *SAVE_FRAME* signal and initializes the readout routine.

All the settings related to the System Trigger (N1, N2, “exposure time” etc.) will be in-flight programmable as part of the instrument initialization routine to be run at the beginning of each observation.

4.3.3.4.2. Second Level Trigger (PDM)

The algorithm working as a 2nd trigger level, presently proposed for JEM-EUSO, is called ‘Linear Track Trigger’ method (LTT) which searches for light points moving with the light speed at 400 km ahead. This method is implemented in the PDM electronic circuit. The strategy of the Track Trigger Method is as follows::

- 1) When a 1st trigger level is issued, the pixels of the entire PDM are divided into 3 categories (Red, Yellow, and White pixels). Red pixels are defined to have a high signal ($N_{phe} \geq N_{thr,r}$). The trigger algorithm starts on a Red Pixel. Yellow pixels hold a moderate signal ($N_{thr,y} \leq N_{phe} < N_{thr,r}$). Only Yellow and Red pixels are used to integrate the signal of the track for triggering purposes. White pixels have low or absent signal. These pixels are discarded immediately, and not used anymore for the trigger analysis. The thresholds of $N_{thr,y}$ and $N_{thr,r}$ depend on the background noise level. Because of the limited computational capacity, the thresholds are set in order to have, in presence of pure background, $N_{red} < 1$ red pixel and $N_{yellow} < 100$ Yellow pixels every GTU.
- 2) This algorithm searches tracks developing with specific directions at the speed of light, taking into account such fundamental characteristics that distinguish an air shower from noises. In the following, we define θ and ϕ respectively as the zenith ($\theta=0^\circ$ means the nadir direction of JEM-EUSO) and azimuth angles of the air shower. Such angles are related either to the ΔX and ΔY distances imaged by the track on the X-t and Y-t projections and to the on-ground pixel size (ΔL) by the following relationships [1]:

$$\phi = \tan^{-1}(\Delta Y / \Delta X)$$

$$\theta = 2 \times \tan^{-1}(C \cdot \sqrt{(\Delta X^2 + \Delta Y^2)})$$

Here, C is a fixed number,

$$C = \Delta L / (c \cdot \text{GTU}).$$

Assuming a fixed time length Δt (i.e. $\Delta t = 9-11$ GTU), inclined showers will be detected as tracks moving through several pixels, while almost vertical EAS will be detected as spots insisting always on the same pixels.

We consider implementing inside the FPGA of 2nd level, 16 different directions, chosen to cover homogeneously the entire θ, ϕ plane. As in the case of red and yellow pixels, the total number of directions is decided at an acceptable level within the computational capacity.

- 3) Upon receiving the alert by a Red pixel, the algorithm defines a ‘box’ of maximum $N_{\text{pix}}/\text{GTU}$ around the Red Pixel that gives the alert, and for N_{pers} GTU centered on the GTU_0 . The content of the Yellow and Red pixels inside the ‘box’ are integrated. The location of the ‘box’ varies from GTU to GTU in accordance with the specific direction in analysis. In particular, if the algorithm is analyzing a vertical shower, the box will insist on the same pixels for the entire N_{pers} GTU, while in the case of horizontal showers, the box will shift by about one row and/or one column of pixels of every GTU. The 2 parameters, N_{pix} and N_{pers} , are related respectively to the width and length of the tracks, as well as to the total number of angular trials and computational capacity. In the present setup, N_{pix} equals 4, and N_{pers} equals 9-11. The width of the track is related to the EAS energy, to the spot size of the optics ($\sim 4\text{mm}$), to the position of the spot on the FS (in the center of a pixel, or in between pixels), and to the response of the PMT (cross-talk). The final configuration will depend on a trade-off between number of directions, dimension of the boxes, and thresholds on Red and Yellow pixels.
- 4) After defining the location of the ‘box’ in the N_{pers} GTU, the content of the Yellow and Red pixels of such boxes is integrated and the total number of photoelectrons (Σ_{track}) is compared to a preset threshold THR (bckg), that depends on the average background level. The THR (bckg) as well as the $N_{\text{thr,r}}$ and $N_{\text{thr,y}}$ strongly depend on the average background level and on the rate of fake events that is acceptable for the experiment. At present, the thresholds (in particular THR(bckg)) are set in order to achieve a trigger rate on fake events between 0.1 Hz/FS and 1 kHz/FS. The stricter condition is applied to match the signaling speed to the ground. It is important to be aware that the rate of real events detected will probably not exceed few events per hour ($\sim 10^{-3}\text{Hz/FS}$) on the entire FS (Table 4.3.3.1).

4.3.3.4.3. Third Level Trigger (PDM cluster)

The software for the 3rd level and lidar is implemented in the DSP tip which is stowed on the cluster control board (CCB). The 2nd trigger level operates at PDM level. However, some tracks will develop crossing different PDMs, typically in case of showers of large zenith angle. It is therefore important to trigger also these events. At the same time, artificial lights such as city lights, seem vertical air showers at few GTU scale. It is also important to avoid such events. For the above reason, the 3rd trigger level is being developed, based on the Track Trigger Method and it has the following characteristics:

- a) more refined and more number of directions will be scanned;
- b) higher flexibility in the starting point of the track;
- c) limits on the total number of GTUs in which the signal exceeds the average background;
- d) lower threshold for events in which near-by PDMs issue a 2nd level trigger in a close time window and space location;
- e) monitor possible failures or anomalies at PMT, EC or PDM levels and, temporarily inhibits their functions.

4.3.3.5. Data Acquisition and handling

4.3.3.5.1. General considerations

JEM-EUSO Data Acquisition and Handling System is designed to maximize detector observation capabilities to meet the various scientific goals, to monitor system status, autonomously taking all actions to maintain optimal acquisition capabilities and handle off-nominal situations. CPU and electronics are based on hardware successfully employed in space experiments such as Pamela, Agile, Altea, Sileye-3, etc..., taking into account recent technological developments in microprocessors and FPGA. Acquisition techniques and algorithms also benefit from the development performed in these missions. Rad-hard technology will be employed, with ground beam tests (eg. GSI, Dubna, Himac) to qualify and test resistance of new devices. Space qualified devices will be employed wherever required by safety and agency requirements.

Particular care will be taken to the use of off-the-shelf technologies in the development of the laboratory models and breadboard systems used to refine and test the various trigger and data reduction algorithms. The same approach will be followed in the use of communication protocols and interfaces (e.g. VHDL, SpaceWire, 1553, 1355 protocols) and in the realization of the ground support equipment. This will allow for a fast development of the software in parallel to the engineering and flight boards, reducing costs and integration time.

Hot/Cold redundancy will be implemented in all systems and in all stages of data processing with the exception of intrinsically redundant devices such as the focal surface detectors.

4.3.3.5.2. Data budget

Data acquisition is based on a hierarchical architecture designed to reduce at each level the amount of data through a series of triggers controlling an increasingly growing area of the focal surface. It is necessary to pass from the $\approx 10\text{GB/s}$ on the FS (Focal Surface) to the $\approx 250\text{kbps}$ which can be downlinked on the ground. Each board and data exchange protocol is compliant to the handle the data and send them to the higher level when needed. As an advanced option it is foreseen to use physical storage on hard disk on board the ISS and send them to the ground. In this case a factor 2 or 3 improvement in the data budget is expected.

Table 4.3.3.2: Data budget and transmission speed at various acquisition levels

Level	From	To	Trigger rate	Reception rate	Total DH budget	Reception speed from each subsystem
1 st PDM control board	EC <i>9EC</i>	PDM control board	200kHz/EC	1.8MHz (total trigger rate on 1 PDM from 9 EC)	518.4 Mbyte/s On a PDM	57.6 Mbyte/s Each EC
2 nd : CCB Cluster Control Boards	PDM control board <i>8PDM</i>	CCB Cluster Control Board	7Hz/PDM (trigger rate from each PDM)	56 Hz/CCB (total trigger rate from all PDM)	18.56 Mbyte/s	2.32 Mbyte/s From 1 PDM to CCB
3 rd CPU	CCB <i>21 CCB</i>	CPU	5.3mHz/CCB (maximum allowed trigger rate incl background)	0.11 Hz/CPU (total Focal Surface trigger rate incl background)	36.5kB/s to mass memory/ISS (total from all CCB) + lidar + IR camera + HK	1.73kB/s from CCB to CPU (each CCB can send about this value of data to CCB), central section more

4.3.3.5.3. Communication protocol

Communication between different layers operates with LVDS to minimize interference and reduce power consumption. All lines are redundant, with each line employing double ODU connectors at each end to increase reliability of the system and resistance to vibrations and thermal stresses. High level communication protocol between CCB and CPU is based on SpaceWire.

4.3.3.5.4. Commands from ground

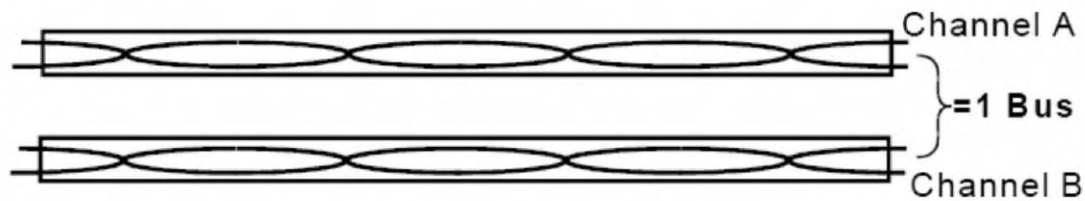
Slow control communication from/to ground is based on MIL-STD-1553B bus.

1553 is a slow speed (1Mbit) reliable bus used for transmission / reception of critical information. In JEM-EUSO the 1553b bus is employed to:

- 1) Switch on/off the instrument or sections.
- 2) Issuing of telecommands from ground.
- 3) Set general acquisition parameters based on detector status. Furthermore they can be used to patch (reprogram) part of the software at CPU, DSP or FPGA levels and dump the memory of each level in case of debugging.
- 4) Reception of keep-alive information from the detector, of nominal events, alarms.
- 5) Switch from mail to spare channel (acquisition, power supply).

1553 characteristics

A 1553B bus consists of two twisted, shielded pairs of copper wires. The speed of the bus is 1 Megabit/second (as compared to fiber optic networks which operate at approximately 100 Megabits/second), but it follows the Military Standard 1553B protocol. Although speed is sacrificed by using this protocol, there are several positive reasons for using the 1553B bus. Specifically, the 1553B is well-proven in space. Additionally, it has significant built-in redundancy capabilities that make it a good choice for space applications.



***A and B are channels.
Each channel has two twisted, shielded, copper wires.
Both channels make one bus.***

9702_098

Figure 4.3.3.8: 1553B Bus

4.3.3.5.5. Downlink / Download

Data download to ISS uses Ethernet protocol for high speed data transfer. Data are subsequently downlinked to the ground via TRDS link or stored on Hard Disks.

Data transmitted to the ground consists mostly of events coming from the FS but include also:

1. Housekeeping information
2. Alarm
3. Calibration data
4. Ancillary information
5. Experimental data

According to available bandwidth data are sent to the ground with highest priority given to housekeeping and alarm information. Experimental data are sent to ground with main priority to high energy particle data and special trigger (e.g. luminous phenomena). Part of the data is stored on board ISS on disk server. Disks are then periodically sent to the ground with Soyuz capsules. Disks storage is expected to triple available bandwidth on board allowing to lower the energy threshold of the apparatus or to save specific triggers belonging to particular class of physics events.

4.3.3.6. CPU SYSTEM

The CPU System is composed of a number of boards devoted to different tasks:

1. CPU
2. Mass Memory
3. Internal Housekeeping interface (I-HK)
4. ISS interfaces (1553 and Ethernet)
5. Fast bus interface for event acquisition

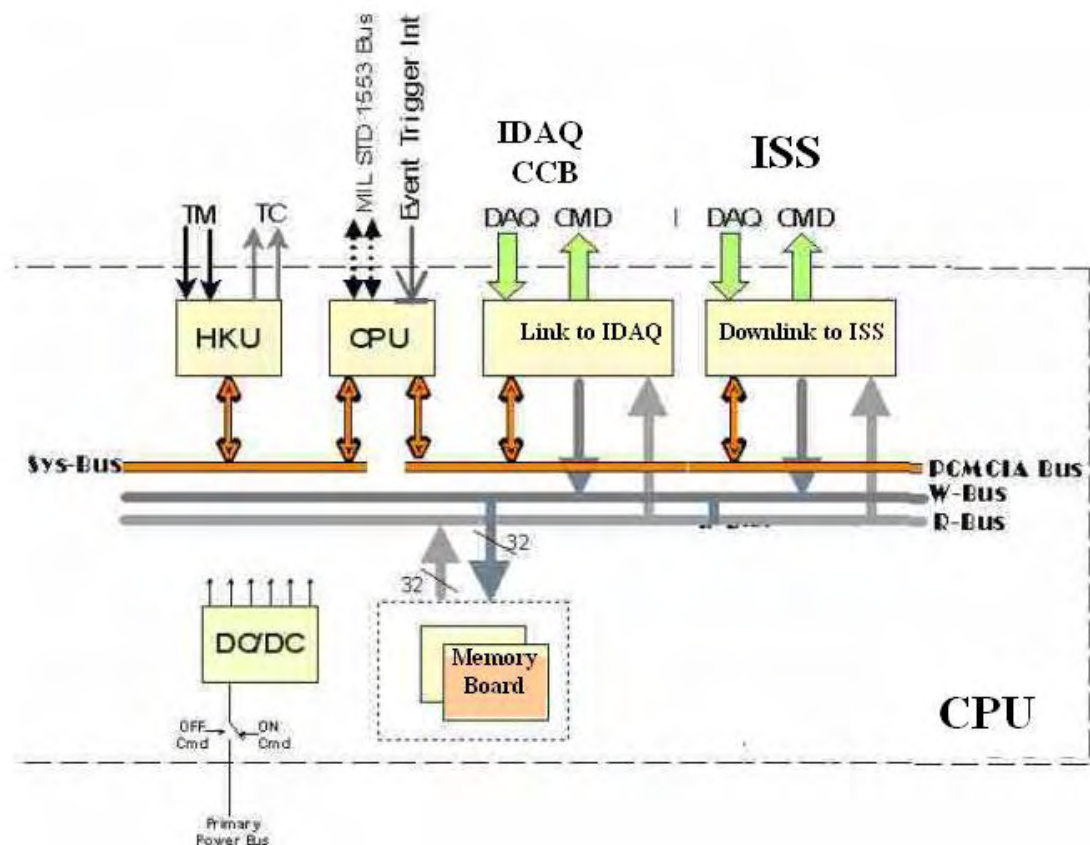


Figure 4.3.3.9: CPU Internal block diagram and interfaces with other subsystems.

The CPU is devoted to the control of the apparatus and the general optimization of the performance of the instrument in terms of data budget and detector status. It is expected to function autonomously and to reconfigure the working parameters with little or no intervention from the ground. It will handle alarm and contingencies in real time minimizing possible damage to the instrument. Long term mission operation and observation planning from the ground will be implemented from the ground with specific telecommands used to overrule the specific operation parameters of the instrument. By sending immediate or time-delayed telecommands it will be possible to define the various operation parameters of the instrument in terms of specific physics objectives or specific situations.

In this scheme most of the computational power resides in the CCB (Cluster Control Boards), with the CPU being charged with trigger handling, telecommand reception and implementation, housekeeping monitor and so on.

The main CPU tasks are:

1. Power on/off of all subsystems
2. Perform periodic calibrations
3. Start acquisition / Run
4. Define Trigger mode acquisition
5. Read Housekeeping
6. Take care of real time contingency planning

7. Perform periodic Download / downlink
8. Handle 1553 commands

4.3.3.6.1. CPU chip

CPU core for high level data acquisition and processing is based on Atmel AT697 Leon Chip. It is a Rad Hard 32-bit SPARC V8 embedded processor, an implementation of the European Space Agency (ESA) LEON2 fault tolerant model. The baseline configuration is based on the Leon2 architecture, although different configurations (Leon3, HIREC) are also being considered. Baseline chip is AT697E, with AT697F as advanced option which is expected to have passed qualification tests by the end of 2008. AT697F is pin compatible to the AT697E, and it will have improved radiation resistant capabilities, >300 krads.

ATMEL AT697 characteristics

The AT697 is a highly integrated, high-performance 32-bit RISC embedded processor based on the SPARC V8 architecture. By executing powerful instructions in a single clock cycle, the AT697 achieves throughputs approaching 1MIPS per MHz, allowing the system designer to optimize power consumption versus processing speed. The AT697 contains an on-chip Integer Unit (IU), a Floating Point Unit (FPU), separate instruction and data caches, hardware multiplier and divider, interrupt controller, debug support unit with trace buffer, two 24-bit timers, Parallel and Serial interfaces, a Watchdog, a PCI Interface and a flexible Memory Controller. The design is highly testable with the support of a Debug Support Unit (DSU) and a boundary scan through JTAG interface. An Idle mode holds the processor pipeline and allows Timer/Counter, Serial ports and Interrupt system to continue functioning. The processor is manufactured using the Atmel 0.18 μm CMOS process. It has been especially designed for space, by implementing on-chip concurrent transient and permanent error detection and correction.

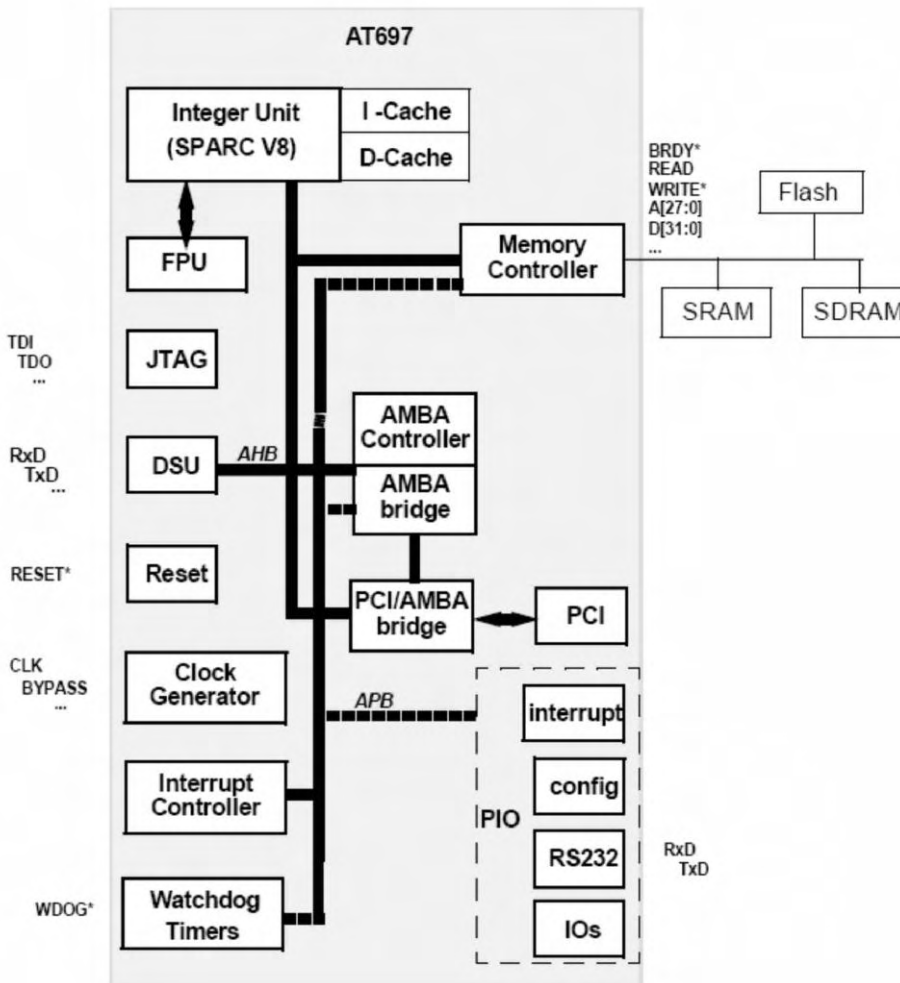


Figure 4.3.3.10: AT697 Internal block diagram

4.3.3.6.2. Software

CPU software is written in C using ERC32 Cross Compilation System (ERC32CCS). This platform was developed by ESA for space applications. ERC32CCS-v2.0.7 is a GNU based cross-compiler system for ERC32 allowing software development and testing on Linux based emulator machines. The same code can then be recompiled for the target application (Atmel chip). Current framework for ERC32 consists of the following:

- GNU C/C++ compiler (egcs-1.1.2)
- GNAT Ada 95 compiler (gnat-3.11p)
- Linker, assembler, archiver etc. (binutils-2.9.1)
- Standalone C-library (newlib-1.8.1 from Cygnus)
- RTEMS real-time kernel with ERC32 support (rtems-4.0.0)
- ERC32 boot-prom utility (mkprom-1.2.7)
- Standalone ERC32 simulator (sis-3.0.5)
- GNU debugger with ERC32 simulator (gdb-4.17 + sis-3.0.5)
- DDD graphical user interface for gdb (ddd-3.1.3)
- Work-arounds for all FPU rev.B/C errors

The `erc32ccs` allows cross-compilation of single or multi-threaded C, C++ and Ada95 applications for ERC32. Using the `gdb` debugger, it is possible to perform source-level symbolic debugging, either on the simulator or on a remote target.

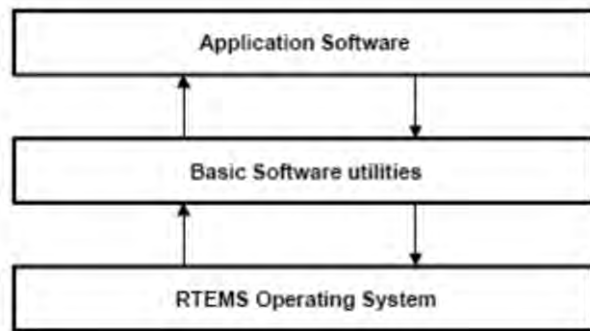


Figure 4.3.3.11: Application and Operating system layers. Data acquisition and all procedures are implemented at an Application Software level

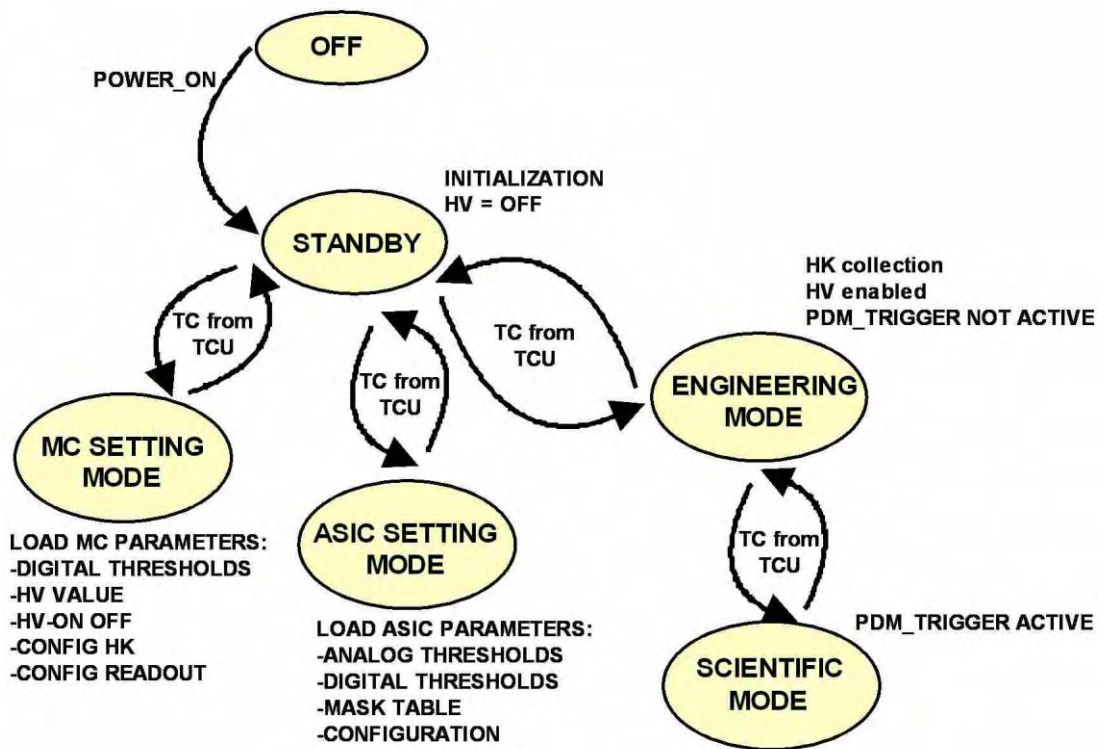


Figure 4.3.3.12: CPU software operational modes.

4.3.3.6.3. Memory board

Memory board is based on rad hard chips (3d cube). Storage is performed on 10 bit / byte, with one bit flip automatic error correction and two bit flip error detection. A total of 4 Gbytes are foreseen. Main task of the memory board are temporary storage of data prior to transmission to ISS. This allows added flexibility during periods of absence of downlink to ground or special

operations.

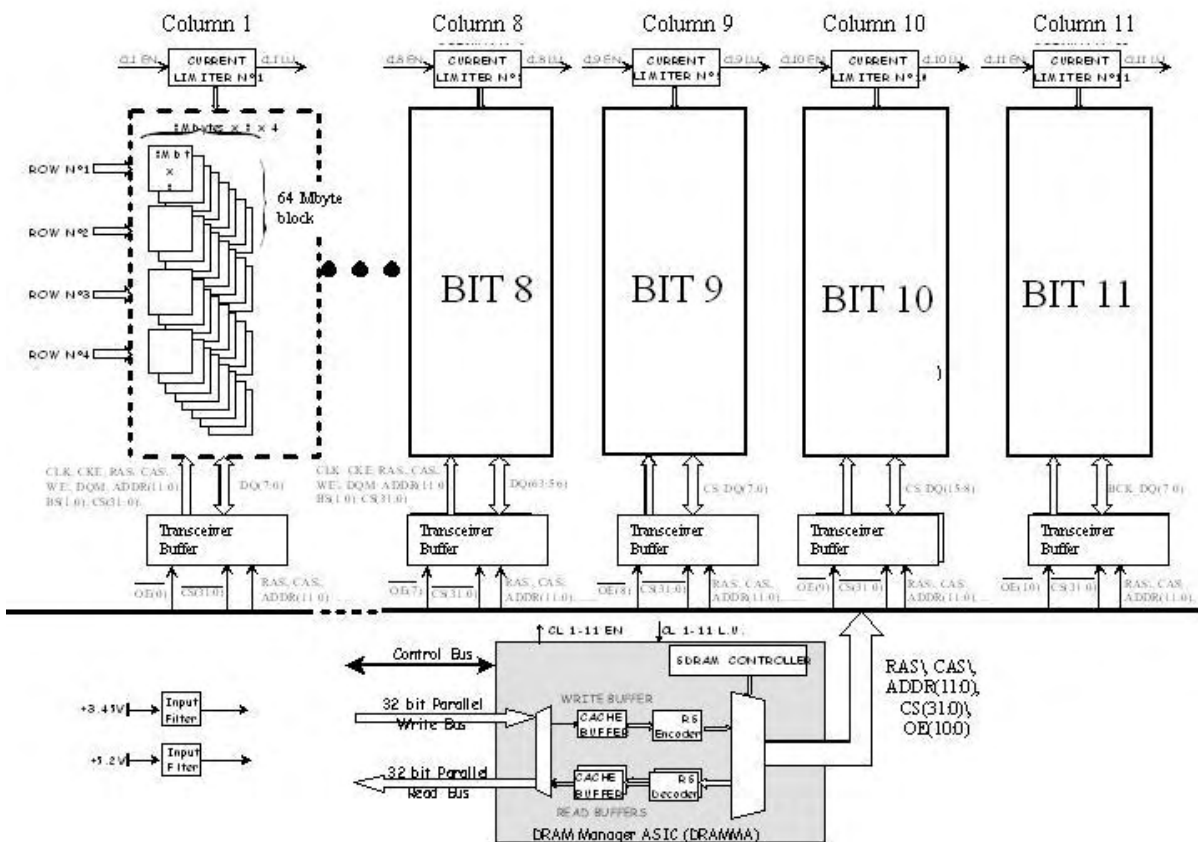


Figure 4.3.3.13: Memory module block: 10 bits are used for error correction of one bit flip and detection of two bit flips. 11th bit is used for spare

This functional module is housed on an “extended” Double Europe PCB (200 x 233 mm).

This module is in charge of four main functions:

- 1) To Send Commands to the experiment Front-End (FE) via a parallel CMD I/F.
- 2) To Receive Science Data Packets (SDP), through a parallel Data Acquisition Interface (DAQ I/F), from the experiment Front-End.
- 3) To manage the Mass Memory (MM) for storing Science Data Packets received from the experiment Front-End or Data Packets coming from the internal CPU module.
- 4) To manage the downlink of data files stored in Mass Memory towards an external Telemetry Adapter Module via a dedicated parallel TAM I/F.

4.3.3.6.4. Fast bus interface

The main building blocks of this module are:

- The parallel CMD I/F that is composed of 10 LVDS differential lines (8 Data out, 1 Strobe out, 1 Ack in).
- The parallel DAQ I/F that is composed of 10 LVDS differential lines (8 Data in, 1 Strobe in, 1 Ack out).

- The parallel TAM I/F that is composed of 10 LVDS differential lines (8 Data out, 1 Strobe out, 1 Busy in).
- A “PIF Core Controller” FPGA including all the module’s control functions as detailed here below:
- PCMCIA Bus I/F
- CMD DMA management
- DAQ DMA management
- MM Parallel Write Bus management
- MM Parallel Read Bus management

4.3.3.6.5. Housekeeping modules

Two different housekeeping modules are foreseen: one internal (I-HK) to the CPU system, linked via serial bus and one external (E-HK), linked to the CPU via digital line. The Housekeeping modules interface the CPU with the aim to distribute command to the CPU users and to collect telemetry for monitoring purposes and optimization of observational parameters.

The internal housekeeping module is devoted to monitor of critical systems, power on/off of secondary power supply etc. I-HK is turned on together with the CPU and enables power on to all subsystems, including E-HK. Task of the latter is the general slow control and monitoring of the status of the apparatus.

I-HK functional module is housed on an “extended” Double Europe PCB (200 x 233 mm). Both single (upon request) or cyclic (periodic) acquisition/commanding operating mode are possible according to the status of the acquisition.

According to the type of signal different acquisitions and control are foreseen. For instance all relays for switch on / off secondary power supply and subsystems are controlled by High Level signals. This approach has the advantage of a great degree of flexibility keeping at the same time a strong robustness and reliability.

A summary of the commanding and acquisition electrical interfaces provided by the module is given here below:

1. Voltage monitor (Primary – 120V 28V; Secondary: +-5V +12V , +3.3V -700V)
2. Current monitor
3. Temperature monitor
4. Contact closure (Lid status, relays)
5. Digital Communication Protocol (Cam Bus)

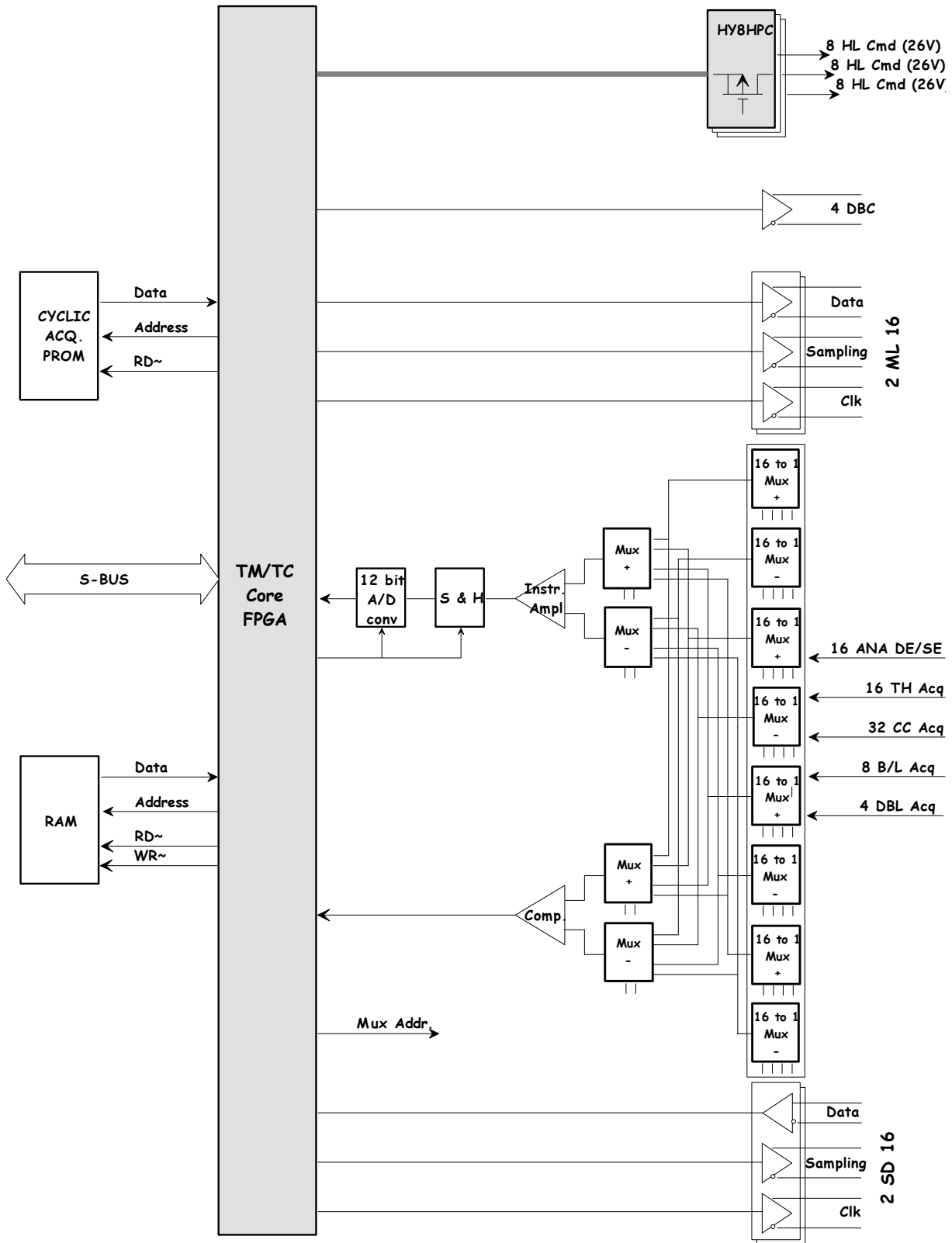


Figure 4.3.3.14: Internal Housekeeping (I-HK) block scheme

Table 4.3.3.3

Commands

Quantity

High Level 26V (HL26) pulsed commands These are power command used to pilot directly the relays of the power supply and dc/dc system. In this way we do not need to go through the secondary lines and we can control the switch on/off of the power supply (main/spare) and control the power on procedure in order to switch on gradually the whole apparatus.	50
Memory Load 16 bit (ML16) serial commands This is the output digital line for controlling the CAM bus and the additional housekeeping board. It is basically a Digital output port. There are four of them to issue commands to different boards independently.	4
Differential Bi-Level (DBC) commands Output command in differential form to issue commands where ground is an issue or in noise-robust environment.	8
Acquisitions	Quantity
Contact Closure (CC) acquisitions Check if a relays has been closed and monitor the start-up procedure.	50
Bi-Level (Bi-L) acquisitions Read the status of one system (8 systems in total)	8
Differential Bi-Level (DBL) acquisitions Read the status of one system in differential in order to be independent from different grounding.	4
Analogue Double Ended (DEA) acquisitions Acquisitions (slow control) through 12 bit ADC, differential related (voltage, current, etc)	50
Analogue Double Ended Thermistor (TH) acquisitions (Betatherm 10K Ω @ 25°C) Thermal resistors readout	50
Serial Digital 16 bit (SD16) acquisitions Input port 16 bit for readout of digital messages from the various boards.	4

4.3.3.6.6. IDAQ board

IDAQ board handles all communication with CCB and other subsystems. It is an FPGA-based interface board taking care of:

1. Event packing and data transfer from CCB to Mass memory
2. Issuing of commands from CPU to CCB
3. Issuing of commands from CPU to FPGA boards
4. Patch / dump of software of CCB and lower level boards
5. Pass-through commands between CCBs

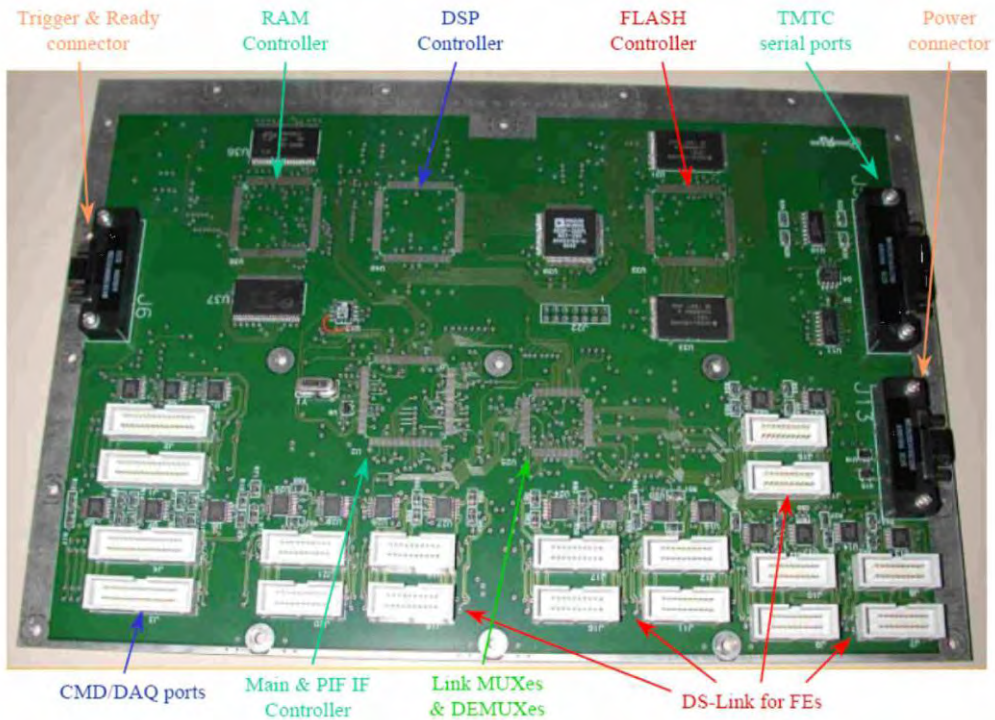


Figure 4.3.3.15: Prototype of the Idaq board based on Pamela development

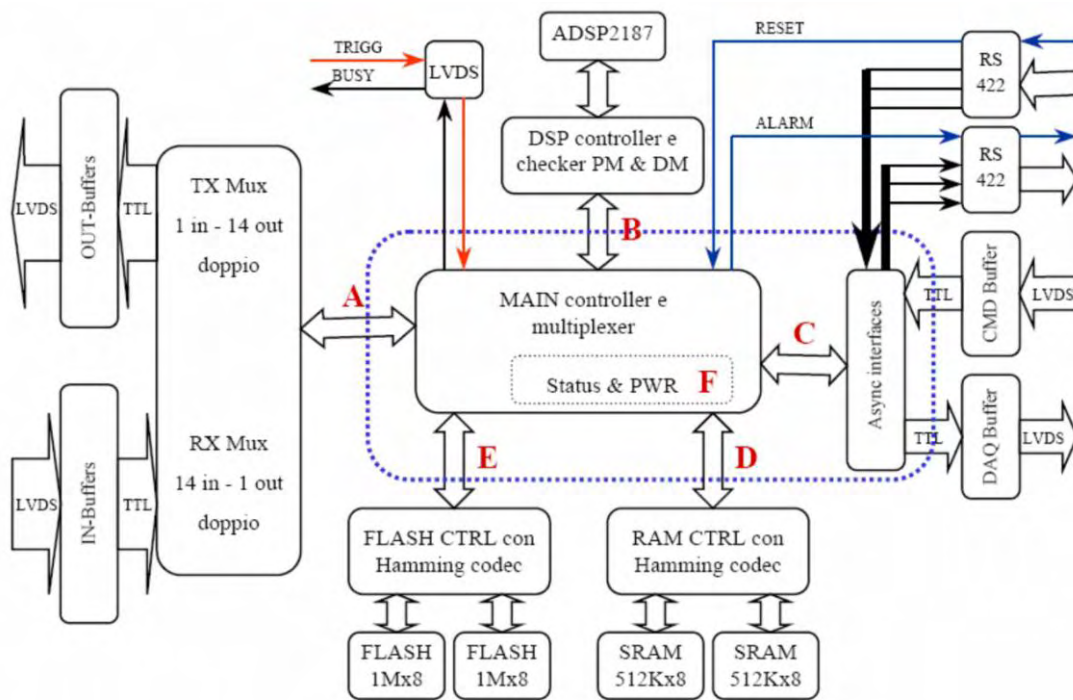


Figure 4.3.3.16: Functional scheme of the Idaq board

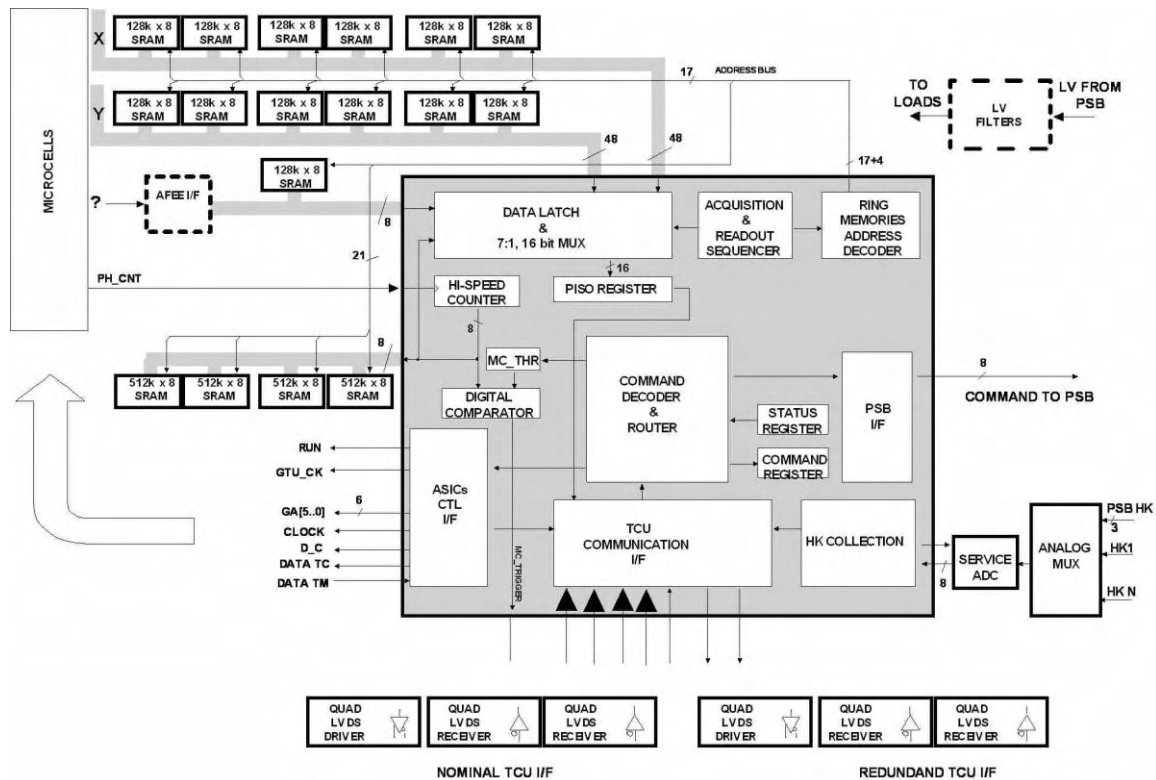


Figure 4.3.3.17: Detailed design of the Idaq board

4.3.3.6.7. Power supply distribution

ISS provides +120V and +28 V current. DC/DC converters will provide all secondary power supplies to the CPU system and all subsystems. At power on the following procedure is followed:

1. Power on of primary
2. Power on of secondary power for CPU system
3. CPU starts up, checks all internal systems
4. I-HK board checks status of the experiment
5. I-HK board switches on all secondary power supplies
6. I-HK board enables power to all subsystems in predefined sequence to avoid large inrush currents and unbalanced power to critical systems
7. E-HK board checks status of subsystems and monitors it in real time
8. In case of failures or contingencies subsystems are switched off.

Note that this approach has the advantage to allow the CPU of JEM-EUSO to keep under control the power on and off of the experiment and monitoring it at all times. A direct power on of the subsystems has the disadvantage of not being able to take care of contingencies or unbalances in the power supply.

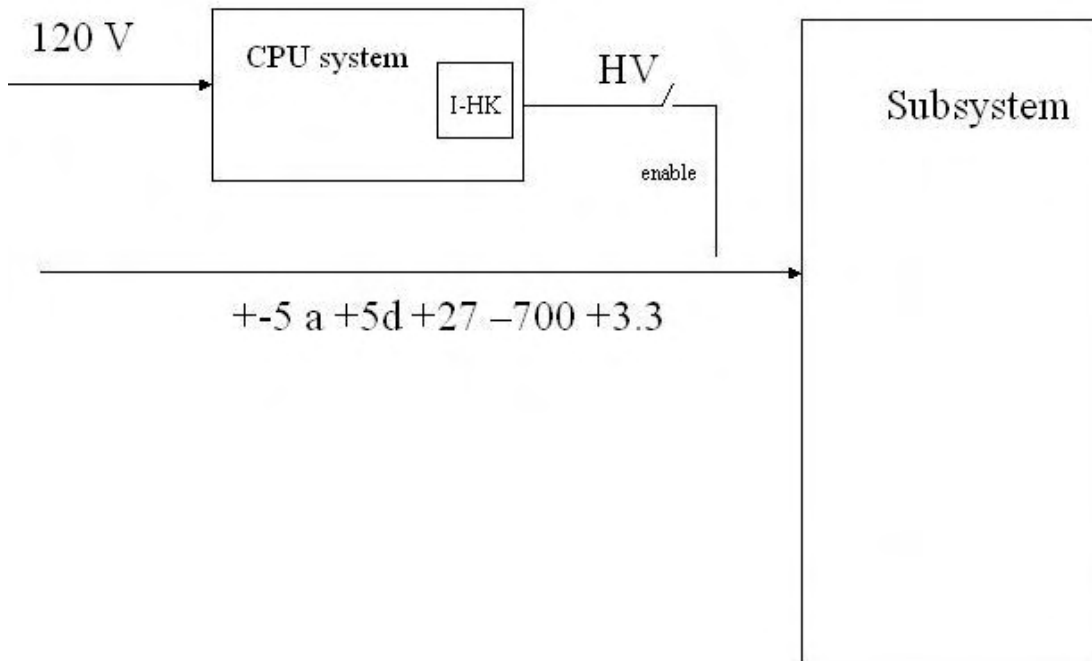


Figure 4.3.3.18: Logical scheme of power supply: power to all subsystems is enabled from Internal Housekeeping board in the CPU system (I-HK)

4.3.3.6.8. Cluster Control Board

Cluster control board is devoted to high performance (1Gflop) trigger system. Each of the 21 CCB performs trigger recognition on a part of the Focal Surface covered by 8 PDM. CCB performs data reduction by three orders of magnitude. In case of track recognition, if the track is close to the boundary of the CCB, data is requested to nearby CCB. Both primary and secondary CCB transfer data to the mass memory of the CPU via the IDAQ.

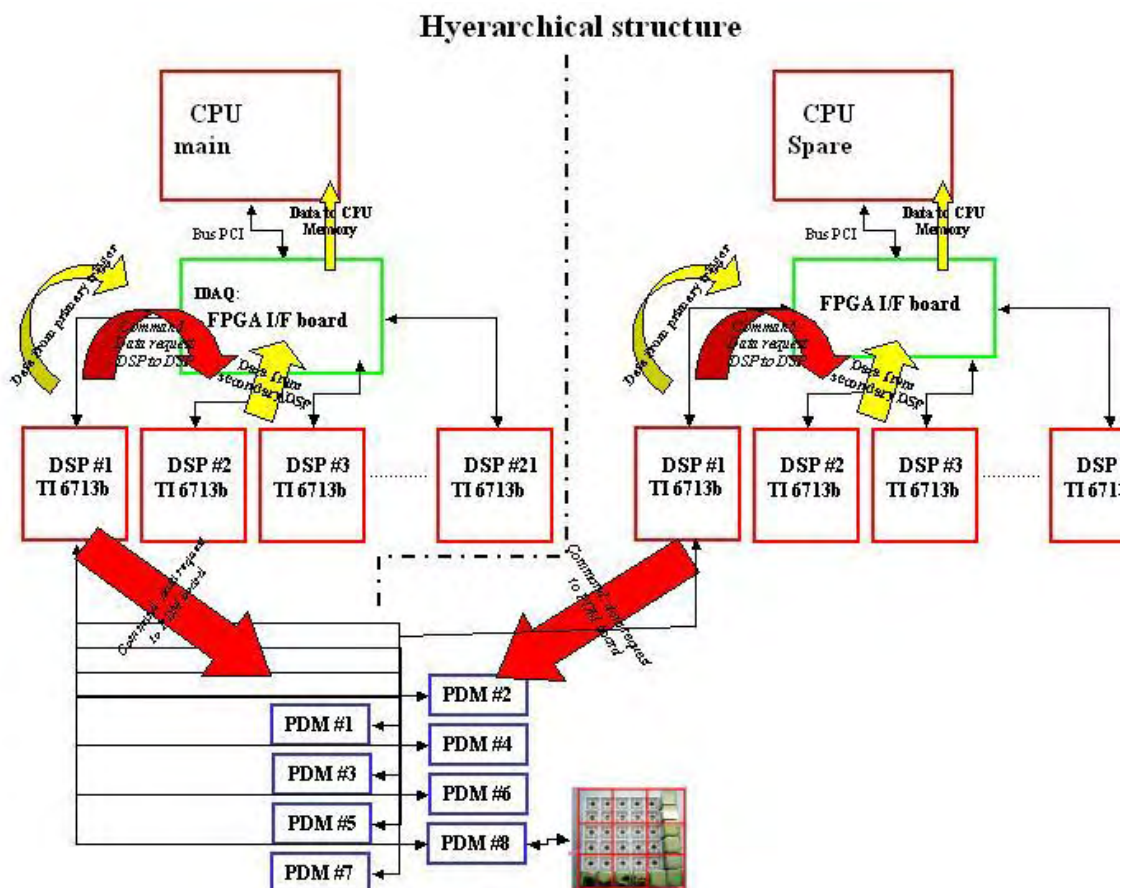


Figure 4.3.3.19: Scheme of the acquisition system of JEM-EUSO. The Structure is organized in a hierarchical system with the CPU controlling via IDAQ the 21 CCB (Cluster Control Boards) with Texas 6713 DSPs. Each CCB controls operations of 8 PDM boards, each devoted to 9 elementary cells.

ISS provides +120V and +28 V current. DC/DC converters will provide all secondary power supplies to the CPU system and all subsystems. At power on the following procedure is followed:

- a. Power on of primary
- b. Power on of secondary power for CPU system
- c. CPU starts up, checks all internal systems
- d. I-HK board checks status of the experiment
- e. I-HK board switches on all secondary power supplies
- f. I-HK board enables power to all subsystems in predefined sequence to avoid large inrush currents and unbalanced power to critical systems
- g. E-HK board checks status of subsystems and monitors it in real time
- h. In case of failures or contingencies subsystems are switched off.

Note that this approach has the advantage to allow the CPU of JEM-EUSO to keep under control the power on and off of the experiment and monitoring it at all times. A direct power on of the subsystems has the disadvantage of not being able to take care of contingencies or unbalances in the power supply.

4.3.3.6.9. Development scheme, Laboratory model, Engineering model

In experiment realization is of critical importance to parallelize development of subsystems on one hand and HW and SW on the other hand. Furthermore, given the distributed nature of the

collaboration, a number of laboratory and engineering prototypes are needed in all stages of development. To meet these requirements, thus reducing integration time and associated costs, we foresee to use off the shelf boards.

In case of the Atmel CPU the boards, based on GR-CPCI-AT697 from Gaisler research support identical functionalities to the flight ones. In case of Hirec model a similar approach is foreseen.

Engineering model will be naturally identical to flight model.

Software development will be performed on the emulator systems, with the ERC32 code compiled to run on standard Linux machines (taking advantage of the cross-compiler characteristics).

HW Characteristics for lab model are:

- AT697 Leon2-ft0.18 @ 100 MHz, with full FT (TMR cells, cache parity, regfile EDAC)
- Meiko FPU
- InSilicon Master/Target PCI core
- 100 MHz operation
- 8 Mbyte flash prom (2M x 32)
- 4 Mbyte static ram with ECC (1M x 40)
- Up to 256 Mbyte PC133 SDRAM with ECC (64M x 40)
- 10/100 Mbit ethernet MAC
- 33 MHz, 32-bit PCI interface with host/satellite/target capability
- Standard RS-232 UART port for DSU
- 120-pins memory and custom I/O expansion connectors (AMP-177-984-5)
- 2 x RS-232 drivers
- 4 x RS-232 drivers
- 4 x RS-422 drivers
- 4 x LVDS drivers

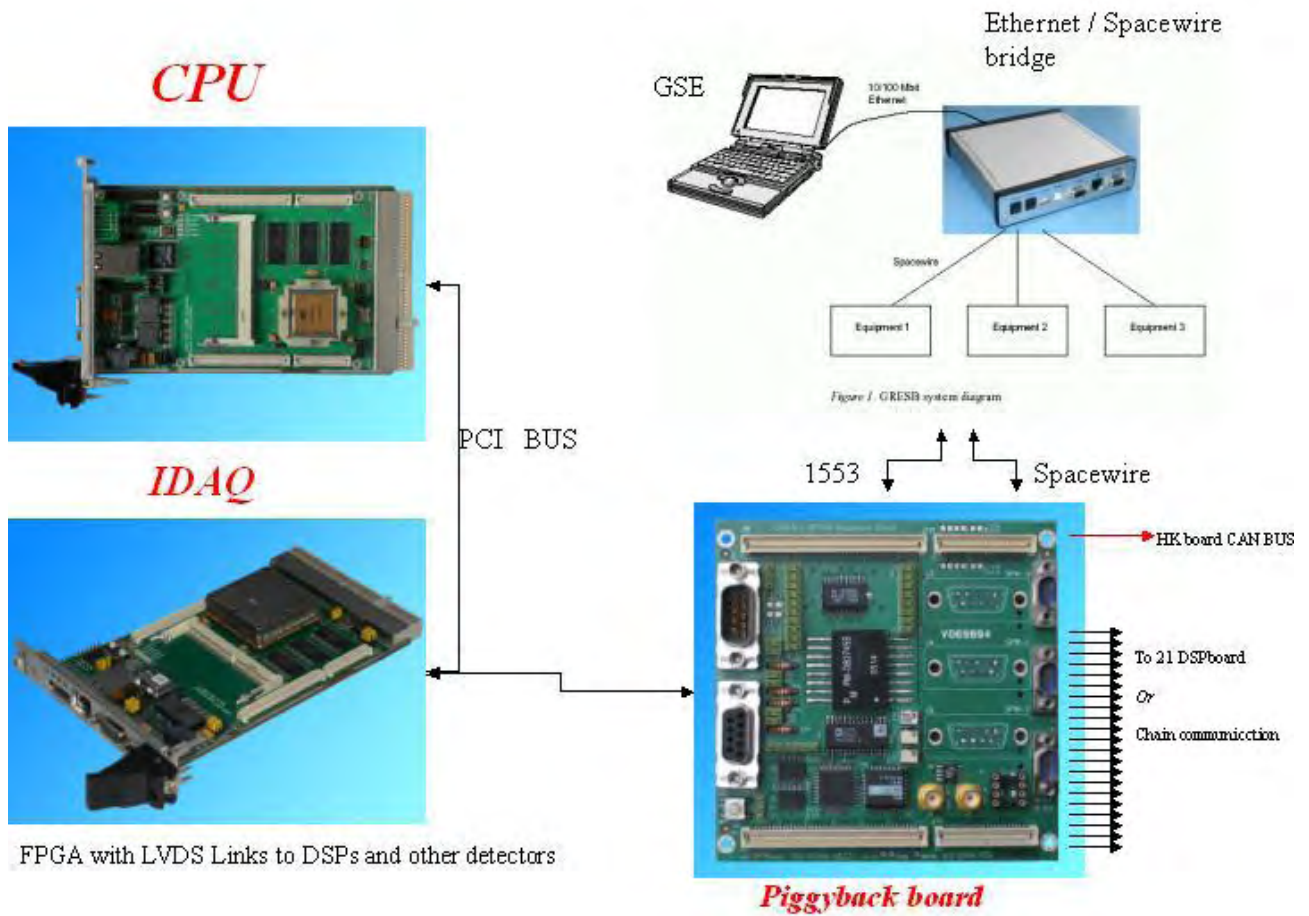


Figure 4.3.3.20: Board breakdown for laboratory model of the CPU system. Connection between CPU and IDAQ board is via PCI bus. CPU and IDAQ are emulated by devoted FPGAs. Link with ISS simulator occurs in SpaceWire protocol. Data command is implemented in 1553 protocol.

4.3.3.6.10. EGSE/Simulator

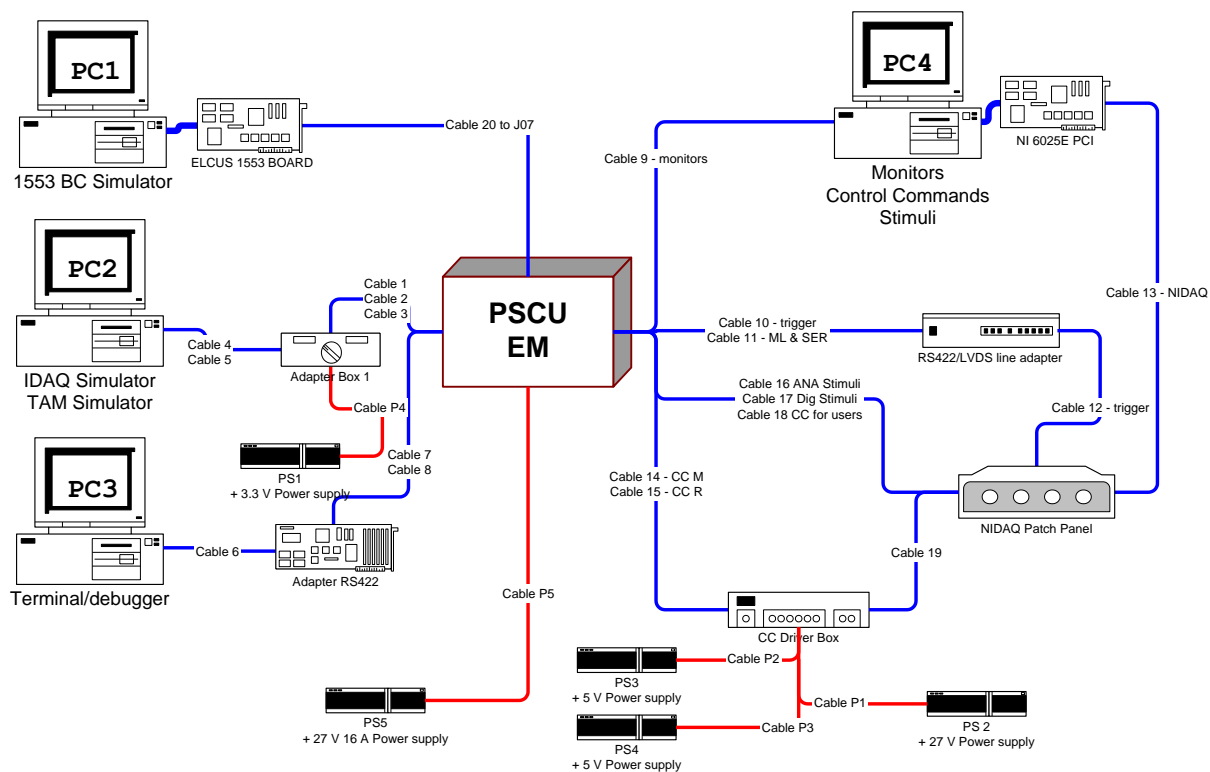


Figure 4.3.3.21: Scheme of the EGSE of the CPU and acquisition system of JEM-EUSO. The CPU system is interfaced to different computer devoted to emulation of specific detector and system function.

The EGSE (Electronic Ground Support Equipment) is devoted to the simulation of all systems connected to the CPU. In this way it is possible to develop and test the HW and SW of the CPU in parallel to other systems and to shorten considerably the time of integration and debugging. They include: the 1553 command simulator (to send commands from ISS/ground and receive replies/status), the terminal/debugger console, linked to the engineering connector of the CPU to monitor register status of the processor and debug SW, the Monitor/ Control Command Stimuli, connected to the Housekeeping port (simulates housekeeping such as Temperature, Current), The IDAQ/High Speed link simulating event data acquisition and so on...

All parts of the EGSE are fully interchangeable with the engineering/flight model version, allowing for gradual integration of one subsystem at a time. Furthermore the EGSE is used to test the logic of working of the experiment, simulating failures and critical conditions in ways not otherwise possible with the real hardware.

4.3.4. Operation

4.3.4.1. Before launch

Keeps constant temperature and keeps out of shock. Covers on the detector surfaces to protect from falling objects

4.3.4.2. Transportation to ISS

4.3.4.2.1. Launch

Follows environment of HTV un-pressurized module. The FS Electronics is STANBY mode. Especially, the HV Power Supply must be power off.

4.3.4.2.2. Standing by phase to attach the ISS and Attaching Phase
Follows environment of ISS. The FS Electronics is STANBY mode.

4.3.4.3. Observation phase

4.3.4.3.1. Normal operation

The FS is the science observation mode synchronizing with the orbit.

4.3.4.3.2. Approaching Transportation Vehicle Phase and ISS attitude controlled phase

The FS Electronics is STANBY mode.

4.3.4.3.3. Onboard calibration mode

The FS Electronics obtains the calibration data.

4.3.4.4. End of mission

The FS Electronics is STANBY mode or power off.

4.3.5. Summary

4.3.5.1. Requirements for the performance

Table 4.3.4.1: Requirements for the performance of the focal surface

	Item	Required value	Note
FSR1	Shape of the focal surface	spherical	
FSR1	Gap on the positions between designed focal surface and the detector	Less than 2mm	
FSR2	Photon detection efficiency	More than 0.12	Effective area ratio × photoelectric quantum efficiency × photoelectron collection efficiency
FSR3	Average pixel size	Less than 4.5mm	Corresponding the field of view of 0.11°(1 mm = 0.023-0.027)
FSR4	Dimension of the focal surface	4.45 m ²	Corresponding to a 30° view angle of the telescope
FSR5	Trigger efficiency	95% @ 10 ²⁰ eV	
FSR6	Gate time(GTU)	<2.5 μsec	
FSR7	Counting Capacity	200/GTU	
FSR8	Electrical noise rate	<50GHz	<250kHz/Pixel
FSR9	Dead time	<3%	

4.3.5.2. Technical Readiness Level

Table 4.3.4.2: Technical Readiness Level of the Focal Surface

	Item	Technical Readiness Level and its reason when selected in Feb./'07	Technical readiness level and reason (as of Apr./'08)	Expected technical readiness level and activities at SDR time (Mar./'09)
FSR1	Shape of the focal surface	TRL3 Structure design in ESA-Phase A EUSO-FS-REP-007 EUSO-FS-REP-011	TRL3	TRL4 To be verified doing an optical performance test.
FSR1	Gap on the positions between designed focal surface and the detector	TRL3 The same as above	TRL3	TRL4 The same as above
FSR2	Photon detection efficiency	TRL4 0.148 was verified by R8900-M36. EUSO-FS-REP-006	TRL4 By improving the photocathode, the improvement up to 0.207 was confirmed.	TRL4 Verification by means of element tests on the trial manufactured PDM.
FSR3	Average pixel size	TRL4 The same as above	TRL3 Same as FSR1	TRL4 The same as above
FSR4	Dimension of the focal surface	TRL4 The same as above	TRL4 Same as FSR2	TRL4 The same as above
FSR5	Trigger efficiency	TRL3 Original design evaluation	TRL3 98.7% was confirmed by Trigger software simulation.	TRL4 The same as above
FSR6	Gate time(GTU)	TRL3 EUSO-PI-REP-005 and the original design evaluation	TRL3 Design evaluation by Trigger software simulation.	TRL4 The same as above
FSR7	Counting Capacity	TRL3 Original design evaluation	TRL3	TRL4 The same as above
FSR8	Electrical noise rate	TRL3 Original design evaluation	TRL3	TRL4 The same as above
FSR9	Dead time	TRL3 Original design evaluation	TRL3	TRL4 The same as above

4.3.5.3. Main Parts

Table 4.3.4.3: Main Parts

	Parts	Total #
Detector	PMT	4932
	High Voltage	137
	HV Divider	1233
EC	EC ASIC	4932
	EC FPGA	1233
PDM	PDM FPGA	137
CCB	DSP	36
MDP	MPU	2

4.3.5.4. Temperature Requirements

Table 4.3.4.4: Temperature Requirements

	Operating	Non-Operating
Detector	$T_0 \pm 10^\circ\text{C}$, $0 < T_0 < +20^\circ\text{C}$	$-30 \sim +50^\circ\text{C}$
Electronics	$-10 \sim +50^\circ\text{C}$	$-30 \sim +50^\circ\text{C}$

4.3.5.5. HK Requirements

Table 4.3.4.5: HK Requirements

	Control			Monitor		
	Item	Width (bit × #)	cycle	Item	Width (bit × #)	cycle
PDM × 137	EC Status	8 × 9	1/orbit	EC Status	8 × 9	8 sec(TBC)
				FS Temp.	8 × 3?	
				FEE Temp.	8 × 9?	
	HV Value	8 × 1		HV Value	8 × 1	
				LV	8 × 1	
				1st Trig. Rate		
				2nd Trig. Rate	8 × 1	
CCB × 19	PDM Status	16 × 1		PDM Status	16 × 1	
	CCB Status	16 × 1		CCB Status	16 × 1	
				3rd Trig. Rate	8 × 1	
MDP × 2				LV	8 × 1	
	MDP Status	16 × 1		MDP Status	16 × 1	
				LV	8 × 1	

4.3.5.6. Budget(Mass, Power, Telemetry)

Mass Budget

Table 4.3.4.6.1: Mass Budget

Item	BEE(kg)	Margin	Total(kg)	Comment
PMT	138	15%	159	28g/PMT × 4932
Elec. Board	91	15%	105	PMT Support, PDM_BOX, CCB, MDP
Cables	86	30%	112	
Total	315		376	

Power Budget

Table 4.3.4.6.2: Power Budget for Science Observation

Item	BEE(W)	Margin	Total(W)	Comment
HV for PMT	72.0	30%	93.6	
EC	208.4	30%	271.0	ASIC:141.0, FPGA:67.4
PDM	31.0	30%	40.3	
CCB	13.0	30%	16.9	
MDP	1.0	30%	1.3	2 System
Loss of V Trans.	172.6	30%	224.4	120V→28V, 28V→HV:0.5, 28V→5V:
Total	498	30%	648	

Telemetry Budget

Table 4.3.4.6.3: Telemetry Budget

Item	BEE(kbps)	Margin	Total(kbps)	Comment
Science DATA	202	15%	233	trigger rate: 0.1Hz

4.3.5.7. Cost and Schedule

Table 4.3.4.7: Cost and Schedule

Item	H20 2008	H21 2009	H22 2010	H23 2011	H24 2012	H25 2013	Total (MYen)
PMT Evaluation	Evaluation		Mass Production				
	40	442	422	345	295	56	1,600
FS Construction	Structure Design		Trial Prod.	1st Product.	2nd Prod.		
Elec. Making	30	464	419	350	290	47	1,600
	BBM Eval.	EM Eval.	PFM Making & Test		Test		

4.3.5.8. Organization

Focal Surface : Hirohiko M. Shimizu(KEK), Yoshiya Kawasaki(RIKEN)

FS Detector : Yoshiya Kawasaki(RIKEN)

FS Electronics : Tokonatsu Yamamoto(Univ. Konan), Marco Casolino(Univ. Rome)

ASIC & 1st Trigger : Tokonatsu Yamamoto(Univ. Konan)

PDM(2nd Trigger) : Shinwoo Nam(Ehwa W. Univ.)

CCB(3rd Trigger) : Andrea Santangelo(Univ. Tubingen)

MDP : Marco Casolino(Univ. Rome)

Trigger Algorithm: Mario Bertaina(Univ. Torino), Osvaldo Catalano(IASF-PA/INAF)

Reference:

[1] O. Catalano, Il Nuovo Cimento, 24-C, N.3, 445-470, 2001

4.4. Atmospheric Monitor

4.4.1. Outline

The aim of the Atmospheric Monitor system is to observe the condition of the atmosphere in the field of view of the telescope. The strength of the fluorescent light and Cherenkov light emitted from EAS and their transmission process depend on the transparency of the atmosphere, cloud coverage and the height of cloud top. These must be determined by the Atmospheric Monitor system of the JEM-EUSO telescope.

In the case of events above 10^{20} eV, the existence of the cloud can be detected by the signals from the EAS [1]. The monitoring of the cloud coverage by JEM-EUSO Atmospheric Monitor, however, is important to estimate the effective observing time with a high accuracy and to increase the confidence level in the events just above the energy threshold of the telescope. The JEM-EUSO mission, therefore, has the Atmospheric Monitor subsystem as far as the impact onto mass and power budget is insignificant. It consists of 1) Infrared camera, 2) Lidar, and 3) slow data of the JEM-EUSO telescope. They are planned to measure the height of cloud top in the accuracy better than 500m (see figure 4.4.1-1). In the year 2007, we determined the basic specifications of the instruments and the conceptual design of them. We will describe the design and problems to be solved in the following chapters.

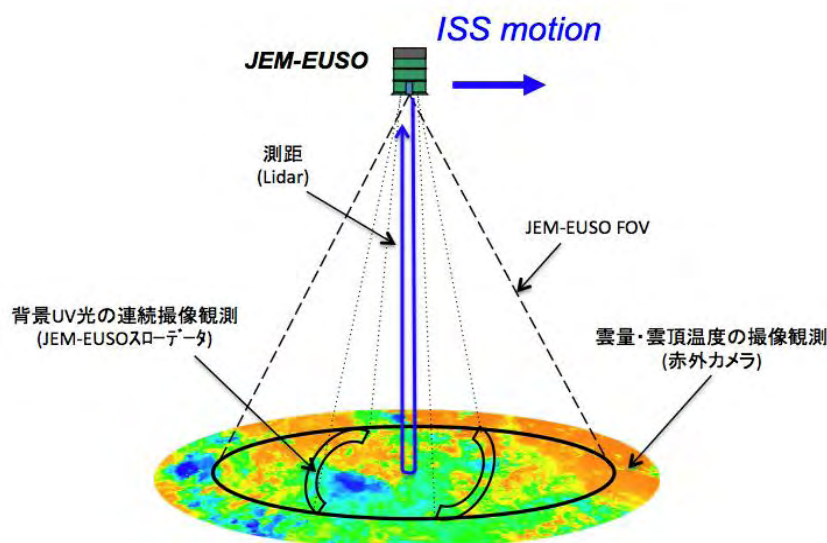


Figure 4.4.1-1. Concept of the Atmospheric Monitor

4.4.2. Infrared Camera

The Infrared camera consists of refractive optics made by Germanium material and uncooled micro bolometer array detector. Interferometer filters that transmit 10-12 μm are used as the filters of wavelength bands. The field of view of the telescope is 60° , which matched to that of the main telescope. The angular resolution, which corresponds to one pixel, is about 0.25° at the center of the field of view. The temperature controlled shutter in the camera and mirrors are used to calibrate background noise and gains of the detector to achieve the absolute temperature accuracy of 3K, as well as sea temperature that are observed by the other satellites. Though the infrared camera takes images continuously at the frequency of video frame rate (= 1/30 sec), transfer of the images takes place every 30 seconds, in which ISS moves half of the field of view of JEM-EUSO telescope. Table 4.4.2-4 summarizes the requirement of the infrared camera.

Uncooled bolometer array can be small, light weight, and less power consumption, since it is different from semiconductor detectors such as HgCdTe, GaAs, InGaAs, which require the cooling system. In recent years, the performance is dramatically advances and is used in space environment in Mars Odyssey and space shuttle mission, STS-85. Planet-C/VCO (Venus Climate Orbiter) , scheduled launch in 2010, is also adopted an infrared camera in mid-infrared (LIR) with a uncooled micro bolometer array detector. A wide field is achieved by the Germanium refraction optics was developed in JAXA for the stratosphere platform mission. On the other hand, EADS/SODERN has experience of the development of infrared camera with an uncooled micro bolometer array for METOP1 satellite and CALIPSO satellite. In JEM-EUSO mission will use these already developed technology as far as possible in the infrared camera.

4.4.2.1. Requirement for the cloud top height

Infrared camera determines the cloud top height within the field of view of JEM-EUSO by taking infrared images. The cloud top height and cloud coverage are obtained by the infrared images and data from Lidar. These data are used in the estimation of the effective observational volume and the reconstruction of the events.

4.4.2.2. The accuracy of the cloud top height

The accuracy of the cloud top height is determined by the requirement for the accuracy of the estimation of the effective volume for the cosmic-ray events, i.e., the accuracy of the spectrum determination. In the following, we will describe the process of requirement determination for the infrared camera.

First of all, flux of EECRs are determined by

$$Flux \propto \frac{N}{ST\Omega} \quad , \quad (1)$$

Where N is the total number of events of EECRs, S is the effective exposure, T is observational time, Ω is the solid angle of the cosmic-rays incident to the earth. Since we can safely assume that both T and Ω are constants, flux are proportional to N/S :

$$Flux \propto \frac{N}{S} \quad , \quad (2)$$

Where N is the sum of the number of events that Cherenkov marks (golden event) N_{golden} and the number of events that EECRs impinge to the cloud area and Cherenkov light is reflected at the cloud top and observed, N_{cloud} . On the other hand, we assume that the area of clear sky in the field of view of JEM-EUSO as S_{golden} , the area of the cloudy sky as S_{cloud} , then the right hand side of the equation (2) are:

$$\frac{N}{S} = \frac{N_{golden} + N_{cloud}}{S_{golden} + S_{cloud}} \quad (3)$$

Here, we assume that $N_{golden} + N_{cloud} = \text{const}$. The effective exposure of the clear sky will be 30% of the are corresponding to (S_{EUSO}) the field of view of the JEM-EUSO as reported in ESA-EUSO Phase-A report:

$$S_{EUSO} = \pi \cdot (430 \times \tan 30^\circ)^2 = 1.94 \times 10^5 \quad [\text{km}^2] \quad (4)$$

$$S_{golden} = 0.3 \times S_{EUSO} = 5.81 \times 10^4 \quad [\text{km}^2]$$

Next, in order to obtain cloudy area, S_{cloud} , we use the statics data of cloud height and the optical depth that is estimated by TOV data as shown in table 4.4.2-1 [2]. We assume that Cerenkov lights reflected only at the cloud with the optical depth (OD) deeper than 1. The number of the total events in such a case is N_{cloud} .

Table 4.4.2-1. Optical depth and the coverage of the cloud as the function of the height

TOVs : Cloud presence				
h>10 km	1.6%	17.9%	3.0%	6.1%
7<h<10	0.5%	3.6%	3.5%	6.3%
3<h<7	0.7%	2.2%	2.9%	5.8%
h < 3 km	1.3%	5.6%	5.1%	16.1%
TOVs+	OD<0.1	0.1<OD<1	1<OD<2	OD>2

Table 4.1.2.2.2-1 TOVs data: Abundance of clouds as a function of optical depth and cloud top altitude (in percent). The Clear Sky Fraction is 30 %. The total probability exceeds 100 % because a supplementary fraction of sub-visible clouds at high altitudes have been added.

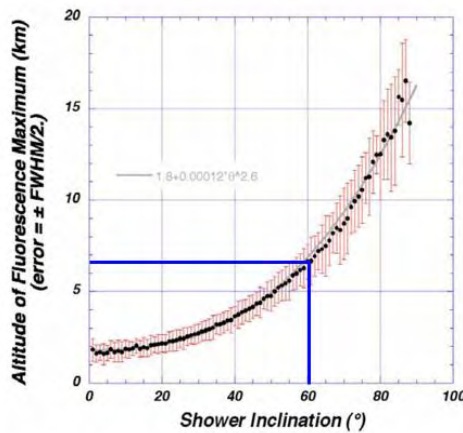


Figure 4.1.2.2.2-1 Average altitude of the maximum of the shower signal (for proton primary), as a function of shower inclination. The error bars represent the FWHM fluctuations.

Figure 4.4.2-1. Relation between zenith angle of the cosmic-rays and the average X_{max}

We interpolate the data by linear function between cloud top height and coverage, and then we get:

$$S_{cloud} = 4551.2 \times h + 27753 \quad [\text{km}^2] \quad (5)$$

This equation allows us to evaluate the area of cloudy sky S_{cloud} (km^2) at the arbitrary height. On the other hand, average height of shower maximum of the event by primary proton with the energy of 10^{20} eV is given by figure 4.4.2-1 [2]. In the case that zenith angle of 60° , average height of the shower maximum is about 6.8 km (blue curve of figure 4.4.2-1). Here, we neglect the frustration arise from the uncertainty of the first interaction point (red bars in the figure) for simplicity. In the case with the zenith angle of 60° , cloud lies lower than 6.8 km, the event can be reconstructed. Therefore, the obtaining of the cloud area in such a case is the equivalent to determine the area that cloud lies in 0-6.8 km: it can be obtained from equation (5):

$$S_{cloud}(h = 6.8\text{km}) = 5.87 \times 10^4 \quad [\text{km}^2]$$

If we assume that the accuracy of the cloud top height determined by Infrared camera is ± 1 km, then cloud top height for the case of zenith angle of 60° is determined as 6.8 ± 1 km. In such a case, error of the cloud top height (green curve of figure 4.4.2-2) is the same as the error of the area of the cloudy sky S_{cloud} (red curve of figure 4.4.2-2). This error (ΔS_{cloud}) is obtained by equation (5):

$$\Delta S_{cloud} = 4.55 \times 10^3 \quad [\text{km}^2]$$

We can evaluate these error in the similar way for the cases of various zenith angle of $0^\circ, 10^\circ, 20^\circ, \dots, 80^\circ$. The results are summaries in table 4.4.2-2. The cloud top heights are also obtained in the similar way for the cases that the errors for the cloud top height is ± 0.5 km and ± 0.2 km.

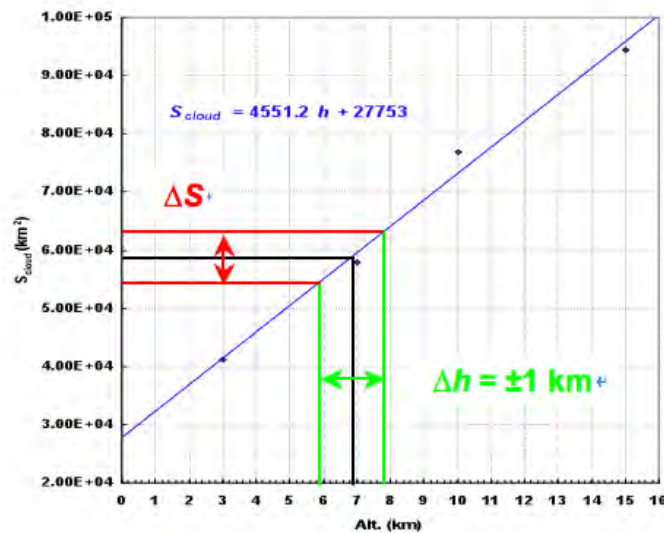


Figure 4.4.2-2. relation between accuracy of cloud top height and cloud coverage

Table 4.4.2-2. The error in effective observation area as the function of incident angles of cosmic-rays, when the accuracy of the cloud top height is ± 1 km.

θ (deg)	X_{\max} alt (km)	S_{golden} (km ²)	S_{cloud} (km ²)	$\Delta h = \pm 1$ (km)	
				$\pm \Delta S$ (km ²)	Error (%)
0	1.5	5.81E+04	3.46E+04	4.55E+03	4.91
10	1.8		3.59E+04		4.84
20	2.2		3.78E+04		4.75
30	2.6		3.96E+04		4.66
40	3.6		4.41E+04		4.45
50	4.7		4.91E+04		4.24
60	6.8		5.87E+04		3.90
70	9.3		7.01E+04		3.55
80	12.3		8.37E+04		3.21

JEM-EUSO will detect one thousand events in the three year. We will call them as golden event:

$$N_{\text{golden}} = 1110$$

Next, N_{cloud} and N_{golden} have the relation bellow:

$$N_{\text{cloud}} = \frac{S_{\text{cloud}}}{S_{\text{golden}}} N_{\text{golden}}$$

For various zenith angle, we can obtain N_{golden} , N_{cloud} , N_{total} ($= N_{\text{golden}} + N_{\text{cloud}}$), $1/\text{sqrt}(N_{\text{total}})$ and summaries in table.4.2-3.

Table 4.4.2-3. Statistical fluctuation for detected events

θ (deg)	X_{\max} alt (km)	S_{golden} (km ²)	S_{cloud} (km ²)	N_{golden}	N_{cloud}	N_{total}	(%)
0	1.5	5.81E+04	3.46E+04	1110	661	1771	2.38
10	1.8		3.59E+04		687	1797	2.36
20	2.2		3.78E+04		722	1832	2.34
30	2.6		3.96E+04		756	1866	2.31
40	3.6		4.41E+04		843	1953	2.26
50	4.7		4.91E+04		939	2049	2.21
60	6.8		5.87E+04		1122	2232	2.12
70	9.3		7.01E+04		1339	2449	2.02
80	12.3		8.37E+04		1600	2710	1.92

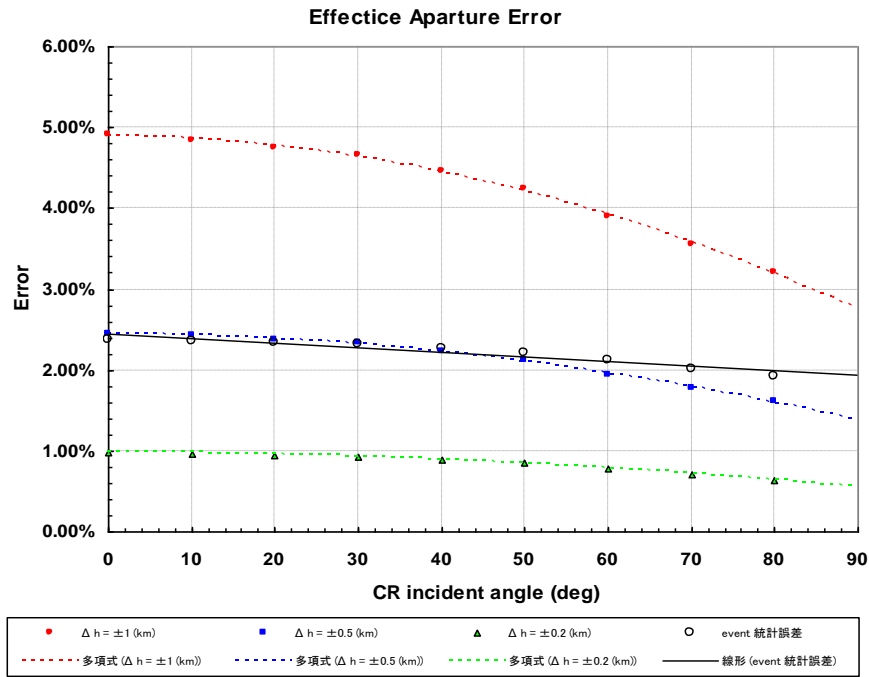


Figure 4.4.2-3. Error in cosmic-ray flux for different incident angles.

Figure 4.4.2-3 summarizes our analysis above. In other words, the accuracy of the cloud top heights less than ± 0.5 km, the error arising from them is at a similar level to the statistical errors. If it is ± 0.2 km, it is significantly smaller than that of the statistical error.

In summary, the accuracy of the cloud top height is required to be less than ± 500 m. The temperature decrease in the troposphere is almost constant and about $0.6^{\circ}\text{C}/100\text{m}$; the difference in height of 500 m corresponds to the difference in temperature of 3 K.

4.4.2.3. Requirement for the Infrared camera

Table 4.4.2-4. Specification for the Infrared Camera

Temperature range	220 – 300 K
Wavelength	10 – 12 μm
Field of View	60°
Spatial resolution	0.25° @ FOV center (= 4.4 mrad) 0.22° @ FOV edge (= 3.8 mrad)
Absolute Temperature accuracy	3 K
Optics	Ge Refractive Optics
Detector	Uncooled Microbolometer array
Digitizing resolution	12 bit
Integration Time	33 msec / image (= video frame rate)

We contacted with EADS/Sodern, aerospace company in France to confirm the feasibility to build an infrared camera attached to JEM-EUSO. EADS/Sodern has experience to build the infrared

camera (IIR) onboard CALIPSO satellite and that of METOP1satellite (IIS). Those are working fine until now. Both Infrared camera uses uncooled micro-bolometer array made by Boeing to make them small and light weight. EADS/Sodern reported us that they can make Infrared camera of JEM-EUS based on the technology of IIR and IIS, though some minor modifications are necessary. We have started further optimization of the infrared camera such as pixel size, design of the wide field optics, and onboard calibration instruments. Table 4.4.2-5 summaries the feasibility report of EADS/Sodern necessary modifications from IIR or IIS. We briefly describe bellow.

(a) Temperature and wavelength range

It is achievable with currently available technologies in EADS/Sodern.

(b) Field of view of Optics

EADS/Sodern developed infrared camera with narrow field of view. (figure 4.4.2-4,-5) and performs survey observations of a wide area by the scanning mirror. On the other hand JEM-EUSO requires one wide-field optics to reduce cost and weight and to avoid mechanics. The field of view of 60 degrees, however, can be achievable relatively easily, since it has been already achieved by other several missions The concrete specifications will be determined not later than SRR(System Requirement review).

(c) Absolute temperature accuracy

It is achievable with currently available technologies of EADS/Sodern. If we use calibrator module that onboard in CALIPSO satellite, even that of 1K would be also achievable. Onboard calibrator will not use in JEM-EUSO in the case that absolute temperature accuracy of 3K is achievable without it, since it may increase mass, size, and power considerably. Conversion curve from the temperature to height can be calibrated directly by Lidar or slow data of the main telescope. This issue will be studied with EADS/Sodern and decided by the time of SRR.

(d) Detector

Most confident detector is the uncooled microbolometer sensor made by Boeing. And EADS/Sodern developed IIR and IIS with them. We will investigate along this line for the JEM-EUSO mission. Although a microbolometer array by Boeing has a pixel size of 320x240, ERADS/Sodern uses only 64x64 pixels. Read-out electronics may have to be newly developed for JEM-EUSO where full pixel will be used. In the case that 320x240 pixel size, special resolution is about 1.8km/pix in the direction of Nadir. This is two times larger than that of JEM-EUSO telescope (800 nm) and allowable.

(e) Mass Size and Power

It is achievable by the current technologies of EADS/Sodern and expected considerably lower than the specification of JEM-EUSO.

In Summary, all the specification can be satisfied if they apply the technologies that used in IIR of the CALIPSO satellite, although some minor developments are necessary for the field of view and pixel size need. The flight model can be manufactured in five years by the cost of 5.5 M€.

Table 4.4.2-5. Feasibility of Infrared camera specifications

Parameter	Target value	CIM compatibility
Survey temperature range	220 – 300K	OK
Wavelength	11 – 13 μm	Filter to be modified
FOV	60°	Optics to be modified
Spatial resolution	0.25 ° @ FOV center (= 4.4 mrad) 0.22 ° @ FOV edge (= 3.8 mrad)	Depending on the image size
Absolute temperature resolution	3 K	OK *
Optics	Ge dioptric system (F=1.0)	OK * - Temperature stability to be discussed
Detector	Uncooled micro-bolometer array device	OK
Image pixel number	320 × 240	64x64 or 128x128 or 240x256 *
Pixel size	37 μm	50 μm
Image resolution	12 bit	OK
Exposure time	33 msec / image (= video frame rate)	OK
Mass	7 kg	5 kg without calibration device *
Dimensions (L × W × H)	200 × 280 × 320 mm	130x250x250 without calibration device *
Power	20 W (operative) 7 W (non-operative)	8 W (operative) without calibration device *

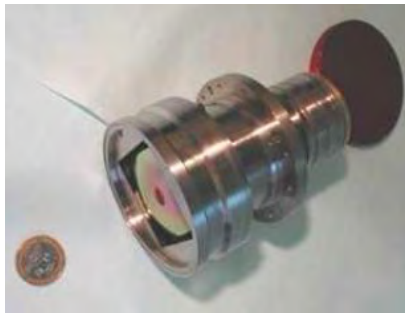


Figure 4.4.2-4. Optics of IIR

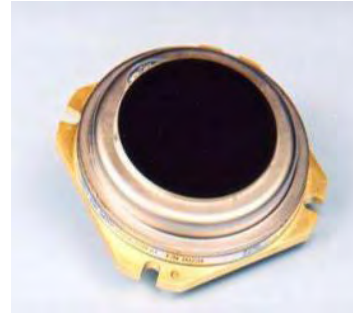


Figure 4.4.2-5. Optics of IIR

4.4.3 Light detection and ranging (Lidar)

4.4.3.1 Purpose and outline

Images of the two-dimensional distribution of clouds are obtained using an infrared camera. The brightness temperature at the cloud top is obtained from the data collected using the infrared camera. Also, the altitude of the cloud top is obtained by estimating the temperature distribution in the altitude direction at the measurement position using an atmospheric model. The cloud distribution and the cloud-top altitude are important parameters for improving the reliability in estimating the energy of ultimate-energy particles from the air shower profile. However, the accuracy in determining the cloud-top altitude using images obtained with the infrared camera is around ± 500 m; thus, it is not possible to satisfy the required accuracy (temperature: ± 1.4 K, altitude: ± 200 m) using the data obtained using the infrared camera alone. The purpose of Lidar is to carry out ranging measurements at several positions in the visual field of the Japan (Japanese?) experiment module-extreme universe space observatory (JEM-EUSO) to determine the cloud-top altitude with high accuracy. The direct observation data of the cloud-top altitude obtained by Lidar serves as calibration data for the data obtained using the infrared camera. The ranging measurement resolution of Lidar is 30 m. From data obtained using both the infrared camera and Lidar, the three-dimensional cloud distribution and cloud-top altitude are determined.

The Lidar system of JEM-EUSO is composed of transmission and receiving systems. The

transmission system comprises a Nd:YAG laser and a pointing mechanism for the irradiation beam. The third harmonic ($\lambda = 355$ nm) of the Nd:YAG laser is used. The JEM-EUSO telescope itself is used for the receiving system of Lidar. Four photodetectors are placed on the focal plane to measure the backscattered light, so that there is a visual field in the laser irradiation direction from Lidar. Because the wavelength of the laser from Lidar is in the range of $\lambda = 330-400$ nm, which is the wavelength range of atmospheric fluorescence and Cherenkov light, the JEM-EUSO focal-plane detector (multianode photomultiplier tube (MAPMT)) can also be used as a photodetector.

4.4.3.2 Transmission device

The laser unit of the Lidar transmission system of JEM-EUSO is almost identical to the laser unit of the BepiColombo laser altimeter (BELA), which is planned to be mounted on a Mercury exploration satellite that is being developed by the European Space Agency (ESA)[3]. A German research group is in charge of the development of the laser unit. The launch of the BepiColombo satellite is planned for 2012, and the BELA laser unit is still in the development phase. The specifications required for the BELA laser unit are a pulse frequency of 20 Hz and a wavelength of 1064 nm. As a result of discussions with a developer and manufacturer of measurement devices used in space, it was confirmed that changing the pulse frequency from 20 Hz to 50 Hz or 100 Hz and the use of the third harmonic ($\lambda = 355$ nm) of the 1064 nm wavelength are possible. The Solid-State Optical Science Research Unit, lead by Dr. Wada of RIKEN, can realize a laser that satisfies the above requirements. The Lidar transmission system is mounted on the JEM-EUSO telescope. The beam is diffused with approximately the level of spatial resolution of the JEM-EUSO telescope used as the receiving system. The control of the irradiation direction of the laser is carried out by means of the beam pointing mechanism, for which two possibilities are considered, i.e., 1) 2-4 laser beams fixed in different directions with each beam irradiated according to a corresponding program, and 2) a micro electro-mechanical system (MEMS) mirror developed by a research group of Ewha Womans University (Korea).

The specifications of the laser system are summarized in Table 4.4.3-1. We will explain the outline of the laser system developed by RIKEN to satisfy the specifications in the table. For the excitation module, a laser rod is placed at the center, around which host crystals not doped with fluorescent ions are fused in a triangular shape to protect the main laser rod. This technique is achieved using ceramic crystalline technology developed in Japan. Furthermore, we adopt a method in which the laser rod is excited using laser diodes, which are placed at the vertices of the triangle of host crystals. For cooling, direct conduction cooling in the metal, without the use of a solvent, is planned. For the resonator, a U-shaped laser resonator with a pair of prisms is used so that the resonator is robust to vibration and torsion. Figure 4.4.3-1 shows the cross section of the excitation module of the laser system. Figure 4.4.3-2 shows the arrangement of the resonator optics.

Table 4.4.3-1. Specification of JEM-EUSO Lidar

Wavelength	355 nm
Repetition rate	50 Hz
Pulse width	5 - 15 ns
Pulse energy	20 mJ/pulse
Beam divergence	0.1 mrad
Bandwidth of filter and transmittance	3 nm / 50 %

Telescope for detection	JEM-EUSO
Detector	MAPMT (JEM-EUSO)
Range resolution	30 m
Steering of output beam	$\pm 15^\circ$ to a vertical axis (TBD)
Exposure time	0.01 sec/shot
Integration time	0.1 sec (= 5 shots)
Mass	17 kg
Dimension*	450x350x250 mm
Power	< 70 W

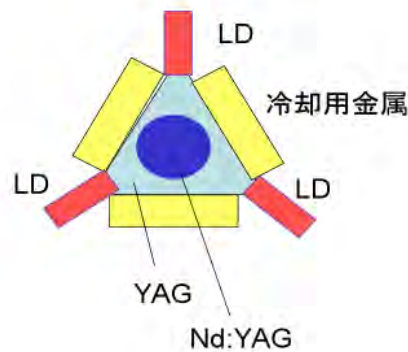


Fig. 4.4.3-1. Pump module(cross section)

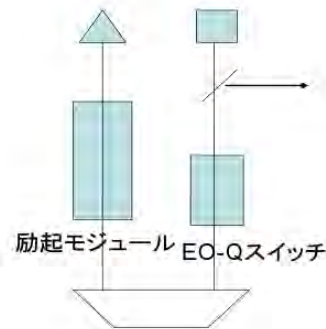


Fig. 4.4.3-2. Cavity configuration

By June 2008 we had succeeded in obtaining an output of 200 mJ/pulse using the excitation module alone by pseudo-CW excitation from three directions with water cooling. Furthermore, frequencies of up to 400 Hz were obtained by a repeated output of 100 mJ/pulse with 20 nm wavelength using a resonator having an electro-optical Q (EOQ) switch, and the basic specifications required for the atmospheric monitoring system were obtained at a fundamental wave of 1064 nm in the laboratory. By the wavelength conversion of this fundamental wave, the third harmonic ($\lambda = 355$ nm) was generated. Under the current conditions, an output of approximately 30 mJ/pulse can be obtained using lithium triborate (LBO) crystals.

Figure 4.4.3-3 shows the expected mounting location of the laser oscillator. It is planned to be fixed using screws on an aluminum fringe that protrudes from a surface perpendicular to the observation direction. Heat is planned to be radiated from this contact surface; thus, rubber with high thermal conductivity is placed between the laser oscillator and the aluminum fringe.

The laser system is driven by a power source of dc 28 V supplied from the main system. The power source and electrical components for controlling the laser, such as the pulse light control circuit, are placed between the main laser system and the laser oscillator for pulse operation. The specifications of the control signal and the control method are currently under consideration.

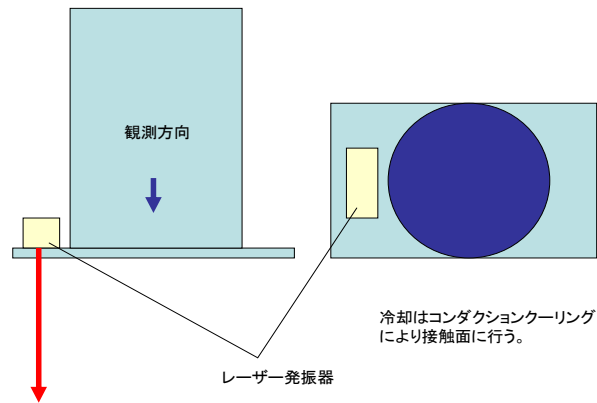


Fig. 4.4.3-3 Accommodation of the Lidar

Two steering methods for the laser beam used in Lidar are currently being examined. The progress of the development of the MEMSs, which is one candidate, is described below.

Figure 4.4.3-4 shows the structure of the MEMS under development. Using the electrostatic force generated at the comblike sections on the outer actuator side and mirror operating side, rotations around the X-Y axes and the axis perpendicular to the X-Y axes are induced. This method has already been tested in an actual space environment. Currently, the steering angle is set at $\pm 6^\circ$ and the mirror system is composed of 8 pixel x 8 pixel, 3 mm x 3 mm mirrors, realizing a fill factor of 90%.

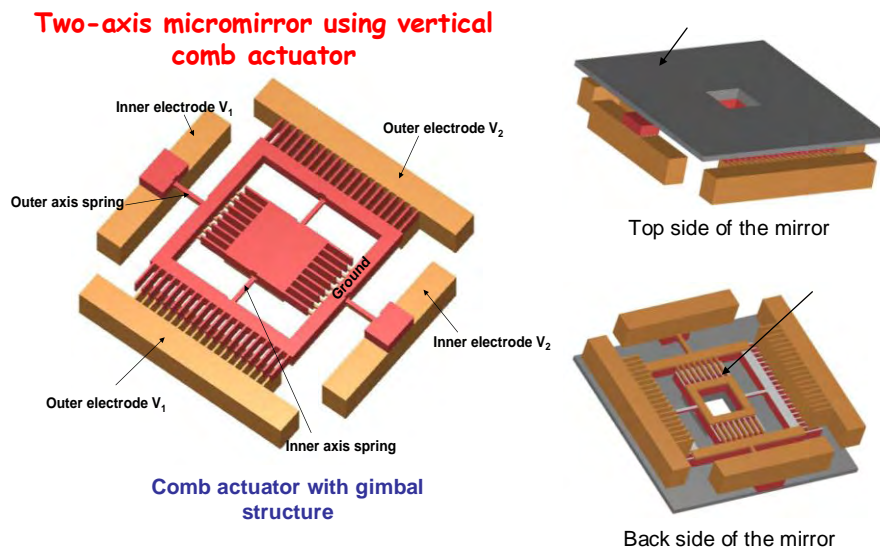


Fig. 4.4.3-4 Basic structure of two-axis micro-mirror

4.4.3.3 Receiving device

The backscattered light of Lidar is expected to be detected by the photocounting method. A photomultiplier tube (PMT) with the specifications shown in Table 4.4.3-2 is expected to be used

as the photodetector. Note that a PMT, the specifications of which are equivalent to those of a multipixel-type MAPMT with high sensitivity in the near-ultraviolet range and used for JEM-EUSO, can also be used as the photodetector in Lidar.

4.4.3.4 Simulation

The JEM-EUSO telescope itself is used as the Lidar receiving system. Therefore, a laser beam with a wavelength of 355 nm, which is the third harmonic of the seed laser (1064 nm), is used for Lidar in order to minimize the changes that arise in the optical systems of the telescope and the focal-plane detector owing to the mounting of Lidar. The performance of Lidar was evaluated by simulation.

The variables and their values used in the simulation are summarized in Table 4.4.3-2. The variables associated with clouds and their values are summarized in Table 4.4.3-3. As the atmospheric model, US Standard Atmosphere 1976 was used.

Table 4.4.3-2. Subsystems specification assumed in the JEM-EUSO Lidar under specification simulation

Item	Value	
Transmitter	Wavelength [nm]	355
	Repetition rate [pulse/sec] Nominal mode, burst mode	10, 100
	Pulse energy [mJ]	10
	Beam divergence [mrad]	0.1
	Optical efficiency [%]	80
Receiver	Receiver aperture [cm]	210
	FOV (lidar detector pixel) [mrad]	0.25
	Band width of a filter FWHM [nm]	3
	Transmittance of a filter [%]	50
	Transmittance of optical system [%]	25
Detector	Quantum efficiency [%]	25
	Dark noise [counts per sec]	500
Aquisition	Range resolution [m]	30
	Injection time	1
ISS	altitude [km]	500

Table 4.4.3-3. Optical parameters of the clouds used for simulation. SR (Scattering Ratio) and O.D.(Optical Depth) are defined at 532nm.

	SR peak altitude [m]	Width of altitude [m]	SR at the peak altitude	Ext-to-backsc Ratio*) [sr]	Angsr. exp	O.D.
Opaque	3000	1500	500	20	0	6.28

Subvisible (cirrus)	9000	1000	10	22	0	$5.12 \cdot 10^{-2}$
---------------------	------	------	----	----	---	----------------------

Figures 4.4.3-5 and 4.4.3-6 show the simulation results. The results for one laser shot and 100 integrated laser shots are shown in Figs. 4.4.3-5 and 4.4.3-6, respectively. The abscissa indicates the altitude and the ordinate indicates the scattering ratio (SR) of the clouds and the signal-to-noise ratio (SNR). The SR in the two figures is obtained when the wavelength is 355 nm, and is different from that shown in Table 4.4.3-3. As shown in the figures, only opaque clouds are detectable using Lidar with the current specifications in the case of one shot, whereas subvisible clouds are detectable with SNR=9 in the case of 100 integrated shots.

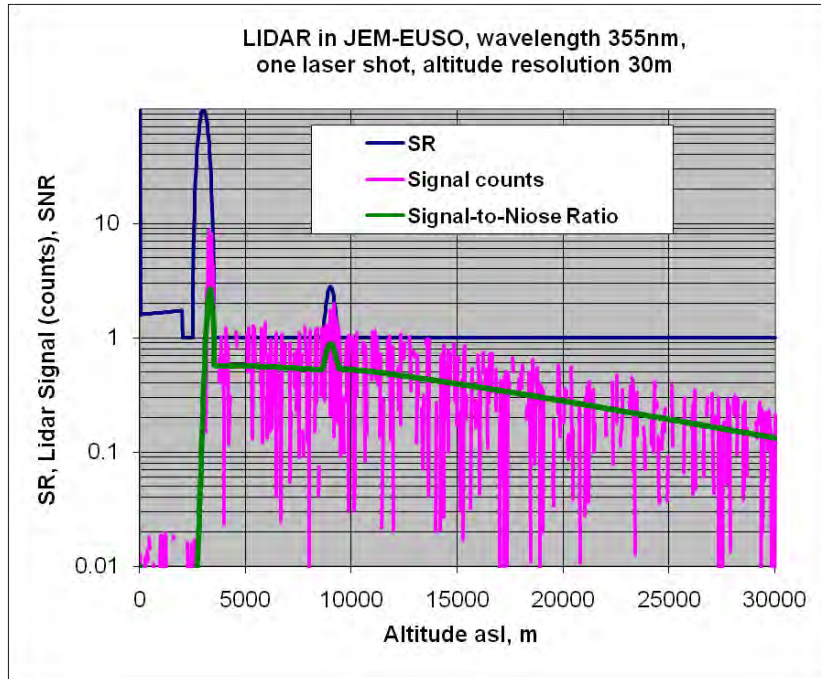


Fig. 4.4.3-5. Calculated signal counts and SNR for single shot measurement with Lidar.

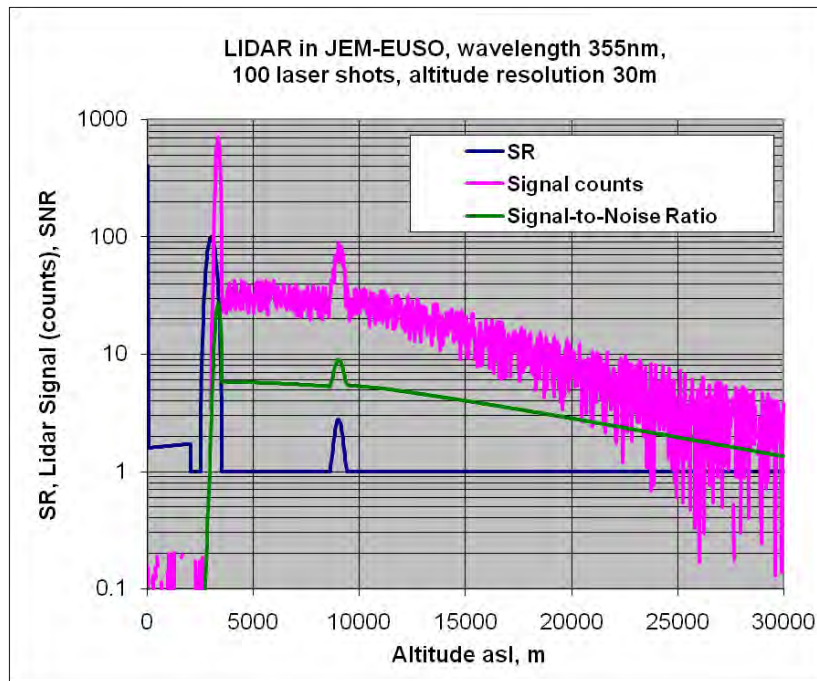


Fig. 4.4.3-6. Calculated signal counts and SNR for integration of 100 measurements with Lidar

4.4.4 Slow data

Among the focal-plane detectors of JEM-EUSO, two photodetector modules (PMDs) with functions to collect slow data, which are arranged parallel and orthogonal to the traveling direction of the International Space Station (ISS), are installed. Slow data are collected in the slow trigger mode (see 4.3.3.2.2). The purposes of collecting slow data are as follows.

- 1) Continuous observation of the background light intensity. The altitude of the cloud top is estimated by analyzing a stereo image of the observed data.
- 2) Observation of airglow and meteors.

The photoelectron signals from MAPMT are converted into digital signals using an application-specific integrated circuit (ASIC). Then, the digital signals are counted at an interval of 2.5 μ s for the purpose of observing the extensive air shower (EAS) using a counter. Along with this observation, counts for a 40 μ s time band are continuously recorded at an interval of 3.5 s. The obtained slow data are input to the two parallel PMDs, and each PMD continuously observes the background near-ultraviolet light. Because the two PMDs observe two discrete spaces that are spatially distant, the altitude of the cloud top can be estimated by analyzing the stereo image [4,5].

The emission of the Herzerg I band of oxygen molecules at an altitude of approximately 95 km, the boundary between the mesosphere and the thermosphere, is prominent in night airglow in the wavelength band of 330-400 nm. It is considered that this emission has a stripe structure with a stripe width of approximately 20-300 km in correlation with the atmospheric gravitational wave, and that the observation of such a structure in detail will be possible by examining the slow data obtained by JEM-EUSO.

4.4.4.1 Specifications required for field programmable gate array (FPGA) of the counter

Ultraviolet light reflected by clouds and incident on the MAPMT is intermittently collected at an interval of 3.5 s with a gate time of 20 μ s. The amount of background light incident on the

MAPMT is estimated to be 1 p.e./2.5 μ s. Therefore, for the integration time of 50 μ s, approximately 20 p.e. of light is expected. It is possible to set the gate time width via appropriate commands to the FPGA, so that the amount counted is within 8 bits, even when the lunar age and distribution of clouds change. The specifications required for the FPGA are summarized in Table 4.4.4-1.

Table 4.4.4-1 Required performance for the JEM-EUSO slow data

Wavelength	330-400nm
Resolution	0.1°
Detector	MAPMT
Count resolution	8 bit
Count integration time	50 μ s
Time interval for a detection	3.5 s

4.4.5 Operation

Each device used for atmospheric monitoring carries out observation while the ISS passes over the night side of the earth. Commands are transmitted from the earth station, and the operation sequences of the atmospheric monitoring devices that are orbiting the earth are programmed by the ISS. Each device carries out observation according to a defined sequence. The data collection is basically only carried out when the ISS is passing over the night side of the earth, however, these devices are turned on or off according to the following rules.

Infrared camera

The temperature of the uncooled bolometer arrays is controlled using a Peltier device. The sensors and cooling element are always turned on when the ISS passes over the day side. The collection of infrared image data is only carried out when the ISS passes over the night side.

Lidar

In order to maintain Lidar stability, the laser head is always turned on when the ISS passes over the day side as well as over the night side. Ranging measurements and data collection are only carried out when the ISS passes over the night side.

Slow data

The on/off switching during slow data collection conforms to the operation of the JEM-EUSO focal-plane detector.

4.4.6 Summary

4.4.6.1. Specification

Table 4.4.6-1. Requested specifications of IR camera for JEM-EUSO

Item	Value
Measurement temperature range	220 – 300 K
Wavelength	10 – 12 μ m
Visual field	60°
Spatial resolution	0.25 ° @ FOV center (= 4.4 mrad) 0.22 ° @ FOV edge (= 3.8 mrad)

Temperature resolution	3 K
Optical system	Geospatial system
Detector	microbolometer
Resolution	12 bit
Integrated time	33 msec / image (= Video frame rate)

Table 4.4.6-2. Specifications of Lidar (Japanese ver.)

Wavelength	355 nm
Repetition rate	50 Hz
Pulse width	5 - 15 ns
Energy	20 mJ/pulse
Beam divergence	0.1 mrad
Interference filter, FWHM	3 nm / 50 %
Telescope	JEM-EUSO
Detector	MAPMT (JEM-EUSO)
Range resolution	30 m
Output beam direction	$\pm 15^\circ$ to a vertical axis
Exposure time	0.01 sec/shot
Integration time	0.1 sec (= 5 shots)
Mass	17 kg
Dimension*	450x350x250 mm
Power	< 70 W (measurement)

Table 4.4.6-3. Specification of Lidar for one module (Germany ver.)
4-modules are used simultaneously

Item	Value
Wavelength of fundamental	1064 nm
Pulse energy	50 mJ
Pulse width	3 ns
Repetition rate	20 Hz
Optical efficiency	5.3%
Wavelength for Lidar	355 nm
Pulse energy	10 mJ
Beam divergence	0.1 mrad

Table 4.4.6-4. Specifications of Lidar with 4 laser modules (Germany ver.)

Item	Value
Wavelength	355 nm
Pulse energy	40 mJ
Repetition rate	80 Hz

Table 4.4.6-5. Slow data

Item	Value
Wavelength	330 – 400 nm
Spatial resolution	0.1°
Detector	MAPM
Count resolution	8 bit
Count integration time	50 μsec
Exposure time	3.5 sec

4.4.2.4. Budget

Table 4.4.6-6. Budget of the IR camera.

Item	Value
Mass	5 kg
Dimensions	130 x 250 x 250
Power	8 W

Table 4.4.6-7 Budget of the Lidar

Item	Germany ver.	Japanese ver.
Mass	30 kg	17 kg
Dimensions	Figs. 4.4.3-2, 4.4.3-3	450x350x250 mm (Fig 4.4.3-9)
Power	100 W (on), 20 W (off)	70 W (on), 35 W (off)

4.4.2.5. Cost

Table 4.4.6-8 shows cost for development of atmospheric monitor system including research and development cost. French researchers will organize budget and research group. Budget is estimated in the assumption which is that the development are performed in Japan.. For reference, budget for development of lidar by Japanese group also are listed.

Table 4.4.6-8 Cost

	FY2008	FY2009	FY2010	FY2011	FY2012	amount
IR Camera (French ver.)	10	400	300	100	70	880
Lidar (Germany ver.)	0	80	320	320	320	1040*
Lidar (Japanese ver.)	10	30	30	100	100	270

(unit 1 million yen)

※ Cost of Lidar in detail.

- Lidar transmission part(4units): 2,800 k€
- Control Electronics of four sets of laser: 1,600 k€

- Manufacturing and Test of the prototype : 1,600 k€
- Integration and verification : 900 k€

4.4.6.2. Schedule

Table 4.4.6-9 and Table 4.4.6-10 show schedules for the IR camera and the Lidar.

Table 4.4.6-9 Schedule for the IR camera development

	2008	2009	2010	2011	2012
Spec.	[Bar spanning 2008]				
Design	[Bar spanning 2008]				
PM manuf.	[Bar spanning 2008]				
PM test	[Bar spanning 2008]				
PFM manuf.	[Bar spanning 2008]				
PFM test	[Bar spanning 2008]				
Final test	[Bar spanning 2008]				

Table 4.4.6-10 Schedule for the Lidar development (Japanese ver.)

	2008	2009	2010	2011	2012
Basic experiment	[Bar spanning 2008]				
PM design	[Bar spanning 2008]				
PM making and test	[Bar spanning 2008]				
PEM design	[Bar spanning 2008]				
PEM making	[Bar spanning 2008]				
Test, improve, and final test	[Bar spanning 2008]				

4.4.6.3. Organization

Atmospheric Monitor Subsystem:

V. Mitev(Centre Suisse d'Electronique et de Microtechnique,Switzerland). Satoshi Wada (Riken)

4.4.6.4. References:

- [1] Takahashi,Y. Et al., *29 Int. Cosmic ray Conf.*, 2005, **8**, 351; EUSO-PI-REP-005(Section D), D36-D38, 21 Apr. 2004.
- [2] EUSO Phase-A Document: Section-D/ D-10
- [3] BepiColombo, http://esa.int/esaSC/120391_index_0_m.html
- [4] Zong, J. et al., *Photogrammetric engineering & remote sensing*, 2002, **68**, 821.
- [5] Hasler, A.F. et al., *Journal of Applied Meteorology*, 1991, **30**, 257.

4.5. Calibration subsystem

4.5.1. Definition

The calibration system is apparatuses that measure the efficiencies of the optics, the focal surface detector and the data acquisition electronics with a necessary precision to determine the energies and the arrival directions of extremely high-energy cosmic rays.

4.5.2. Outline of the calibration system

A cosmic ray produces a shower of particles in the atmosphere, and only the billions of produced electrons are of interest here. The number of electrons produced locally depends strongly on the local density. That density cannot be measured directly, only the altitude above ground of that local production. The transformation of altitude in density relies on models, themselves based on prior observations with specialized instruments like balloons equipped with manometers and thermometers. Indeed, altitude to density is well known, and knowing if it is winter or summer is generally enough. The accuracy is a few percent.

These electrons ionize the air nitrogen and produce photons in a few bands from 300 to 430 nm. This transformation is called the N₂ fluorescence yield. It is known with a 5% accuracy at 1 bar, 20°C and no pollutants. It is known to 10 – 15% at lower pressures. The JEM-EUSO collaboration will measure in a laboratory this fluorescence yield with unprecedented accuracy from 0.1 to 1 bar, -50°C to +30°C, and with different pollutants like water and methane. The emission of the produced photons is isotropic. The shower electrons produce also Cerenkov light, along a cone whose axis is the shower development axis. This light will splash on the ground, and a certain fraction of it (5 to 10%) goes back isotropically. Some N₂ and Cerenkov photons will reach JEM-EUSO instrument and will be detected by the Focal Surface (FS).

The energy of a cosmic ray is essentially proportional to the amount of detected light. In order to determine the maximum in the EAS development, it is required to determine the emitted amount of light accurately. Therefore it is necessary to know attenuation and conversion factors between the source and the detector.

The detected number of photoelectrons (ΔS) from the light source (intensity ΔQ) at distance r is expressed by the following equation:

$$\Delta S = \frac{\varepsilon \kappa \eta g T_l T_f T_e T_a A}{4\pi r^2} \Delta Q$$

where ε is the quantum efficiency of the detector, η is the collection efficiency of the detector, g is the relative variation of the detector gain, κ is the fraction of light which reaches the designed pixel, T_l is the throughput of the Fresnel lens system, T_f is the transmittance of the optical filter, T_e is the trigger efficiency (count loss), T_a is the transmittance of the atmosphere, A is the entrance pupil area of the telescope and r is the distance to the light source. The terms ε , η , κ , g , T_f , T_e and T_l are related to the instrument and are determined from the efficiency measurements of the Fresnel lenses, the optical filter, the focal surface detectors, and the trigger electronics. The amount of detected light is affected by the atmosphere (T_a), so that characterization of the atmosphere is necessary. Since onboard measurements of the atmosphere are described in the section of Atmospheric monitor, only the atmospheric monitor on ground is described in this section.

Fresnel lenses have a certain transmittance, measured before launch (this is an efficiency measurement). This transmittance can deteriorate, so that the variations have to be measured in order to take them into account during the analysis of the events. This will be accomplished by sending a light through them up to the FS. This light will be absolutely determined by taking a known percentage of the emitted photons towards a NIST photodiode, accurate to 1.5%.

The FS transforms the photons falling on it into pulses. Each photon gives a pulse, representing one photoelectron (p.e.), at a focal surface (FS) detector with a certain probability. This is a typical

efficiency (product of quantum efficiency of the photocathode by the collection efficiency to collect the emitted pe on the first dynode). Typical values are 30 - 35% and the efficiency will be measured with accuracy of better than 2% on ground. Each of the 200,000 pixels has their own efficiency, to be measured independently and 600,000 if 3 colors are used. This efficiency naturally, takes into account the filter (or filters) glued to the silica holding the photocathode effects.

During the launch and the flight, transmittance of lenses and filters and the efficiency of detectors can deteriorate by vibrations of the PMT, radiations on the filter(s), too strong illumination, change of gain, etc. This efficiency must be measured regularly during the flight and it must be made with light going directly from the light source to the FS, without any obstacle in between because, as seen earlier, to determine the lenses efficiencies, the FS efficiencies are used. So, first the FS efficiencies have to be measured, then, the lenses ones.

The variations of the parameters are estimated from the experiments with acceleration in time so far carried. The degradation of ε , η , κ , g , T_b , T_f will be less than 5-10% during the 5 year operation. The error in the reconstructed height of the light source by 10km varies as $1/r^2$ and affects on r by only 5%, because JEM-EUSO observes EASs from high altitude, 400km. κ and g may change by less than a few % due to the variation of the surrounding temperature. In addition to those, status monitor of each detector and electronics is necessary.

Absolute efficiency measurement should be completed on ground because onboard resources are limited. Only relative variation of the detector gain and efficiency, and the transmittance of the optics with time will be measured on board. If the variation of MAPMT gain is detected and not very big, it can be adapted by the change of the supplied high voltage and the trigger threshold in the front-end electronics, regularly. Bad detectors can be shut off completely if necessary. In the present baseline, onboard calibration is relative one, but observing the moonlight was evaluated as a possible absolute method.

The calibration method in flight is summarized in Table 4.5.1 and the detail is described in the following sections.

Table 4.5.1 Comparison of calibration methods.

Comma means that each term before and after the comma is determined independently.

Method	Observables (product)	Comments
LED (on FS)	$\varepsilon\eta g T_l^2 T_f T_m, T_e$	T_m : reflectivity of the lid T_e will be determined from the linearity check with light intensity.
LED (behind the lens)	$\varepsilon\eta g T_f, T_e$	T_e will be determined from the linearity check.
Night background	sky $\varepsilon\eta g T_l T_f T_e T_\alpha$	This is available during the science observation.
Moonlight	$\varepsilon\eta g T_l T_f T_e T_\alpha$	Candidate of a absolute calibration source.
YAP	$\varepsilon\eta g$	The pixel with a YAP pulsar is used as a standard pixel to ensure the calibration accuracy by LED light sources.
Ground flasher	$\varepsilon\eta g T_l T_f T_e T_\alpha, \kappa$	GLS can be deployed at many places because they are relatively less expensive. Multi-wavelength is available by band pass filters.

Airborne flasher	$\varepsilon\eta gT_l T_f T_e, \kappa$	The effect of atmospheric transmittance can be neglected, but the calibration cannot be done frequently.
Ground LIDAR	$\varepsilon\eta gT_l T_f T_e T_a, \kappa, r$	The transmittance of the atmosphere will be obtained as a function of height. It can be used as an artificial EAS to study the accuracy of the event reconstruction.

The instrument calibration will be described in the following sections for four categories.

- Pre-flight calibration
- On-board calibration
- Calibration in flight with on-ground instruments
- Atmospheric monitor

4.5.3. Pre-flight calibration

4.5.3.1. Calibration of PMT

In this stage, MAPMTs are selected to satisfy the requirements and are sorted into several groups with the parameter of gain.

Photon detection efficiency (=quantum efficiency \times collection efficiency), uniformity of sensitivity, gain, cross-talks are measured for each MAPMT with the optical filter. MAPMTs with similar gain will be used together for a PDM. The response to the various intensity of light and supplied voltage is studied and the database of MAPMT characteristics will be made. The measurement accuracy will be less than 5%.

4.5.3.1.1. Absolute efficiency measurement

One PMT per 10 PMTs is defined as a standard one, whose absolute efficiency is measured. This method was used for the absolute efficiency measurement of the PMTs for the photon yield measurement[5]. As shown in Fig.4.5.1, UV LED light (at wavelengths of 340nm, 360nm and 385nm) is diffused in an integrating sphere. The variation of light intensity is monitored with a photo-diode, precisely calibrated at the National Institute of Standards and Technology (NIST, USA), during the PMT measurement. This method gives an absolute efficiency with a good accuracy. In order to obtain accuracy better than 1%, a faint light is required where the number of two p.e.s per pulse is less than 1%. The first integrating sphere has a role of splitter. The two spheres attenuate the light significantly by one millionth, so that a photo-diode and a PMT, which have quite different gains, can see the light simultaneously. The ratio of light intensity between at the point where the PMT is attached and where the photo-diode is attached is measured in advance.

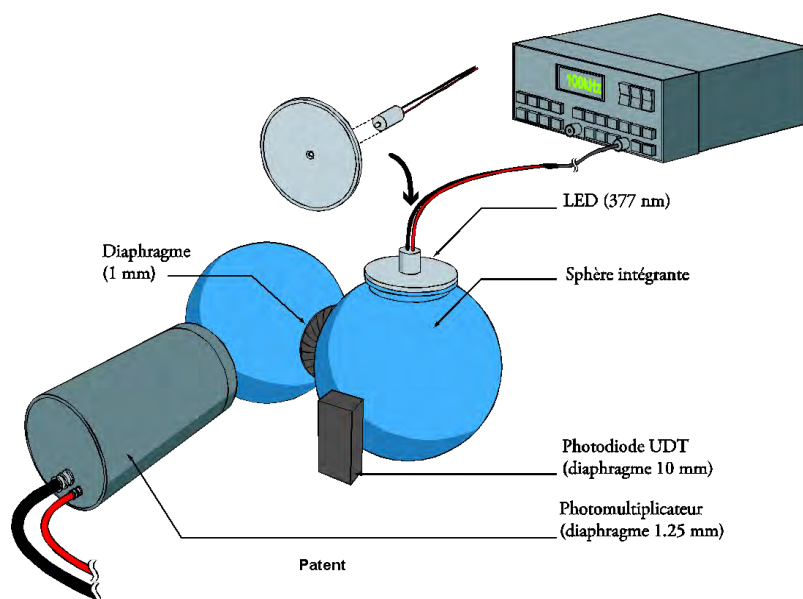


Fig. 4.5.1

Schematic figure of the absolute calibration system. UV light is diffused in an integrating sphere and detected simultaneously by a PMT to be calibrated and a photo-diode precisely calibrated at NIST to obtain the PMT absolute efficiency precisely.[5]

The measurement of PMT consists of two parts: One is taking single p.e. spectrum in order to check the lost counts below the discrimination level. The other is done with a discriminator, and the number of coincident signals between the discriminator output and the LED pulser is counted. Taking single p.e. spectrum takes longer time because of the dead time of ADC, but counting can run faster (about 100 times) and then the efficiency measurement with good statistics can be done in a short time. This method gives an accuracy of the calibration by less than ~2% [5]. The advantage of this method is independence of the light intensity and the emission pattern of the source (LED).

The apparatus for the absolute efficiency measurement has been already built for JEM-EUSO. Preliminary result about photon detection efficiency of an ultra-bialkali MAPMT was about 32% with reproducibility less than 1%, which is consistent with the previous measurement with relative systematic error of 15%. The measurement accuracy would be less than 2% even if taking into account the accuracy of the photo-diode. Spectroscopic absolute efficiency will be taken for some PMTs in the range between 300nm and 450nm with a Xenon lamp and a spectroscope.

4.5.3.1.2. Relative efficiency measurement for all the PMTs

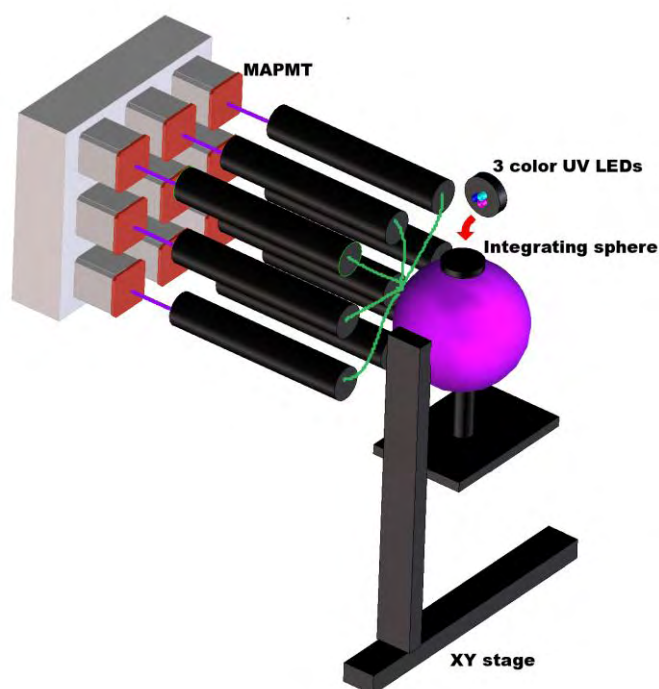


Fig. 4.5.2

Schematic figure of the PMT characterization system. Light from 3 color LEDs is diffused in an integrating sphere, and divided so that single photoelectron spectra for 9 PMTs can be taken simultaneously. The light source with the sphere can move on a XY stage so that 2 dimensional distribution of photo-cathode sensitivity can be taken. The variation of the light intensity is monitored with a photo-diode attached to the sphere during the measurement.

As shown in Fig. 4.5.2, UV light from LEDs (Wavelengths are 340nm, 360nm and 385nm) is attenuated and collimated to make a faint UV beam with a point spread function of ~ 0.1 mm. Light from 3 color LEDs is diffused in an integrating sphere, and divided by optical fibers and collimated so that single photoelectron spectra for 9 PMTs can be taken simultaneously. The light source with the sphere can move on a XY stage so that 2 dimensional distribution of photo-cathode sensitivity can be taken. The variation of the light intensity is monitored with a photo-diode attached to the sphere during the measurement. At present, a collimated UV LED light at 370nm is used to characterize MAPMTs to be used for JEM-EUSO one by one. This characterization system will be extended to measure the efficiency of ~ 10 PMTs in parallel (Fig.4.5.2).

The basic measurement is taking single photoelectron spectra of each pixel with faint UV light from LEDs at the three wavelengths. Linearity to light intensity and the gain variation with supplied voltage are taken for five kinds of conditions, respectively. Then 2 dimensional distribution of photocathode efficiency is taken with 1mm step. If 10 PMTs are measured simultaneously, about 1 year is necessary to finish the characterization of 10,000 PMTs estimated from the current measurements,. The absolute efficiency of all the PMTs will be determined if a PMT with known absolute efficiency is used as a reference in each measurement.

4.5.3.2. Calibration of PDM

After the selection and grouping, the MAPMTs are assembled as PDMs with electronics. First, it is confirmed whether the expected number of photoelectrons corresponding to the intensity of light is counted using the apparatus described in the previous section. Next, the PDM will be installed in vacuum as a simulated space environment to check the stability of the gain. The temperature of the voltage divider circuit will be monitored during the stability check.

In order to study the response of PMTs at various positions on the focal surface, PDMs are illuminated with the angle distribution of light determined from the optics simulation. Thirdly, uniformity of photon detection efficiency, gain and count are checked with a realistic JEM-EUSO optics and parallel collimated UV light. For the calibration including the second and the third trigger circuits, emulated EAS images with a LED array light source are illuminated with a parabolic mirror or optical fibers. One of the candidate light source for the calibration with a real optics is a UV LASER light reflected by a rotating mirror to make a moving bright point on FS like an EAS image.

4.5.3.3. Calibration of the telescope

We assemble the JEM-EUSO flight model and make a final calibration table of effective transmittance of the lenses, focal surface image, photon detection efficiency and gain of the detector, gain of the electronics circuit and cross talks with a collimated and parallel UV light. One of the candidate light sources is the combination of UV LASER and a mirror like for the PDM calibration.

4.5.4. Calibration in flight

The major features for the on-board calibration systems are listed below.

- Spectro-radiometry in the range 330nm-400nm
- Appropriate light intensity for photon counting
- Background $<10^4$ photons/(pixel s)
- Light weight
- Low power consumption
- No movable components
- Monitoring function of the light intensity
- Structure and size to fit the JEM-EUSO telescope
- Uncertainty of the absolute intensity $< 10\%$ (TBC)

In addition to the above features, the following conditions are required.

- The light source works stably during the JEM-EUSO operation
- Non-uniformity of the intensity $<20\%$ (TBC). (Uniformity is calibrated on ground before the launch.)

4.5.4.1. Efficiency measurement of the focal surface with LED light sources [2] [6]

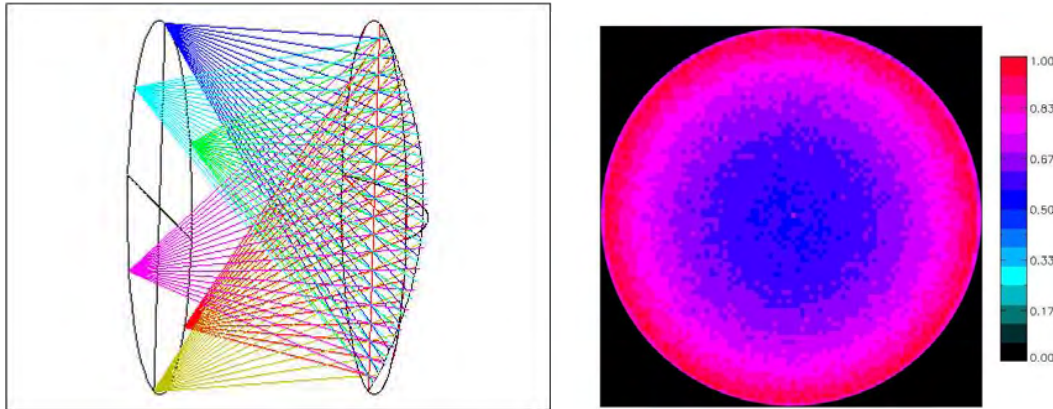


Fig.4.5.3

Raytrace simulation when light sources are placed along the edge of the lens facing on the focal surface (left) and the intensity distribution at FS (right).

4.5.4.1.1. Optical design

Several light sources are set on the support of the last lens before the focal surface and illuminate the focal surface. The light source should be small enough to create no obstruction. Fig.4.5.3 shows the intensity distribution on the focal surface calculated by a raytrace simulation. The intensity is uniform within a factor of two. This uniformity is enough to observe single photoelectrons. The intensity of each light source is adjusted so that the number of photoelectrons per pulse is few enough (The probability of more than one p.e. is less than 2%). In order to obtain enough intensity on the focal surface (5×10^9 photons/s, 1 second exposure is assumed) with a single light source, the power should be larger than 10^{15} photons/s.

4.5.4.1.2. Light source

Two or three kinds of LEDs with wavelength 340nm, 360nm and 385nm, which have similar wavelengths of major fluorescence lines from Nitrogen, are used for the diffused light source. For redundancy, 2 pieces for each wavelength are used for one light source. Those LEDs have a light power of ~ 1 mW, so that they satisfy the requirement in the previous section. The pinhole diameter and the LED-pinhole distance can be adjusted to define the emission solid angle and the photon flux diffused by a Teflon sheet (Fig.4.5.4). The stability of the light source is monitored by a photo-diode precisely calibrated at NIST. Instead of the Teflon sheet, an integrating sphere with 30mm in diameter may be used as a diffuser. The emission angle distribution from an integrating sphere follows $\cos\theta$ law, ideally and the intensity monitor by a photo-diode is easier.

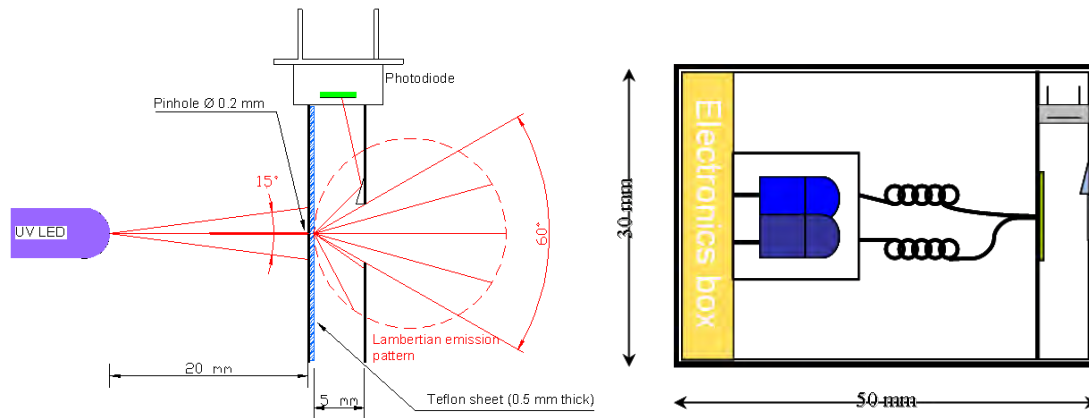


Fig. 4.5.4 Schematic figure of the LED light source for the on-board calibration.

The light from LED is diffused by a Teflon sheet to illuminate large area, and a part of light is monitored by a photo-diode precisely calibrated at NIST. Three color LEDs are used in the range of 300nm-400nm. [2]

Since LEDs are semiconductor devices, it is necessary to study the radiation hardness. GaN based materials such as GaN, InGaN are used for UV or blue LEDs. Blue LEDs with GaN based materials are reported to be radiation hard up to 10^{13} protons/cm²[3]. We irradiated 70MeV protons to candidate UV LEDs with wavelengths of 340nm, 360nm and 385nm by up to 2×10^{11} protons/cm², which is more than the expected irradiation (1.6×10^{11} protons/cm²) if JEM-EUSO is assumed to fly in the South Atlantic Anomaly (SAA) for 5 years all the time, and found no significant decrease in intensity. Generally, GaN based LEDs are radiation harder than GaAs based ones. Therefore GaN based LEDs will work in the JEM-EUSO environment. The photo-diode will be shielded with 4mm-thick aluminum to protect from irradiation effects.

4.5.4.1.3. Calibration of the detector and the electronics

Each channel of front-end electronics will be calibrated with the LED light sources or with night sky background. Cosmic rays are observed with the resolution that single photoelectrons can be discriminated with. For the calibration purpose, single photoelectron spectra will be taken with higher resolution. In order to reduce the amount of data, this measurement will be done once a week or a month. Status of the detectors and the electronics will be monitored with simplified procedure several times per day. It will be checked whether each detector and electronics work with night sky background during the observation or the LED light source during the day. The average and the variance of the count for each channel are monitored every orbit.

4.5.4.2. Efficiency measurement of the lenses with a LED light source

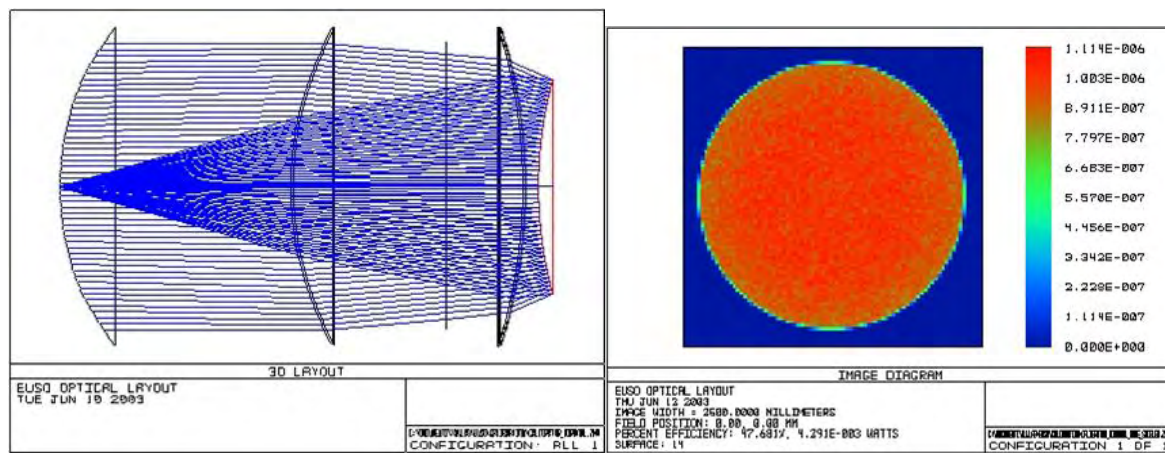


Fig.4.5.5 Raytrace simulation when a LED light source is settled at the center of the focal surface and the light is reflected at the rear side of the lid (left). The expected intensity distribution is shown in the right figure[2].

4.5.4.2.1. Optical design

A light source is settled at the center of the focal surface as shown in Fig.4.5.5. The light passing through the lenses is reflected by a diffused reflector on the rear of the lid and is detected by the focal surface detectors. Using the FS efficiency previously measured, the lens efficiency is determined.

4.5.4.2.2. Light source

Essentially the same box as that used for the measurement of the FS efficiency, diffused light source with LEDs at 340nm, 360nm and 385nm, is adopted.

4.5.4.3. Natural light source (Night sky background)

The balloon and Russian satellite experiments show that, outside of illuminated cities, the background of stars reflected on earth is constant with a precision better than the desired resolution expected for the shower energy determination. Hence, that background can be used while data taking, outside of the showers. The SLOW-MODE is another way to look at that.

4.5.4.4. Man made sources on ground

Light sources are deployed on ground for the atmospheric monitor and their light is observed by JEM-EUSO to obtain the attenuation factor of UV light in the atmosphere. As a light source, flasher and LIDAR are considered. Flasher is relatively less expensive, so that it is deployable at many places on ground. Wavelength dependence of the attenuation can be obtained by using band pass filters. The wavelength of on-ground LIDAR is 355nm, the third harmonic of YAG:Nd. The atmospheric transparency can be studied as a function of height by detecting back-scattered light of LIDAR. Systematic errors in the energy and the arrival direction determination of JEM-EUSO can be evaluated experimentally by reconstructing LIDAR events as simulated EASs.

4.5.4.4.1. Flashers[2][4]

Ground flashers work as “standard candles” placed around all over the world during the

JEM-EUSO mission. The flasher consists of high intensity Xe lamps in short microsecond flashes. There will be 20 ground-based units deployed at host stations in different geographical locations (Table 4.5.2) to cover various atmospheric conditions and 1 airborne unit. ISS will fly over one flasher in average every night. The airborne unit is to be installed on an upward directed portal of a P3B research aircraft stationed at NASA Wallops Flight Facility. It flies under the orbit of ISS at the altitude of 1-6 km above both land and sea every month during the JEM-EUSO mission. Xe lamps are used as a light source. The Hamamatsu flash lamp L6404 has an light intensity of 2J per flash. The expected signal detected by JEM-EUSO is about 500 photoelectrons for clear nights (Fig.4.5.7). The maximum flash-to-flash variation for this lamp is ~3% and the spatially non-uniformity is less than 5% over a 60° field of view. The duration of over-flights range from 5 to 70 seconds, so that typically 100 flashes per over-flight will be observed by JEM-EUSO. Atmospheric transmittance will be determined with a few percent accuracy by repeating measurements.

Table 4.5.2 Candidate deployment sites of ground flashers

Place	Latitude	Altitude
Haleakala, HI	20°N	3.0km
Climax, CO.	39 °N	3.5km
Mt. Washington, NH	44 °N	1.9km
Jungfrauoch, Switzerland	47 °N	3.5km
Mt. Norikura, Japan	36 °N	2.8km
Mt. Hermon, Israel	33 °N	2.0km
Chacaltaya, Bolivia	16 °S	5.3km
Alma-Ata, Kazakhstan	43 °N	3.0km
Mexico City, Mexico	19 °N	2.3km
Kwajalan Atoll, USA	11 °N	0.0km

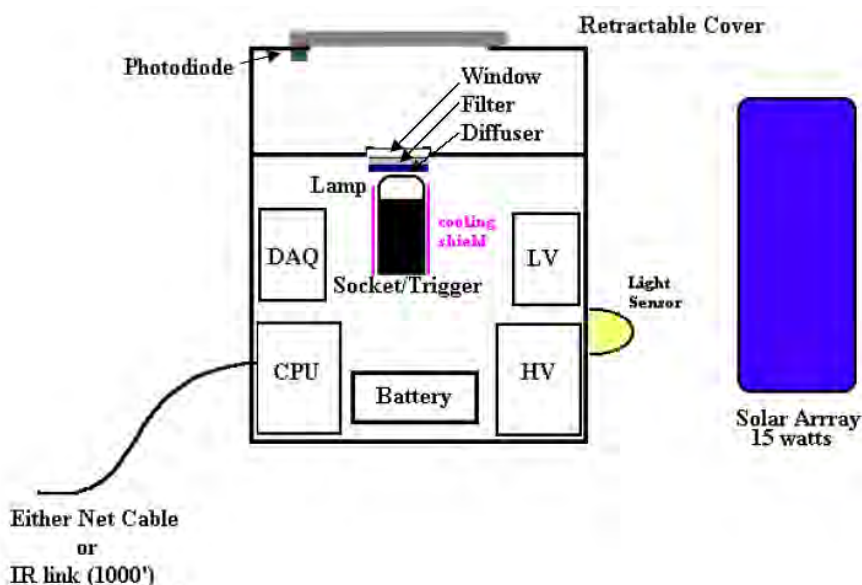


Fig.4.5.6 Schematic figure of an on-ground Xe flasher station [2].

As shown in Fig.4.5.6, one ground flasher consists of 4 lamps with band pass filters at 337nm, 357nm and 391nm, which corresponds to the wavelength of main N₂ fluorescence lines, and one broad band filter similar to that on JEM-EUSO. The intensity of the lamps is monitored by a photodiode precisely calibrated at NIST.

These lamps will be controlled by way of the Internet and flash at ~30Hz when JEM-EUSO flies over the station. The image of a ground flasher moves at ~0.03°/0.03s. If a light source passes through at the center of the FoV, about 2000 flashes will be observed by JEM-EUSO and the atmospheric attenuation will be well determined.

If the onboard LIDAR shoot at a ground light source, height dependence of the attenuation will be obtained. The accuracy and the systematic error of the onboard LIDAR will be estimated by comparing the data from the onboard LIDAR and from the ground flasher.

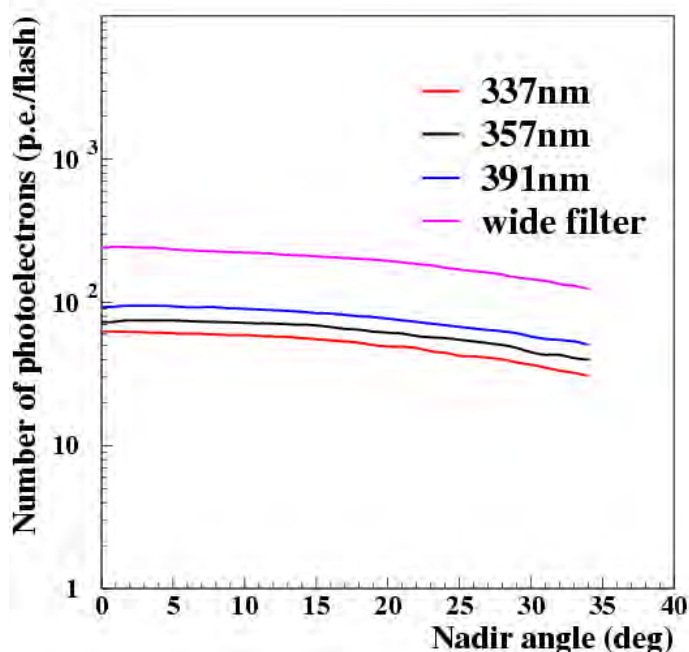


Fig.4.5.7 Number of photoelectrons detected by JEM-EUSO from a flash of a ground Xe flasher. The number of detected photoelectrons is shown as a function of the nadir angle of JEM-EUSO. Only the attenuation of Rayleigh scattering is taken into consideration in clear night condition. If Mie scattering is included, the intensity will decrease by a few 10% [2].

In order to use the ground flasher as a light source for absolute calibration, the factor of the attenuation in the atmosphere should be subtracted from the observation results. The transmittance of the atmosphere will be determined with LIDAR or observation of standard stars like Vega in U band at the ground flasher stations. Averaging the intensity for appropriate time will reduce the effect of flickering stars.

When the lenses deteriorate (vibrations, radiations, dust, etc.) not only the transmittance will decrease, but also the PSF should increase (slight change of index, of dispersion, of shape of the Fresnel grooves...). Then a light source position on earth will look bigger on the FS, with two results: less light per pixel and blurred image cause less accurate determination of EAS directions. The other is the slight raise of threshold for the showers. Since the ground flashers are point

sources for JEM-EUSO, focusing quality of the optics can be checked. The increase of focal image is taken into account for the simulation and the data analysis.

4.5.4.4.2. Ground LIDAR[2]

Since we can emulate EASs with the third harmonic of NdYAG LASER (355nm), ground LIDARs may be an effective tool for calibration. In order to emulate the EAS of 3×10^{20} eV with an elevation angle of $\sim 20^\circ$, we need the output of 50mJ at least. Once the power and the elevation angle of the LASER, we can determine the size of the receiver (~ 1 m in diameter). The signals back-scattered at 30km and 60km are about 800 photoelectrons and 20 photoelectrons / $2.5 \mu\text{s}$. If we shoot 100 times, for example, more than 1000 photoelectrons will be observed and the atmospheric properties are determined well (Fig.4.5.8). We can measure the transparency with an accuracy of 5-10% after ~ 100 shots.

As a ground light source the shot in the elevation angle of $20-30^\circ$ is optimum and probably the fixed directional LASER may be robust and minimize the maintenance of the mechanical parts of the system. The LASER can be tunable up to 10-30Hz. In these horizontal shot, the LASER beam reaches the top of the atmosphere after traveling ~ 30 km, where the Rayleigh scattering is dominant. The beam travels in pure molecular region for another 30km and we can get the boundary condition for the LIDAR equation, because we can know the ratio of the back-scattered intensity to the beam intensity in the pure molecular region. Then we can solve the LIDAR equation to obtain the transmittance of the atmosphere as a function of height.

The LASER beam with an elevation angle of 20° can be seen as a track of 30-50km long from JEM-EUSO. If the scattering is dominated by the Rayleigh process, the number of photons at the entrance of JEM-EUSO can be calculated. The scattering angles of photons that JEM-EUSO will receive are always larger than 40° . In such large scattering angles, Rayleigh process usually dominates under good weather condition. We will use photons scattered above 3km where the scattering is better described only by the Rayleigh process. Simultaneous operation of the on-board LIDAR system and the ground LIDAR system gives us more detailed information about the atmosphere and more redundant measurements. It will also reduce the systematic error in the measurement significantly.

The systematic errors and the resolutions of arrival direction and energy determination determinations by JEM-EUSO can be evaluated experimentally by reconstructing LIDAR events.

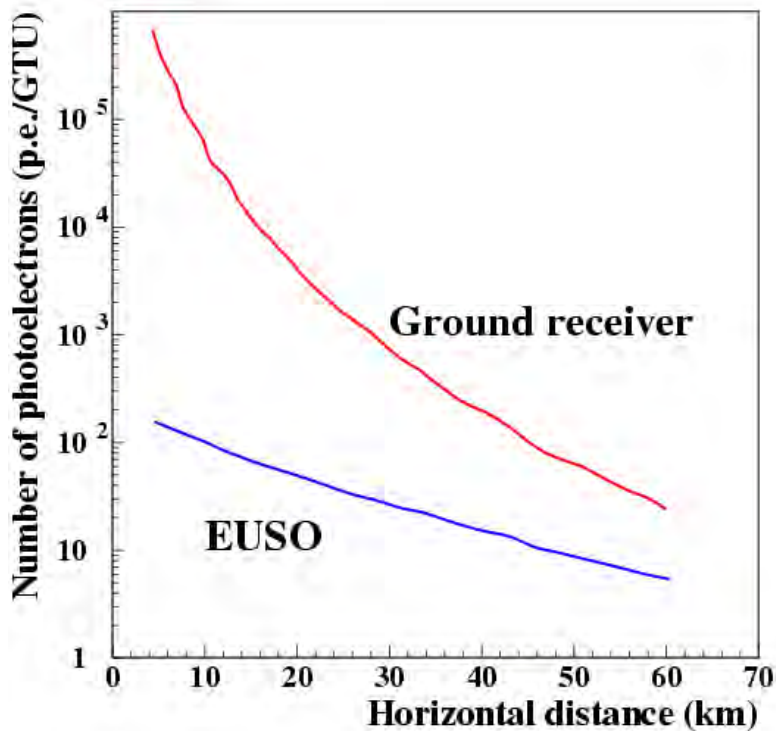


Fig.4.5.8 Expected number of photoelectrons per GTU ($2.5\mu\text{s}$) detected by EUSO and a ground receiver from a ground LIDAR (50mJ/shot, 355nm NdYAG third harmonic) shooting with elevation angle of 20° [2]. The ground LIDAR receiver is assumed to be 1 meter in diameter and 10% in quantum efficiency. More than several photoelectrons can be detected by EUSO up to 60km in horizontal distance. The signal detected by the ground LIDAR receiver is strong enough to characterize the atmosphere in detail after ~ 1000 shots. We can obtain atmospheric transmittance by using ground LIDARs and the onboard LIDAR with high accuracy and less systematic errors.

4.5.4.5. Onboard LIDAR and Infrared camera

These instruments are mainly used to measure the height of the clouds top. They also give some knowledge on the atmosphere transparency between the shower and JEM-EUSO.

4.5.4.5.1. Onboard LASER

It is composed of only a laser, for the receptor is the JEM-EUSO telescope. The two variables in a laser are the timing, which does not need to be monitored, and the emitted light intensity. Part of this light should be sent to a NIST photodiode.

4.5.4.5.2. Onboard infrared camera

Its "calibration" is provided by the manufacturer. The camera measures the cloud top temperature which gives its altitude through a well known model.

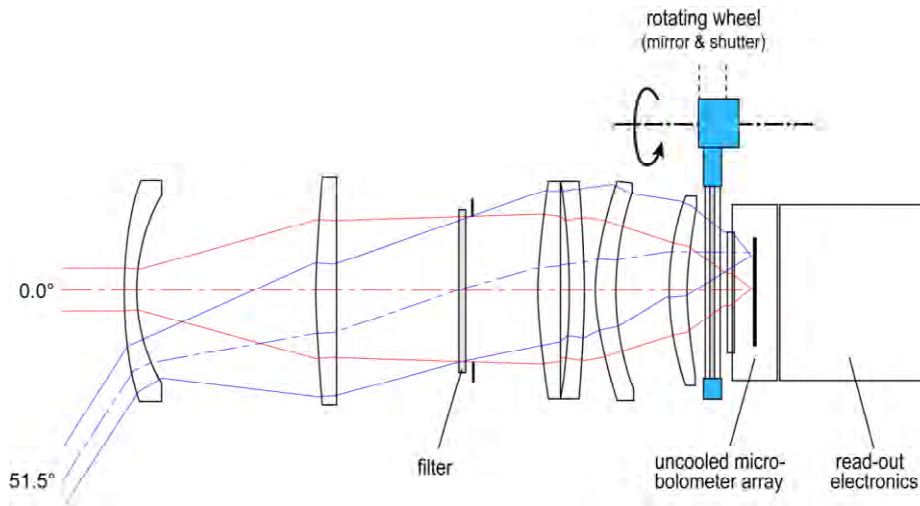


Fig 4.5.9. Schematic design of the infrared camera

Between the uncooled microbolometer array sensor and the optics, a wheel can place in the path of the infrared rays a mirror (Fig.4.5.9). Then the CCD will look at itself. If a regular thermometer is fixed to the sensor, it calibrates itself in an absolute way. The precision is then 3° K, corresponding to 200 m.

A better, but maybe not necessary, calibration can be realized if one can make the camera look at vacuum (during the day with a on-off mirror), or to some simple black bodies in the 11 – 13 μm range. Then the precision would reach 1°K.

4.5.4.6. Advanced options

4.5.4.6.1. YAP pulsars

In order to increase reliability of the calibration with LED light sources, calibration with YAP light pulsars are performed. YAP light pulsar consists of YAIO₃ scintillator and a ²⁴¹Am isotope and emits steady intensity of UV light at around 350nm. YAP pulsars are used for calibration purpose in the field of high-energy physics experiments. One YAP pulsar is put on a pixel per PDM. The pixel is dedicated to the calibration as a standard pixel to monitor the variation with time. The response to the LED light sources is compared with that to the YAP pulsar to guarantee the calibration accuracy with LEDs. YAP pulsars have weak temperature dependence, so that it is calibrated well before the launch. The long-time stability of the light intensity of YAP pulsars should be checked in a laboratory.

4.5.4.6.2. Natural light source (moonlight)

In addition to the artificial light sources described above, light sources in Nature will be utilized which is considered to be stable for a long time. One of those sources is the reflection of the moonlight. The moon is one of the nearest astronomical objects and its spectrum has been measured precisely. When the moon with phase α is at the zenith angle of θ , the expected number of photoelectrons detected by JEM-EUSO of the reflected and scattered light by the earth is expressed as the following equation[1]:

$$I_{\text{Moon}}(\theta, \alpha) = 40 \cos \theta \times 10^{-0.4(1.5|\alpha| + 4.3 \times 10^{-2} \alpha^4)} [\text{pe/pixel}/2.5 \mu\text{s}]$$

When the moon is full it is too bright to observe cosmic rays, but is within the dynamic range of the front-end electronics. Therefore, reflected moonlight could be a good calibration source. The stability of the intensity in various atmospheric conditions will be studied in detail.

4.5.4.6.3. Cross calibration with on ground experiments

Differences may arise in results of between JEM-EUSO and ground based experiments, especially in the energy spectrum. The difference in energy determination of between JEM-EUSO and a ground based experiment can be checked directly by observing a same shower, but it is very rare to observe 10^{20} eV showers at the same time. Observing LIDAR beam shots at an observatory for ultra-high energy cosmic rays such as the Pierre Auger Observatory, the Telescope Array Experiment may give us information about mutual calibrations between JEM-EUSO and ground based experiments.

4.5.5. Operation

During the science observation, the count rate of each pixel is monitored and the average and the variance are calculated for each pixel every orbit. The photon detection efficiency and the linearity of each pixel are examined by the onboard LED sources during the day. For precise calibration, single photoelectron spectra will be taken once a week with the LED light sources for each pixel. When JEM-EUSO flies over a ground light source, the instrument calibration and atmospheric monitor will be performed. The calibration frequency is about once per day and 1-5 hours per year will be used for the observation of ground light sources.

4.5.6. Summary

4.5.6.1. Specification

1. Requirements

Table 4.5.3 Requirements to the onboard calibration

Calibration subsystem (total)			
	Item	Required value	Note
CSR1	Observation wavelength	330-400 nm	
CSR2	Accuracy on the calibration of the light intensity	Less than 18% (TBC)	

2. Technical readiness level

Table 4.5.4 Technical readiness level of the onboard calibration

	Item	Technical Readiness Level and its reason when selected in Feb./'07	Technical readiness level and reason (as of Apr./'08)	Expected technical readiness level and activities at SDR time (Mar./'09)
CSR 1	Observation wavelength	TRL3 Verified by two types of ultraviolet LED (360nm, 380nm TBC).	TRL3 Choose two candidates of ultraviolet LED, and verify them by calculations based on the characteristics of the optics and detector.	TRL4 Verification by means of the evaluation of BB model, which consists of the combination of the elements of test manufactured calibration device, optics, and focal surface detector.
CSR 2	Accuracy on the intensity of	TRL3 Verified by a calibration device in the laboratory.	TRL3 Verified by a calibration device in the laboratory.	TRL4 Verification by BB model evaluation,

	the calibration light			which consists of the combination of the elements of test manufactured calibration device, optics and focal surface detector with help of simulation.
--	-----------------------	--	--	---

3. Main parts

Refer the section of costs.

4. Temperature requirements

Same for the focal surface detector and the electronics.

5. HK requirements

TBD (temperature monitor around YAP pulsars, etc)

4.5.6.2. Budget

Mass

Item	BEE(kg)	Margin	Total mass(kg)	Comments
LED light source	7	30%	9	1kg ×7, TBC
YAP	1	30%	2	

Power

In operation:

Item	BEE(W)	Margin	Total power (W)	Comments
LED light source	8	30%	11	TBC

N
on-

operation:

Item	BEE(W)	Margin	Total power (W)	Comments
LED light source	0	30%	0	

Tel
eme

try

Item	BEE(kbps)	Margin	Total data rate (kbps)	Comments
LED light source	6	30%	8	Detail is described below.

Total data rate 30Mbits/orbit [TBC]=~ 6kbps

single photoelectron spectra

4Mbits/orbit (Full data/week)

data for ground flasher

1.5Mbits/orbit

data for ground LIDAR

1.5Mbits/orbit

background monitor during the science observation

6Mbits/orbit

data for detection efficiency and linearity check

15Mbits/orbit [TBC]

4.5.6.3. Costs

Table 4.5.5 Costs for the calibration subsystem (Unit: million yen)

	FY2008	FY2009	FY2010	FY2011	FY2012	FY2013

Efficiency measurement of PMTs	10	38	5	4	3	0
Onboard LED light sources	1	1	2	1	0	0
On ground flashers	9	10	10	14	38	10
On ground LIDARs	0	1	1	7	32	3

Total=200M¥

4.5.6.4. Fabrication schedule

Table 4.5.6 Fabrication schedule of calibration instruments

	FY2008		FY2009	FY2010	FY2011	FY2012	FY2013
Pre-flight PMT calib.	design	trial	Fabric	calibration			
Onboard LED	design	trial	Fabrication		Testing		
Onboard YAP	Design		Trial fabrication, testing	Fabrication, Testing			
Ground Flasher	concept		detailed design		Fabrication, Testing		deployment
Onboard LIDAR	concept		detailed design		Fabrication, Testing		deployment

4.5.6.5. Organization (Group leaders)

Calibration subsystem P.Gorodetzky (APC Paris), N.Sakaki (Aoyama)

Pre-flight calibration N.Sakaki (Aoyama)

Onboard calibration E.Pace (Firenze)

Ground flasher M.Christl (NASA)

Ground LIDAR N.Sakaki (Aoyama)

Reference :

[1] F. Montanet, EUSO-SIM-REP-009, 2004.

[2] EUSO collaboration, EUSO – Report on the Phase A study – (EUSO-PI-REP-005), 2004.

[3] S.M. Khanna et al., IEEE trans. Nucl. Sci., 51 (2004) 3585.

[4] J.H. Adams Jr., M. Christl and the EUSO Collaboration, Proc. Int. Cosmic Ray Conf. (Tsukuba), (2003) 919.

[5] G.Lefevre, Doctor thesis, Universite Paris 7 Denis Dederot (2006).

[6] E.Pace, Proposal for the EUSO instrument Calibration System (TR1-2003), XUV Lab, Universita di Firenze (2003).

4.6. Support Sensor

JEM-EUSO has attitude sensors and one GPS. Attitude sensor consists of a star sensor (VSC: Visual Star Camera) and a gyroscope (RLG: Ring Laser Gyroscope) (Figure 4.7.1).

The absolute attitude ($<0.05\text{deg}$) of JEM-EUSO is obtained by VSC, while RLG (Total Error: $<0.04\text{deg}$) is operated as the backup of VSC, which can not work when star is not able to be seen. GPS is used to measure time with an absolute accuracy better than $1\mu\text{sec}$. We are planning to use the support sensors which are compatible with the sensors developed and used in MAXI (Monitor of All-sky X-ray Image). However, improvement for GPS may be required to match the requirement of the higher time accuracy ($<1\mu\text{sec}$) than that of the GPS in MAXI ($<0.01\text{msec}$), in order to accurately catch the instant of the thunder light generation.

The specifications of MAXI support sensors are as follows.

VSC : Bias Error: $\pm 10\text{arcsec}(\text{max}) \times \pm 10\text{arcsec}(\text{max})$

RLG : Total Error: $<0.04\text{deg}$

GPS : Time accuracy: $<0.01\text{msec}$

4.7. Bus System

Bus System consists of structure part, structural control (mechanism) system, data processing unit, and power distribution unit, electrical system installation, and thermal control system (Figure 4.7.1). Inner and outer interfaces are described in paragraph 4.7.5.

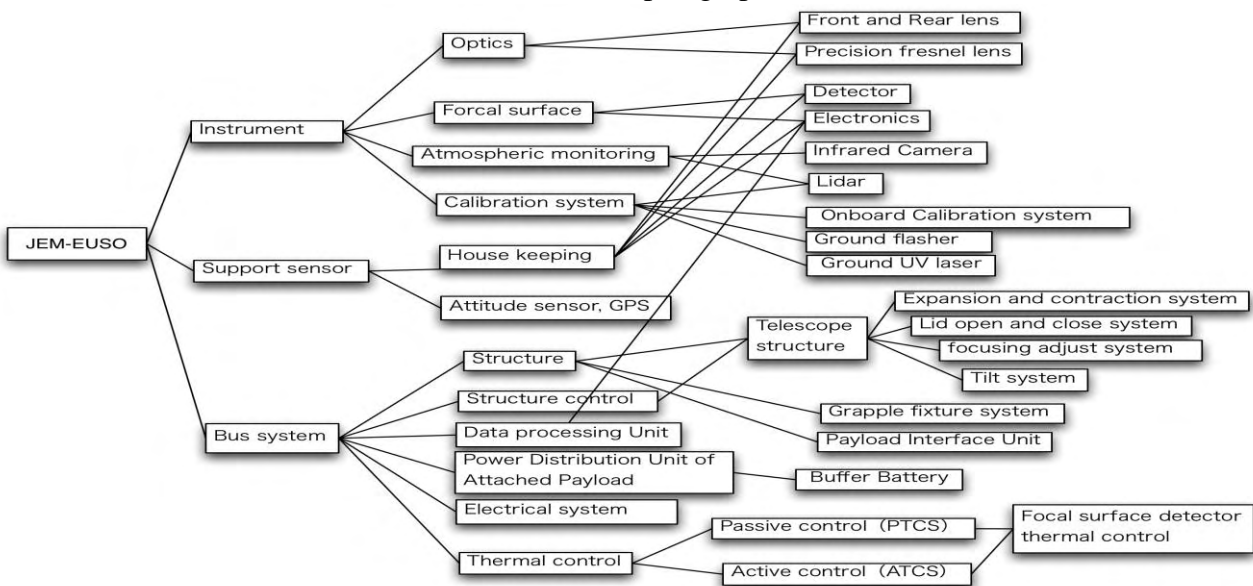


Figure 4.7.1 Breakdown of JEM-EUSO Telescope

4.7.1. Structure part

4.7.1.1. Accommodation of JEM-EUSO to HTV

Accommodation of JEM-EUSO to HTV from viewpoint of a size has been studied through phase-A study and was described in detail in the “Incidental Conditions study result Report” submitted to JAXA in Nov. 2007. One of the main results is that Case-C (2.6m in diameter, of which the lateral part is cut) is determined as the current baseline which satisfies most the scientific requirements and requirement of HTV envelop.

4.7.1.2. Structural Design

The front lens and its supporting structure are slotted into the pallet. Supporting structure without affecting the separation/latch mechanism such as TSM, HSM, HDM, and wiring of the

flexible shaft cables on the pallet (Figure 4.7.2). In addition, the cylinder of the telescope is divided into three rings, and by moving these rings in the axis direction, the telescope is deployed (Figure 4.7.3, 4.7.4). The overall drawings based on these design concepts are shown in Figure 4.7.3 and 4.7.4.

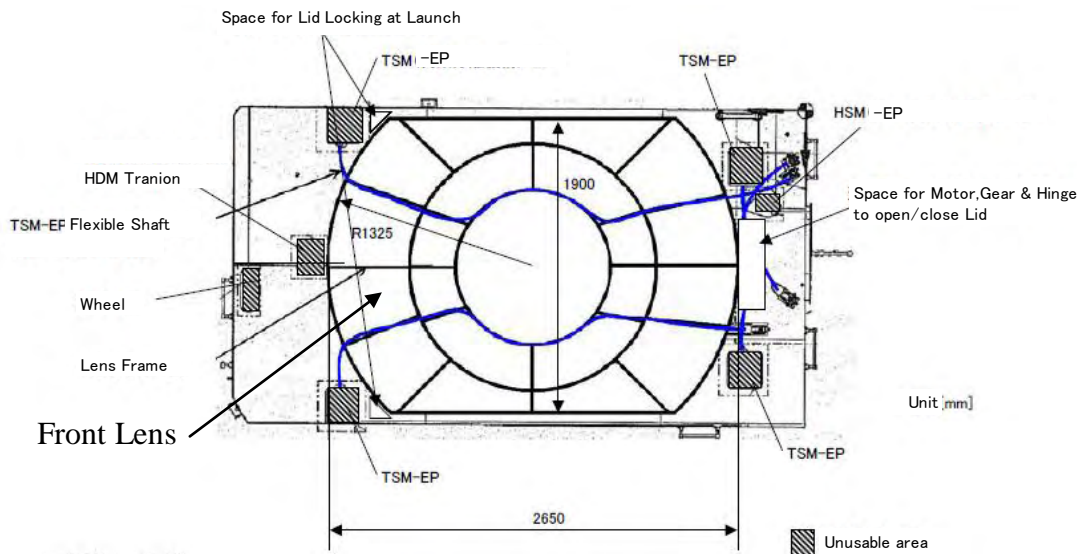


Figure 4.7.2 Bottom view from nadir (ref. [7.1])

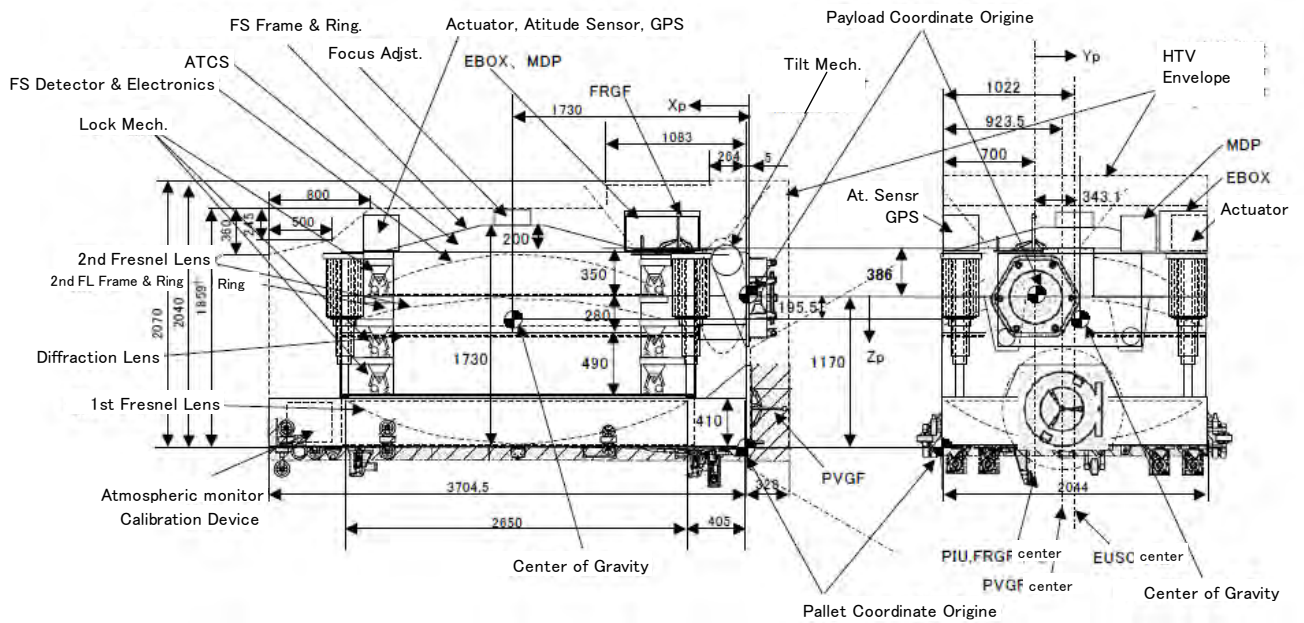


Figure 4.7.3 Side view of JEM-EUSO (stowing configuration in HTV) (ref. [7.1])

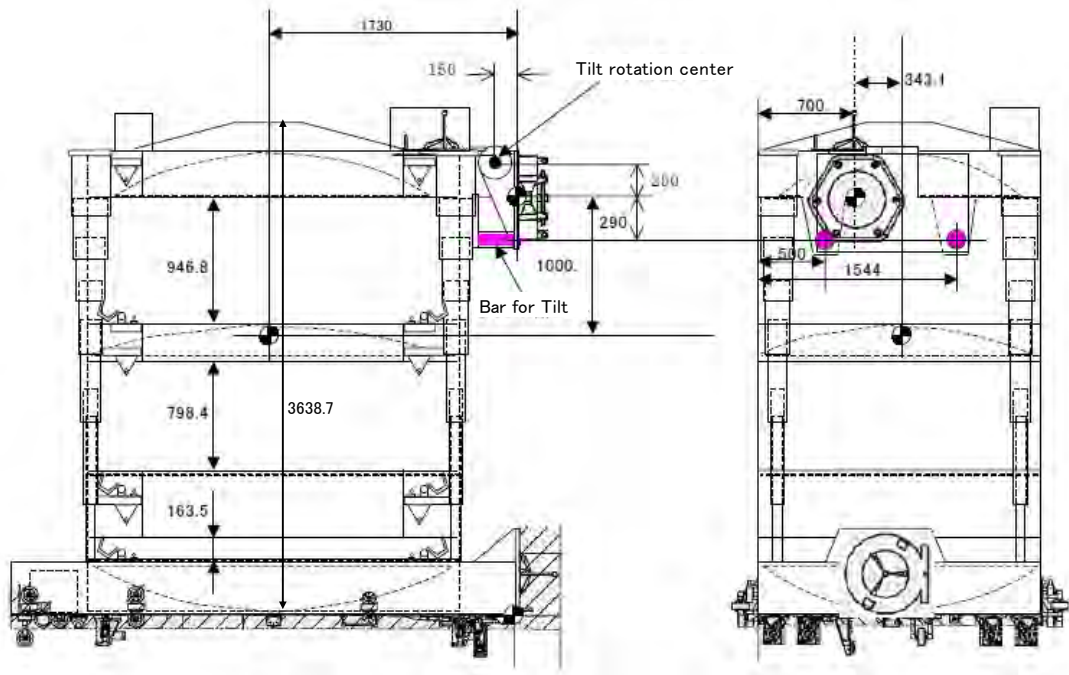


Figure 4.7.4 Side view of JEM-EUSO (observation configuration) (ref. [7.1])

Observation state of JEM-EUSO to JEM/EF is shown in Figure 4.7.5. JEM-EUSO is planned to EFU#2 port of JEM/EF. For this case, possible interference exists with the standard payload for EFU#4. The EFU#9 port can be used as a backup option without any physical interference. The corridor for EVA activity (30 inches width from the corner of the exposed facility) confirmed to be secured.

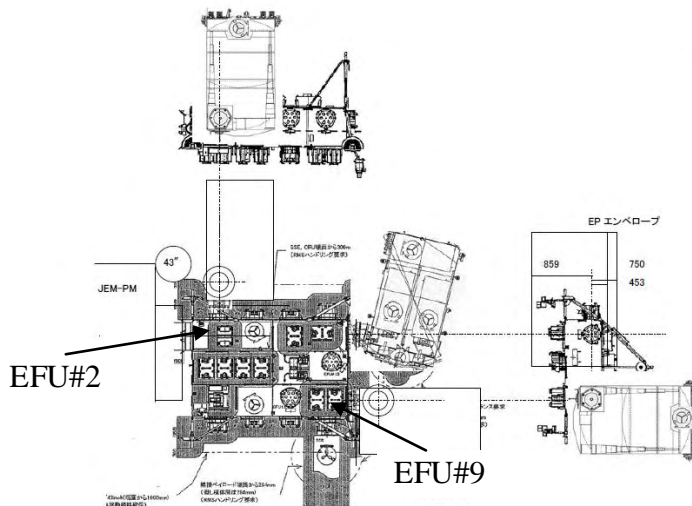


Figure 4.7.5 Attached state of JEM-EUSO to EFU#2 or EFU#9 of JEM/EF (ref. [7.1])

Radio interference with the PROX antennae located in the pressurized module, found to be less severed compared to the standard payloads even for the EFU#2, if telescope is shrunk to stowing mode and is tilted by 80 degrees (see Figure 4.7.6).

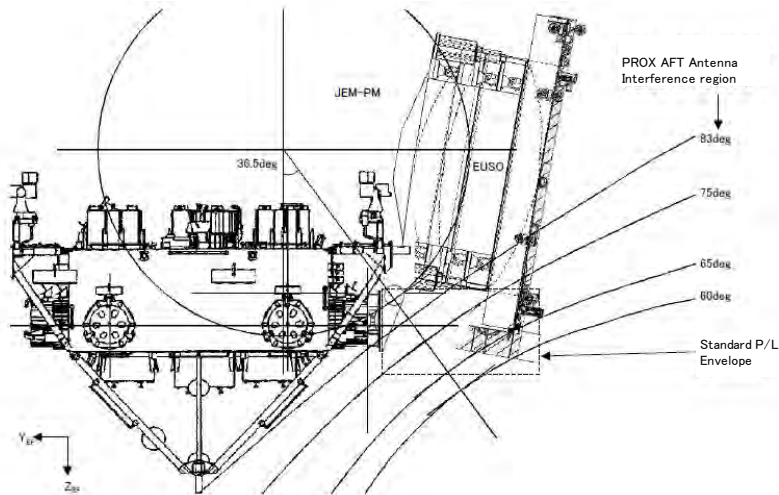


Figure 4.7.6 PROX Antenna Interference in case of JEM-EUSO attached to EFU#2 tilted by 80 degrees (ref. [7.1])

4.7.1.3. Structural Analysis

Structural analysis for the structure mentioned above has been done by an engineering company named IHI AeroSpace.

4.7.1.3.1. Natural Frequency analysis of observation state

The analysis of telescope in observation mode in deployed state was done. Natural Frequency turned to be as high as 1.7Hz under the boundary condition that telescope was fixed to PIU (Payload Interface Unit). It is larger than the minimum required value of 1Hz. It can be increased to around 2Hz by reinforcing PIU adapter. Figure 4.7.7 shows the model structure for the simulation.

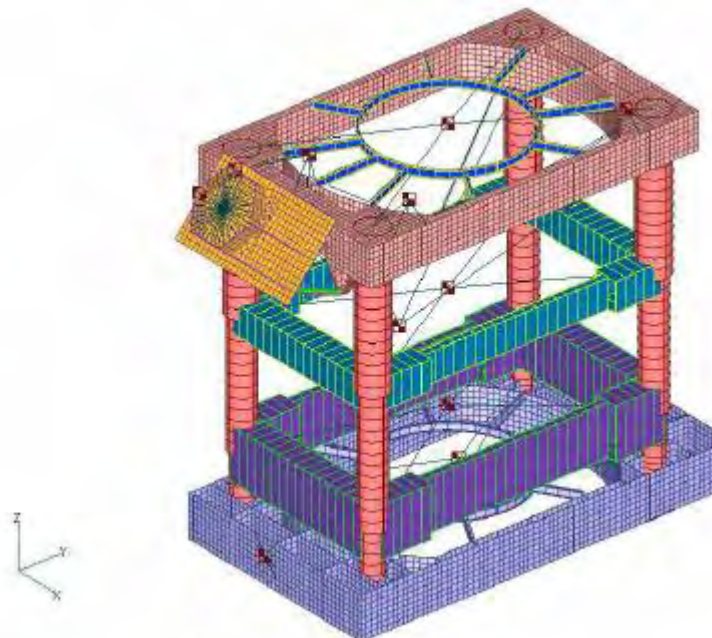


Figure 4.7.7 Structural simulation model / Observation (Deployed) state (Tilt angle: 40°) (ref. [7.1])

4.7.1.3.2. Natural Frequency analysis of stowing state

we found that minimum natural frequency was 25.6Hz and that it satisfies the requirement of launch time rigidity, over 25Hz. Figure 4.7.8. shows the model to use in this analysis.

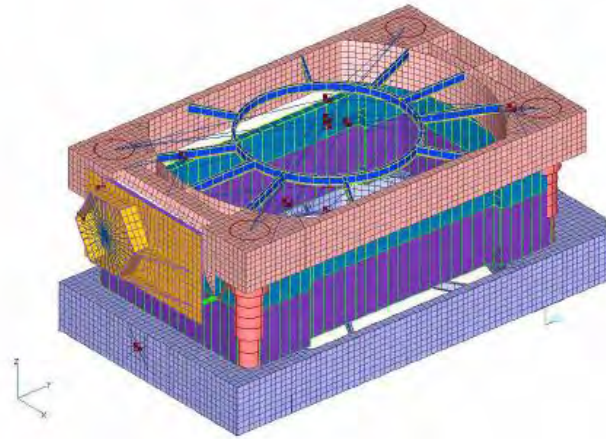


Figure 4.7.8 Structural simulation model / Launch (Stowed) state (Tilt angle:0°) (ref. [7.1])

4.7.1.3.3. Static analysis of launch state

Static analysis was performed for various kinds of accelerated loads to obtain. Margin of Safety (MS) value was calculated by stress in the structure and failure stress of material (A7075-T7351). The minimum MS was MSu=2.10 in the vicinity of connection point between TSM and pallet frame. It means that the designed structure satisfied the strength requirement at launch. The result of the calculation in case of the load by which the minimum MS value is obtained, is shown in Fig. 4.7.9,

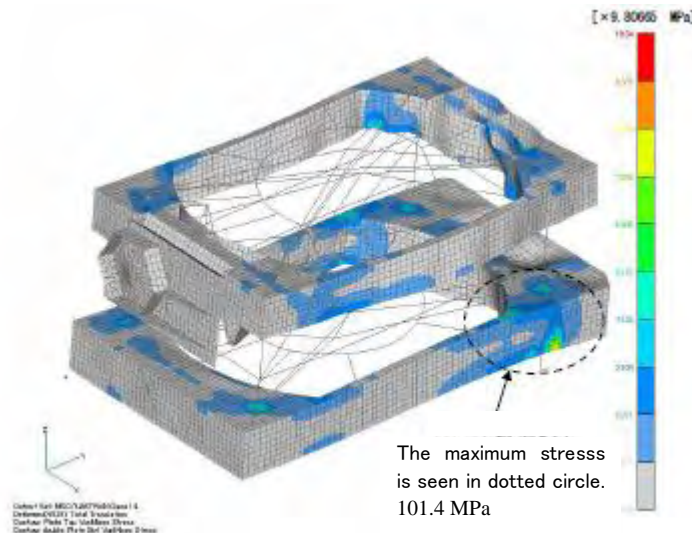


Figure 4.7.9 Stress Distribution (ref. [7.1])

4.7.2. Structure Control (Mechanism) system

Regarding the Structure Control (Mechanisms) of the bus system, we studied the following points: opening/closing of lid, stowing/deploying mechanism, tilting mechanism and adjusting mechanism of focus.

4.7.2.1. Lid

Conceptual study and design of the lid were done by a company, which has experience and expertise in space engineering. We confirmed the durability for 30,000 times opening/closing operations for 5 years and estimated the mass (14.1kg including the lid, driving mechanism, support structure, etc.) and driving power (around 3.4W for opening operation for 6 seconds) (Figure 4.7.10).

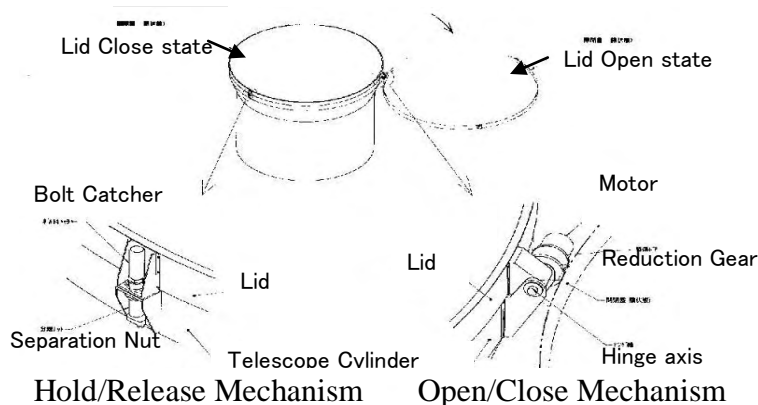
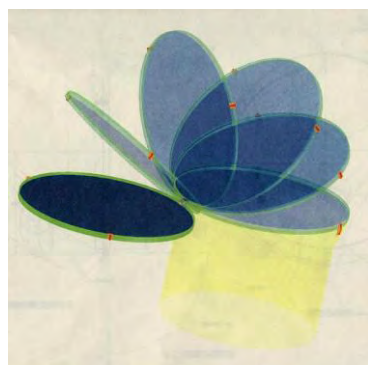


Figure 4.7.10 Conceptual diagram of opening/closing of the lid

Secondly, we have studied of PMT durability test. In the case that the lid in opening mode accidentally remains open even in the daytime, the focal surface may be exposed to diffusive light in the earth daytime. We have testes that surface remains durable for a few years to continue the observation in the earth nighttime, as long as the high voltage is not applied. Even in that case, the detector could be partly be deteriorated by reflection on the mirror surface, such as the water surface of shallow lake, caused by the sunlight on earth. It would be better to keep the lid closed during the daytime in order to maintain the performance of the detector as long as possible. In addition, it is necessary to close the lid to protect the telescope from bad environmental conditions which are caused by approaching of HTV, re-boosting etc..

Based on these studies, we decided to design the lid and opening/closing mechanism with as high reliability as possible, then to repeat opening/closing action of the lid in every orbital cycle in the early stage of the operation. When we detect an anomaly in the mechanism, it will be appropriate to keep the lid in open state to avoid locking in the closed state, because we loose all the function of the instrument.

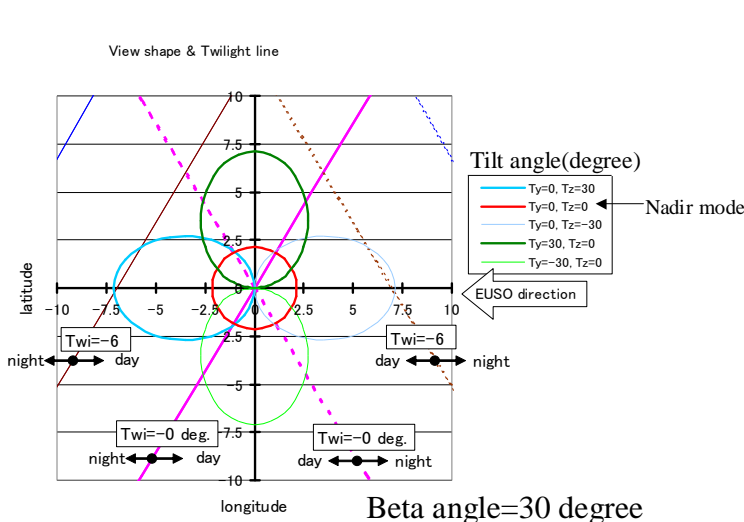
4.7.2.2. Deploying / Stowing Mechanism

The telescope cylinder is divided into three rings, and they are moved by four inflatable masts. Regarding the deploying/stowing mechanism of the telescope, Inflatable Sunshield In Space (ISIS) Telescope Mast™ supplied by NORTHROP Grumman company is confirmed to have excellent reliability. These four masts will be installed outside the telescope and extended synchronously. See Figure 4.7.3 and 4.7.4 for details.

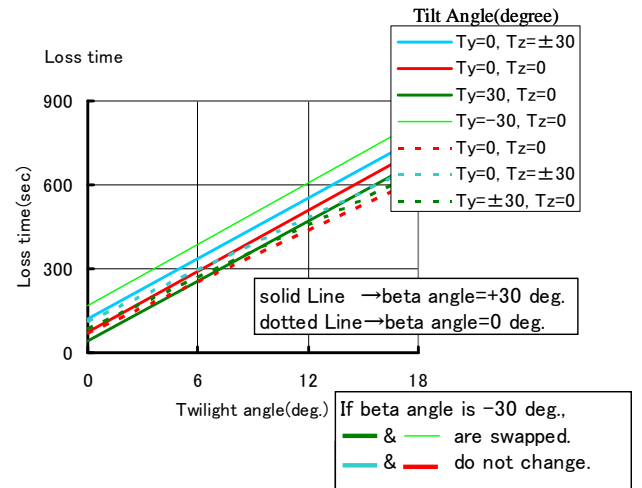
4.7.2.3. Tilt Mechanism

Tilt mechanism is installed near PIU (Payload Interface Unit) in order to tilt the whole telescope. (figure 4.7.3 and 4.7.4.) To avoid radio interference of PROX antenna, the capability of tilt angle should be at least 80 degrees. See Figure 4.7.6. Thus we can assure 30-40 degrees of the required tilt angle for observation.

We studied of the tilt angle and its direction, using crepuscule line angle and beta angle as parameters. By evaluating the observable time (time period in which whole FOV occupies night area on earth) for the various tilt directions, we confirmed that the difference among each case was very small (maximum 25 seconds) (Figure 4.7.11).



View shape on Earth for various Tilt angles



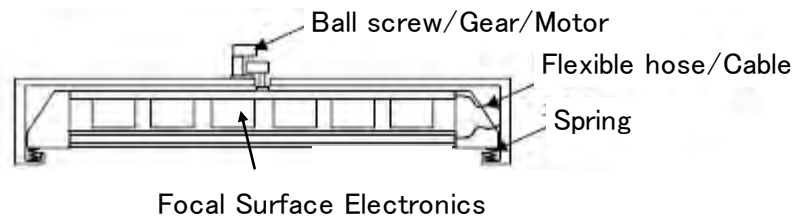
Observation Loss Time vs Twilight Angle

Figure 4.7.11 Tilt Angle analysis

4.7.2.4. Focusing adjustment Mechanism

Figure 4.7.12 shows that conceptual design of focusing adjustment Mechanism

In Observation State:



At Launch:

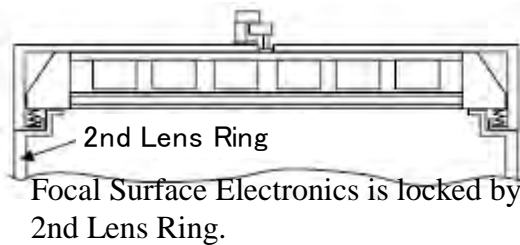


Figure 4.7.12 Focusing Adjustment Mechanism (ref. [7.1])

4.7.3. Data Processing Unit / Power Distribution Unit

The following figure shows the overall system diagram including the relation between the mission and data processing unit/power distribution unit.

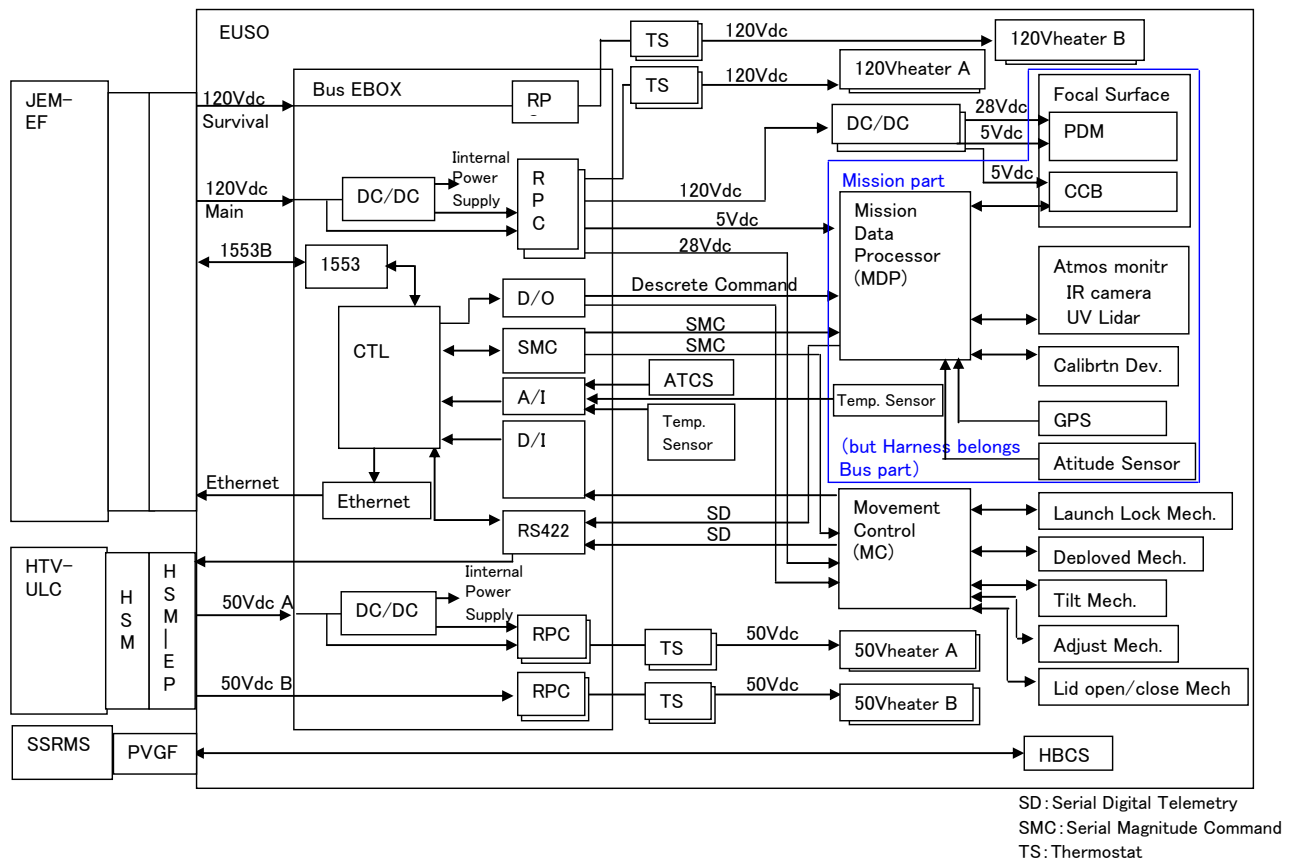


Figure 4.7.13 Bus System Block diagram

4.7.3.1. Data Processing Unit

Data processing in the bus system consists of data processor (CTL) in the EBOX and movement controller (MC) outside the EBOX (Figure 4.7.13).

The major functions of data processor (CTL) in EBOX are:

- communication interface among JEM/EF, CTL by payload bus2(1553B) and Ethernet,
- communication interface between mission system and CTL,
- acquisition of HK data of mission system,
- interface between power distribution unit in EBOX and CTL, and ON/OFF control of power supply by power distribution unit to each device,
- The function to start/stop the trigger of the installed JEM-EUSO software (JES), which processes the data observed by focal surface detector and atmospheric monitor. And it is also necessary to have a rewritable and non-volatile memory for software storage.
- interfacial function of distributing the 1PPS clock signal from GPS to MDP and VSC electronics(VSCE),
- interfacial function of ATCS.

Movement controller (MC) accepts signals from DP and controls movable mechanisms (telescope deploying/contracting, lid opening/closing, focus adjusting and telescope tilting) and then actuates these mechanisms into the required position/state. HK and position data are also acquired by MC and sent to CTL.

4.7.3.2. Power Distribution Unit

The major functions of power distribution unit (DC/DC inside/outside EBOX, Fig.4.7.13) are:
 (a) receiving power from JEM/EF, transforming it into appropriate voltage and supplying required power to each device in the telescope, (ON/OFF actions of power supply can be controlled by CTL) .
 (b) receiving survival electric power from JEM/EF, and supplying its power to each heater in JEM-EUSO system,

Optimization of power supply to Focal surface electronics which consists of PDM (Photo Detector Module), CCB (Cluster Control Board) and MDP (Mission Data Processor) was done. The following combination of 8 DCDC converters, realizes the least power conversion loss. Figure 4.7.14 shows voltage distribution diagram.

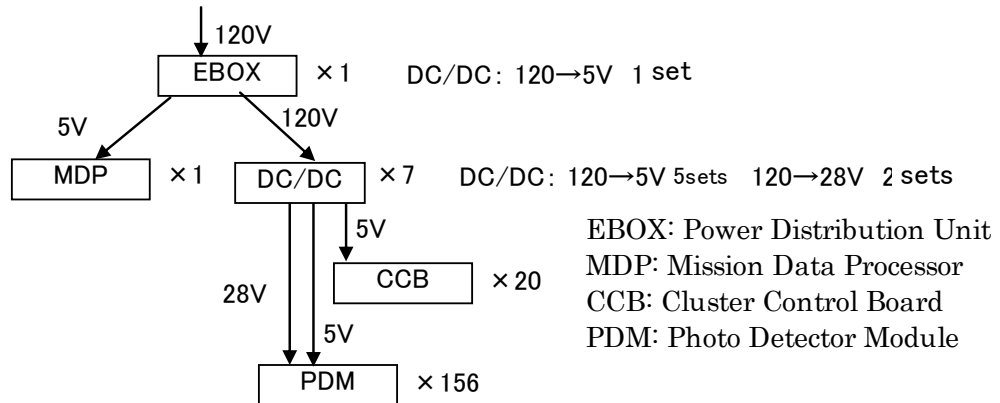


Figure 4.7.14 Voltage distribution diagram (ref. [7.1])

Power consumption rate of the telescope is much different between operating state (daytime) and non-operating state (nighttime). In order to smooth the difference, we studied the utilization of buffer battery. Li ion battery is preferable for a space mission because of high energy density (165Wh/kg), high Energy efficiency (96%) and low thermal loss and no memory effect etc.. Reference: EUSO-IM-TN-003. If the depth of discharge (DOD) is less than 25%, instead of full discharge (100% DOD), we would need a battery of over 4 times larger, however, battery life for 25%DOD will be expected 50 times longer than that of 100% DOD. In addition, in case of 25%DOD, charge/discharge of 40,000 times is possible [EUSO-IM-TN-003]. In case of JEM-EUSO, as around 20,000 times charge/discharge is estimated for three years, then the operation for about six years will be possible with 25%DOD.

By smoothing the power by buffer battery, the necessary powers of the mission such as 1400W in operation and 360W in non-operation become possible, even if the supplied maximum power from the bus is limited to 950W. In this operation, necessary mass of battery is estimated about 47kg, even in case of preparing two batteries for redundancy. Battery mass is included as item 'buffer battery' in the Table 4.7.8.1 of Mass budget.

4.7.4. Thermal Control and Thermal Analysis

4.7.4.1. Thermal Control

Thermal control system is composed of active thermal control system (ATCS), passive thermal control system (PTCS) and PIU (Payload Interface Unit) cover (Figure 4.7.13).

If SiPM is used as focal surface detector, ATCS has to dissipate actively the heat by electronics devices to keep the detector at less than -15[°C]. As the electronics devices are installed near

detector backside surface, they should also be cooled by ATCS. Supply of coolant from PIU structure for ATCS to detector surface frame is relatively easy by connecting flexible hose at tilt mechanism. EBOX for bus system box and movement controller (MC) installed on detector frame are also cooled by ATCS. Atmospheric monitor and calibration devices which are not installed on detector frame are cooled by PTCS because their heat generation rate is small, and also it is difficult to supply coolant for ATCS. ATCS diagram obtained from the above study is shown in Table. 4.7.15.

The devices requiring the Survival heaters are only atmospheric monitor, calibration system, and attitude sensors, which are cooled by PTCS. Then we estimate that these Survival heaters can satisfy the restriction of less than 100[W].

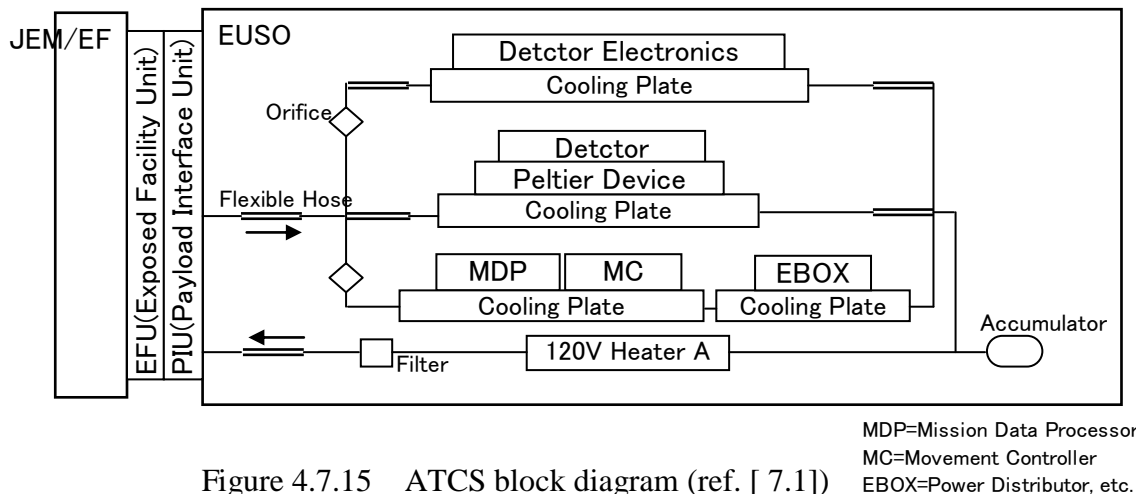


Figure 4.7.15 ATCS block diagram (ref. [7.1])

External surface of the cylinder structure of the telescope and the lid are thermally insulated by multi-layered insulation (MLI) material (PTCS). PIU cover is the cover which is used to insulate thermally PIU part in the launch phase.

4.7.4.2. Thermal Analysis

The analysis was done for two cases: using PMT as a detector, and SiPM as a detector. We understood that, in case of the PMT detector, a special cooling device was not necessary because it satisfied the temperature requirements, even if the energy consumption of PDM influenced the rise of the temperature of the focal surface detector. As for the SiPM detector, if we succeed in making a design which insulates the sensor surface from the heated MLI, we estimate that the necessary quantity of the heat dissipation will be maximum around 50[W] with the lid, and around 300[W] without the lid. Refer to Annex 2 for details.

4.7.5. Interface

4.7.5.1. Definition of interface

JEM-EUSO bus system part has external interfaces to each part of JEM system, JEM operational control system/JEM experiment operation system, HTV un-pressurized carrier, JEMRMS (JEM remote manipulator system). Meanwhile, JEM-EUSO system part has internal interfaces to mission equipments in JEM-EUSO system, JEM-EUSO sensors etc.

4.7.5.2. External interface

JEM-EUSO bus system part has electrical, mechanical, thermal and electromagnetic interfaces to HTV un-pressurized carrier, JEM exposed facility and JEMRMS. The system part also has logical interfaces to JEM pressurized module/JEM inter-orbit communication system and JEM operational control system/JEM experiment operation system.

Interfaces between JEM-EUSO bus system and each part/system are shown in Table 4.7.3.

Table 4.7.3 External interfaces between JEM-EUSO bus system part and each part/system

	Elec.I/F	Mech.I/F	Ther.I/F	ElMg.I/F	Logi.I/F
HTV un-pressurized carrier	○	○	○	N/A	N/A
JEM Exposed Facility	○	○	○	○	N/A
JEMRMS	N/A	○	○	○	N/A
JEM pressurized module / JEM inter-orbit com. sys.	N/A	N/A	N/A	N/A	○
JEM operational cntl. sys / JEM experiment oper. sys.	N/A	N/A	N/A	N/A	○

Note) ○: interface exists.

4.7.5.3. Internal interface

JEM-EUSO bus system part is interfaced with the following equipments. These relations are shown in Figure 4.7.13.

In addition, the following Table 4.7.4 shows interface conditions for major components (mechanics, power supply, communication, heat, etc.) between bus system and mission equipments.

Table 4.7.4 Interface conditions between mission and bus equipment

	Comments	Mechanical			Electric Power		Telemetry		Thermal		FOV	Others
		Dimension [mm]	Mass [kg]	Mechanical I/F	Power [W]	Voltage [V]	Telemetry speed ¹ [kbps]	No. of Channel Kinds of Signal	Thermal Requirement	Thermal I/F		
Optics	1st(Front) Lens	Lateral cut	2650x1900x15	173(150) ¹	-	-	-	-	-	-	±30°	Accuracy of Lens installation: Tab.4.7.5
	Iris	Fig.4.7.2	180x5	Included in Lens Frame	-	-	-	-	-	-	-	
	Precision Fresnel	Fig.4.7.3	2376x1900x10	55(47) ¹	-	-	-	-	-	-	-	
	2nd(Rear) Lens	Fig.4.7.4	2650x1900x15	166(144) ¹	-	-	-	-	-	-	-	
Atmospheric Monitoring	IR CAMERA		130x250x250 (TBC)	7(5) (TBC)	Fixed by fastener to Frame.	11(8) (TBC)	5(TBC)	21(16) (TBC)	TBD	-30~+60°C	±30°	-
	Lidar	Laser unit etc. Lidar Power Supp	Riken Type 450x350x250 (TBC)	22(17) (TBC)	Frame.	91(70) (TBC)	28(TBC)	4(3) (TBC)	TBD	-	±15°	-
Calibration	Calibration Device	LED light source	1x Focal Surface 30q x50x7pc. 8x Rear L (TBC)	10(7) (TBC)	Fixed by fastener to Frame.	11(8) (TBC)	5(TBC)	8(6) (TBC)	TBD	TBD	-	-
		YAP Pulsar	137x Focal Surface	50 x1x137sheet ¹ (TBC)	1(1) (TBC)	sticked to each PMT	-	-	-	-	-	-
Support Sensor	Attitude Sensor : VSC(Visual Star Camera) & RLG(Ring Laser Gyroscope)	VSC & Baffle	MAXI complbl. JKC-99017 for VSC, Electronics	1 (TBC)	Fixed by fastener to Cold Plate.	7.5 (TBC)	28 (TBC)	TBD	TBD	-40~+35°C (TBC)	18.4x13.4°	VSC Precision: (0.05°) (TBC)
		RLG	NASDA-ESPC-3055 for RLG	1.2 (TBC)	-	-	-	-	-	-20~+70°C (TBC)	-	RLG total error: (0.04°)
		GPS antenna	MAXI complbl. NASDA-ESPC-	0.1 (TBC)	Fixed by fastener to Frame.	2 (TBC)	5(TBC)	TBD	TBD	-30~+60°C	-	GPS Precision: <1μ sec (TBC)
	GPS Electronics		70x50x40 (TBC)	0.3 (TBC)	Frame.	0.3 (TBC)	-	-	-	-	-	
Electronics Circuit	Mission Data Processor	MDP	2 sets (1 set= redundancy)	300x300x400 (TBC)	Fixed by fastener to Cold Plate.	2(1) (TBC)	5V x 2ch	Telemetry to/from EBOX via MDP: Discrete Command x 1ch(TBC) Serial Magnitude Command x 1ch(TBC) Serial Digital Telemetry x 1ch(TBC) Fig.4.7.13	Electronics Device: in operating mode: -10~+50°C in non-operating mode: -30~+50°C	Cooled by Cold Plate for MDP.	-	-
	Focal Surface Electronics & Detector	COB (Cluster Control Board)	19 sets(TBC)	162x162x20 (TBC)	Board+Cable: 105+112(91+86)	17(13) (TBC)	5V+28V x 20ch (TBC)	Science Data: 233/202 (TBC) Mission HK: 8(6) (TBC)	PMT: in operating mode: 0~70/+20°C in non-operating mode: -30~+50°C	Cooled by Cold Plate for Detector.	-	-
		PDM/PMT.FEE PDMCB)	137 sets(TBC) Fig.4.3.2.8	Focal Surf. total: 2379x1900 PDM: 162x162x200 (TBC) Fig.4.3.2.8	159(138) (TBC)	PDMs are fixed by fastener to Support Frame or Cold Plate.	PDM:311(238) HV:94(72) Converter Loss :94(72)	-	-	-	-	-

* : value1(value2) means value1-margin included value, (value2)=BEE value.

4.7.6. Summary

4.7.6.1. Requirements for the performance

Table 4.7.5 Requirements for the system

Item	Required value	Note
Enclosure structure	Primary natural frequency: more than 2Hz (observation mode) more than 25Hz (at launch) Performance of the light shielding: less than 1GHz on the whole focal surface Insulation performance: I/R emittance < 0.05	Protecting the instrument from the potential dangerous environmental elements (EUS-SP-AI-0002) is required.
Opening and closing of the lid	Frequency: twice/ orbit(90 minutes) Duration: less than 5 minutes Endurance: more than 5 years, more than 30,000 times of opening and closing	Redundancy in actuator electronic circuit is required.
Expansion mechanism	Stowing mode in HTV: should be settled in HTV envelope Should not have a physical interference except with EFU#4, when placed in EFU # 2 or EFU # 9 of JEM-EF Should be able to change repeatedly between: stowing mode/ observation mode during the mission	HTV envelop: report about the results of the study of collateral conditions (figure 2.1) Should be able to be expanded for the observation mode on JEM-EF
Tilt mechanism	30~45°	Operating once every 6 months, approximately 10 times during the entire mission
Focus adjustment mechanism	Moving range and step range of the optical segment: Range: more than ±12.5 mm Step: less than 1.25 mm	EUSO-OM-DESIGN-001-02
Accuracy of the installation of the lenses	Coaxial Tolerance: within ±2.5 mm Parallel Tolerance: within ±2.5 mrad Accuracy of the position: within ±2.5 mm	

4.7.6.2. Technical readiness level

Table 4.7.6 Technical readiness level of system

Item	Technical Readiness Level and its reason when selected in Feb./'07	Technical readiness level and reason (as of Apr./'08)	Expected technical readiness level and activities at SDR time (Mar./'09)
Enclosure structure	TRL3 Structural Analysis was	TRL3 Perform a modal and	TRL3 Perform more detailed

	done. (EUS-RP-AI-0005)	structural analysis by means of FEM, then verify the concept design.	modeling of the expansion mast and others and to be verified by modal and structural analysis by means of FEM.
Lid	TRL3 soft sail/sandwich panel (EUS-RP-AI-0005)	TRL3 Perform concept design by simple analysis and verify the endurance. Estimated weight 14.1kg, driving power 3.4 W.	TRL4 Perform an inspection test of the function by means of the BB model of opening-closing mechanism, and verify basic functions.
Expansion mechanism	TRL3 Stowing capability in HTV was verified, concept of truss expansion mechanism.	TRL3 Verification of basic functions and the estimation of weight (80kg), doing analysis of the vibration and the structure of the concept design of JEM-EUSO, which has 4 expanding masts in HTV.	TRL4 Perform quantitative evaluation of the weights, resistance, etc. of expanding masts and other expansion systems by a simulation, and then select an expansion system.
Tilt mechanism		TRL3 Perform the concept design of the tilt mechanism and estimate the weight (40kg).	TRL3 Perform analysis of the vibration and the structure of the basic design, and verify functions.
Focusing length adjustment mechanism	TRL3 Adjust mechanism concept.	TRL3 Redo the concept design of the adjusting mechanism and estimate the weight (20kg).	TRL3 Perform analysis of the vibration and the structure of the basic design, and verify functions.
Heat control	TRL3 Heat analysis by means of a simple model was done. (EUS-RP-AI-0005, etc.)	TRL3 Analyze temperatures of lenses, focal surface, etc., by a simple model, then, verify the in-plane distribution (4.5°C), which satisfies the required temperature, and estimate the quantity of heat discharge (without lid 300W).	TRL3 Verify the particularities, doing analysis of the heat by means of the detailed mathematical model of focal surface detector module.
System / electronics		TRL3 Concept design on the	TRL4 Design the part regarding

		move.	the interface with JEM/EF, and do its BB model test.
--	--	-------	--

4.7.6.3. Principal pieces

Pieces related to main systems:

Structure : Enclosure structure,
lid,
Expansion mechanism (rings, expansion mast),
Focus adjustment mechanism,
Lens frame,
Focal surface supporting structure

Temperature : ATCS system

Electricity : Power distributor,
Harness

IHI will be in charge of arrangement and procurement.

4.7.6.4. Temperature requirements

The following table shows the permissible range for the temperature:

Table 4.7.7 Requirements for temperature range

Item	Temperature range in operating mode	Temperature range in non-operating mode	References
Fresnel lenses	$T_0 \pm 10^\circ\text{C}$ ($-30 < T_0 < 30^\circ\text{C}$)	$-45 \sim 55^\circ\text{C}$	
Focal surface	$T_0 \pm 10^\circ$ ($0 < T_0 < 20^\circ\text{C}$)	$-30 \sim 50^\circ\text{C}$	EUSO-IIDD-0001-1.4
System electronics circuits & battery	$-10 \sim 50^\circ\text{C}$	$-30 \sim 50^\circ\text{C}$	
Atmospheric monitoring	$-30 \sim 60^\circ\text{C}$ (TBC)	$-30 \sim 60^\circ\text{C}$ (TBC)	

4.7.6.5. HK requirements

TBD

4.7.6.6. Budget

The following table shows each budget of mass, electricity, and telemetry. The column of margin in the table indicates the uncertainty of the BEE. If the uncertainty is relatively large: 30%, small: 15%, no uncertainty: 0%.

• Mass Budget

Table 4.7.8.1 Mass budget

	Sub-System	component	Margin included			commentts
			BEE kg	margin %	Mass kg	
1	FS	Detector	138	15%	159	28g/PMT x 4932PMT=28 x (137PDMx36)=138
2	FS	Electronics(board)	91	15%	105	bord91
3	FS	Electronics(cable)	86	30%	112	cabl86
4	Sy	FS support frame	120	15%	138	ESA_frame80+guide,spring40
5	Sy	ATCS	50	15%	58	Elec. device only coolong50
6	Sy	Deploy/Stow Mech.(4 masts)	80	15%	92	20kg x 4=80
7	Sy	Lock Mech.(3 steps)	60	15%	69	5kg x 4/step x 3steps=60
8	Op	Rear Lens (CYTOP)	144	15%	166	CYTOP15mm weight (PMMA15mm)
		Rear Lens (PMMA)	(84)	(15%)	(97)	PMMA15mm weight
9	Op	Focus Adjustment Mech.	20	15%	23	Adjustment mech. 20kg
10	Op	Frame+Ring for Rear Lens	55	15%	64	ESA frame25 +ring30
11	Op	Plane Lens (PMMA)	47	15%	55	Plane PMMA 10mm weight
		Curved Lens (PMMA)	(55)	(15%)	(64)	Curved PMMA 10mm weight
12	Op	Frame+Ring for Diff. L	55	15%	64	ESA frame25 +ring30 (include Iris)
13	Op	Front Lens (CYTOP)	150	15%	173	CYTOP15mm weight (PMMA15mm)
		Front Lens (PMMA)	(89)	(15%)	(103)	PMMA15mm weight
14	Atm	Atmospheric Monitoring	22	30%	29	Atmos28(IR5,LIDAR17)
15	Cal	Calibration	8	30%	11	Calb 8(LED7,YAP1)
16	Sy	Preparatory Battery	30	30%	39	Batt30
17	Sy	Pallet Frame	230	15%	265	EP main structure (include Front Lens Ring)
18	Sy	FRGF	15	0%	15	actual measurement value
19	Sy	PIU	36	0%	36	analytical value
20	Sy	EBOX	32	15%	37	67%up of EPC21
21	Sy	Actuator	32	15%	37	same as EBOX
22	Sy	Tile Mech.	40	15%	46	10kg x 2 + strctr20
23	Sy	MLI of outer cylindar	63	15%	73	0.5kg/m2 x area72m2 + exp/cont strctr27
24	Sy	PVGF	15	0%	15	actual measurement value
25	Sy	Harness, Flex. shaft, Fastener	48	30%	63	3% of BEE value
26	Sy	MLI Insulation Material	30	30%	39	MLI 30
Summation			1697		1983	

(value): PMMA Lens value

By redesigning optics, we found that by using PMMA as material for lens, we could reach almost the same ability of CYTOP optics. Numbers in parentheses in table 2-2 refer to the cases of PMMA. Gross weight with PMMA is 1584 kg (BEE) and 1853 kg with margin.

Table 4.7.8.2 Mass budget for each component of the subsystem

Component	BEE kg	margin %	Margin included MASS kg
Optics	471	16%	545
Focal Surface	315	19%	376
Atmos. Monitor	22	30%	29
Calbration	8	30%	11
BUS System	881	16%	1022
SUM	1697		1983

• Electric power Budget

Table 4.7.9.1 Electric power budget

Sub-System	component	during Scientific Observation			comments
		BEE watt	margin %	Margin included Power watt	
1	OP	0	15%	0	
2	Sy	138	15%	159	Obserb: EBOX50w, Convert loss83w, Supply loss5w Non Obserb: EBOX40w, Convert loss101w, Supply loss6w
3	Sy	0	15%	0	
4	FS	498	30%	648	Estimated Power518w for M36PMT By DCDC optimization, 518-20=498w
5	Atm	78	30%	102	IRcamera20w, Lidar70w(Obsrv) , Non-obsrv 1/2 of Obsrv
6	Cal	8	30%	11	Obsrv. 8
7	Sy	5	15%	6	Estimation from MAXI data
Summation		727		926	

	Sub-System	component	during Non Scientific Observation		
			BEE watt	margin %	Margin included Power watt
1	OP	Focuss Adjustment Mech.	10	15%	12
2	Sy	Bus EBOX	147	15%	170
3	Sy	Movement Control(MC)	10	15%	12
4	FS	F S Electronics	77	30%	101
5	Atm	Atmospheric Monitoring	39	30%	51
6	Cal	Calibration	0	30%	0
7	Sy	Atitude Sensor	5	15%	6
Summation			288		352

Table 4.7.9.2 Electric power budget for each component of the subsystem

Component	during Scientific Observation			POWER
	BEE watt	margin %	margin included watt	
Optics	0	15%	0	
Focal Surface	498	30%	648	
Atmos Monitor	78	30%	102	
Calbration	8	30%	11	
BUS System	143	15%	165	
SUM	727		926	

Component	during Non Scientific Observation			POWER
	BEE watt	margin %	margin included watt	
Optics	10	15%	12	
Focal Surface	77	30%	101	
Atmos Monitor	39	30%	51	
Calbration	0	30%	0	
BUS System	162	16%	188	
SUM	288		352	

• Telemetry Budget

Table 4.7.10.1 Telemetry budget

	component	BEE kbps	margin %	Margin included	comments
				Telemetry kbps	
1	Scientific Data	202	15%	233	Trigger rate 0.1Hz
2	Mission HK	6	30%	8	1200 data/2sec
3	Atmospheric Monitoring	19	30%	25	IR camera16+Lidar3
4	Calibration	6	30%	8	ESA-EUSO Estimation
5	BUS H&S	9	15%	11	1000 data/1sec
Summation		242		285	

Table 4.7.10.2 Telemetry budget for each component of the subsystem

Component	BEE kbps	margin %	margin included Telemetry kbps
Focal Surface	202	15%	233
Atmosph. Monitor	19	30%	25
Calibration	6	30%	8
BUS System	15	27%	19
	242		285

4.7.6.7. Cost

The cost of bus is not mentioned in this document because the estimation by the engineering company is not determined yet. For reference, the cost estimation of the whole bus system was around 3 billion yen, 1 year ago.

4.7.6.8. Schedule

The following is the schedule for bus system by the engineering company in charge (Figure 4.7.16).

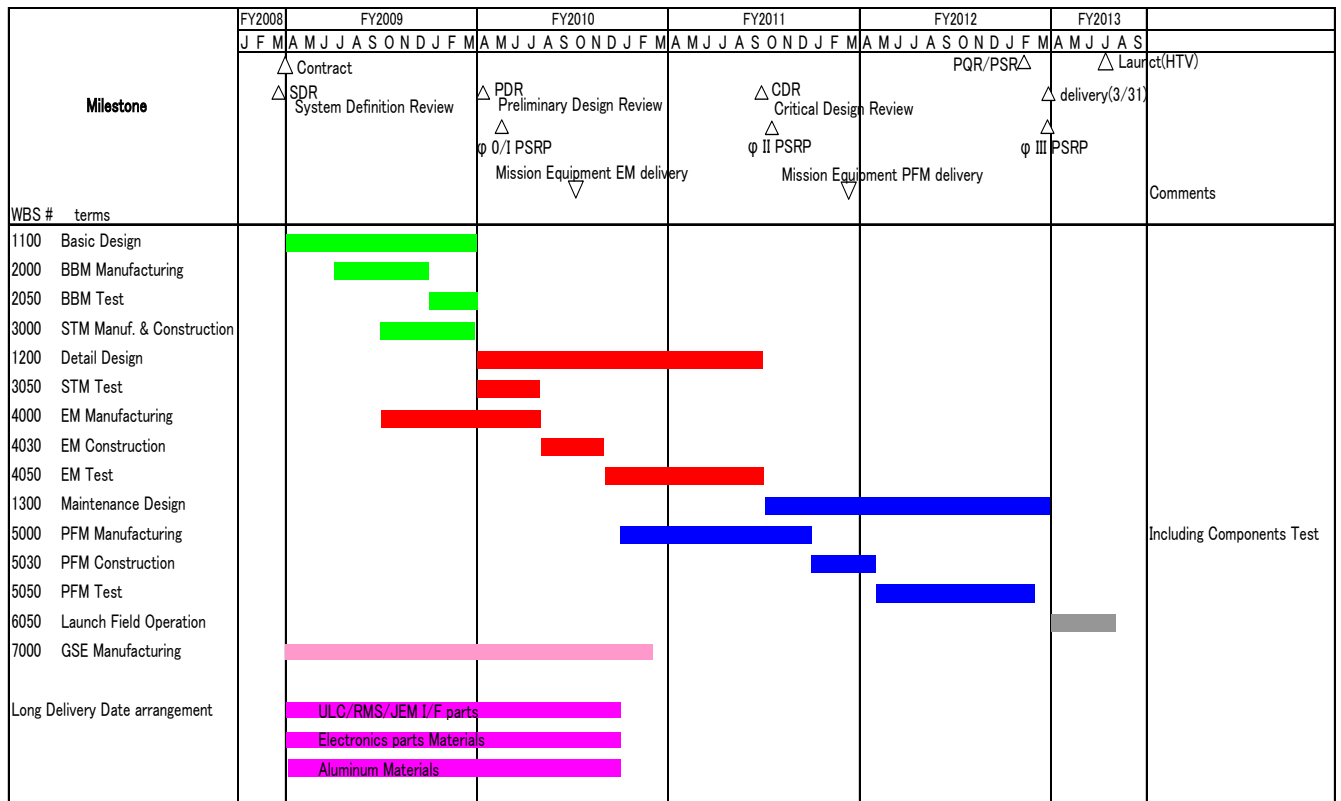


Figure 4.7.16 System development schedule (ref. [7.1])

4.7.6.9. Structure

Basic specifications will be provided by the mission side. Based on this, the engineering company, which is under contract to JAXA will promote system development by cooperating closely with mission side.

4.7.6.10. References

[7.1] IHI AEROSPACE ENGINEERING Co., LTD. :

Conceptual design support/ achievement report (Vol.3) about the mission candidates of 2nd phase utilization of JEM-EF

5. Expected Performance

5.1. General Outline of END-to-END Simulation

In JEM-EUSO, a higher performance compared to ESA-EUSO (min) will be accomplished through improvements in both hardware and software, like new lens material, an advanced optical design, a developed focal surface device with a high quantum efficiency and a more efficient triggering algorithm.

The END-to-END simulation code has been developed considering hardware characteristics of the JEM-EUSO optical system, the focal surface detector and output signal control circuit. Pseudo-observational data has been generated by executing the code for various EAS longitudinal developments pooled in the EAS database. The accuracies of cosmic ray energy, arrival direction and longitudinal development could be estimated by reconstructing EAS profiles with the most suitable algorithm. The END-to-END simulation code is also used for successive improvements of the hardware system to upgrade their accuracies.

To progress of scientific researches, JEM-EUSO has set requirements for experimental accuracies as below,

- (a) The expected number of events: >1000 events with energies of $>7 \times 10^{19}$ eV
- (b) Threshold energy: 5×10^{19} eV
- (c) Angular resolution: $< 2.5^\circ$
- (d) Energy resolution: $< 30\%$
- (e) X_{\max} resolution: $< 120 \text{g/cm}^2$

The simulation code consists of three components: EAS generation, telescope simulation and EAS event reconstruction parts.

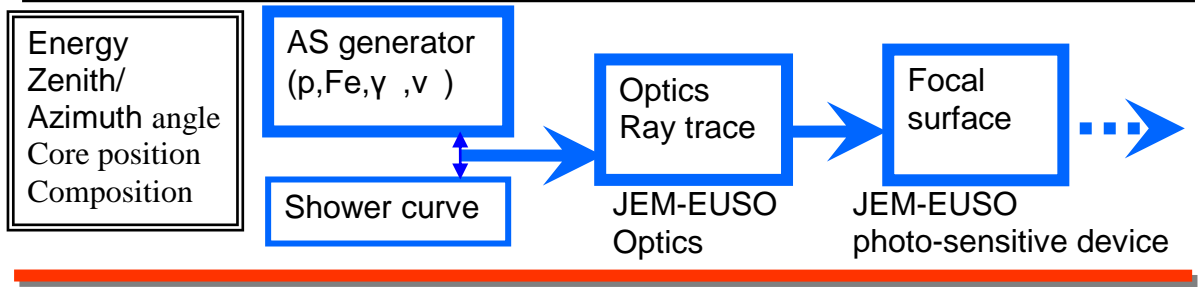
EAS generation code generates EAS longitudinal profile in atmosphere initiated by assumed chemical compositions for zenith angle of $0-90^\circ$ and energy of $>10^{18.5}$ eV. Air fluorescence and Cherenkov light emissions are also calculated taking into account their yields, absorption and scattering in atmosphere, and then the characteristics of the photons (i.e. wavelength, arrival time and spatial position of emission) on the optical lens of the telescope are evaluated.

In telescope simulation code, characteristics of hardware responses to incident photons, photoelectrons and analogue/digital signals have been taken into accounts. Hardware performance on optical system, focal surface detector and output signal control circuit has been estimated. Finally pseudo-observational data including overall hardware responses will be generated.

In addition, EAS event reconstruction code determines EAS energy, arrival direction and longitudinal development from simulated pseudo-observational data produced by former two processes, and is used for evaluating their accuracies. This code also contributes as a feedback for the studies related to the development of analytical algorithms and hardware improvements aiming at the excellent telescope's capability with the best accuracies. The scheme of current END-to-END simulation is shown in Figure 5.1.

Scheme of JEM-EUSO Simulator

Input Parameters



Event data processing

Output

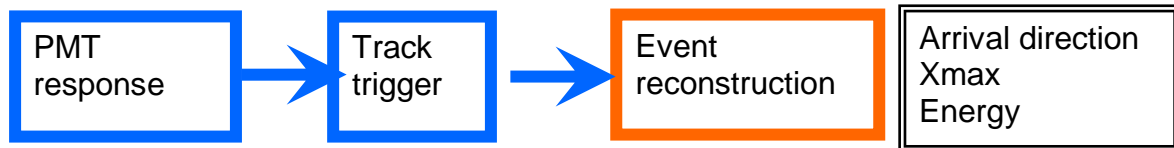


Figure 5.1 A procedure of JEM-EUSO END-to-END simulation

5.2. Baseline Estimation

We set some assumption and conditions in End-to End simulation as the baseline estimation.

- (a) Optical lens with ϕ 2.65m-side cut type (First and third lens: CYTOP, second one: PMMA000)
- (b) Ultra Bialkali MAPMT (36pixels)
- (c) Time resolution of 2.5μ sec(GTU)
- (d) Track trigger method to event trigger
- (e) Standard background photons as 500

photons/m² /sr/ns

- (f) EAS events with Cherenkov mark

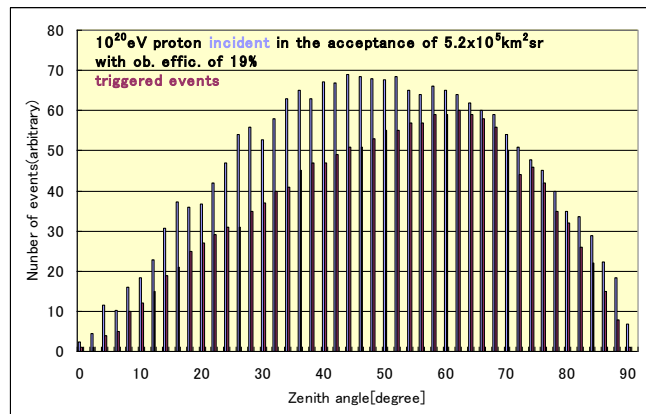


Figure 5.2 Zenith angle dependence of JEM-EUSO acceptance

5.2.1 JEM-EUSO Effective Acceptance

JEM-EUSO telescope will be installed at the outboard platform of the Japan Experiment Module (JEM) of the International Space Station, and will go round the earth at a level of 430km with a period of 90min. EAS observation will be carried out in the night area of earth, then a minimum duty cycle of 19% was estimated after taking into accounts the passage in a region of high background light intensity and actual data deficit ratio of EASs with a zenith angle $<45^\circ$ due to incomplete EAS reconstruction by a cloud shielding.

Observational acceptance of JEM-EUSO for EAS events depends on EAS energy and arrival direction. Acceptance reaches the maximum value at a zenith angle of about 45° as a result of a larger integrated solid angle in azimuth and a smaller effective area projected on the perpendicular

plane to the EAS axis with an increasing zenith angle.

Geometrical acceptance is expected as $5.2 \times 10^5 \text{ km}^2 \text{ sr}$ with field of view $\pm 30^\circ$. A time integrated acceptance could be $1.7 \times 10^6 \text{ km}^2 \text{ sr year}$, assuming a duty cycle of 19% and (2+3) years observations in (nadir mode and tile mode). This is just 1060 times and 25 times larger than those of 10 years observation of AGASA and Auger experiment, respectively. In an actual observation, there will be untriggered events, events without Cherenkov mark in a field of view and also missing events by incomplete reconstruction due to the small number of incident photons.

In Figure 5.2, acceptance for EAS of 10^{20} eV initiated by proton is shown as a function of zenith angle. A case of clear sky was assumed here. Acceptance for golden EASs with enough accuracy is also obtained to be $5.2 \times 10^5 \text{ km}^2 \text{ sr}$.

In the case of JEM-EUSO tile mode observation, a larger volume of target atmosphere to observe EAS could be achieved (Figure 5-3(left)). A field of view increases with a tilt angle, as shown in Figure 5.3(right).

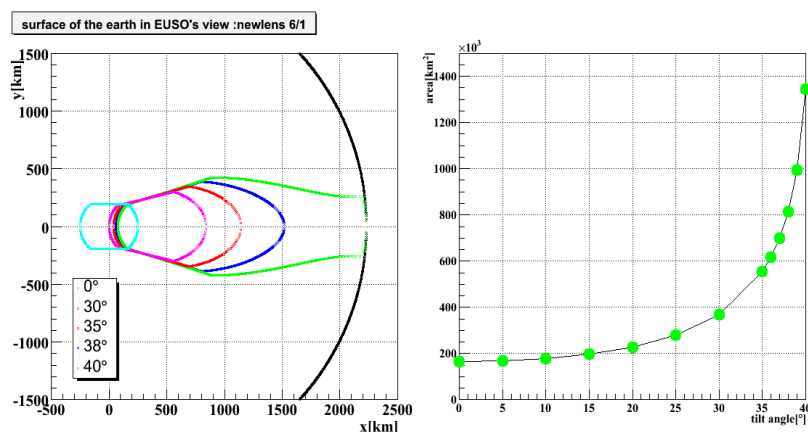


Figure 5.3 Field of views with different tilt angles(left), and its zenith angle dependence(right).

5.2.2 Triggering Efficiency

In JEM-EUSO, air fluorescence light from EAS has to be observed in a background light emitted from ground and airglow sources. Therefore, optimized EAS triggering method will be required to acquire the EAS events efficiently with the best S/N avoiding fake triggers.

Figure 5.4 shows the energy dependence of triggering efficiencies of JEM-EUSO with an assumption of background light intensity of $500 \text{ photons/m}^2 \text{ sr/ns}$. Track trigger method has been applied to the individual time profile of photo-electrons from MAPMT. The triggering efficiencies for the tilt mode observations with tilt angle of 30° , 35° , and 38° are also shown in the same figure.

The triggering efficiencies at 10^{20} eV is 86% for Nadir mode observation, and EAS threshold energies is estimated to be $5.0 \times 10^{19} \text{ eV}$ at 50% detection efficiency level. In addition, the triggering efficiencies of EAS hit within a radius of 100km in a field view are shown with red squares and threshold energy becomes smaller to $2.7 \times 10^{19} \text{ eV}$ because of a better performance of optical system and smaller impact parameters.

Other 3 lines show the triggering efficiencies for cases of tilt mode observation with different tilt angles. It shows that threshold energy increases due to a longer distance from the EAS axis to JEM-EUSO, however, an increase of acceptance by tilt mode observation has an important advantage over it. In figure 5.5, energy dependence of effective acceptances with a combination of triggering efficiencies and an increase of field of view is shown. Relative advantage of tilt mode observation could be seen as 1.8 times and 2.4 times larger effective acceptances at 10^{20} eV and $10^{20.5} \text{ eV}$, respectively than nadir mode observation.

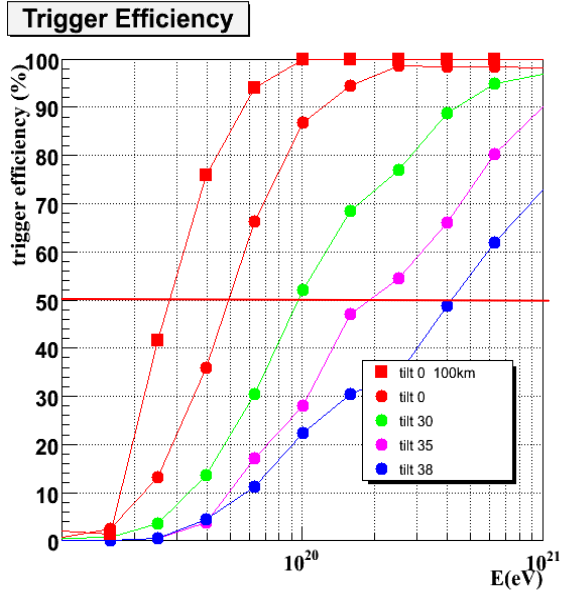


Figure 5.4 The energy dependence of triggering efficiencies with different tilt-angles

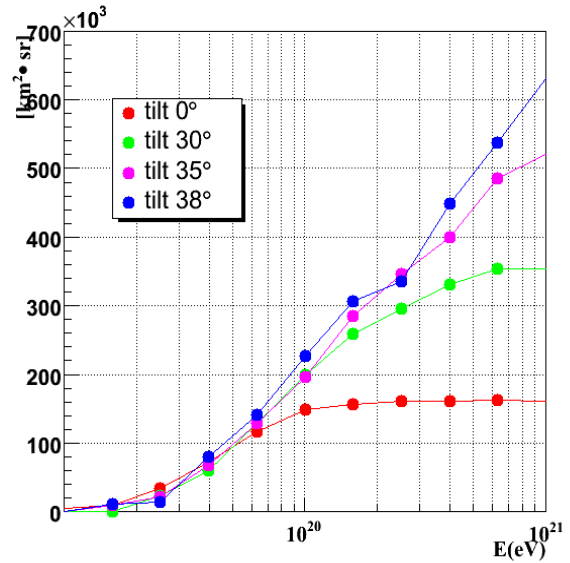


Figure 5.5 The effective acceptances as a function of the energy and tilt angles.

5.2.3 Expected Number of Triggered Events

In JEM-EUSO, it is possible to estimate the expected number of triggered EAS events by taking into account primary cosmic ray energy spectra, geometrical acceptance ($5.2 \times 10^5 \text{ km}^2 \text{ sr}$), a duty cycle of 19% and the triggering efficiencies which depend on energy and zenith angle.

The expected number of triggered events is shown as the integrated numbers at any energies in Table 5.1. The expected number of events with energy $> 7 \times 10^{19} \text{ eV}$ and $> 10^{20} \text{ eV}$ are almost 290/year and 64/year by JEM-EUSO, respectively if the energy spectrum is assumed as a flux $J(E)E^3$ of $2.0 \times 10^{24} [\text{eV}^2 \text{ m}^{-2} \text{ s}^{-1} \text{ sr}^{-1}]$ at $2 \times 10^{20} \text{ eV}$ and GZK cutoff in the spectrum.

A study in lower energy region is also important from the point of cross calibration with AUGER result and a study of anisotropy with the highest statistics. JEM-EUSO has also potential to study EAS around $3 \times 10^{19} \text{ eV}$ with more than 1000 events per year.

Moreover, the tilt mode observation with tilt angles of 30° , 35° , and 38° can increase the statistics as shown in Table 5.1. About 110 events with energy $> 10^{20} \text{ eV}$ can be expected in the observation with a tilt angle of 38° . We plan the 2 years nadir mode and 3 years tilt mode observation, then the expected numbers will be 1800 and 450 events for energies of $> 7 \times 10^{19} \text{ eV}$ and $> 10^{20} \text{ eV}$, respectively, in the planned period. Furthermore, 25 events with $> 10^{20.5} \text{ eV}$ will be expected by JEM-EUSO with a reality of the highest energy study.

Table 5.1 The expected numbers of triggered events per 1 year

Log(>E)	Nadir	Tilt angle of 30°	Tilt angle of 35°	Tilt angle of 38°
19.7	1140	1200	1350	2080
19.8	490	560	680	1060

20.0	64	75	95	110
20.2	12	17	21	28
20.4	5.0	8.5	10	13
20.6	2.0	3.9	4.6	6.0
20.8	0.8	1.5	2.0	2.4
21.0	0.2	0.4	0.4	0.6

5.2.4 Angular Resolution

Arrival direction of triggered EAS is determined by reconstructing the length of the EAS image and its spatial position in atmosphere from the recorded photoelectron position and time transition in the focal surface coordinates. Image length changes depending on energy and zenith angle. A distortion of EAS image by background photons affects to an accuracy of EAS axis reconstruction.

Angular resolutions for triggered EAS events have been estimated with assumptions of 500photons/m²/sr/ns as a standard background photons. Angular resolutions for proton EAS of 10^{19.5}eV, 10²⁰eV, 10^{20.5}eV and 10²¹eV were obtained as a function of zenith angles in Figure 5.6. Left and right figure show resolutions for EAS hit within a radius of 200km and 100km in a field of view, respectively. Resolutions becomes better in larger zenith angles because of longer EAS image at the focal surface and requirement of < 2.5° in angular resolution are satisfied above 45°. Resolution of 1.0° can be estimated for EAS of >10²⁰eV and >60° and it is enough resolution for the study of cosmic ray origin.

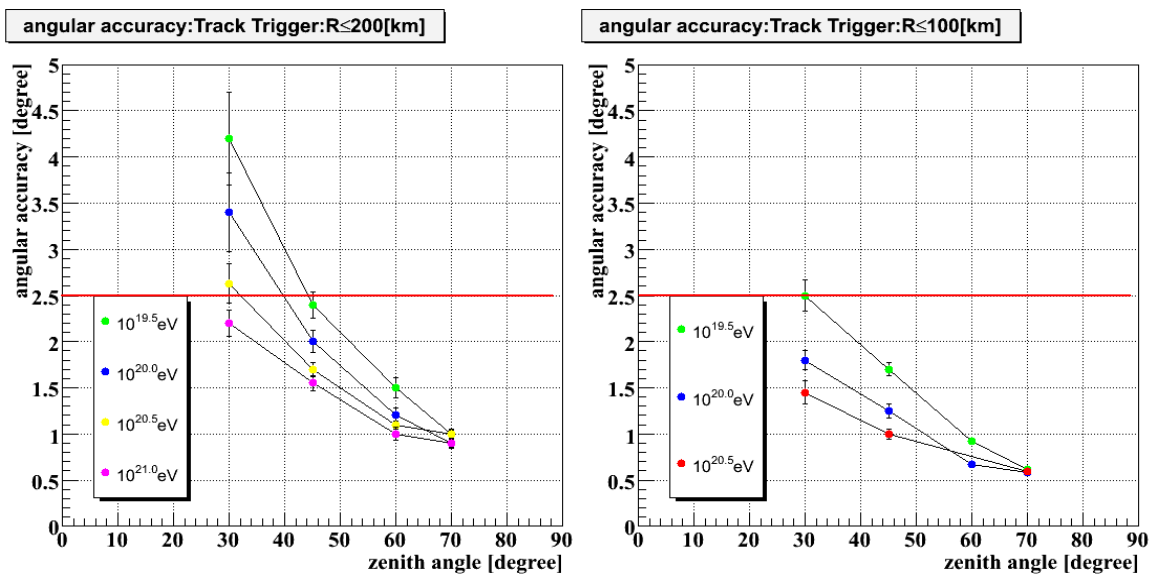


Figure 5.6 Angular resolutions as a function of energy and zenith angle(left and right figures for events within a field of view of 200km and 100km, respectively).

5.2.5 X_{\max} Resolution

After the determination of EAS axis, EAS energy and X_{\max} are obtained from the reconstructed longitudinal development estimated from produced photon numbers and fluorescence light yield at any positions along the axis. X_{\max} resolutions for proton EAS of 10^{19.5}eV, 10²⁰eV, 10^{20.5}eV and

10^{21} eV were obtained as a function of zenith angles in Figure 5.7. Left and right figure show resolutions for EAS hit within a radius of 200km and 100km in a field of view, respectively. Resolutions do not depend on zenith angles and resolutions of 100g/cm^2 - 200g/cm^2 are estimated within a radius of 200km in a field of view.

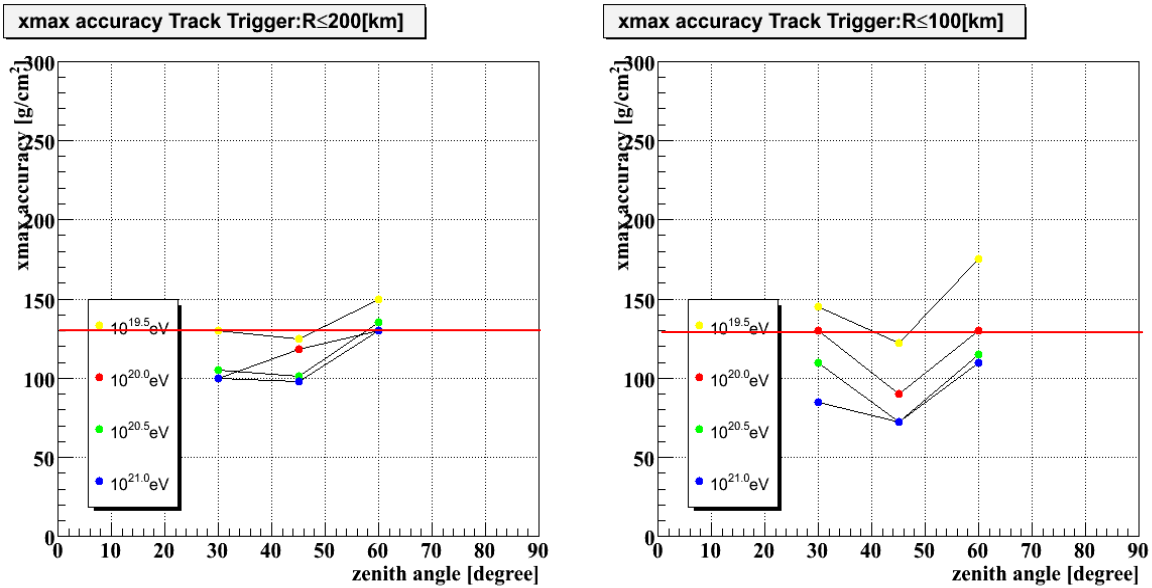


Figure 5.7 X_{max} resolution as a function of energy and zenith angle(left and right figures for events within a field of view of 200km and 100km, respectively).

5.2.6 Energy Resolution

Energy determination has been estimated by the reconstructed longitudinal structure. Energy resolutions for EAS of $10^{19.5}\text{eV}$, 10^{20}eV , $10^{20.5}\text{eV}$ and 10^{21}eV were obtained as a function of zenith angles in Figure 5.8. Left and right figure show resolutions for EAS hit within a radius of 200km and 100km in a field of view, respectively. Energy resolutions becomes to be $<30\%$ for EAS with zenith angle above 45° and accuracy of 15% could be expected for EAS of $>10^{20}\text{eV}$ in a radius of 100km.

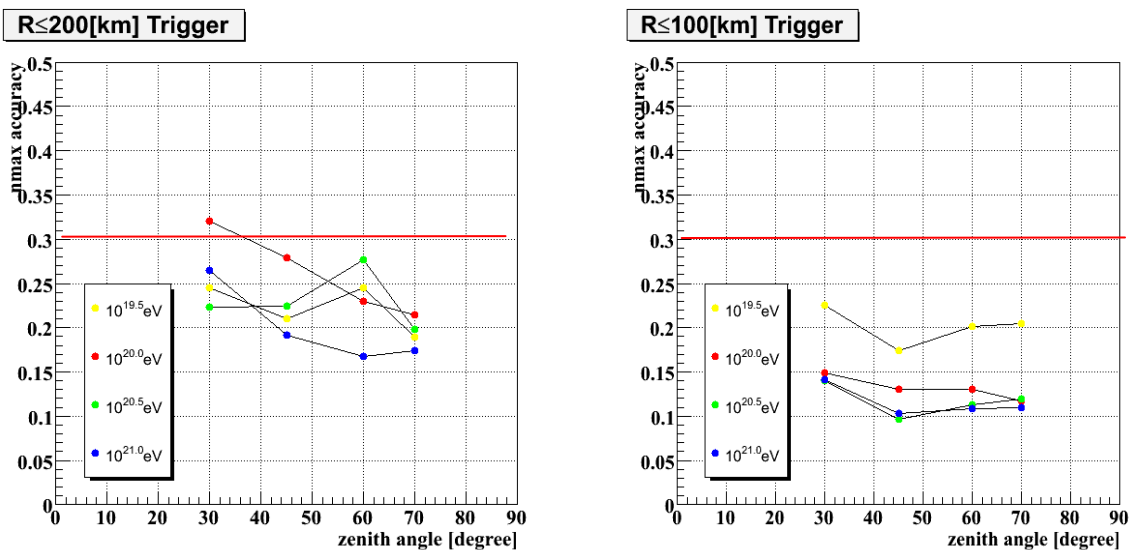


Figure 5.8 Energy resolution as a function of energy and zenith angle(left and right figures for

events within a field of view of 200km and 100km, respectively).

5.2.7 Detection Sensitivity for UHE Neutrinos

JEM-EUSO with a field of view of ± 30 degrees will cover the atmospheric mass of 2×10^{15} kg as a target matter for incident neutrinos. Observational targets will be the electromagnetic and hadronic EASs induced by an inelastic interaction between neutrino (i.e. electron, muon and tau neutrino) and atmospheric nucleus. For the detection of neutrino EASs, a rejection power of $>10^{-4}$ is required to discriminate candidates from usual EASs of $>10^{19.5}$ eV accumulated with a rate of 6,300 events/year.

Neutrino EASs are expected to develop at lower altitudes compared to those of proton/nucleus EASs with same zenith angles because of smaller interaction cross-section. Therefore, X_{\max} is the most suitable observable to discriminate the candidates from background EASs. When 1×10^7 neutrinos of 10^{20} eV incident to a target volume of atmosphere with zenith angle of $0-95^\circ$ and X_{\max} distribution of neutrino EASs produced is shown in Figure 5.9. A generation probability of neutrino EASs is 0.009% with energy dependent. Its distribution is almost uniform in the area of target volume. On the other hand, proton induced EASs of $10^{19.5}$ eV shows a distribution with an average X_{\max} of 810 g/cm^2 with 60 g/cm^2 in 1σ standard deviation as shown by yellow region in the same Figure.

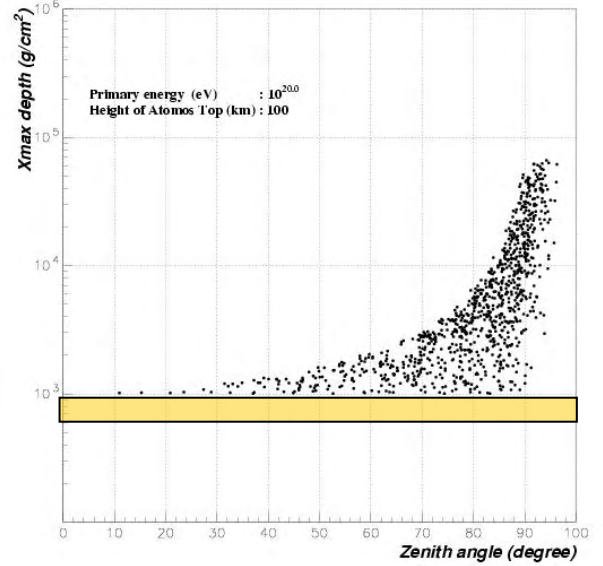


Figure 5.9 X_{\max} distribution of neutrino EAS in JEM-EUSO target volume.

Neutrino EASs can be observed preferably as the large inclined EASs because of a long interaction mean free path, but they will be candidates in which the Cherenkov mark will not be observed. In addition of events with no Cherenkov mark due to the cloud, the width of EAS profile (time duration) in different zenith angles is useful for the estimation of X_{\max} as the autonomous method.

Assuming a neutrino intensity of $1/\text{km}^2/\text{day}$ above 10^{19} eV and an effective acceptance of $2\pi \times 2 \times 10^{15} \text{ kg sr}$, the number of incident neutrinos in the JEM-EUSO target volume is estimated to be $2 \times 10^4/\text{year}$. After taking into account the interaction probabilities of neutrinos and triggering efficiencies for produced neutrino EASs, X_{\max} of neutrino EASs are calculated. In a case of $X_{\max} > 1,400 \text{ g/cm}^2$ for a rejection of background EASs, 2.1 neutrino EASs per year are detectable by JEM-EUSO observation.

Figure 5.10 shows the detection sensitivities of JEM-EUSO (nadir and tilt mode observation)

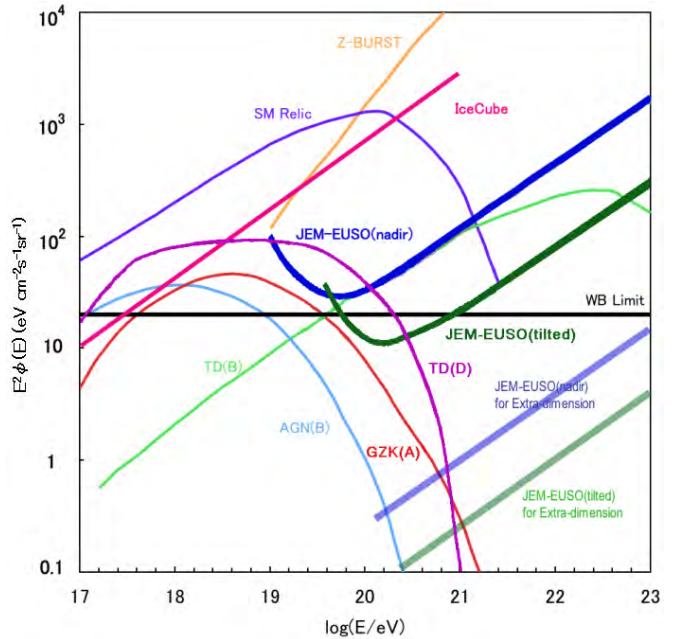


Figure 5.10 The expected neutrino intensities with some models and sensitivity of JEM-EUSO to UHE neutrinos (blue: nadir mode green: tilt mode).

drawn by blue and green line, respectively. in neutrino intensities. Expected fluxes of neutrinos from Z-burst model, GZK neutrinos, AGN origin and some top-down process are also shown in the same Figure.

5.2.8 Comparison with Other Instruments

The Auger experiment in Argentina (southern hemisphere) covers an acceptance of $7 \times 10^3 \text{ km}^2 \text{ sr}$ corresponding to 44 times AGASA extension and Telescope Array(TA) experiment in Utah, USA has carried out observation with an surface detector(SD) acceptance of $1.4 \times 10^3 \text{ km}^2 \text{ sr}$ as listed in Table 5.2. An acceptance of JEM-EUSO will be $5.2 \times 10^5 \text{ km}^2 \text{ sr}$, which is just 74 and 370 times larger than those of Auger and Telescope Array experiment, respectively, and an integrated exposure of JEM-EUSO is estimated as $1.7 \times 10^6 \text{ km}^2 \text{ sr year}$ by 2 years nadir and 3 years tilt mode observation with a duty cycle of 19%. This exposure is comparable to 25 times of Auger and 85 times of TA hybrid observation for 10 years.

The number of events for EAS $>10^{20} \text{ eV}$ observed by Auger experiment are expected as 3/year assuming ‘‘GZK’’ energy spectrum. In case of JEM-EUSO (nadir), the statistics will be more than 18 times of Auger due to a larger integrated acceptance. Consequently JEM-EUSO will show much higher advantage in performing astrophysical studies by means of super GZK energy cosmic rays.

Though Auger experiment will accomplish a hybrid observation by surface detectors and air fluorescent telescopes, an observational efficiency does not exceed about 10%. JEM-EUSO has an advantage in the EAS statistics exceeding by far that of Auger, therefore, much higher accuracy is expected from JEM-EUSO observation. Moreover, detection of neutrinos in this energy region will be a promising research task for JEM-EUSO thanks to the large acceptance which counterbalance with the small interaction cross-section of neutrino.

Experiments	Acceptance ($\text{km}^2 \text{ sr}$)	Operational Year	Period	Observational Efficiency (%)	Exposure ($\text{km}^2 \text{ sr year}$)	Relative exposure to AGASA	Relative exposure to Auger
AGASA	160	stop	13	100	1.6×10^3	1	0.02
Auger South	7,000	2006-2015	10	100	7.0×10^4	44	1
Telescope Array							
SD	1,400	2006-2015	10	100	1.4×10^4	9	0.2
FD	6,700		10	10	6.7×10^3	4	0.1
Hybrid	1,400		10	10	6.7×10^3	4	0.1
Total					2.0×10^4	13	0.3
TUS	30,000	2009-2014	5	20	3.0×10^4	20	0.5
JEM-EUSO							
nadir	520,000	2013-2014	2	19	2.1×10^5	130	3
tilted	2,580,000	2015 -2017	3	19	1.5×10^6	940	21
Total					1.7×10^6	1,060	25

Table 5.2 Comparative table in other instruments and JEM-EUSO

5.3. Advanced Estimation

5.3.1. Reconstruction of Observed Events in Cloudy Sky

The expected cloud possession will be nearly 30% in a field of view of JEM-EUSO. In this case, EAS Cerenkov mark can not observe, and shower profile under the cloud will not be measured. Average height of cloud is generally lower (around 4,000m) in the night time than that in daytime. Therefore, shower profiles with X_{\max} will be possible to reconstruct for EASs with zenith angle of $>60^\circ$. With data of Cerenkov mark at the cloud, X_{\max} can be estimated by the shape method. This method is used for the characteristic which the time width of shower profiles is related to the height of X_{\max} . This method has already been studied in the phase-A study of ESA-EUSO, and the accuracy of X_{\max} determination was estimated to be $120\text{g}/\text{cm}^2$. This provides us a reliable analysis even for data taken in the cloudy sky and the observation efficiency will be increased by 20% larger than that in the observation under the fine sky.

5.3.2. Performance with Advanced Optics and Photosensitive Device

Performance advancement in JEM-EUSO has been estimated with the improvements on the hardware systems telescope. Firstly, an interference filter which has highly transmission coefficient only around the wave lengths of EAS fluorescence lights. Consequently, S/\sqrt{N} becomes better by 1.4 times due to the shielding of background lights. S/\sqrt{N} will be better by 1.6 times and 2.0 times with an alteration to a half size pixel of focal surface device and a time resolution of $0.5 \times \text{GTU}$ (baseline design), respectively. Figure 5.11(left) shows the triggering efficiencies with assumptions of 3 improvements mentioned above. Threshold energy at 50% triggering efficiency is improved as $10^{19.3}\text{eV}$ and $10^{19.9}\text{eV}$ for nadir mode and tilt mode (38°) observation, respectively. Effective acceptance of JEM-EUSO with advanced design can be estimated as shown in Figure 5.11(right). Effective acceptance in tilt mode observation will exceed that of nadir mode observation at an energy of $10^{19.3}\text{eV}$, and 2.4 times, 3.3 times and 4 times larger acceptance will be achieved in tilt mode observation with 38° for events of $10^{20.0}\text{eV}$, $10^{20.5}\text{eV}$ and $10^{21.0}\text{eV}$, respectively. The expected numbers of observed events are listed in Table 5.3 with such advanced design of JEM-EUSO. The list shows the numbers of events which could be observed from 2 years nadir and 3 years tilt mode observation.

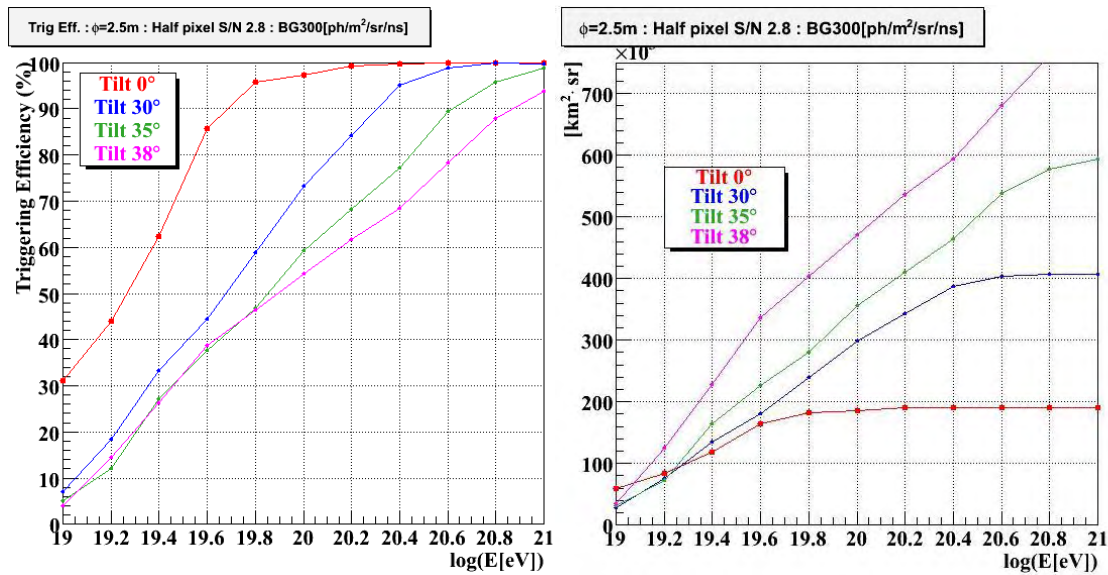


Figure 5.11 Trigger efficiency (left figure) and effective observation area(right figure) by

Advanced design.

Table 5.3 The number of observed events in advanced design.

$>7 \times 10^{19} \text{eV}$		Standard	X2.2	X2.8
Nadir	1/year	290	410	420
Tilt 38°	1/year	390	920	990
Total	1/5years	1800	3580	3810

$>10^{20} \text{eV}$		Standard	X2.2	X2.8
Nadir	1/year	64	71	72
Tilt 38°	1/year	110	180	190
Total	1/5years	450	680	710

5.4. Summary

The END-to-END simulation related to the JEM-EUSO experiment is done and development and the execution have been done. EAS generation code generates EAS longitudinal profile in atmosphere initiated by assumed chemical compositions for zenith angle of $0-90^\circ$ and energy of $>10^{18.5} \text{eV}$. Air fluorescence and Cherenkov light emissions are also calculated taking into account their yields, absorption and scattering in atmosphere, and then the characteristics of the photons (i.e. wavelength, arrival time and spatial position of emission) on the optical lens of the telescope are evaluated. In telescope simulation code, characteristics of hardware responses to incident photons, photoelectrons and analogue/digital signals have been taken into accounts. Hardware performance on optical system, focal surface detector and output signal control circuit has been estimated. Finally pseudo-observational data including overall hardware responses will be generated. In addition, EAS event reconstruction code determines EAS energy, arrival direction and longitudinal development from simulated pseudo-observational data produced by former two processes, and is used for evaluating their accuracies. This code also contributes as a feedback for the studies related to the development of analytical algorithms and hardware improvements aiming at the excellent telescope's capability with the best accuracies.

We set some assumption and conditions in End-to End simulation as the baseline estimation.

- (a) Optical lens with ϕ 2.65m-side cut type (First and third lens: CYTOP, second one:PMMA000)
- (b) Ultra Bialkali MAPMT (36pixels)
- (c) Time resolution of $2.5 \mu \text{sec}$ (GTU)
- (d) Track trigger method to event trigger
- (e) Standard background photons as $500 \text{photons/m}^2 \text{/sr/ns}$
- (f) EAS events with Cherenkov mark

[Trigger Efficiency and Expected Numbers of Observed Events]

The triggering efficiencies at 10^{20}eV is 86% for Nadir mode observation, and EAS threshold energies is estimated to be $5.0 \times 10^{19} \text{eV}$ at 50% detection efficiency level. In addition, the triggering efficiencies of EAS hit within a radius of 100km in a field view are shown with red squares and threshold energy becomes smaller to $2.7 \times 10^{19} \text{eV}$ because of a better performance of optical system and smaller impact parameters. Threshold energies for tilt mode observation with different tilt angles become higher by 70% due to a longer distance from the EAS axis to JEM-EUSO, however, a increase of acceptance by tilt mode observation has an important advantage over it. Energy dependence of effective acceptances with a combination of triggering efficiencies and an

increase of field of view is shown. Relative advantage of tilt mode observation could be seen as 1.8 times and 2.4 times larger effective acceptances at 10^{20} eV and $10^{20.5}$ eV, respectively than nadir mode observation.

Integrated apertures of JEM-EUSO is estimated as $2.1 \times 10^5 \text{ km}^2 \text{ sr year}$ and $1.5 \times 10^6 \text{ km}^2 \text{ sr year}$ for nadir and tilt mode observation respectively, therefore we plan the 2 years nadir mode and 3 years tilt mode observation, then the expected numbers will be 1800 and 450 events for energies of $>7 \times 10^{19}$ eV and $>10^{20}$ eV, respectively, in planned 2 years nadir mode and 3 years tilt mode observation.

[Angular Resolution]

Requirement of $< 2.5^\circ$ in angular resolution is satisfied with energy of $>10^{19.5}$ eV and zenith angle of $>45^\circ$. In addition, resolution of 1.0° can be estimated for EAS of $>10^{20}$ eV and $>60^\circ$ and it is enough resolution for the study of cosmic ray origin. Expected resolutions will improve and satisfy the requirement even for EAS with energy around $10^{19.5}$ eV when EASs hit at the center of JEM-EUSO field of view.

[X_{max} Resolution]

Resolutions do not depend on zenith angles and resolutions of 100 g/cm^2 - 120 g/cm^2 are estimated within a radius of 200km in a field of view.

[Energy Resolution]

Energy resolutions becomes to be $<30\%$ for EAS with zenith angle above 45° and accuracy of 15% could be expected for EAS of $>10^{20}$ eV in a radius of 100km.

6. Operation

In the present chapter, we describe the scenario of JEM-EUSO launch, attachment to JEM port, commissioning and regular operation and the sketch of ground segment for regular operation is mentioned.

6.1. Launch and attachment to JEM-EUSO Port.

As the baseline scheme of JEM-EUSO Telescope accommodation on HTV, we employ the side cut scheme (see Section 4.7.1.1). After HTV docks in on ISS Docking Port, Space Station Remote Manipulator System (SSRMS) takes out JEM-EUSO and pass to JEM Remote Manipulator System (JEMRMS). JEM-EUSO is installed onto EFU#2 port of JEM/EF where JEM-EUSO is expanded to operational shape using autonomous mechanism (see Figures 4.7.3 and 4.7.4 for JEM-EUSO storage and deployment). Throughout these processes, two grapple fixtures on JEM-EUSO are needed for SSRMS and JEMRMS. The configuration of grapple fixture for JEM-EUSO and Payload Interface Unit (PIU) is designed as in the case for standard JEM/EF payload. EFU#2 Port accommodates 2.5t payload with up to 3kW power supply capacity and heat wasting capability.

Figure 6.1 shows the JEM-EUSO location on the EFU#2. For this configuration, possible interference exists with the standard payload on EFU#4. On the other hand, the JEM-EUSO has more than one meter margin to the pressurized module and is secured against external vehicular activities (EVA).

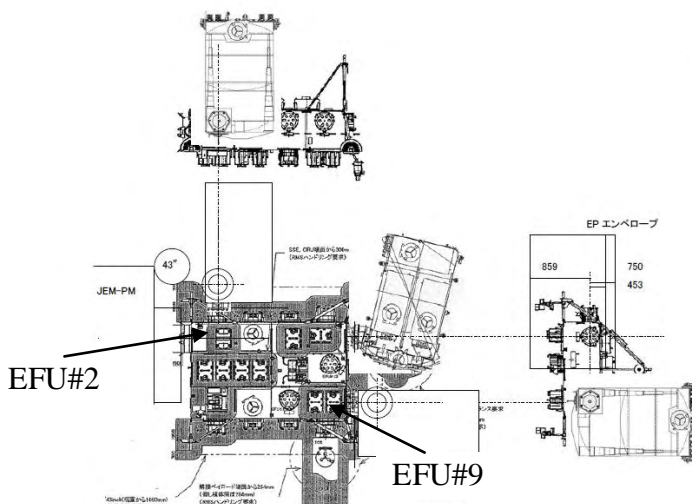


Figure 6.1 Configuration of JEM-EUSO on EFU#2 Port

6.2. Commissioning

For a first few months after deployment, we will devote to commissioning for JEM-EUSO telescope. In this phase we will perform pilot EECR event observation and establish the performance index of >90% level by adjusting the equipment and finalizing operational parameters. This index will be defined by the rate of the observed EECR events with satisfying the required quality. The analysis procedure will be verified with the actually observed air shower event data.

6.3. Regular observation

In the regular observation phase, the operation scheme is characterized by the local solar time on the orbit, mainly observation at nighttime and standby under daylight with ~90-minute-cycle of regular routines as the orbital period. Besides normal operation, the active safety measures are required to cope with sudden incident during the observation. Especially against the possible malfunctioning in daytime, the even more elaborate functions need to be ready to minimize the damage by daylight.

In order to design the system of the elementary function such as opening the lid and sequence of those functions, or command system, we have defined about 200 commands so far. This number will rise according to ongoing hardware development and other requirements. These commands are implemented in the emulating software that has been developed for test command flow of possible operational occasions such as regular observation sequence (see following section).

6.3.1. Observation

In the regular observation phase, EECR observation is started at the termination of the twilight and is halted before the dawn. The observation is not halted under the moonlight unless the case of crescent moons. Under moonlight, the background noise rate is too high to acquire the good quality data. Due to too short nighttime to secure warm-up time and efficient observation time on the orbit, regular observation is fully suspended in a few days around the full moon.

In every orbital period, the standard routine is repeated every ~90minutes. Taking the local solar time being 12 hours as the origin, this routine is described as follows

Mid-day to twilight

- 1) Starting up sub-systems. Setting operational parameters on each subsystem. Apply HV on MAPMT to operational level. Starting MAPMT pre-observation calibration sequence.
- 2) Opening lid. Starting trigger logic. Starting data acquisition (DAQ; start of EECR observation)
- 3) Before dusk. Stopping DAQ (termination of EECR observation). Halting trigger logic. Shutting lid. Starting post-observation calibration.
- 4) Ramping down HV on MAPMT to standby status (see following description). Data downlink upon request. Halting sub-system

The time of EECR observation is shortened by the presence of well waxed moon above the horizon. JEM-EUSO accommodates the system for issuing clearance or blocking the command execution. The act of opening lid, for example, is permitted only if sunshine, twilight and intense moonlight are absent. In case of applying HV on MAPMT to the operational level, the status of lid mechanism should be normal. This is a typical example of fail-safe scheme to take into account the possibly happening worst case that both power-off HV and shutting lid would be out of control. During the regular operation, this system stationary alerts HK data and status from subsystems are stationary alerted. The presences of thundercloud or/and intense manmade light sources are also monitored for putting active safety measures in motion.

During the daytime, the lid is closed to protect JEM-EUSO telescope from severe degrading. To reduce the power consumption, powers for subsystem except essential component are off. Even this case, MAPMT power supply is left on but the voltage on the first dynode is controlled to minimize the effect by stray light.

The downlink of scientific, HK and subsystem monitor data is practiced during the daytime. In ordinary occasion, prompt accessibility to those data are not mandatory. The size and frequency of downlink highly depends upon the JEM-EUSO operation. For example, the flexibility of downlink protocol increases if the common data storage and computing facility is

equipped on JEM-EUSO pressurized module.

6.3.2. Trouble shooting

Throughout JEM-EUSO operation at any phase, it is possible that the potential trouble or malfunction of subsystems occur. This, to wide degrees, would possibly result in spoiling scientific capability of the entire mission. To recover such occasion, we investigated a number of possible situations, likely or not, and studied for troubleshooting. The following is an example case of trouble shooting scheme on lid mechanism malfunctionning.

In the regular operation, one may assume the troubleshooting against malfunctioning by the following measures,

- 1) Less frequent lid operation
- 2) Lid kept open

In each case, we aim at salvaging the quality of data even in troubleshooting operation. In case 1) and 2), we relieve the required lower limits of the performance indices of 70% and 50%, respectively (TBC).

In Fig. 5.2, we summarize the measures for troubleshooting in the flowchart.

The basic scheme is described in the following. For example, if the malfunction of lid is found in daytime, the regular operation is suspended even before the terminator. In this case, sounding the lid mechanism and related subsystems is carried out to fix the trouble as early as possible. In similar occasion in the nighttime, emergent ramping down of HV on MAMPT and defocusing of the focal surface detector are alerted to secure the focal surface detector. In the case HV system is also failure, the main power is also switched off. Unless the trouble is solved in short time scale, the operation is shifted in the above mentioned 1) or 2) for long-term troubleshooting. In case of 2), the lid is only tried to be closed to avoid the polluting the lens such as when HTV approaches ISS. Currently, the further more serious cases of troubles are in argument.

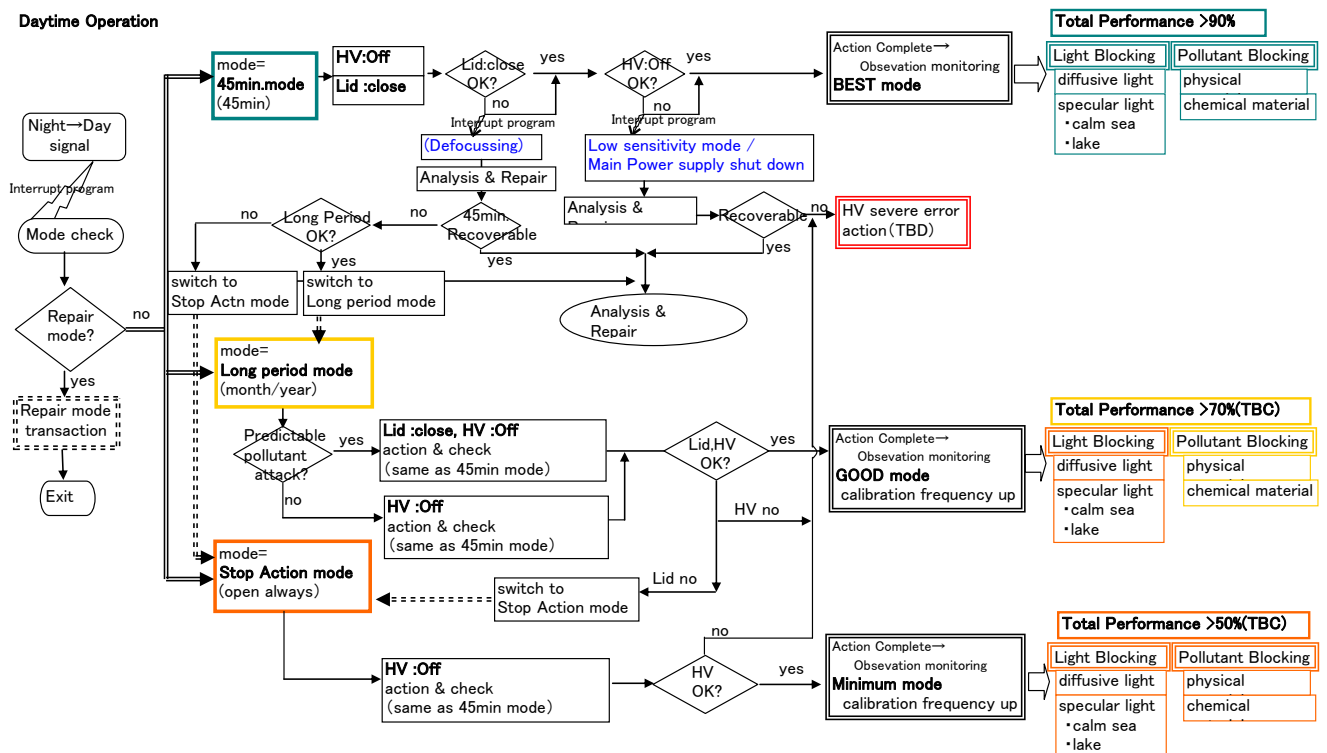


Figure 6.2 Flowchart of lid trouble shooting

6.3.3. JEM-EUSO telescope pointing

The optical axis of the JEM-EUSO telescope stationary is pointed downward to the ground for EECR observation and protection against sunshine. In first two years, JEM-EUSO telescope is pointed toward the nadir (nadir mode) and then moved upward toward by ~40 degrees (tilt mode). The scientific merit of tilt mode is the enhancement of sensitivity against EECRs with higher energies. It is planned to only once change the pointing direction at the beginning of tilt mode operation, however, the operation of JEM-EUSO may require changing the tile angle or reverting back to nadir mode. The mechanism for such control will be equipped.

6.4. Ground segment

In the present section we describe the ground segment and related activities during the regular operation, which have been applied in the past- and present-running space experiments.

The principal ground segments are ISS ground station, JEM Mission Control Room (MCR) and our own Space Operation and Data Centre (SODC). The end-to-end communication is established via NASA's Tracking and Data Relay Satellite (TDRS).

Among them, SODC is the primary component for JEM-EUSO during the regular scientific operation and consists of the following three unit providing the key functionalities.

- Unit 1 [Mission activity planning/telecommand unit]
- Unit 2 [Data process/system monitor unit]
- Unit 3 [Data management and archiving unit]

6.4.1. Mission activity planning and telecommand unit

Mission activity planning and telecommand unit is responsible for uplink of telecommand and operational parameters to JEM-EUSO. This unit includes the mission planning task. The mission plan in which the detailed operational command sequence is defined is renewed every several days taking into account the ISS orbital motion and other conditions. It is ideal that the mission plan is autonomously carried out onboard, however, it is possible that the changes of the plan are required according to the increasing background level or/and JEM and ISS operational constraints. In Unit 1, the telecommand for such remote controls are generated and are uplinked to JEM via MCR.

In addition, Unit 1 has the functions to enable development and test of telecommands, related software, system patches, et cetera. To debug and to verify the action of newly developed telecommand, Unit 1 accommodates the test facility that includes principal subsystems.

6.4.2. Data process and system monitor unit

The main task of data process and system monitor unit is reception and processes of the downlink data (scientific, monitor, HK, etc). Here all the data is transferred to SODC via MCR. The data are sorted into two classes, requiring frequent-possible downlink or not.

The scientific data such as EECR event data are supposed to be downloaded as little frequent as even once a day. These data are processed in the quick-look analysis to give the preliminary information to scientist. In this analysis, the calibration data such as MAPMT calibration and atmospheric monitoring are reflected.

On the other hand, monitor data from subsystems, HK data, MAMPT calibration data are required to be available permissively more frequently. These data goes through pile-line process and are delivered to ground staffs on duty.

6.4.3. Data management and archiving unit

Data management and archiving unit is responsible for all data management, data distribution and the development of related software. It should be noted that the scientific data will be public-domain after a certain period (details to be determined).

Unit 3 manages raw data from JEM-EUSO, calibration data, atmospheric data, HK data and analysed scientific data plus related information (ex. ISS attitude). The user interface is also developed and delivered with transparent data to retail users. The reconstruction software and subsystem manuals are also managed in this unit.

6.4.4. SODC staff on duty

We will establish 24-hour operation of SODC mainly to monitor the system status. It is expected that about 20 persons of permanent staffs and visiting researchers participates in SODC activities during regular operation. The significant part of tasks, such as mission plan uplink, is performed in daytime on the ground.

The activity in each SODC unit co-runs along with the regular operation. For each unit, we will designate the responsible scientist. In daytime, operating staffs are deployed with a ratio of 2:2:1 for Unit 1:2:3. During night, at least two staffs are on duty to monitor the system and anytime responsible scientist and subsystem experts are in touch. In the commissioning phase, PI and these key persons will devote to establishing the operation scheme.

Reference:

[1] 'Kibo JEM E/F Platform Utilization Handbook, JDX-2006150

7. Development Plan

According to the JAXA documents on call for proposal for the mission candidates of 2nd phase utilization of JEM-EF, the plan is divided into two phases: feasibility study phase (2007 and 2008 fiscal year) corresponding to phase-A, and the development phase (years after 2008 fiscal year) corresponding to phases after phase-B and later. At the end of 2008 fiscal year, the evaluation shall be made whether the plan is advanced into phase B or not. The launch opportunity is estimated in 2013. The development schedule map is shown in Table 8.1.

7.1. Feasibility study phase

We will do the conceptual design and preparation study for Phase-A for 2 years, in 2007 and 2008.

7.1.1. Plan

The key elements of telescope are manufactured, assembled and tested in feasibility study phase. Two sets of main elements: front lens, rear lens, diffractive optical elements, and photo-detector module (PDM) will be manufactured and assembled in the prescribed positions to make the test apparatus. This apparatus plays the role of elemental test model of telescope functions. A beam of UV laser is impinged from the front lens to the focal surface and the path along the optics, transmittance of the optics and sensitivity of the detectors are measured and compared with those designed. An air shower is simulated by a swing of the beam to verify the trigger efficiency of the trigger electronics. The data measured in this test apparatus will be used in the software simulator of JEM-EUSO telescope to estimate the performance of the entire telescope in terms of arrival direction and energy of the extreme energy particles, and X_{\max} of the EAS and energy threshold.

The prototype of the atmospheric monitor is manufactured to design the actual atmospheric monitor effectively.

Mechanical parts such as lid, enclosure cylinder and the tilt mechanism are manufactured and their technical robustness was verified. Radiation and vibration/impact tests will be done for important parts of these mechanisms.

The air-fluorescence observation from the air-shower has been well established in ground observations such as HiRes and Auger experiments. However JEM-EUSO will challenge to observe the air-shower from the space for the first time. In order to make sure the ability of our instrument, we are planned the balloon experiment with laser and detectors.

Furthermore we join TUS (Track Ultraviolet setup) experiment on the Russian Foton satellite that will be the pathfinder of JEM-EUSO. The end-to-end verification of the air-fluorescence observation from orbit will be performed by TUS that will be launched in 2011.

7.1.2. Implementation structure

RIKEN will work as a hub of corporations of space organization (JAXA, NASA, ESA), universities, and research institutions in Japan (Konan Univ., Saitama Univ., KEK, NAOJ, etc.) and international partners (Univ. Alabama in Huntsville, etc.) in feasibility study phase. Major members of JEM-EUSO collaboration are listed with their responsibilities:

Table 7.1 Division of roles

Project PI	Toshikazu Ebisuzaki (RIKEN)
Instrument Manager	Fumiyoshi Kajino (Konan Univ.)
Project Science	Yoshiyuki Takahashi (RIKEN, Univ. Alabama in Huntsville)
Project Manager	Hiroshi Mase (RIKEN)

Optics system	Roy Young (NASA/MSFC), Yoshiyuki Takizawa (RIKEN)
The Whole Focal Surface	Hirohiko M. Shimizu(KEK), Yoshiya Kawasaki (RIKEN)
Focal Surface Detector	Yoshiya Kawasaki (RIKEN)
Focal Surface Electronics	M. Casolino (University of Roma “Tor Vergata”), Tokonatsu Yamamoto (Konan Univ.)
Calibration system	P.Gorodetzky (CNRS, APC), Naoto Sakaki (Aoyama Gakuin Univ.)
Atmospheric Monitor	V.Mitev (Centre Suisse d’Electronique et de Microtechnique), Satoshi Wada (RIKEN)
End-to-End Simulation	D.Naumov (JINR Dubna), Naoya Inoue (Saitama Univ.)
System	JAXA

Below is the organization of JEM-EUSO in development stage.

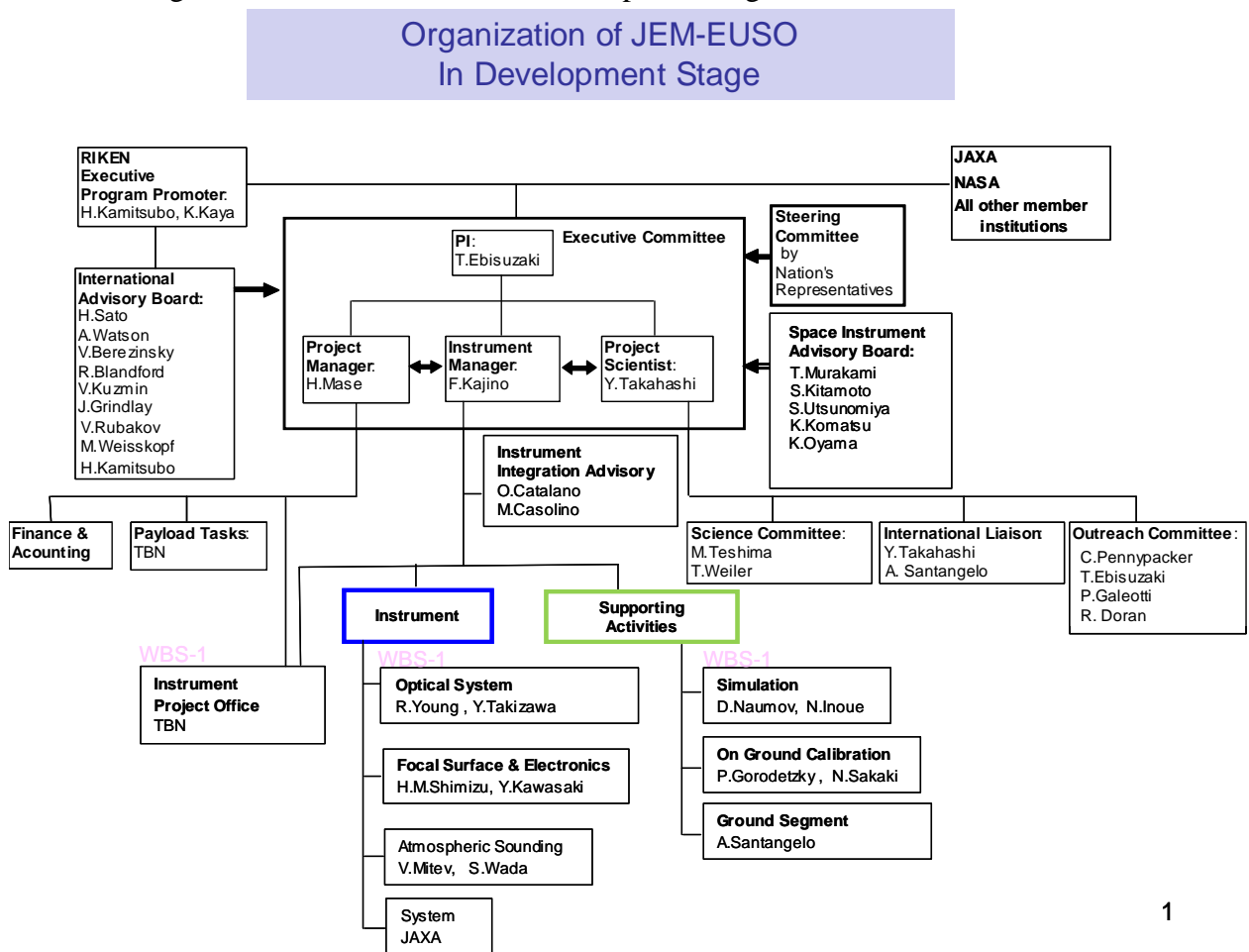


Figure 7.1 Organization of JEM-EUSO in development stage

7.2. Development phase

The organization for the development phase will be discussed and determined by RIKEN, JAXA and participated organizations during feasibility phase taking into account the opinions of the international science community.

7.3. Cost Budget

Total cost, including the manufacturing cost and the observation operating cost, is estimated

about 12 billion yen, in which we estimate 9 billion yen for the mission and 3 billion yen for the bus system.

Japan will pay the bus system cost taking the responsibility of integration, and the mission cost will be shared by Japan, USA, Europe and other countries with almost the same share. Basically, each part will pay around 3 billion yen.

The following is the cost for the development year by year.

Table 7.1 JEM-EUSO Breakdown of the Development cost year by year

Cost Breakdown		mission ready						unit: million YEN=0.01M\$					SUM	
		Fiscal year 2008	Fiscal year 2009	Fiscal year 2010	Fiscal year 2011	Fiscal year 2012	Fiscal year 2013	Fy '14	Fy '15	Fy '16	Fy '17	Fy '18		
Mission	Optics	24	411	1,040	720	656	449							3,300
	F S(Detector)	40	442	422	345	295	56							1,600
	FS(Electronics)	30	464	419	350	290	47							1,600
	Atmospheric Monitoring	10	402	350	284	89	15							1,150
	Calibration	20	50	18	26	73	13							200
	Operation & Ground Sup	0	0	0	0	30	30	120	120	120	120	120		660
Mission sum		124	1,769	2,249	1,725	1,433	610	120	120	120	120	120	8,510	
Bus System		150	500	750	1,000	500	100							3,000
Contingency		10.00	90.00	126.00	115	83	66							490
Summation		284	2,359	3,125	2,840	2,016	776	120	120	120	120	120	12,000	

Table 7.2 is a rough draft of the charges of each country. We will fix the details of each cost by negotiating with relevant institutes by SDR (System Definition Review Mar., 2009).

Table 7.2 JEM-EUSO Development cost share year by year

Cost Share		unit: million YEN=0.01M\$											SUM
		Fiscal year 2008	Fiscal year 2009	Fiscal year 2010	Fiscal year 2011	Fiscal year 2012	Fiscal year 2013	Fy '14	Fy '15	Fy '16	Fy '17	Fy '18	
Japan	RIKEN	45	120	300	300	300	225	40	40	40	40	40	1,490
	University	13	30	54	83	180	80						440
	JAXA(Mission)	40	50	250	250	250	230						1,070
	JAXA(System)	150	500	750	1,000	500	100						3,000
	Japan sum		248	700	1,354	1,633	1,230	635	40	40	40	40	40
USA		30	830	925	607	386	22	40	40	40	40	40	3,000
EU,Korea,Mexico		6	829	846	600	400	119	40	40	40	40	40	3,000
Summation		284	2,359	3,125	2,840	2,016	776	120	120	120	120	120	12,000

Table 7.3 Cost share of development & manufacturing by each country

unit: million YEN=0.01M\$

Cost Share		Japan	France	USA	Swiss	Russia	Korea	Italy	Germany	Mexico	Spain	Summation
Mission	Optics	588		2,712								3,300
	FS Detector	80		5		29		45	436			3,200
	Electronics	80	47	5			515	465	50	14	29	
	PDM manufacturing	1,280	30				30	30	30			
	Atmospheric Monitoring	385	445		320							1,150
Calibration	29	23	55		45		5	28	15		200	
Operation & Ggoround Supp	313	40	100	9	40	40	40	40	19	19	660	
Bus System		3,000										3,000
Contingency	mission	122.5	25	122.5	14	5	25	25	25	2	2	367.5
	system	122.5										122.5
合計		6,000	610	3,000	343	119	610	610	609	50	50	12,000

8. Preparations status

8.1. JEM-EUSO working group

JEM-EUSO working group (WG) has been approved by Steering Committee for Space Science of ISAS/JAXA on June 2006. RIKEN as a hub of corporations, Konan Univ., Aoyama Gakuin Univ., Saitama Univ., etc. are performing research in each role. Research communication meeting is usually held monthly and coordination of each other's researches is managed.

8.2. Activity of Planning Committee at RIKEN Discovery Research Institute

RIKEN Discovery Research Institute has settled "Planning Committee for promoting JEM-EUSO" (Chairperson: Professor Fumitaka Sato, Konan University). The committee discussed the scientific impacts of JEM-EUSO and its organizational problems to promote it. A report was submitted to the director of RIKEN Discovery Research Institute, Dr. Koji Kaya.

The committee concluded as follows:

- i) Scientific impacts of JEM-EUSO mission will be very high. It will open up the new astronomy with charged particles to explore extreme universe.
- ii) It is appropriate to submit the proposal of phase-A study of JEM-EUSO from RIKEN, because
1) it had the responsibility of the development of the focal surface in ESA-EUSO; 2) it has experience of the first phase utilization of ISS/JEM; the Monitor of All-sky X-ray Image (MAXI) and the space mission of High Energy Transient Explorer-2 (HETE-2).
- iii) It is necessary to clarify the responsibilities and role sharing between RIKEN and JAXA, when JEM-EUSO mission will be selected.
- iv) JEM-EUSO mission is the international scientific project promoted by Japanese science community. Eight countries, Italy, France, German, Switzerland, USA, Russia, the Republic of Korea and Mexico will participate in JEM-EUSO. It is necessary to form an appropriate organization and a well-thought-out practicable plan in the Phase-A study.

8.2.1. Selection as the mission candidates of 2nd phase utilization of JEM-EF

Based on the above report, we applied recruitment of the mission candidates of 2nd phase utilization of JEM-EF of which the deadline was Feb. 2007. Then our mission was adopted as a candidate in May 2007. Thus RIKEN and JAXA made a contract for collaborative scientific research and they started 2 years' conceptual design and preparatory research.

8.2.2. International Collaboration Meeting and International symposium

The following International Collaboration Meeting and International Symposium have been organized from Jan. 2007 to Jun. 2008.

- | | |
|-----------|--|
| Jan. 2007 | The first International Collaboration Meeting |
| Mar. 2007 | International Symposium on "Astronomy and Astrophysics of the Extreme Universe".
Proceedings will be published soon. |
| Jun. 2007 | The first International JEM-EUSO meeting (Wako, Japan)
The first International Advisory Board meeting (Wako, Japan) |
| Nov. 2007 | The second International JEM-EUSO meeting (Wako, Japan) |
| Jan. 2008 | The second International Advisory meeting (Wako, Japan)
The advisory report of this meeting is attached as Annex 3 in the end |
| Jun. 2008 | The third International JEM-EUSO meeting (Wako, Japan) |
| Oct. 2008 | The fourth International JEM-EUSO meeting (Turin, Italy) |

8.2.3. Preparation of budget and improvement of organization at RIKEN

Following the report by the above planning committee, RIKEN did a budgetary request of 2008, as a part of the budget of fundamental scientific research. Then RIKEN succeeded in getting about 45 million yen as a part of JEM-EUSO manufacturing cost of which RIKEN is in charge. In addition, "The research of extreme energy particles" was included in the midterm plan (Apr. 1 2008~Mar.31 2013) of RIKEN, as a part of fundamental scientific research. Furthermore, RIKEN is planning to ask an increase in budget paid by RIKEN, in the budgetary request of 2009. Using the above budget as a resource, we have formed the Research Advancement Group of Extreme Space, in the Advanced Science Institute of RIKEN set up in 2008 (refer to Annex 4 for its organization in the end). This was highly advised by the above planning committee and by the third International Advisory Board meeting, and the collaboration between MAXI and JEM-EUSO, which will use the JEM/EF equally, for the space observation, became ready. They will collaborate closely. In addition, international cooperation research team was set up on Jul. 1, 2008. The team is composed of main members from main countries. Mr. Yoshiyuki Takahashi is in charge of team head, as well as responsible for USA. The role of this team is to monitor the international situation and to do the coordination of technology and budget, by supporting the applications for budget in each country.

We are also negotiating for the increase of the mission budget for stowing JEM-EUSO on the space station, in cooperation with the section in charge of JAXA. The universities other than RIKEN are planning to apply subventions for large scale scientific research (specially-promoted, particular field, academic foundation, etc.), and they have already started preparing the application.

8.3. Preparation status in each country

JEM-EUSO is an international project that can be realized by international cooperation. At present time, confirmation of international role-sharing is in progress, mainly by Japan and USA. Regarding the mass for the launch, we will get to work on NASA and ESA through the participants of USA and Europe during the examination phase after the adoption, toward the regeneration of international sharing.

8.3.1. U.S.A.

U.S.A. is in charge of optics of JEM-EUSO and also is contributing to detector, trigger method and ground flashers for calibration. NASA has selected the USA participation to ESA-EUSO, permitting the expenditure of 36M\$ for the entire mission. However, this plan has been frozen because ESA had postponed the Phase-B. NASA/MSFC, as the hub of JEM-EUSO in USA, is requesting to permit resumption on this plan. All members of ESA-EUSO including new members have announced the desire of immediate resumption of this plan to join in JEM-EUSO

NASA/JSC (Johnson Space Center) that is in charge of the utilization of JEM in NASA, has shown a positive response to the use of EFU#2 for JEM-EUSO. NASA has the right of usage of 49 % of JEM-EF.

8.3.2. Europe

At ESA as well as in Europe, distrust of ISS and Space Shuttle increased since last autumn. Since then, as it was decided that all the ISS stowing experiments will not to be included in the budget of the scientific section, this experiment cannot be paid with this budget. However, gaining support from other departments such as manned space station department is considered favorable. Preparation status in each country is as follows:

In Italy, "Studio di Astrofisica delle Alte Energie (AAE) - Proposta di nuove Missioni ed

Occasioni di missione (2 anno)" was adopted by the Italian Space Agency, as a preparatory study of the JEM-EUSO in Italy, and 74k euros of expense was accepted. This will allow a full-scale qualification for the budget requirement, and the above is a preparatory budget allocation. In addition, JEM-EUSO was adopted as "Italo-Japanese collaborative scientific research program", and 100kEuro budget has been allocated by the Italian Ministry of Foreign Affairs ("Ministero degli Affari Esteri, Direzione Generale per la Promozione e Cooperazione Culturale") for JEM-EUSO in the fiscal year 2008.

French JEM-EUSO team will submit their proposal to the CNES (Centre National d'Études Spatiales) and to the CNRS, and a preparatory meeting among CNES, CNRS, and the Director of RIKEN Discovery Research Institute, was held in March in Paris. In addition, JEM-EUSO was adopted as the new "Franco-Japanese collaborative scientific research program", sponsored by CNRS.

In Germany, the group of Mr. Teshima of Max-Planck-Institut (MPI) obtained 1M euros, as 5 years' R&D cost for the development of the JEM-EUSO detector (SiPM) from the internal budget of MPI. In addition, Professor Andrea Santangelo of University of Tübingen, a key figure of German JEM-EUSO team, is planning to do an application of around 4M euros, from September to October in 2008, as a matching fund between German Aerospace Center (Deutsches Zentrum für Luft-und Raumfahrt) and MPI. In addition, Switzerland and Spain show their intention to participate.

8.3.3. Korea

Prof. I. Park of Ehwa, as the leader of the team, is developing an electric circuit for triggering purposes to be stowed in the telescope and MEMS mirror for the deflection of the Lidar beam.

8.3.4. Mexico

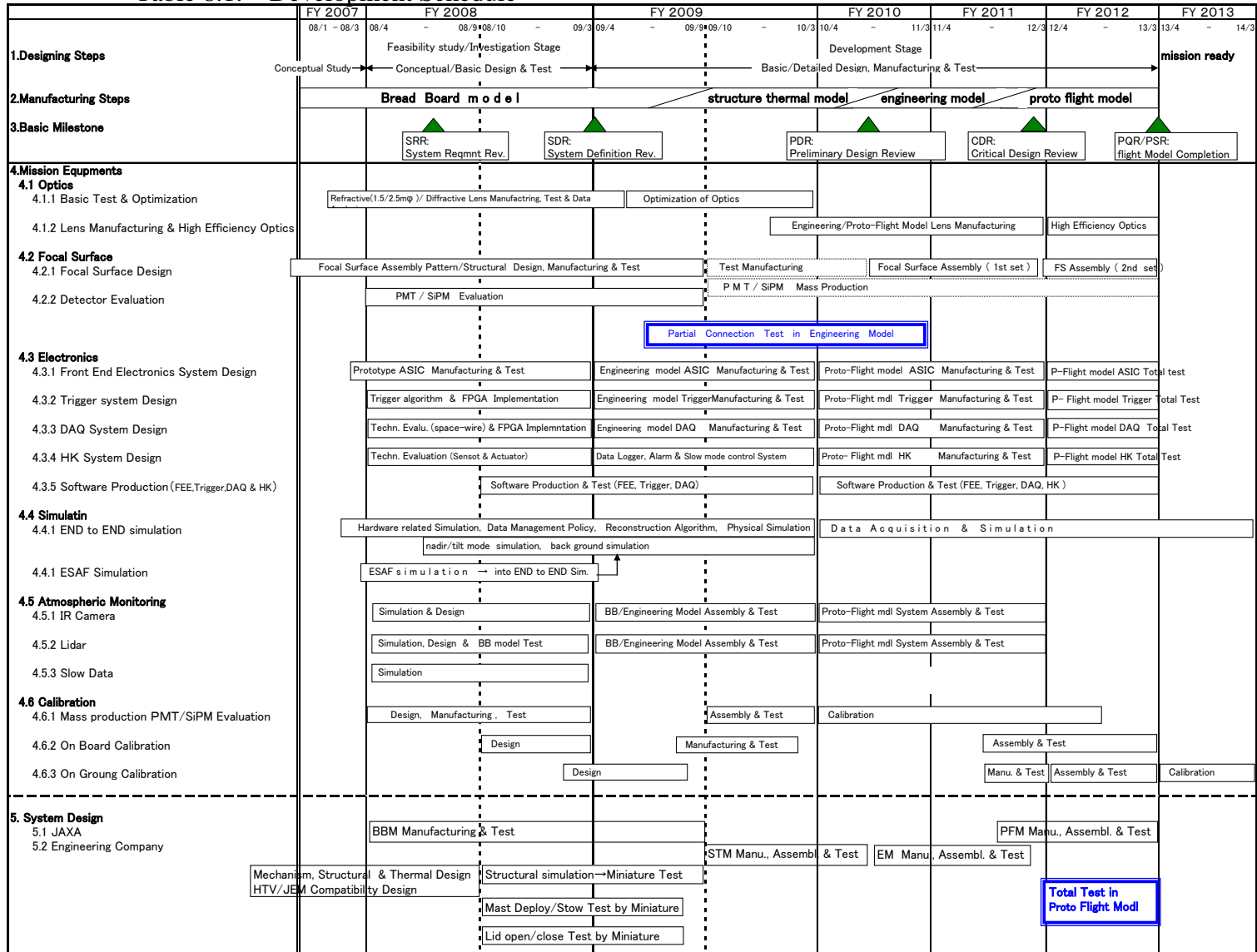
Universidad Nacional Autonoma and Benemerita and Universidad Autonoma de Puebla are showing their intention to participate.

8.3.5. Russia

SINP MSU and Dubna JINR announced to participate in JEM-EUSO. Japan JEM-EUSO team will join TUS experiment to verify the technologies (photomultipliers and readout electronics) that will be used in JEM-EUSO. TUS is promoted by MSU and will be scheduled to launch in 2009. Possibility of cooperation in detector developments is under discussion.

8.4. Development Schedule

Table 8.1. Development Schedule



Annex 1 : Dictionary of abbreviations

AGASA	Akeno Giant Air Shower Array
AGN	Active Galactic Nuclei
ASIC	Application Specific Integrated Circuit
CCB	Cluster Control Board
CPU	Central Processing Unit
DCDC	DC to DC Converter
DSP	Digital Signal Processor
EAS	Extensive Air-Shower
EC	Elementally Cell
EFU	Exposed Facility Unit
ESA	European Space Agency
EUSO	Extreme Universe Space Observatory
EVA	Extra-Vehicular Activity
FSA	Focal Surface Assembly
FPGA	Field Programmable Gate Array
GRB	Gamma-Ray Burst
GTU	Gate Time Unit
GZK	Greisen-Zatsepin-Kuz'min
HAS	Horizontal Air-Shower
HiRes	High Resolution Fly's Eye Cosmic Ray Observatory
HK	House Keeping
HSM	Harness Separation Mechanism
HTV	H-II rocket Transfer Vehicle
ISCCP	International Satellite Cloud Climatology Project
ISS	International Space Station
JAXA	Japan Aerospace eXploration Agency
JEM	Japan Experiment Module
JEM/EF	Japan Experiment Module / Exposure Facility
JEMRMS	JEM Remote Manipulator System
LHC	Large Hadron Collider
Lidar	LIght Detection And Ranging
LPM	Landau-Pomeranchuk-Migdal
MAPMT	Multi-Anode Photomultiplier Tube
MC	Movement Controller
MDP	Mission Data Processor
MLI	Multi-Layer Insulation
MPU	Micro Processor Unit
NASA	National Aeronautics and Space Administration
NBE	Narrow Bipolar Event
PDM	Photo Detector Module
PDMCB	PDM Control Board
PIU	Payload Interface Unit
PMMA	Poly- MethylMethAcrylate
PMT	PhotoMultiplier Tube
RLG	Ring Laser Gyroscope
PSF	Point Spread Function
RMS	Remote Manipulator System

SSRMS	Space Station Remote Manipulator System
TIROS	Television Infrared Observation Satellite
TOVS	TIROS Operational Vertical Sounder
TSM	Tie-down Separation Mechanism
UAS	Upgoing Air-Shower
VSC	Visual Star Camera

Annex 2 : Temperature analysis

The analysis in case of PMT was done by RIKEN using a simple model, which does not take into consideration shadows made by surrounding structures. On the other hand, the analysis in case of SiPM was done using a mathematical model made by the engineering company (IHI AeroSpace), which has experiences in space experiments. This model is more accurate because it takes into consideration shadows made by surrounding structures.

A1.1 Analysis in case of PMT

The case of using M36 (Baseline) as PMT was analyzed using the simple model by RIKEN. The telescope was considered to be a cylindrical shape. And the observation time was 45 minutes, a half of 1 orbital cycle (90 min.).

Regarding the electric power setting, we examined the following 2 cases:

(1) In case of the necessary electric power 641W in the nighttime (the sum of: PDM, CCB, MDP, EBOX (mission) 498W, EBOX (BUS) 138W, Altitude Sensor 5W), and 229W in the daytime as BEE value of M36 PMT.

(2) In case of the necessary electric power $383W \times 1.3 = 498W$ (nighttime), $77 \times 1.3 = 101W$ (daytime) only for PDM as margin included value of M36 PMT. $\times 1.3$ means 30% margin value.

The temperature and the necessary heat sink in case of (1):

To achieve allowable temperature (temperature on the focal surface: less than $30^{\circ}C$), if the function of the lid is normal, cooling power around -50W is required. Figure A1.1 shows the

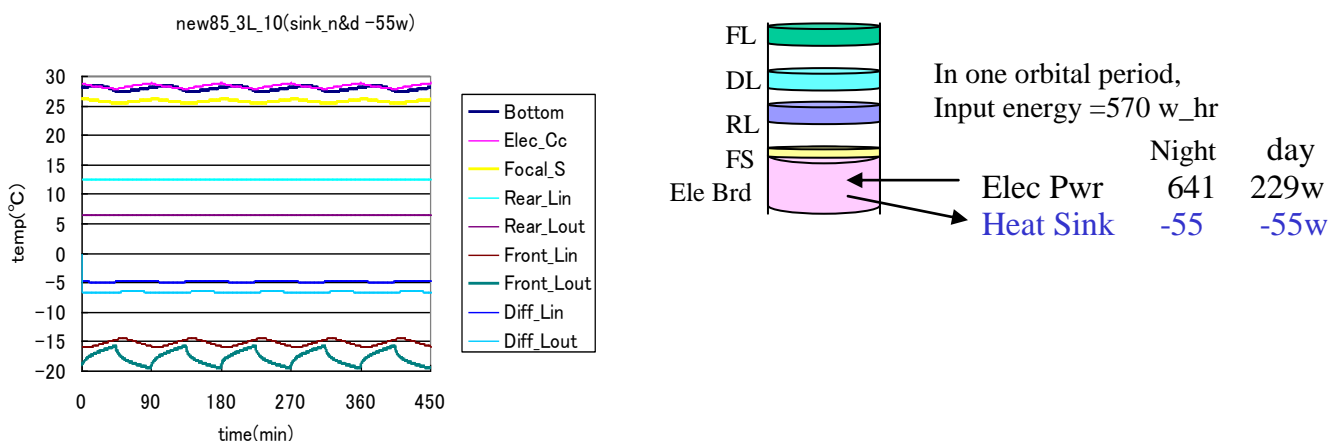


Figure A1.1 Temperature distribution in case of a large electric power

If the lid remains open and its function is suspended, the albedo of the sun enters the telescope during daytime. Thus, larger cooling power is required (around -285W).

The temperature and the necessary heat sink in case of (2):

To achieve allowable temperature (temperature on the focal surface: less than $30^{\circ}C$), if the function of the lid is normal, it is necessary to remove only the energy consumption of PDM, and we concluded that a special cooling device to satisfy the temperature requirements of the focal surface detector is not necessary.

Figure A1.2 shows the results.

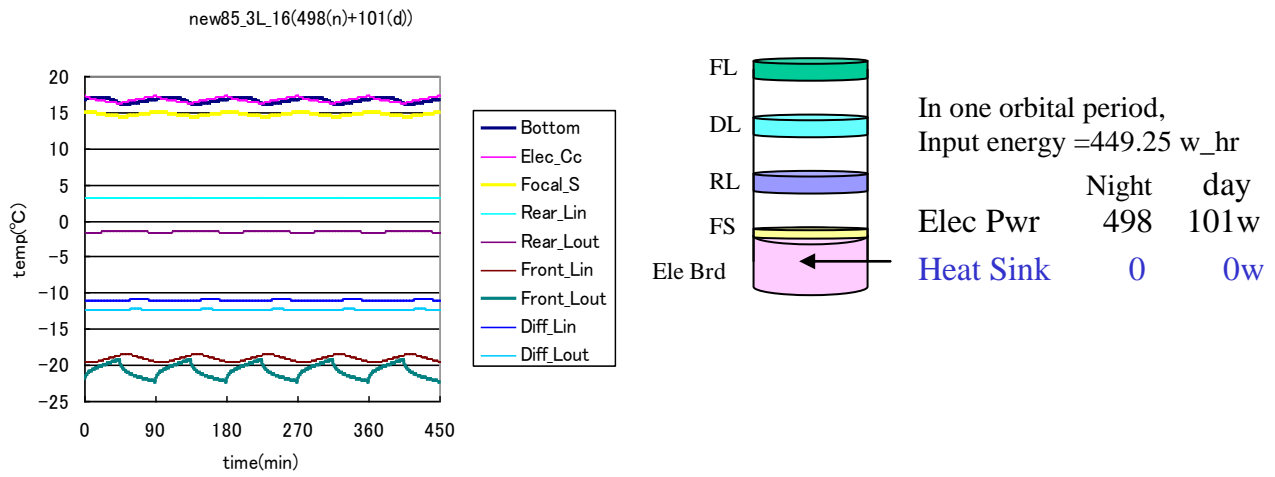


Figure A1.2 Temperature distribution in case of a small electric power

However, if the lid remains open and its function is suspended, the albedo of the sun enters the telescope during the daytime. Thus, larger cooling power is required (around -145W).

A1.2 Analysis in case of SiPM

Figure A1.3 shows the model of JEM-EUSO and the time conditions for the observation.

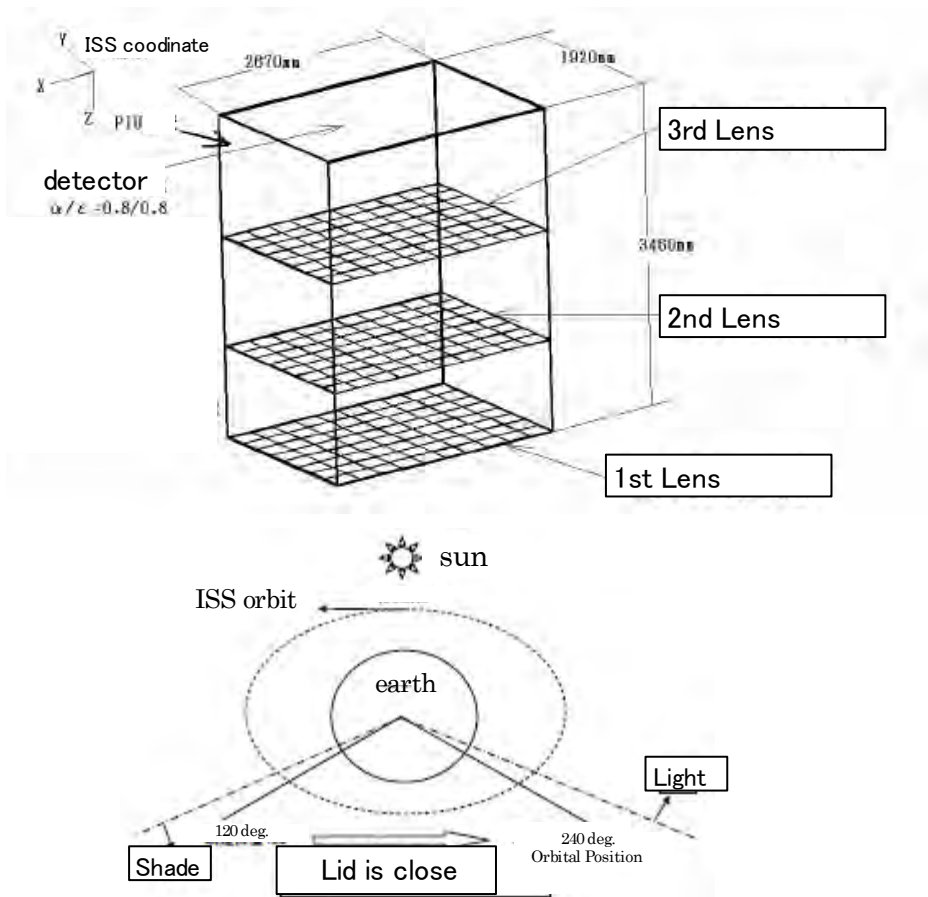


Figure A1.3 Model of JEM-EUSO and observation time (ref. [1])

After the analysis, the temperature variation of the inner surfaces of lens was maximum 4.5[°C]

with the lid, less than 1[°C] without the lid. In this analysis, the lens was considered as monolithic, and there was no modeling of the frame and the ring. In addition, we did not take into consideration the heat conduction between the lens and the MLI, which is the external cylinder of the telescope. However, we are highly confident to achieve the target temperature variation, less than 10[°C], by thermally combining the divided lens by the metallic frame and ring, and by making effort in designing to reduce the heat conduction between MLI of the external cylinder of the telescope.

Furthermore, assuming the SiPM detector, the necessary quantity of heat dissipation to keep the sensor surface less than -15[°C], dissipating the generated heat by the electric devices associated with detector, was at maximum around 100W with the lid and at maximum 350W without the lid. In this analysis, we considered that there was only MLI on the sensor surface, and that the thermal input around 50[W] caused by the heated MLI by the radiation to the sensor surface, is included. Thus, if we succeed in making the design to insulate heat flow between the sensor surface and the MLI, we estimate that the necessary quantity of the heat dissipation will be maximum around 50[W] with the lid, and around 300[W] without the lid. If we cool the sensor surface till -15[°C] with the Peltier device, and dissipate the heat to ATCS, the necessary electric power to cool using the Peltier device will be about 2.7 times of the necessary heat dissipation. So we estimate the necessary electric power to keep the sensor surface -15[°C], maximum around 135[W] with the lid, and maximum around 800[W] without the lid. All the above results show the efficacy of the lid. In the meanwhile, we also understand that the thermal impact in case of its trouble is also large. The following figure shows the not homogeneities of each lens with the lid. Refer to figure A1.4.

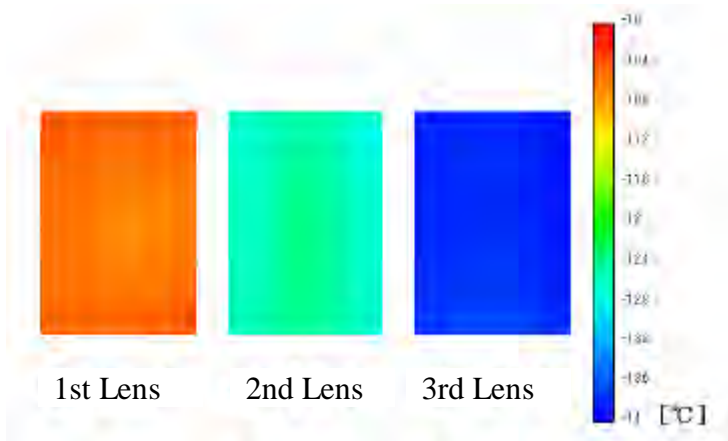


Figure A1.4 Contour of lens temperature ($\beta=0^\circ$, with opening/ closing of the lid) (ref. [1])

February 1, 2008

Recommendations

The international advisory board of JEM-EUSO program is organized to recommend RIKEN for the basic plan to promote studies of extreme energy universe. The board members are as follows:

- Dr. H. Sato (Chair, Konan University and Yukawa Memorial Foundation, Japan)
- Dr. A.A. Watson (University of Leeds, UK)
- Dr. V. Berezhinsky (INFN, Laboratori Nazionali del Gran Sasso, Italy)
- Dr. R. Blandford (Stanford University, USA)
- Dr. V.A. Kuzmin (Institute for Nuclear Research of the Russian Academy of Sciences, Russia)
- Dr. J. Grindlay (Harvard University, USA)
- Dr. V. Rubakov (Institute for Nuclear Research of the Russian Academy of Sciences, Russia)
- Dr. M.C. Weisskopf (NASA/MSFC, USA)
- Dr. H. Kamitsubo (RIKEN, Japan)

JAXA (Japan Aerospace Exploration Agency) selected JEM-EUSO in May 2007 as the candidate mission of the second utilization phase of Japanese Experiment Module (JEM) of ISS. The phase-A study began in September 2007 in cooperation with JAXA and RIKEN.

The second meeting of the international advisory board was held on 31st January and 1st February 2008. Unfortunately, three members (Dr. R. Blandford, and Dr. V.A. Kuzmin and Dr. V. Rubakov) were absent in the meeting. The first day was devoted to the discussions of the science objectives of JEM-EUSO and this part of the meeting was openly offered to the science communities.

Based on the discussions in this 2nd meeting, we recommend the following.

1) Science Objectives

JEM-EUSO will be the first space observatory to detect air showers induced by the extreme energy cosmic-rays. It is designed to detect, in a few years of operation, more than a few thousands of events with energy greater than 7×10^{19} eV. This number exceeds the critical value to observe all the sources at least once within one hundred Mpc even when the Greisen-Zatsepin-Kuzmin (GZK) suppressions are at work. Hence, JEM-EUSO is very likely to initiate a new astronomy with these charged particles (10^{19} eV $< E < 10^{21}$ eV). Because they are deflected by only several degrees by galactic and extragalactic magnetic fields, these extreme energy particles can be traced back to the origin in the measured arrival direction, just like in the usual astronomy with photons. A sign of the spatial small-scale clustering of the events was also reported by AGASA. On November 9, 2007, the Pierre Auger Observatory reported the likely small-scale correlation of the arrival directions of 27 cosmic-rays with the positions of nearby active galactic nuclei (AGNs) and also, a mid-scale clustering around Cen-A. Details of the new observation by the Pierre Auger Observatory are reported by one of its leading members (AW) and discussed in the meeting. The board concludes that this important result of the Pierre Auger Observatory strongly supports the main objectives of JEM-EUSO which has an exposure per year about 60 times larger than that of the Pierre Auger Observatory.

One of the board members (VB), at this meeting, presented the predictions of neutrino flux based on various conventional and unconventional physics in this meeting. According to his report, JEM-EUSO has an ability to detect the predicted neutrino fluxes for many models and in the negative case to set significant constraints.

In conclusion, the board approved the soundness and compelling nature of the science objectives of JEM-EUSO and recommends the executive committee to keep the efforts along this line.

2) International Collaborations

JEM-EUSO has been promoted by international collaborations among ten countries: those are Japan, USA, France, Italy, Germany, Mexico, Republic of Korea, Russia, Spain, and Switzerland. Organizational structure and

role-sharing among international partners are appropriate, beside the part of software development. The board recommends to executive committee to strengthen the software development of both on-board electronics and analysis in ground.

3) Organization in RIKEN

RIKEN, as the PI institution, is expected to perform the major role and contribution to the JEM-EUSO mission, in cooperation with JAXA, NASA, and all other member institutions. The designs, productions, integrations, and verifications of the parts of the telescope will be carried out by many institutions, individually and cooperatively, and in parallel to other sub-systems. RIKEN has an obligation and ability to promote such an international collaboration project; it has a great heritage of successful promotion of several major international projects. RIKEN-RAL laboratory and RIKEN-BNL center are such examples. The board believes that a central organization for the common ground is necessary to be established in RIKEN so that all the participants and the community to get together and to bring in their contributions. It is most desirable to include the world experts of various related fields to make the frontier of extreme universe science synergistically very effective and productive.

Ohmori Material Fabrication Laboratory has unequalled technologies for the precise fabrication of optical devices in world wide. The advisory board believes that their contribution is essential for the manufacturing of optics of JEM-EUSO.

MAXI (Monitor of All-sky X-ray Image), being developed and fabricated under the collaboration among JAXA, RIKEN, Osaka University, Tokyo Institute of Technology, and Aoyama Gakuin University, Nihon University, and Kyoto University will explore the all-sky energetic sources, via nearly continuous coverage of a large fraction of the entire sky in X-rays; it will be launched in early 2009 as the first phase mission of JEM-EP and its hardware is presently near completion. MAXI will be operated for several years after the launch. From both technical and scientific aspects, the heritage of MAXI, as the preceding mission for exploration of the energetic universe, is critically important to the successful completion of the JEM-EUSO mission. Furthermore, one of the members (JG) pointed that the objectives of MAXI includes the monitoring of time variation of AGNs which

are the promising candidates of the origin of the EECRs. The board recommends that JEM-EUSO team may strengthen their cooperation with the RIKEN MAXI members, for synergetic evolution of pioneering studies of extremely energetic universe.

Dr. H. Sato



Dr. J. Grindlay



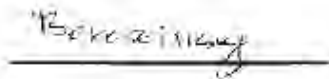
Dr. A. A. Watson



Dr. M.C. Weisskopf



Dr. V. Berezhinsky



Dr. H. Kamitsubo



Annex 4 : Research Advancement Group of Extreme Space

as of Jul. 1, 2008

Group Head : Kazuo Makishima (Makishima Cosmic Radiation Lab., Chief Scientist)

(1) Cosmic X-ray Research Team

[Team Head : Kazuo Makishima Chief Scientist (Makishima Cosmic Radiation Lab.)]

Tatehiro Mihara Senior Scientist (Makishima Cosmic Radiation Lab.)
Nobuyuki Kawai Senior Visiting Scientist (Research Advancement Group of Extreme Space)
Atsumasa Yoshida Visiting Scientist (Research Advancement Group of Extreme Space)

(2) Optics Fabrication and Application Research Team

[Team Head : Hitoshi Omori Chief Scientist (Omori Materials Fabrication Lab.)]

Kazutoshi Katahira Full-time Researcher (Omori Materials Fabrication Lab.)
Kouki Maekawa Associate Visiting Researcher (Omori Materials Fabrication Lab.)
Yosuke Hachisu Associate Visiting Researcher (Omori Materials Fabrication Lab.)

(3) Particle Astrophysics Research Team

[Team Head : Toshikazu Ebisuzaki Chief Scientist (Ebisuzaki Computational Astrophysics Lab.)]

Yoshiyuki Takizawa Researcher (Ebisuzaki Computational Astrophysics Lab.)
Yoshiya Kawasaki Associate Visiting Researcher (Ebisuzaki Computational Astrophysics Lab.)
Hiroshi Mase Associate Visiting engineer (Ebisuzaki Computational Astrophysics Lab.)
Fumiyoshi Kajino Senior Visiting Scientist (Research Advancement Group of Extreme Space)
Naoya Inoue Visiting Scientist (Research Advancement Group of Extreme Space)
Masahiro Teshima Senior Visiting Scientist (Research Advancement Group of Extreme Space)
Masaki Fukushima Senior Visiting Scientist (Research Advancement Group of Extreme Space)
Hirohiko Shimizu Senior Visiting Scientist (EN'YO Radiation Lab.)

(4) Solid State Laser for Astronomical Observation Research Team

[Team Head : Satoshi Wada Research Unit Leader (Solid-State Optical Science Research Unit)]

Akinori Saito Associate Visiting Researcher (Solid-State Optical Science Research Unit)
Takayo Ogawa Associate Visiting engineer (Solid-State Optical Science Research Unit)

(5) International Cooperative Propulsion Research team

[Team Head (adjunct) : Yoshiyuki Takahashi (Prof. Department of Physics, Univ. of Alabama)]

Toshikazu Ebisuzaki (Ebisuzaki Computational Astrophysics Lab., Chief Scientist)
Philippe Gorodetzky (Astro-Particle and Cosmology Lab., Prof. Emeritus at CNRS)
Piergiorgio Picozza (Istituto Nazionale di Fisica Nucleare (INFN), Prof. Univ. of Roma)
Andrea Santangelo (Prof. Institute for Astronomy and Astrophysics, Univ. of Tübingen)
Il Hung Park (Prof. Department of Physics, Ewha Womans Univ.)